Design and measurement of multi-antenna systems toward future 5G technologies

Cyril Buey

UNIVERSITÉ CÔTE D'AZUR

ÉCOLE DOCTORALE
SCIENCES ET TECHNOLOGIES DE L'INFORMATION ET DE LA COMMUNICATION

THÈSE DE DOCTORAT

Conception et Mesure de systèmes Multi-Antennes pour les Futures Technologies 5G

Cyril Buey

Laboratoire d'Electronique, Antennes et Télécommunications (L.E.A.T.)

Présentée en vue de l'obtention du grade de docteur en électronique **d'**Université Côte d'Azur
Dirigée par : Jean-Yves Dauvignac
Co-encadrée par : Philippe Ratajczak
Soutenue le : 19 Avril 2018

Devant le jury, composé de :
Canneva Florian
Dauvignac Jean-Yves
Ferrero Fabien
Lizzi Leonardo
Ratajczak Philippe
Sharaiha Ala
Vigneras Valérie
Vuong Tan-Phu

orange™

Conception et Mesure de systèmes Multi-Antennes pour les Futures Technologies 5G

Jury :

Président du jury

Valérie Vigneras, Professeure, INP de Bordeaux

Rapporteurs

Ala Sharaiha, Professeur, Université Rennes 1
Tan-Phu Vuong, Professeur, INP de Grenoble

Examinateurs

Jean-Yves Dauvignac, Professeur, Université Côte d'Azur
Fabien Ferrero, Maitre de Conférence, Université Côte d'Azur
Philippe Ratajczak, Ingénieur, Orange Labs
Florian Canneva, Ingénieur, Ethertronics France
Leonardo Lizzi, Maitre de Conférence, Université Côte d'Azur

Titre : Conception et Mesure de systèmes multi-antennes pour les futures technologies 5G**.**

Résumé :

Dans le cadre de cette thèse nous étudions les technologies porteuses de la 5ème génération de communication mobile telle que le MIMO et Massive MIMO ainsi que les divers challenges amenés par l'apparition de ces nouvelles technologies.

Le chapitre 1 présente l'évolution des systèmes de communication sans fil (2G, 3G, 4G et 5G) ainsi que leurs principales caractéristiques. Le chapitre décrit ensuite les réseaux locaux de type « WLAN » Il donne ensuite les caractéristiques principales des Réseaux locaux ainsi que les types d'antennes généralement utilisées dans les terminaux mobile et les point d'accès sans fil. Ce chapitre se termine sur une conclusion donnant les objectifs des travaux réalisés dans la thèse.

Le deuxième chapitre se consacre dans un premier temps à la comparaison de différentes méthodes de test permettant la caractérisation des performances des antennes MIMO. Dans un second temps, le chapitre décrit la mise en œuvre de deux bancs de mesure spécifiques pour la caractérisation des performances des antennes MIMO en WLAN et LTE. Le premier banc de mesure a été réalisé à partir d'instruments de mesures Rhodes & Schwarz (générateur de signaux et analyseur de spectre). L'opportunité de travailler avec EURECOM nous a amenés à développer un second banc de test en utilisant l'OpenAirInterface, une plateforme open-source exploitant des systèmes de radio par logiciel.

Le chapitre 3 présente la conception et la réalisation d'une série de prototypes de routeur Wi-Fi constitués de huit antennes. Chaque prototype est réalisé à partir d'antennes différentes (imprimées, 3D…) ou présente une configuration différentes afin de mener des études comparatives. Nous avons également réalisé une seconde série prototypes de routeur Wi-Fi constitué de huit antennes imprimés sur plastique grâce à la technologie LDS. Les différents prototypes sont caractérisés expérimentalement en mesurant l'adaptation, le gain, l'efficacité et le couplage entre éléments. Une campagne de mesure a ensuite été réalisée avec ces prototypes sur le banc de test évoqué ci-dessus pour extraire des critères de performance antennaire utiles pour les applications MIMO. Ces études ont pour objectif d'apporter des éléments d'optimisation sur les techniques MIMO d'un point de vue antennaire. Enfin dans la dernière partie du chapitre, l'étude se consacre à l'évaluation de l'influence du diagramme de rayonnement des antennes sur les performances du routeur multi-antenne. Une nouvelle structure d'antenne présentant un digramme directionnel est réalisée, caractérisée puis tester sur le banc de test dédié.

Le quatrième et dernier chapitre de cette thèse est dédié aux fréquences millimétriques qui sont au cœur de la 5G. Ce chapitre présenta la conception et la réalisation d'un prototype de téléphone constitué de quatre antennes millimétriques. Une mesure permettant de prendre en compte les interférences avec le corps humain a été mise en place pour étudier les contraintes liées à l'implantation d'antennes millimétriques dans les futurs terminaux mobiles.

Mots clés : MIMO, Wi-Fi, 4G, 5G, Mesure d'antennes

Title: Design and measurement of multi-antenna systems toward future 5G technologies

Abstract:

In this thesis, we are studying the main technologies carrying the 5th generation of mobile communication such as MIMO and Massive MIMO as well as the various challenges brought by the appearance of these new technologies.

Chapter 1 presents the evolution of wireless communication systems (2G, 3G, 4G and 5G) and their main features. The chapter then describes local area networks of the "WLAN" type. It then gives the main characteristics of Local Area Networks as well as the types of antennas generally used in mobile terminals and wireless access points. This chapter ends with a conclusion giving the objectives of the work done in the thesis.

The second chapter focuses in a first time, to the comparison of different test methods allowing the characterization of the performances of the MIMO antennas. In a second step, the chapter describes the implementation of two specific measurement setup for the performance characterization of MIMO antennas in WLAN and LTE. The first test bench was made from Rhodes & Schwarz measuring instruments (signal generator and spectrum analyzer). The opportunity to work with EURECOM led us to develop a second test bench using the OpenAirInterface, an open-source platform exploiting software radio systems.

Chapter 3 introduces the design and realization of a series of Wi-Fi router prototypes consisting of eight antennas. Each prototype is made from different antennas (printed, 3D ...) or has a different configuration to conduct comparative studies. We also made a second series of Wi-Fi router prototypes consisting of eight antennas printed on plastic using LDS technology. The different prototypes are experimentally characterized by measuring adaptation, gain, efficiency and coupling between elements. A measurement campaign was then carried out with these prototypes on the test bench mentioned above to extract antennal performance criteria useful for MIMO applications. These studies aim to provide optimization elements on MIMO techniques from an antenna point of view. Finally, in the last part of the chapter, the study is devoted to the evaluation of the influence of the antenna radiation pattern on the performance of the multi-antenna router. A new antenna structure presenting a directional diagram is realized, characterized and tested on the dedicated MIMO-OTA test bench.

The fourth and final chapter of this thesis is dedicated to the millimeter frequencies that are at the heart of 5G. This chapter presented the design and realization of a mobile phone prototype consisting of four millimeter antennas. Measurements to take into account the

interference with the human body has been set up to study the constraints related to the implantation of millimeter antennas in future mobile terminals.

Keywords: MIMO, Wi-Fi, 4G, 5G, OTA Measurement

Remerciements

Je tiens tout d'abord à remercier Monsieur Ala Sharaiha et Monsieur Tan-Phu Vuong pour avoir accepté d'être les rapporteurs de cette thèse. J'aimerais également adresser un remerciement particulier à Madame Valérie Vigneras pour me faire l'honneur de présider le jury lors de la soutenance. Je remercie également Monsieur Florian Canneva d'avoir accepté de prendre part au jury de cette thèse.

Je tiens ensuite à remercier Monsieur Jean-Yves Dauvignac pour son accueil chaleureux au sein du LEAT, pour avoir accepté le rôle du directeur de thèse et pour sa présence dans ce jury. Un grand merci à Leo pour faire partie de ce jury, pour sa relecture attentive des articles et ses bons conseils pour les présentations orales lors des conférences mais aussi pour tous ses encouragements positifs et sa sérénité contagieuse.

Je souhaite remercier tout particulièrement Fabien pour son encadrement pendant ses trois années de thèse, pour son dynamisme, sa disponibilité, son enthousiasme, sa pédagogie, pour tous ses conseils, son expérience, sa vision des choses et pour toute la motivation et la bonne humeur qu'il a su me transmettre au quotidien. Je remercie tout aussi particulièrement Philippe pour son encadrement pendant ces trois ans, pour sa grande disponibilité, son expertise inégalée sur la plupart des sujets que j'ai pu aborder, pour ses conseils techniques précieux sur les outils de simulation, la conception, le diverses réalisations, les méthodes de mesures et bien sûr pour la bonne humeur qu'on a partagé dans notre bureau Sophiapolitain. Encore merci à vous deux pour votre encadrement complémentaire sans lequel tous ces travaux n'aurait pas été possible.

Je tiens également à remercier toute l'équipe de la Turbie pour m'avoir accueilli et formé, pour m'avoir transmis vos connaissances et pour m'avoir fait grandir professionnellement et personnellement. Je remercie Jean-Louis pour ses nombreux conseils, pour son recul et sa vision des choses et ses critiques constructives qui m'ont souvent aidé. Merci à Éric pour tous ses conseils sur les systèmes de mesure et pour sa rigueur. Merci à Theoni pour le travail que nous avons réalisé ensemble, pour toutes les pauses partagées et pour son amitié. Merci à Laurent pour ses nombreuses interventions informatiques. Merci à Frédéric pour tous les prototypes qu'il a réalisé pour ma thèse et pour m'avoir montré les ficelles de la mécanique avec passion. Merci à Jean-Pierre et Roger pour les parties de ping-pong fort déstressantes. Je remercie Christian et Jean-Marc pour les coups de main

qu'ils m'ont données sur certains designs et mesures d'antennes. Plus généralement je remercie Delphine, Éric et les Alain pour tous les bons moments passés et leurs bons conseils. Merci à tous pour le baby-foot. Je remercie aussi tous les collègues d'Orange à Sophia avec qui j'ai partagé de bons moments autour d'un café.

Je souhaite remercier toute l'équipe du LEAT avec qui j'ai pu collaborer, notamment Laurent pour son aide sur les mesures sur le banc 3D. Je remercie tous mes collègues et amis thésard du LEAT avec qui j'ai passé de très bons moments entre conversations absurdes et débats houleux aussi bien au labo qu'en dehors. Merci à Mathieu, Kaoutar, Chaka, Cheik, Lamia, Calypso, David, Abdellah, Fabien, Oualid, Akimu, Assane, Innocent, Florence, Van-Hieu et a tous ceux que j'aurai oublié !

Je tiens à remercier Monsieur Amaury Veille de la société Smart Plastic Product pour son expertise sur les plastiques et sur la technologie LDS. Je remercie également Monsieur Valérie Guillet d'Orange Labs Belfort pour les travaux réalisé avec les prototypes.

Enfin, je tiens à remercier tous mes proches, famille et amis. Un grand merci à mes parents, à mon frère et à ma grand-mère pour leur soutien, leurs encouragements, pour m'avoir toujours poussé pour en arriver là. Le plus grand des merci à Marie, avec qui j'ai partagé ma vie pendant ces années de thèse, merci d'avoir été présente à chaque instant, pour m'encourager, me soutenir, me supporter et m'aimer quoi qu'il arrive. Merci à Stan, Julie et Nils qui font le déplacement pour la soutenance. Merci à tous mes amis Lyonnais pour leur amitié intacte malgré la distance qui nous sépare. Merci à Enrique pour ton humour.

Merci à tous ceux qui ont fait de thèse un moment particulier.

Table of content

ABSTRACT **11**

1. CONTEXT AND MOTIVATIONS **13**

1.1. EVOLUTION OF WIRELESS COMMUNICATION NETWORKS 15

1.1.1. 2G Cellular Network *15*

1.1.2. 3G Cellular Network *16*

1.1.3. 4G Cellular Network *17*

1.1.4. 5G Cellular Network *20*

1.2. WIRELESS LOCAL AREA NETWORK (WLAN) 22

1.3. ANTENNAS FOR CELLULAR COMMUNICATIONS AND LOCAL NETWORKS 25

1.3.1. Antenna Parameters *25*

1.3.2. Mobile Phones and Access-point Antennas *27*

1.3.3. Base Station Antennas *30*

1.4. MOTIVATION OF THE THESIS 31

1.5. REFERENCES 32

2. OVER-THE-AIR MEASUREMENT SYSTEMS FOR MIMO ANTENNAS **33**

2.1. MIMO OVER-THE-AIR MEASUREMENT 35

2.1.1. MIMO OTA Measurement with Two-Stage Method *37*

2.1.2. MIMO OTA Measurement with Reverberant Chamber *38*

2.1.3. MIMO OTA Measurement with Multi-probe technique *39*

2.2. MIMO OTA MEASUREMENT WITH RHODES&SCHWARTZ INSTRUMENTATION 40

2.2.1. Testbed Overview *40*

2.2.2. System Configuration *42*

2.2.3. Validation of the Measurement Setup *44*

2.3. MIMO OTA MEASUREMENTS WITH OPENAIRINTERFACE 46

2.3.1. OpenAirInterface *46*

2.3.2. Testbed Overview *48*

2.3.3. System Configuration *49*

2.3.4. Validation of the measurement setup *50*

2.4. SYNTHESIS OF MIMO OTA MEASUREMENT AND CONCLUSIONS 52

2.5. REFERENCES 53

3. MIMO ANTENNA DESIGN FOR MULTI-STANDARD GATEWAY / WI-FI, LTE, 5G **54**

3.1. MULTI ANTENNA SYSTEMS 57

3.1.1. MIMO Systems and characteristics *57*

3.1.2. Diversity Techniques *58*

3.1.3. Spatial Multiplexing 61
3.1.4. Beamforming 62
3.1.5. Massive MIMO Systems 63
3.2. DESIGN OF 8-ANTENNA PROTOTYPES 64
3.2.1. Box Design for LDS Technology 65
3.2.2. Hook Shaped Antenna printed on a PCB substrate 68
3.2.3. Printed IFA with PCB technology 73
3.2.4. PIFA with PCB technology 77
3.2.5. Mixed prototype with hook shaped antennas, PIFA and IFA on PCB technology 82
3.2.6. Hook-shaped printed on the sides of a plastic box with LDS technology (S1) 85
3.2.7. Hook-shaped antenna printed on the top of a plastic Box with LDS technology (T2) 88
3.2.8. Summary of the different prototypes 90
3.3. MEASUREMENTS RESULTS WITH OPENAIRINTERFACE 92
3.3.1. Prototypes comparison 92
3.3.2. Antenna selection in multi-antenna devices 95
3.4. DIRECTIONAL ANTENNAS 99
3.4.1. Directivity enhancement with AMC 99
3.4.2. Directivity enhancement using a reflector 106
3.5. CONCLUSION AND PERSPECTIVES 121
3.6. REFERENCES 122

4. MIMO ANTENNA DESIGN BEYOND 6 GHZ FOR HAND EFFECT INVESTIGATION ON HANDSET DEVICES 124

4.1. EVOLUTION AND CHALLENGES FOR MOBILE DEVICES TOWARD 5G 126
4.1.1. Millimeter-Wave Antenna for 5G Handset Devices 126
4.1.2. User Effect and Body Loss below 6 GHz 128
4.1.3. User Effect and body Loss beyond 6 GHz 129
4.2. MEASUREMENT SETUP FOR HAND EFFECT INVESTIGATION 130
4.3. PRELIMINARY STUDY A WITH 11 GHZ PROTOTYPE 131
4.3.1. Single Antenna structure and dimensions 132
4.3.2. Mobile Phone Prototype at 11 GHz 133
4.3.3. Hand effect Measurement 133
4.3.4. Conclusion of the study at 11 GHz 137
4.4. ADVANCED STUDY WITH A 15 GHZ PROTOTYPE 138
4.4.1. Single Antenna structure and dimensions 138
4.4.2. Mobile Phone Prototype at 15 GHz 139
4.4.3. Free Space Measurement 141
4.4.4. Beamforming Computation 147

4.4.5. Measurement with hand effect 153

4.4.6. Beamforming Computation with Hand Effect 160

4.4.7. Conclusion of the study at 15 GHz 165

4.5. CONCLUSION AND PERSPECTIVES 165

4.6. REFERENCES 167

CONCLUSION 169

LIST OF PUBLICATIONS 171

APPENDIX: Polycarbonate Dielectric Properties Characterization.....172

Abstract

In recent years, telecommunications witnessed exponential growth, especially in mobile communications. The increasing demand for high data-rates has led the telecommunication industries to increase transmission capacity, to improve the signal to noise ratio and to expand the operating bands of cellular communications. The 4G developed and deployed in the last ten years is close to reaching its full potential regarding throughputs and channel capacity. With 5G on the horizon, many new challenges emerged for antennas designers especially regarding the Massive MIMO technology and the new operating band in the millimetric spectrum.

The main objective of this thesis is to study the problematics involving the improvement on actual Wi-Fi, LTE technology and the development of the future 5G network. More specifically, we will study the implementation of a large number of antennas in a small terminal and the way to experimentally characterize those multi-antenna systems in the low frequencies. Indeed, measurements of multi-antenna systems become more and more challenging and expensive when increasing the number of antennas. Moreover, the integration of a large number of antennas within a device limited in volume needs to be carefully considered regarding the mutual coupling between elements and the correlation envelop. Considering the new 5G applications in frequency bands above 6 GHz, we wanted to explore the problematic of human interaction in handset devices at millimeter wave frequencies.

Chapter 1 gives an introduction to the context surrounding the thesis and the different studies we conducted in this work. This chapter aims to presents the recent advancement in the mobile and local communication networks. An overview of the main standards is stated as well as the basis of antenna parameters and technology. This chapter introduces the motivations of the thesis.

Chapter 2 focuses on measurement setup for MIMO antenna systems. We present an overview of the existing systems such as the two stage method, the reverberant chamber and the multi-probe technique with channel emulator. Then, the chapter explicit the work conducted to develop our measurement system by presenting two approaches. The first setup was designed using Rhodes & Schwartz equipment. The second testbed leverage the OpenAirInterface, an open-source platform using Software Defined Radio boards.

In chapter 3, we present the design of several 8-antenna gateways for Wi-Fi and LTE applications. In a first time, the study aims to evaluate the performance of the Laser Direct Structuring technology, a method allowing to printed antennas directly on a plastic case. A set of multi-antenna gateways has been realized with PCB and LDS technology to compare the two techniques accurately. In the second time, we investigate the influence of directional antennas within a multi-antenna system. Two methods have been studied to realize directional antennas. It's finally with a dipole and a reflector that we manage to compare an omnidirectional and a directional configuration. Each realized prototype has been evaluated in free-space and with a beamforming configuration thanks to the OpenAirInterface testbed presented in the second chapter.

Eventually, chapter 4 presents the investigation of the hand effect on high frequency antennas for future 5G mobile phones. The study aims to evaluate the negative impact of the user's hand on beamforming capabilities of 15 GHz antennas. We leverage a 3D spherical scanner with a fixed AUT to measure the antenna 3D radiation pattern in the presence of a real human hand.

1. Context and Motivations

Table of content Chapter 1

1.1. Evolution of Wireless Communication Networks 15
1.1.1. 2G Cellular Network 15
1.1.2. 3G Cellular Network 16
1.1.3. 4G Cellular Network 17
1.1.4. 5G Cellular Network 20
1.2. Wireless Local Area Network (WLAN) 22
1.3. Antennas for Cellular communications and Local networks 25
1.3.1. Antenna Parameters 25
1.3.2. Mobile Phones and Access-point Antennas 27
1.3.3. Base Station Antennas 30
1.4. Motivation of the Thesis 31
1.5. References Chapter 1 32

For centuries, humans created ways to communicate over very long distances. Many early telecommunication systems were used, from the Greek hydraulic semaphore systems to smoke signals, drums and homing pigeons have been used throughout history by different cultures. Chains of beacons were commonly used to relay signals in the Middle Ages. Despite the cleverness of those systems, they all suffered from the very few bit of information they could transmit. It's only around the end of the 18th century that electricity has been involved in telecommunications, thanks to the work of several scientists including Laplace, Ampère or Gauss. The first operating electrical telegraph was built at the beginning of the 19th century. This technology saw a few evolution until the electric telephone was invented in the 1870s. In the same time, a series of experiments demonstrated the existence of the electromagnetic waves theorized by Maxwell. Since then it will not be long before the first wireless telephone call was conducted. The 20th century has seen an incredible acceleration in the electrical technology development resulting in the creation of the first cellular network.

1.1. Evolution of Wireless Communication Networks

It was almost forty years ago that the first generation (1G) of mobile communication network was launched in several countries over the world. Mobile 1G established the foundation of cellular communications [I-1]. Those cellular networks were primary analog systems designed only for voice communication using frequencies around 900 MHz. The technology was based on the frequency modulation technique (FM) to process voices signals and Frequency Division Multiple Access (FDMA) to assign a specific frequency for each user.

1.1.1. 2G Cellular Network

Mobile networks evolved every ten years or so to support the growing data-rate demands. Indeed at the beginning of the 90s, the second generation (2G) of mobile communication was announced with a digital modulation scheme [I-2]. Shifting from analog to digital allowed some improvements in system performance especially regarding spectral efficiency. Thanks to Code Division Multiple Access (CDMA) or Time Division Multiple Access (TDMA) the system can handle multiple numbers of users. The digital technologies allowed providing new services such as Short Message Service (SMS). The Global System for Mobile Communication (GSM) is the common standard for the 2G. One of the key features of the GSM is the Subscriber Identity Module (SIM) card which contains the phone number and the user's subscription information. As presented in Fig. 1-1 [I-3], the GSM network is mainly composed of three parts: the Mobile Station with the mobile equipment and the SIM card, the Access network with the Base Transceiver Station (BTS) and the Base Station Controller (BSC) and the Core Network (CN).

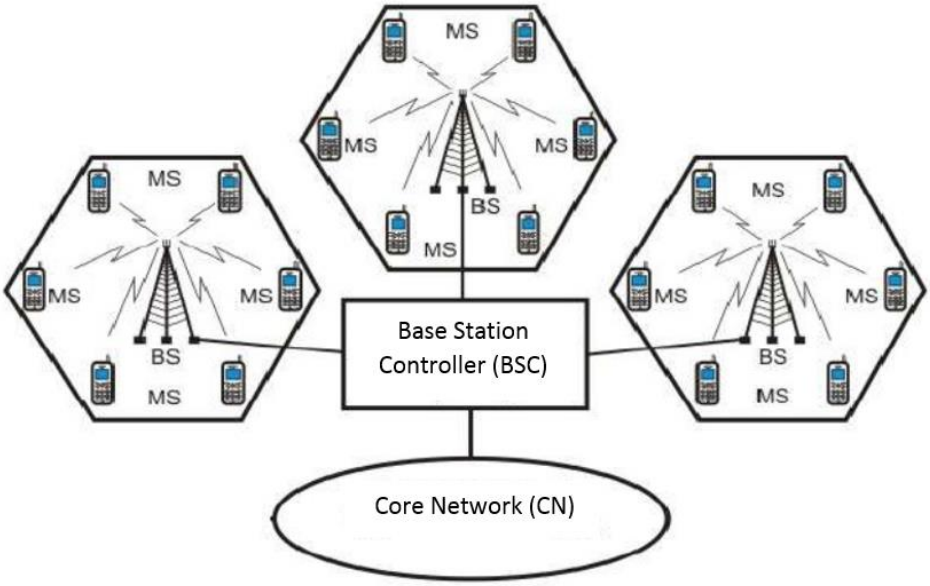

Figure 1-1: Schema of a GSM Cellular Network [I-3].

The General Packet Radio Service (GPRS) standard is an evolution of the GSM standard which allows packet-based internet connections. The GPRS can be considered as an optional function implemented in the core network of the GSM. Often called 2.5G, GPRS was able to provide throughput up to 85 Kbit/s. This technology provided to users data services like MMS (Multimedia Messaging Service) and Wireless Application Protocol (WAP) to allow accessing the internet through mobile devices.

The next step in the evolution of the GSM standard was the Enhanced Data rates for GSM Evolution (EDGE) allowing improved data transmission rates up to three times more than with GPRS. EDGE is considered as a pre-3G (or 2.75G) technology and was initially deployed in 2003. EDGE requires no hardware or software changes to be made in GSM core networks. Indeed the key of the technology is the use of a higher modulation scheme (8-PSK – Phase-Shift Keying) in addition to the GMSK (Gaussian Minimum-Shift Keying) modulation used in GPRS.

1.1.2. 3G Cellular Network

Around the year 2000, the third generation of mobile communication introduced high-speed Internet access, highly improved video and audio streaming capabilities by using technologies such as Universal Mobile Telecommunication System (UMTS) based on the Wideband Code Division Multiple Access (W-CDMA) [I-4]. The most popular radio interface is the W-CDMA, using 2100MHz frequency for transmission, a 5MHz bandwidth and Frequency Division Duplexing (FDD) for multiplexing. The

beginning of broadband communication is standardized by the International Telecommunication Union (ITU) with the IMT-2000 standard. Downlink data rates of several Mbit/s started are achieved.

The downlink data rate was increased to 14Mbit/s, and 28Mbit/s with the improvements called High Speed Packet Access (HSPA) HSPA and HSPA+ around the year 2008. HSPA is an amalgamation of two mobile telephony protocols, High Speed Downlink Packet Access (HSDPA) and High Speed Uplink Packet Access (HSUPA), which extends and improves the performance of existing 3G mobile telecommunication networks utilizing WCDMA protocols. An improved 3GPP (3rd Generation Partnership Project) standard, Evolved HSPA (also known as HSPAC), was released in late 2008 with a worldwide utilization beginning in 2010. HSPA has been deployed in over 150 countries by more than 350 communications service providers (CSP) on multiple frequency bands and is now the most extensively sold radio technology worldwide, although LTE is closing the gap rapidly.

Another improvement on the 3G systems towards 4G was the LTE (Long Term Evolution, 3.9G), targeting downlink data rates up to 100Mbit/s. LTE specification allows the usage of QPSK, 16QAM and 64QAM modulation types and a channel bandwidth of up to 20MHz, with FDD and TDD (Frequency/Time Division Duplexing) for duplexing schemes. The use of MIMO (Multiple Input Multiple Output) is allowed and can increase the maximum data rate from 100Mbit/s to 326Mbit/s. The downlink uses the OFDMA (Orthogonal Frequency Division Multiple Access) for access scheme.

1.1.3. 4G Cellular Network

In 2008 the ITU defined the International Mobile Telecommunications-Advanced (IMT-Advanced) standard surpassing the capabilities of the IMT-2000. IMT-Advanced is the fourth generation (4G) mobile communication technology [I-5]. LTE radio access technology offers a full 4G broadband platform. The key technology to support high data rates in 4G systems are MIMO systems. MIMO enables multi-streams transmission for high spectrum efficiency, improved link quality, improved Signal to Noise ratio (SNR) thanks to beamforming techniques using antenna arrays. To develop the existing LTE network, the 3GPP defined the LTE-Advanced (LTE-A or 4G+) standard to meet IMT-Advanced requirements. LTA-A can theoretically achieve throughput rates of 1 Gigabit per second. LTE-A supports heterogeneous networks with co-existing macro, micro, small cells, and Wi-Fi access points. Figure 1-2 presents the number of devices connected to each generation of mobile communication since 2016 and the prediction toward 2021 [I-6]. 4G has become this year the most used standard in the world.

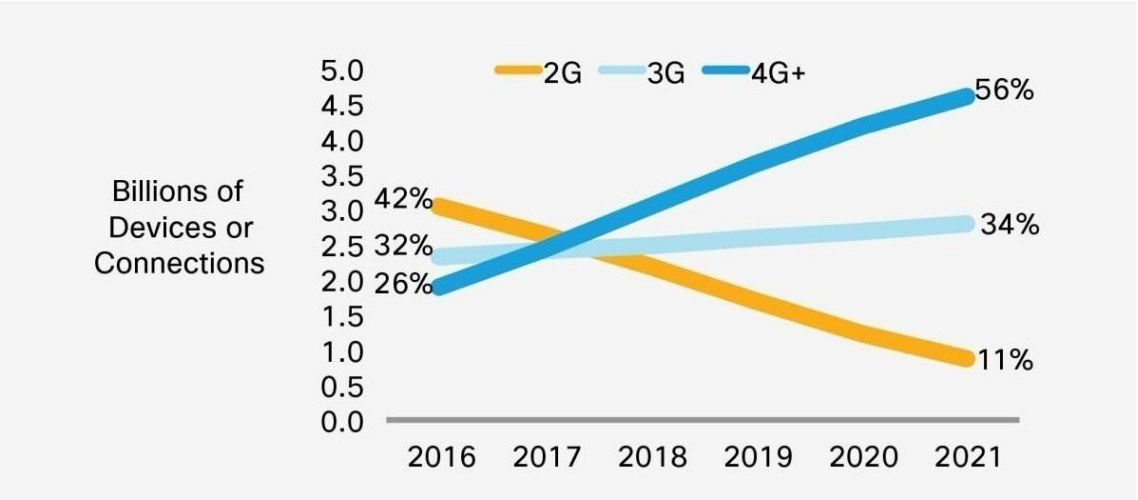

Figure 1-2: Number of devices connected to each standard [I-6].

As the demand for capacity in mobile broadband communications increases dramatically every year, wireless providers must be prepared to support up to a ten time increase in total mobile traffic by 2020, requiring researchers to seek higher capacity and to find new wireless spectrum beyond the 4G standard. Indeed the number of connected objects is estimated to reach 50 billion by 2020 while the mobile data traffic is expected to grow from 2.5 Exabyte per month to 24.3 Exabyte per month by 2019 as presented in figure 1-3 [I-7].

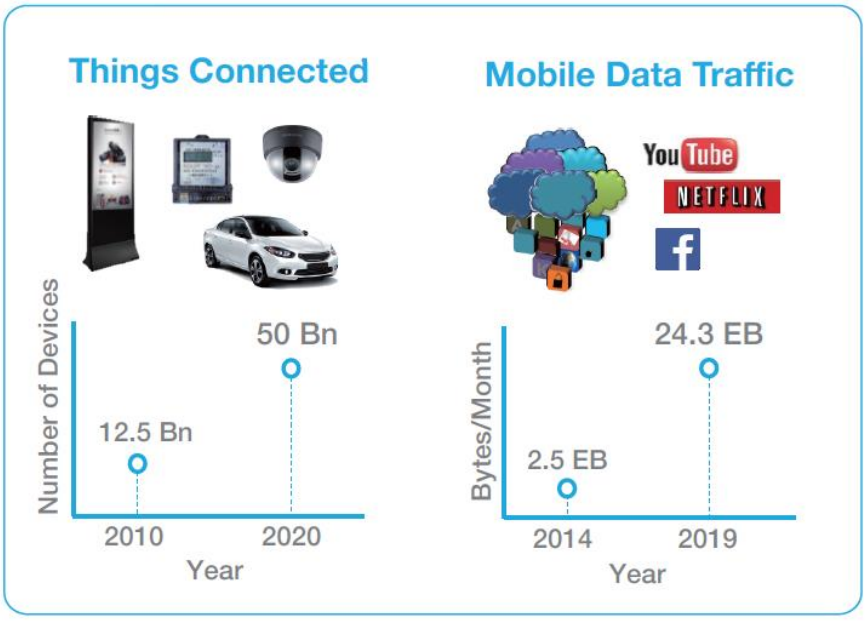

Figure 1-3: Estimation of the number of connected objects in 2020 and the Global Mobile Data Traffic in 2019 [I-7].

LTE is a 3GPP-based standard established as the next generation mobile technology interoperating with W-CDMA, GSM, and CDMA2000 systems. LTE addresses some of the critical issues in the network: spectrum flexibility and efficiency. The uplink and downlink channels are two to four times more

spectrally efficient than (HSPA). LTE uses orthogonal frequency division multiple access (OFDMA) on the downlink and single carrier-frequency division multiple access (SCFDMA) on the uplink. The LTE-A use QPSK, 16QAM, and 64QAM modulation scheme to achieve 1 Gbps peak data rates for the low-mobility users in downlink and 500 Mbps for uplink [I-8].

LTE supports flexible spectrum allocation and is defined in more than 40 frequency bands around the world supporting spectrum from 450 MHz to 3.8 GHz. Figure 1-4 [I-9] presents the allocation of LTE frequency bands in France per mobile service providers. Both Frequency Division Duplex (FDD) and Time Division Duplex (TDD) are supported, as well as different channel bandwidths of 1.4, 3, 5, 10, and 20MHz in the available spectrum and up to 100 MHz with carrier aggregation.

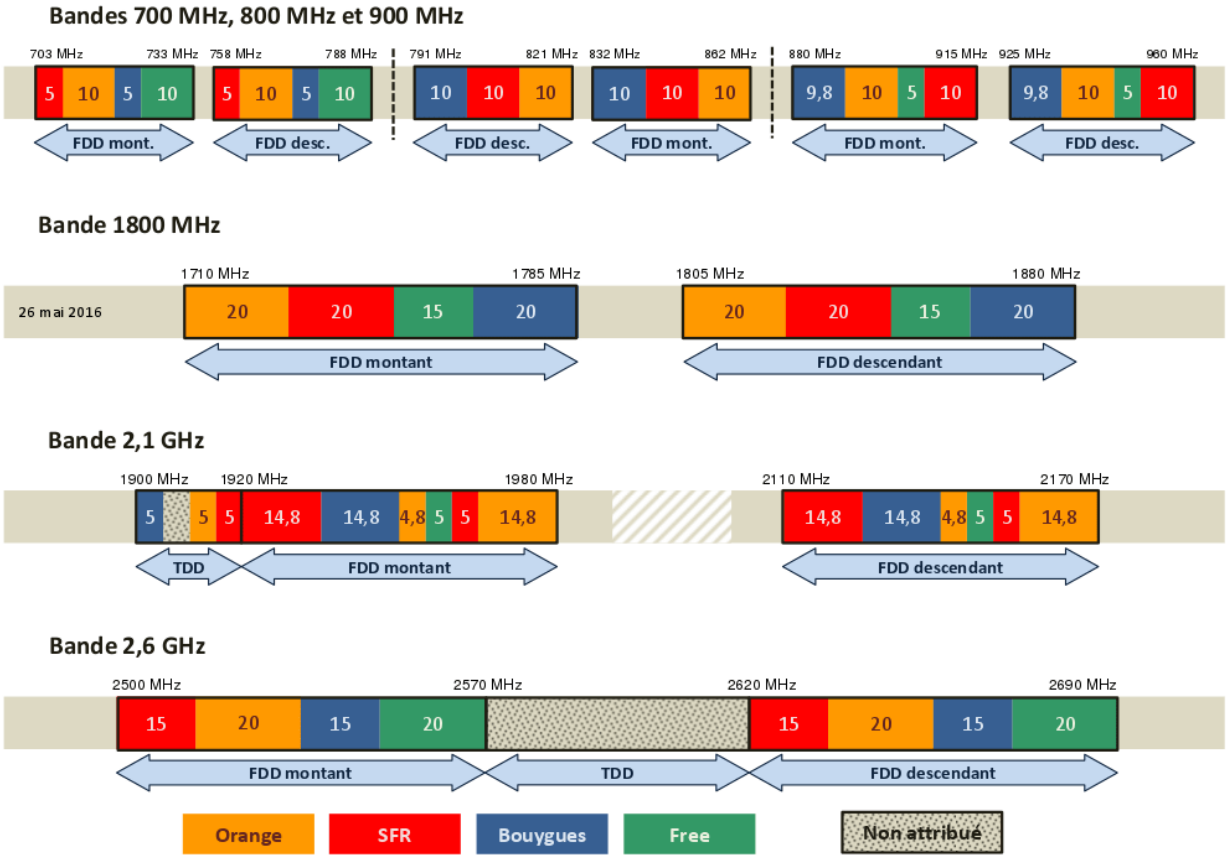

Figure 1-4: Frequency bands Allocation in France per Mobile Service Providers [I-9].

Carrier Aggregation provides the ability to combine across multiple carriers, multiple bands, as well as across licensed and unlicensed spectrum to increase the maximum data rates available for users. Figure 1-5 [I-10] presents three types of carrier aggregation. The first method is the contiguous intra-band carrier aggregation (a) uses two adjacent frequency channel. The second method, the non-contiguous intra-band carrier aggregation (b) aggregate two channel in the same band but separated

by others channels. Finally, the inter-band carrier aggregation (c) uses two channels from two different bands.

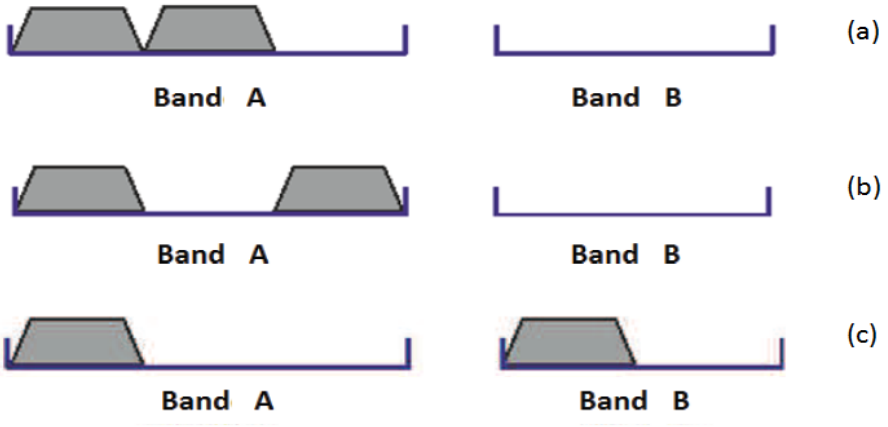

Figure 1-5: Carrier Aggregation Methods in LTE-A [I-10].

One of the key technology enabling fast data-rates is Multiple Input Multiple Output (MIMO) antennas, including beamforming and spatial multiplexing up to eight downlink and four uplink antennas. LTE-Advanced supports theoretical peak data rates up to 1Gbps is on the downlink when using Carrier Aggregation with 4x4 MIMO. The MIMO technology will be presented in more detail in the third chapter.

1.1.4. 5G Cellular Network

The fifth generation (5G) is today under development to support the predicted increased in mobile data traffic. The key performance indices are presented in figure 1-6 [I-7] with a comparison with 4G performance.

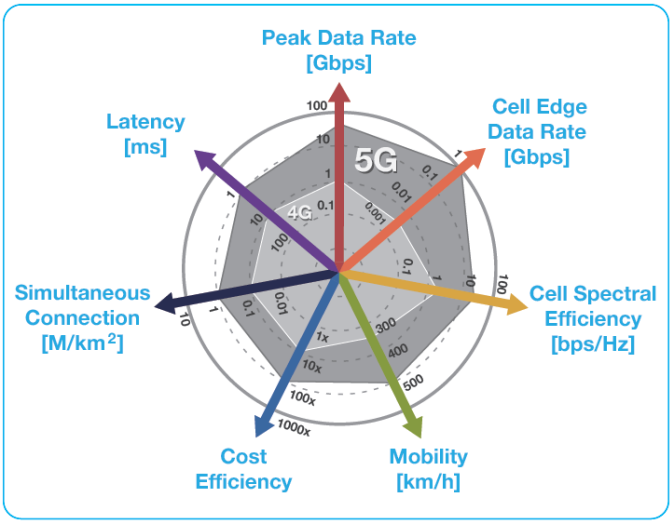

Figure 1-6: Key Performance Comparison between 4G and 5G [I-7].

The main differences compared to the 4G network will be the use of a much greater spectrum in millimeter-wave frequency bands and highly directive beamforming antennas at both the user

equipment and the base station with Massive MIMO antennas. 5G will benefit from a higher capacity for many simultaneous users in the covered area. Also, 5G will come with lower infrastructure costs since the backbone networks will move from copper and fiber to mm-wave wireless connections, allowing rapid deployment and mesh-like connectivity with cooperation between base stations.

The main objective of 5G is to overcome the current limitations of 4G. This concept involves an evolution of wireless network to reach the expected demand for data and a revolution in the network architecture to design an economical and easily scalable network to anticipate the large scale deployment planned for 2022. Many challenges are ahead for the engineering community to reach the key performance required for the 5G network resumed by Huawei [I-11] in figure 1-7.

Figure 1-7: 5G Key Performance Assessment [I-11].

The baseline of 5G systems is to provide gigabit-rate of data services regardless of a user's location. 5G network deployments are expected to be much denser compared to 4G networks to ensure this quality of service so making cost-effective implementation is a very important condition. Moreover, 5G have to considerably enhance its capacity compared to 4G to enable massive connectivity to assimilate the increasing number of connected objects. 5G technology also aims to a very low latency below one millisecond and very low energy consumption. In terms of application, 5G will be more than the next generation of mobile communication delivering ultra-broadband services such as ultra HD video streaming. Indeed this network will open a new set of use cases and markets. 5G technology will contribute to the machine to machine (M2M) application like autonomous vehicles, wearable devices and to connect millions of industrial sensors for example.

Regarding the spectrum, the actual bands below 6 GHz won't be enough to support the growing demand for data when more spectrum is essential to achieve the 5G vision. As a result, some applications of 5G is likely to operate on much higher frequencies. Many frequency bands are discussed in the industry to support the future 5G applications such as 10 GHz, 28 GHz, 32 GHz, 43 GHz, 46 GHz to 50 GHz, 56 GHz to 76 GHz, and 81 GHz to 86 GHz. The amount of potential spectrum above 20 GHz is several GHz. The use of spectrum sharing and flexible spectrum usage techniques might be used to optimize the spectrum utilization. The main challenge will be to overcome the lousy propagation

characteristics in those frequencies caused by atmospheric attenuation, blockage, and reflections. It has been acknowledged that MIMO and beamforming will be required to overcome the propagation challenges. The beamforming will need to adapt to the users and the environment to deliver the signal to the user.

Many challenges are yet to come to create a green network for 5G, but some key technologies are emerging to improve energy efficiency. We can cite for example the Centralized or Cloud RAN (C-RAN), a system that centralizes processing resources which already demonstrate its advantage regarding network deployment and energy saving. C-RAN is a suitable architecture for 5G networks to achieve the user-centric vision ("no-more cell") of 5G theoretically providing higher data rate and less service variation between the cell-center and cell-edge regions. Moreover, the modulation and coding schemes need to evolve to achieve the desired link level performance. Turbo coding and Quadrature Amplitude Modulation (QAM) employed in the 3G and 4G systems are no longer suitable for 5G. Various promising advanced modulation and coding schemes have received considerable attention recently. Green Networks will need to use renewable energy, such as wind and solar energy as an alternative power supply for networks, and bioelectric, kinetic and thermal energy for terminals.

Massive MIMO spatial multiplexing has the potential to become a game changing technology in the cellular communications space, allowing for increased cellular capacity and efficiency in high traffic urban areas [I-12]. The diversity that multipath propagation introduces is exploited to allow for data transfer between a base station and multiple users at the same time and frequency resource. Due to reciprocity of the channel between the base station antennas and the users, all the signal processing complexity can be kept at the base station, and the channel characterization can be done in the uplink.

1.2. Wireless Local Area Network (WLAN)

Most of the Wireless Local Area Networks (WLAN) are based on the 802.11 standards developed and frequently updated by the Institute of Electrical and Electronics Engineers (IEEE). IEEE 802.11 is a set of MAC and PHY specifications enabling the link between two or more devices using wireless communication in a limited and local coverage area both for personal or professional utilization. The first 802.11 (Infrared) protocol was created in 1997, but it is only 2 years later in 1999 that IEEE 802.11b become widely used. WLANs have become very popular under the brand Wi-Fi thanks to the ease of installation and use. Wi-Fi is a trademark of the Wi-Fi Alliance which can be used only for the product that respects a set of interoperability certifications.

As presented on figure 1-8, WLAN can provide a connection to the internet through a gateway or access point especially in the 2.4 GHz Industrial, Scientific and Medical (ISM) and 5 GHz Unlicensed National Information Infrastructure (U-NII) frequency bands but also in the 900 MHz, 3.6 and 60 GHz unlicensed bands. The Wi-Fi coverage can extend from a small area (apartment, house, restaurant…) to large area of several square kilometers if many access points are interconnected (airports, hotels…). Nowadays a lot of devices can use the Wi-Fi technology including computers, phones, tablets, video-games consoles, smart TVs, speakers or printers.

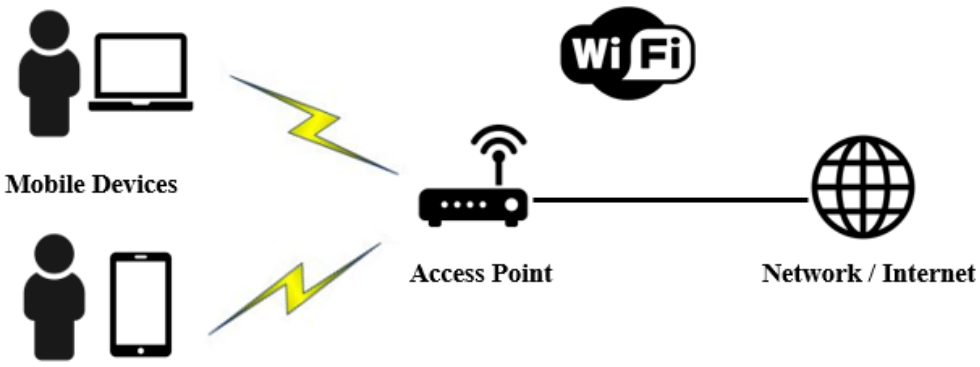

Figure 1-8: Schema of a Wi-Fi Network.

Many evolutions of the standard followed the first 802.11 protocol such as 802.11a, 802.11g, 802.11n, 802.11ac, 802.11ad with significant improvement in data rates. The most relevant characteristics of the main protocols are resumed in table 1-1. Each standard presented uses either 2.4 GHz, 5 GHz or both frequency bands. As we can see in this table 802.11b and 802.11g control their interference by using direct-sequence spread spectrum (DSSS) and Complementary Code Keying (CCK) modulation technique plus the orthogonal frequency-division multiplexing (OFDM) for the 802.11g release while other protocol only uses OFDM. We can note that the first 802.11 protocol could use Infrared (IR) and Frequency Hopping Spread Spectrum techniques. Moreover, we can see that the MIMO dimensions have been integrated into WLAN standards since the 802.11n release in 2009 by providing a protocol able to operate with 2 to 4 antennas.

Other protocols and amendments have been released such as 802.11ad, 802.11ah, and 802.11ai respectively in 2012, 2016 and 2017. Wireless Gigabits Alliance (WiGig) promoted the 802.11ad protocol which provides data rates links up to 6.8 Gbps in the 60 GHz band with more than 2 GHz bandwidth. 802.11ah protocol opens the 900 MHz frequency band and provides and extended range and data rates up to 350 Mbps. It also benefits from low energy consumption to create large sensor network and support the Internet of Things (IoT) concept. Finally, the 802.11ai standardize a fast initial link setup (FILS) function that enables a wireless LAN client to achieve a secure link setup within 100

milliseconds in the 60 GHz frequency band. It should be noted that the next release of Wi-Fi is planned for the end of the year with the 802.11ax aiming for data rates over 10 Gbps in the 2.4 and 5 GHz bands.

Table 1-1: Main Characteristics of WLAN Standard.

802.11 network PHY standards						
Protocol	802.11-1997	802.11b	802.11a	802.11g	802.11n	802.11ac
Release date	Jun. 1997	Sep. 1999	Sep. 1999	Jun. 2003	Oct. 2009	Dec. 2013
Frequency	2.4 GHz	2.4 GHz	5 GHz	2.4 GHz	2.4 / 5 GHz	5 GHz
Bandwidth	22 MHz	20 MHz	20 MHz	20 MHz	20 / 40 MHz	20 / 40 / 80 / 160 MHz
Modulation	DSSS / FHSS / IR	DSSS / CCK	OFDM	DSSS / CCK / OFDM	OFDM	OFDM
Modulation Scheme	BPSK, QPSK	BPSK, QPSK	BPSK, QPSK, 16QAM, 64QAM	BPSK, QPSK, 16QAM, 64QAM	BPSK, QPSK, 16QAM, 64QAM	BPSK, QPSK, 16QAM, 64QAM, 256QAM
Max data rate	2 Mbps	11 Mbps	54 Mbps	54 Mbps	600 Mbps	3.5 Gbps
MIMO Streams	-	-	-	-	2 - 4	2 - 8
Range (m) In. / Out.	20 / 100	35 / 140	35 / 120	35 / 140	70 / 250	35 / 120

Numerous types of access points are proposed in the market. The most common of them, set up in homes, are routers that incorporate a digital subscriber line and a Wi-Fi access point (provided by telecoms operators) which provide Internet access and easy interoperability of all devices connected to it. Other routers may include a cellular Internet radio modem and Wi-Fi access point which provides Internet access over 2G, 3G or 4G networks. The even modern smartphone can now act as a Wi-Fi access point. Those gateways use Wi-Fi chipset which takes into account more and more antennas to increase the throughput. The corresponding antenna array has an increasingly important role to play whereas design constraints are more and more restrictive in terms of volumes, size, coverage polarization diversity, and costs.

Radiations of Wi-Fi devices are limited in France by a threshold on the Equivalent Isotropic Radiated Power (EIRP) resulting in a relatively short covering range for WLANs. The different limitations are presented in the following table 1-2. The table also highlights frequencies not allowed outdoor. Those limitations may involve the integration of regulation mechanism called Transmitter Power

Control (TPC) to automatically adjust the transmission power level in 5 GHz bands in access points. Moreover, Dynamic Frequency Selection (DFS) techniques are used to monitor operating frequencies of radars and to avoid any interferences with them.

Table 1-2: Maximum Authorized Power in France in the 2.4 GHz and 5 GHz Frequency bands.

Frequencies MHz	Indoor EIRP Limit	Outdoor EIRP Limit
2400 - 2483,5	**100 mW**	**100 mW**
5150 - 5250	**200 mW**	-
5250 - 5350	**100 mW**	-
5470 - 5725	**500 mW**	**500 mW**

Many cities around the world announced plans to construct citywide Wi-Fi networks. There are many successful examples such as Mysore which became India's first Wi-Fi-enabled city by setting up hotspots and covering the complete city. The city of Minneapolis deployed 117 free of use gateway and thus cover almost 100% of the city (more than 400 000 inhabitants over 150 km²). The city of Helsinki in Finland also provides free Wi-Fi everywhere. The Wi-Fi citywide concept can compete with the cellular networks.

1.3. Antennas for Cellular communications and Local networks

1.3.1. Antenna Parameters

In this section, we present very succinctly the main characteristics used to describe and analyze antennas performance [I-13].

An antenna is often described with its radiation pattern which is defined as a mathematical function or a graphical representation of the radiation properties of the antenna as a function of space coordinates. The radiation pattern is determined in the far-field region and represented as a function of the directional coordinates. The radiation pattern can be classified as isotropic, directional or omnidirectional. An isotropic radiator is defined as “a hypothetical antenna having equal radiation in all direction.” This ideal radiation is not realizable, but it is often used as a reference for expressing the directive properties of a real antenna. The omnidirectional pattern represents an antenna radiating the same amount of energy in almost every direction while a directional pattern radiates more effectively in some direction than others. The directional pattern is defined as one “having the property

of radiating or receiving waves more effectively in one direction." Figure 1-9 presents examples of directional and omnidirectional patterns.

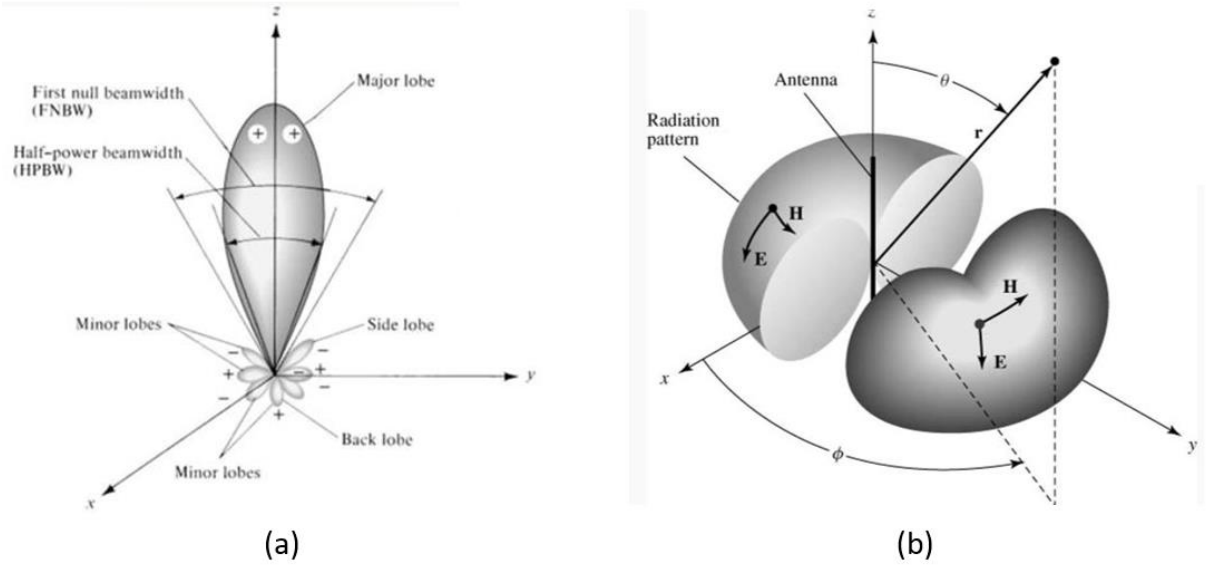

Figure 1-9: Example of (a) directional and (b) omnidirectional pattern [I-13].

From this pattern, we can get the directivity of the antenna which is the ratio of the radiation intensity in a given direction to the radiation intensity averaged over all directions. For an isotropic source, the directivity will be unity.

The antenna gain of the antenna is closely related to the directivity. In addition to the directional capabilities, it accounts for the efficiency of the antenna. The gain does not take into account reflection losses and polarization mismatches. The total antenna efficiency is used to take into account losses at the input terminals and within the structure of the antenna. Such losses might be due to reflections because of the mismatch between the transmission line and the antenna as well as conduction and dielectric losses.

The polarization of an antenna in a given direction is defined as "the polarization of the radiated wave when the antenna is excited." The polarization of the antenna can be classified as linear, circular or elliptical. Polarization is called linear if the vector that describes the electric field at some point of space is always directed along a line. Linear and circular are in fact special cases of elliptic. Each type of polarization has its own advantages and disadvantages. An RF system designer is free to select the type of polarization, according to the system requirements. Figure 1-10 presents a graphic representation of each polarization.

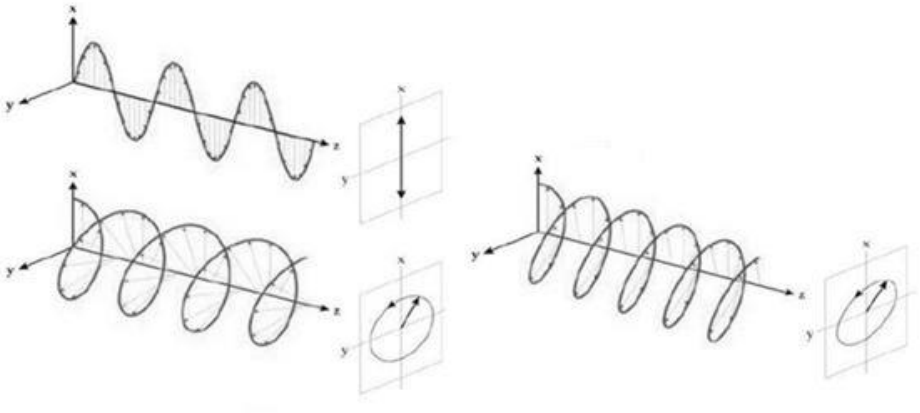

Figure 1-10: Graphical illustration of linear, circular and elliptic polarization [I-13].

The input impedance is defined as “the impedance presented by an antenna at its terminals or the ratio of the voltage to current at a pair of terminals.”

Finally, the bandwidth of an antenna expresses its ability to operate over a wide frequency range. The bandwidth is usually given as a percentage of the nominal operating frequency. The bandwidth can be considered to the range of frequencies where the antenna characteristics are in an acceptable value. The radiation pattern of an antenna may change dramatically outside its specified operating bandwidth.

1.3.2. Mobile Phones and Access-point Antennas

Following the evolution of cellular networks, the characteristics of mobile phone antennas changed, driven by technical and esthetical requirements. More details about the evolution of mobile phones antennas and possible techniques are presented in [I-14]. Until the end of the 1990s, mobile phones were equipped with external antennas, generally helix type, monopole (whip) or a combination of both for dual band operations. Figure 1-11 shows two example of external antennas. Those antennas have a very good efficiency but a high Specific Absorption Rate (SAR). The SAR is a measure of the rate at which energy is absorbed by the human body when exposed to an electromagnetic field.

(a) (b)

Figure 1-11: Examples of External Antenna for Mobile Phones (a) Monopole and (b) Helix [I-14].

In the late 1990s, mobile phones designers started to integrate internal antennas in their devices [I-15], [I-16]. Inverted F-Antenna (IFA) and Planar Inverted F Antenna (PIFA) were the choice of predilection for mobile antenna designers. The IFA has basically folded monopole with a connection to the ground plane. IFA have inherently narrow bandwidths, but the wire element can be replaced by a plate to increase the bandwidth and then become a PIFA. Quickly, PIFAs took over monopoles because of its advantages like low SAR, compact size, easily tunable, simple structure, easy fabrication and low manufacturing cost and are now extensively used in mobile phones [I-17]. The position of shorting pin and feeding point can be optimized for matching. The bandwidth of PIFA can be improved by using various techniques like using a thick air substrate or by varying the size of ground plane. Figure 1-12 presents three type of PIFA for mobile phones.

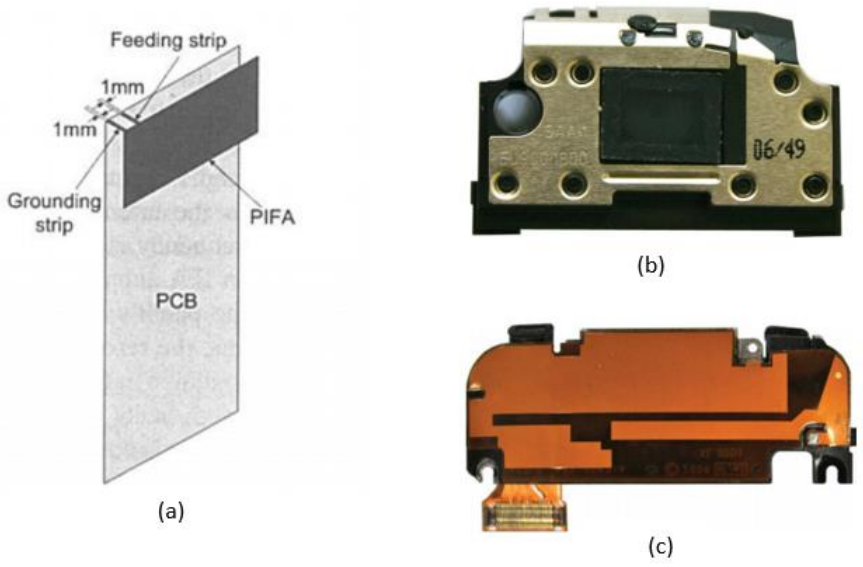

Figure 1-12: Examples of PIFA Used in Mobile Phones (a) PIFA concept, (b) folded metal sheet and (c) Flex technology [I-17].

In recent years, wireless communication progressed very fast, introducing new standard and new frequency bands. This development brought many challenges in the design of mobile devices, especially for the antenna which must now support multiband operations while being small, light and efficient. LTE technology was once again a great challenge due to the low frequency used in its standard and the need for miniaturization.

Many studies introduced multi-band antennas for GSM, UMTS, LTE, Bluetooth and Wi-Fi in mobile phones. A multiband antenna is basically designed to operate on several frequency bands [I-18]. For example, a lot of designs and tests have been presented to achieve multi-band operation from PIFA structure. Multiband behavior can be easily obtained by creating some slots in the rectangular plate to alter the current. There are a lot of techniques to design a multiband antenna that can cover the entire operating bands of the mobile phone application [I-19]. Using some parasitic elements (either connected to the ground plane or left floating) coupled by the main antenna can create additional resonances. This type of antenna is designed in such a way that one part of the antenna can be made active for one band. Another common technique is the usage of matching networks, either distributed along the antenna element or introduced directly at the feed to change the antenna input impedance in the desired way. The matching network can be realized with passive or active elements.

Another major internal antenna type used in mobile phones was the planar monopole antennas, which do not have a direct connection to the system ground plane. This type of antennas may require a ground clearance region in the vicinity (generally on one edge of the PCB) for acceptable performance. Techniques, like adding parasitic elements or adding parallel branches to the radiating element, can be used for multiband operations. This type of antenna was not used in the mobile terminals until recently due to the high SAR values exceeding the limits. The opportunity to place the antenna at the bottom of the mobile phone enabled their usage since the SAR values were now suitable due to longer distance between the antenna and head when the antenna is on the bottom of the mobile terminal. Finally, wideband antennas are also a suitable solution thanks to their ability to cover very large band of the spectrum.

The same kind of antennas can be found in Wi-Fi access points. Figure 1-13 shows 3 modern gateways. Fig 1-13 (a) presents an Asus router which proposes a classical but efficient solution with eight external antennas with high efficiency to increase coverage and reliability. On Fig. 1-13 (b), the Google OnHub with 7 integrated dual-polarization antennas on the upper side of a vertical device covering 360 degrees in the horizontal plane. Finally, Fig 1-13 (c) shows the inside of the Orange Livebox 4 with 7 integrated PIFA (3 at 2.4 GHz and 4 at 5 GHz) in the corner of a horizontal device.

(a) (b) (c)

Figure 1-13: Three Different Type of Access Point from (a) Asus, (b) Google and (c) Orange.

The figure 1-14 shows two antennas used in the Livebox, the mainstream Wi-Fi access-point developed by Orange.

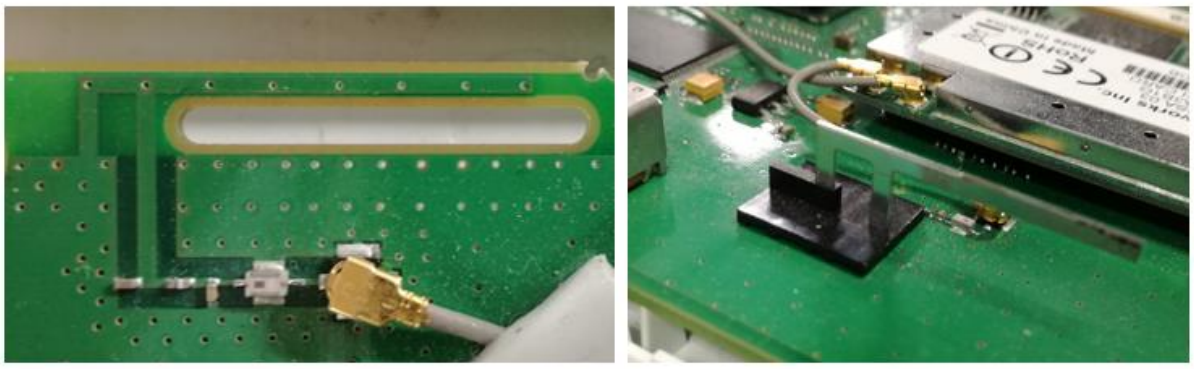

Figure 1-14: Pictures of a printed IFA and a 3D PIFA used in a Orange Livebox.

1.3.3. Base Station Antennas

A few constructors provide a base station for network deployment. It comes to the internet access provider to choose which base station is suitable for its network regarding a great number of criteria [I-20]. The first criterion is the frequency band of operation for each array because it directly affects the size of the base station. Of course, the return-loss which is the amount of energy reflected back from an antenna RF port, and the port-to-port isolation between different RF ports of the antenna are two fundamental antenna parameters. Regarding the application, the number of arrays (1 to 5 column in modern antennas) and the size of the array are decisive factors since it influences respectively the tilt range of the horizontal and vertical beam. Finally, the maximum gain in every direction is a crucial parameter for the choice of a 4G base station. Many other parameters are taken into account such as cross-pol isolation, the antenna polarization (two orthogonal polarizations from each array in most of the case), the level of the side lobes which is important for reducing system interferences, the width

of the antenna main beam, the front-to-back ratio (measure of how much energy is radiated behind the antenna).

(a) (b)

Figure 1-15: Picture of (a) a Tri-Sectorial Base Station and (b) the inside of a LTE base station.

1.4. Motivation of the Thesis

This chapter presented the fundamental knowledge of the antennas fields and the main technologies surrounding the evolution of mobile and local networks. In this context, the thesis focuses on MIMO antennas, one of this breakthrough technology of enabling high data rates for 4G and Wi-Fi technologies. The first idea driving this project was to create a new concept of Livebox for Orange, starting from improving the flaws of the existing device. The point was to exploit fully the capabilities of the WLAN 802.11 standard in terms of MIMO techniques. Especially we focus on 802.11n at 2.4 GHz and 802.11ac at 5 GHz. We also evaluated the concept of multi-antenna for femtocell using LTE standard at 2.6 GHz. For this purpose, we propose to study antenna implementation and manufacturing techniques inside a small access point to improve the efficiency of the global system. An important target of the thesis is the development of accurate testbed to assess the radiated performance of a system with beamforming capabilities.

In the context of the ongoing 5G research, we will propose to study antennas for mobile phone in frequencies above 6 GHz. This study aims to analyze the losses caused by users at such frequencies and to evaluate the capabilities of beamforming techniques to compensate those losses.

1.5. References

[I-1] Qualcomm, “The evolution of mobile technologies: 1G to 2G to 3G to 4G LTE”, June 2014.

[I-2] T.S. Rappaport, S. Sun, R. Mayzus, H. Zhao, Y. Azar, K. Wang, G.N. Wong, J.K. Schulz, M. Samimi, F. Gutierrez, “Millimeter Wave Mobile Communications for 5G Cellular: It Will Work!,” Access, IEEE, vol. 1, pp.335-349, 2013.

[I-3] Shreyash borad, “Cellular Networks”, October 2011.

[I-4] Trillium Digital Systems, Inc., “Third Generation (3G) Wireless White Paper”, March 2000.

[I-5] Arun Agarwal, Kabita Agarwal “The Next Generation Mobile Wireless Cellular Networks – 4G and Beyond”, American Journal of Electrical and Electronic Engineering, 2014, Vol. 2, No. 3, 92-97.

[I-6] “Cisco Visual Networking Index: Global Mobile Data Traffic Forecast Update, 2016–2021”, 2017.

[I-7] Samsung Electronics Co., 5G vision, White Paper, February 2015

[I-8] Ian F. Akyildiz, David M. Gutierrez-Estevez, Elias Chavarria Reyes, “The evolution of 4G cellular systems: LTE-Advanced”, Physical Communication, 2010.

[I-9] www.arcep.fr.

[I-10] Aykut Cihangir, “Antenna Designs Using Matching Circuits For 4G Communicating Devices”, March 2014.

[I-11] Huawei Technologies Co., 5G: A technology vision, White paper, February 2014.

[I-12] Radio Frequency Systems, “Technical Analysis: Beamforming vs. Massive MIMO”, March 2014.

[I-13] C. Balanis, “Antenna Theory: Analysis and design”, April 1982.

[I-14] C. Rowell, E.Y. Lam, “Mobile-Phone Antenna Design,” IEEE Antennas and Propagation Magazine, Vol. 54, No. 4, August 2012, pp 14-34.

[I-15] Marta Martinez Vazquez, “Design of antennas for mobile communications devices: practical aspects” IEEE AP-s Distinguished Lecture 2012.

[I-16] A. K. Skrivervik, J.-F. Zurcher, O. Staub, and J. R. Mosig, “PCS Antenna Design: The Challenge of Miniaturization”, Antennas and Propagation Magazine, vol. 43, no. 4, August 2001.

[I-17] Trinh, Le Huy & Ferrero, Fabien & Staraj, R & Ribero, Jean-Marc. (2013). Mobile phone antenna for 2G, 3G, and 4G standards. 195-202. 10.1109/ATC.2013.6698105.

[I-18] C.-H. Ku, H.-W. Liu, and Y.-X. Ding, “Design of Planar Coupled-Fed Monopole Antenna for Eight-Band LTE/WWAN Mobile Handset Application”, Progress In Electromagnetics Research C, vol. 33, 185-198, 2012.

[I-19] S. Jeon, S. Oh, H.H. Kim, and H. Kim, “Mobile handset antenna with double planar inverted-E (PIE) feed structure”, Electronices Letters, vol. 48, no 11, May 2012.

[I-120] R. Bhagavatula, R.W. Heath Jr., and K. Linehan, “Performance Evaluation of MIMO Base Station Antenna Design.” 2008.

2. Over-The-Air Measurement Systems for MIMO Antennas

Table of content Chapter 2

2.1. MIMO OVER-THE-AIR MEASUREMENT 35
2.1.1. MIMO OTA Measurement with Two-Stage Method 37
2.1.2. MIMO OTA Measurement with Reverberant Chamber 38
2.1.3. MIMO OTA Measurement with Multi-probe technique 39
2.2. MIMO OTA MEASUREMENT WITH RHODES&SCHWARTZ INSTRUMENTATION 40
2.2.1. Testbed Overview 40
2.2.2. System Configuration 42
2.2.3. Validation of the Measurement Setup 44
2.3. MIMO OTA MEASUREMENTS WITH OPENAIRINTERFACE 46
2.3.1. OpenAirInterface 46
2.3.2. Testbed Overview 48
2.3.3. System Configuration 49
2.3.4. Validation of the measurement setup 50
2.4. SYNTHESIS OF MIMO OTA MEASUREMENT AND CONCLUSIONS 52
2.5. REFERENCES 53

2.1. MIMO Over-The-Air Measurement

In the last few years, the wireless communication witnessed the emergence of new technologies subsequent to the exponential increase of the mobile traffic data [II-1]. Multiple Input Multiple Output (MIMO) techniques have been established as one of the spearheads of these new technologies, enhancing spectral efficiency and increasing channel capacity. The latest LTE release targets up to 8x8 MIMO schemes as well as the 802.11ac WLAN standard. Multi-antennas techniques such as beamforming, spatial multiplexing, and diversity, aim to take advantage of channel characteristics to increase data rates or reliability [II-2] through SNR improvement.

Characterizing this type of radiating system in a repeatable and controllable environment is very challenging. Indeed from the classical measurement results like S-parameters and radiation measurements, we are only able to check that our system is working in free space, which is needed but not sufficient [II-3]. Testing the mobile device in this way does not accurately describe the performance that the user might truly have.

Multiple antenna systems need to be tested in real life conditions in order to understand the end-to-end performance of a MIMO device. Assessment of MIMO antenna radiated performance needs to take into account the global telecommunication system and channel characteristics instead of considering the radiating element alone. The so-called Over-The-Air (OTA) measurements are performed at the system level and include modulation code schemes (MCS) and 3GPPP and IEEE standards [II-3].

To better predict the real-world performance of mobile devices, OTA tests have been developed to measure the RF performance of a mobile device. The developed systems are able to simulate various RF environments in a repeatable and controlled way. All critical parts of the mobile terminal design (antennas, RF front-end, baseband processing) are integrated into an OTA test in order to find the right antenna configuration. The radiated characteristics of the multipath channel and the MIMO antenna are included during the OTA measurement process. OTA testing can be used to identify whether the MIMO antenna design has acceptable performance over a wide variety of multipath environments. OTA tests, in addition to the classical handset tests, serve to provide a better feel for the real world performance of the mobile device. It has become necessary to include OTA testing of MIMO antenna performance.

In the ideal case, testing MIMO devices would be as simple as testing SISO devices, but since MIMO performance is closely tied to the channel characteristics, it makes MIMO OTA testing much more challenging and complex. The SISO test does not require a fading channel while MIMO OTA testing needs accurate channel models.

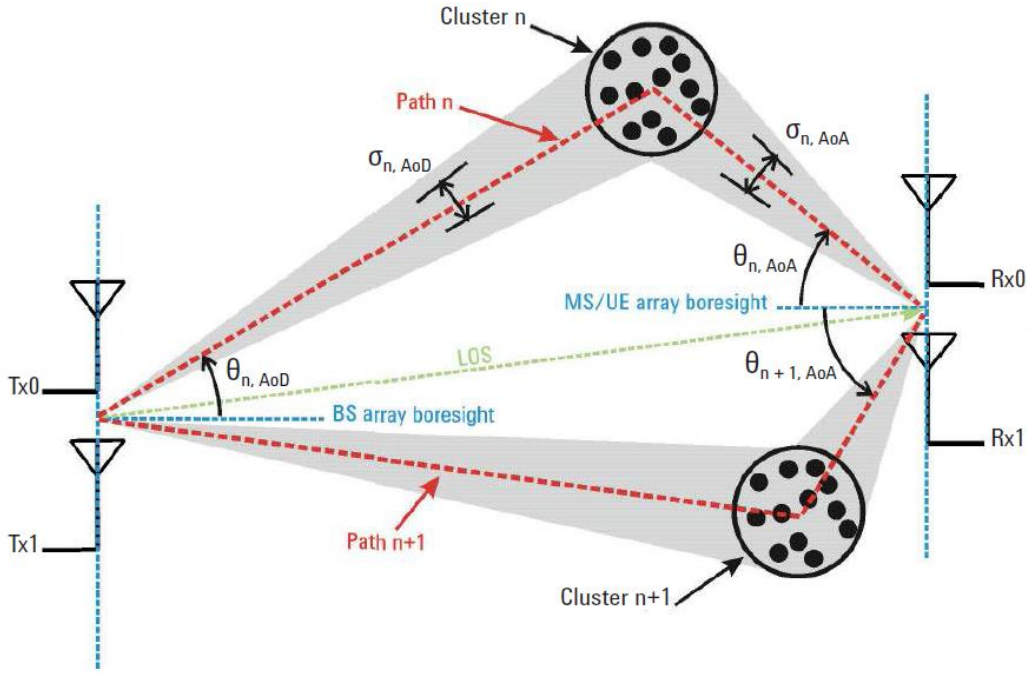

Figure 2-1: Schema of a 2x2 MIMO system with multipath reflections [II-4].

Several over-the-air (OTA) test methods have been proposed to characterize the radiated performance of multiple input multiple output (MIMO) devices. We present in this thesis the three main OTA test methods: the two-stage OTA method, the multiple test probes OTA method and the reverberation chamber method. Industrial OTA test beds to assess MIMO performance often rely on radio channel emulators which are expensive equipment proposed only by few suppliers (Agilent, Rhodes&Schwarz, Satimo, Anite) and are still under development for Massive MIMO techniques [II-4]. It has been shown that the different OTA measurement techniques will have approximately the same performance. The selection of the OTA test system is then based on the complexity, flexibility, and cost to the end-user as explicated through [II-5], [II-6] and [II-7].

2.1.1. MIMO OTA Measurement with Two-Stage Method

The two-stage "Over-The-Air" (OTA) method provides an accurate and cost-effective measurement system for MIMO devices. The technique combines the benefits of a traditional anechoic chamber with the flexibility of the channel emulator. The channel emulator is a measuring instrument for reproducing the actual radio wave propagation environment of mobile communication. It reproduces the fading environment defined by 3GPP. The emulated channel is based on standard channel models describing the variations of the electromagnetic waves between a radio transmitter and a receiver, as a function of time, frequency, and space.

The two-stage method is based on the knowledge that antenna characteristics can be measured independently and then mathematically combined [II-8]. The channel characteristic can also be mathematically added while combining antenna patterns. The first stage of the method is the acquisition of antennas array gain pattern in an anechoic chamber as shown in figure 2-2. Considering the configuration of the measured UE, the array gain can be measured passively using a VNA or actively using a base station emulator. Either 2D or full 3D far-field pattern measurement can be used for this method. The second stage in the two-stage OTA method consists of a conducted test of the UE using a base station emulator and a channel emulator. The channel emulator will combine the actually measured 2D or 3D antenna gains with the selected MIMO channel model. Different results can be obtained with this method such as BER, FER, channel coefficient or correlations coefficient. The channel capacity can finally be calculated from those resulted elements. This method can also be run with simulated results on antennas gain.

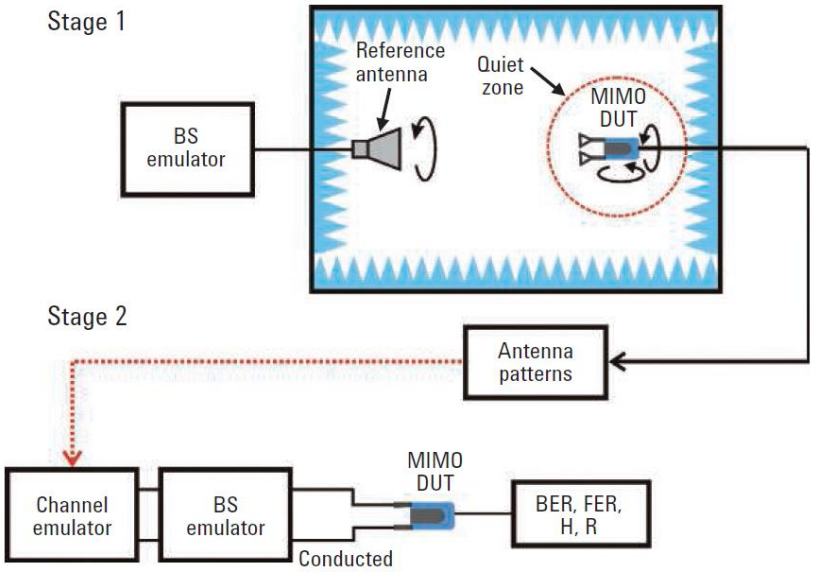

Figure 2-2: Test configuration using the two-stage OTA method for a 2x2 MIMO device [II-4].

2.1.2. MIMO OTA Measurement with Reverberant Chamber

The second OTA measurement technique which is widely used to evaluate the performance of MIMO system in a realistic environment is the reverberation chamber. A reverberation chamber is a metal cavity without absorber, completely shielded from the external signal and including a mode stirrer allowing creating different environment configurations. The mode stirrer consists of metallic plates that rotate during the testing phase. Movements of the plate create a statistical isotropic Rayleigh fading channel between reference antennas and the MIMO DUT. It means that over a complete mode-stirring sequence all different angle-of-arrivals to the DUT is equally probable and that the signal amplitude exhibits a Rayleigh distribution. The schema of a classic setup with the reverberant chamber is presented in figure 2-3.

The reverberation chamber is particularly useful when evaluating MIMO devices developed for indoor communications. This measurements method allows acquiring several performance parameters for wireless terminals and electrically small antennas [II-9], [II-10] such as radiation efficiency, impedance mismatch, diversity gain, MIMO capacity, Total Radiated Power (TRP), Total Isotropic Sensitivity (TIS) or Average Fading Sensitivity (AFS).

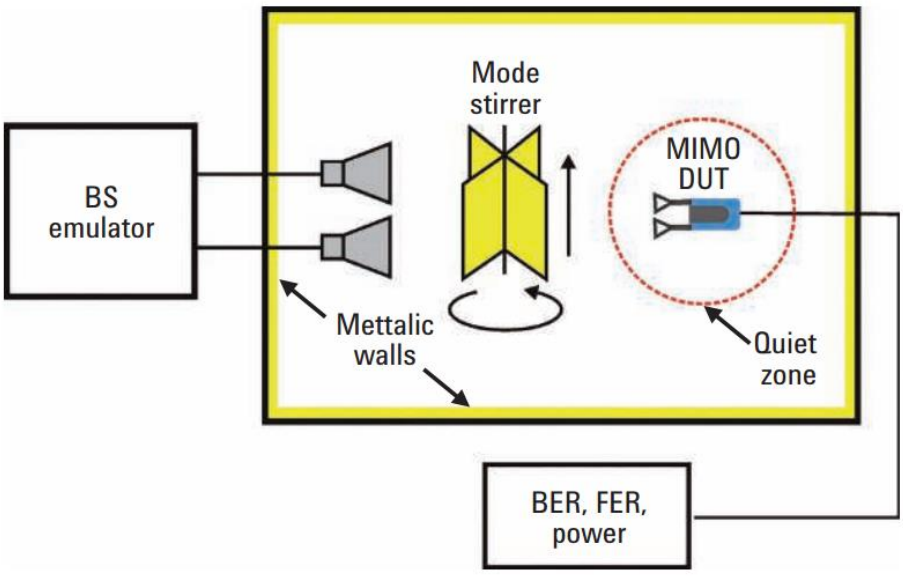

Figure 2-3: Test configuration for a 2x2 MIMO system using a reverberation chamber [II-4].

2.1.3. MIMO OTA Measurement with Multi-probe technique

The last OTA test method presented is the multi-probes technique. This method requires an anechoic chamber and a large number of probes placed inside the chamber in order to surround the MIMO DUT. This method aims to emulate a multipath environment by managing spatial parameters the Angle of Arrival (AoA) and the Angular Spreads (AS). Figure 2-4 presents the configuration of a multi-probe system with an anechoic chamber.

The signal generated by Base Station emulator is modified by the channel emulator that creates multi-path signals including path loss, fading, delay spread, Doppler spread or polarization. Those signals are then amplified by the amplification unit and transmitted simultaneously to different locations by probes. The probes can be used to represent the direct signal, multi-path signals or interferers, thus creating a specific RF propagation environment at the DUT position.

This method is scalable from a single cluster to a full 3D implementation. MVG provides on the shelf compact multi-probes systems with their StarMIMO range [II-11].

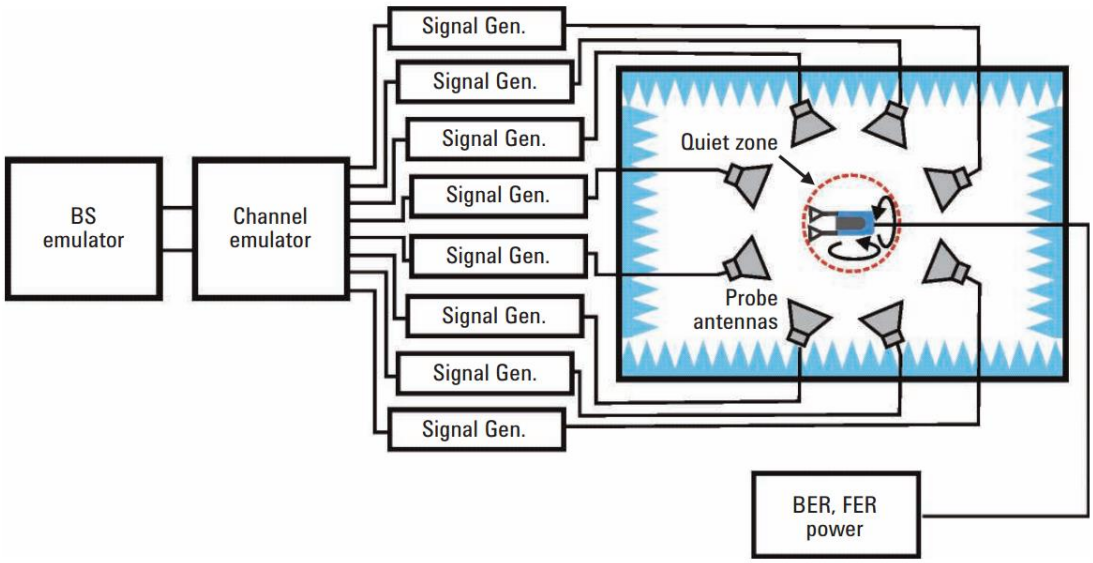

Figure 2-4: Test configuration for the multiple test probe OTA method using an anechoic chamber and channel emulator [II-4].

2.2. MIMO OTA Measurement with Rhodes&Schwartz Instrumentation

In this section, we present the design of an OTA test bed for MIMO access point using Rhodes&Schwarz (R&S) instrumentation such as vector signal generator (SMBV100A) and signal and spectrum analyzer (FSV, FSW). As we described in the first part of this chapter, besides free space measurement (matching, isolation, gain...) additional relevant criteria on the antenna system need to be studied after in a real environment [II-12]. In this case, the EVM is monitored after the spatial demultiplexing, using a specific test bench [II-13], [II-14].

2.2.1. Testbed Overview

In order to provide information about the performance of a MIMO system in a real channel, we propose to use the dedicated test-bench using vector signal generators and spectrum analyzers. We intend to get the statistical result by performing a great number of measurements. The overview of the measurement setup is presented in figure 2-5. Some pictures of the different elements of the testbed are presented in the figure 2-6.

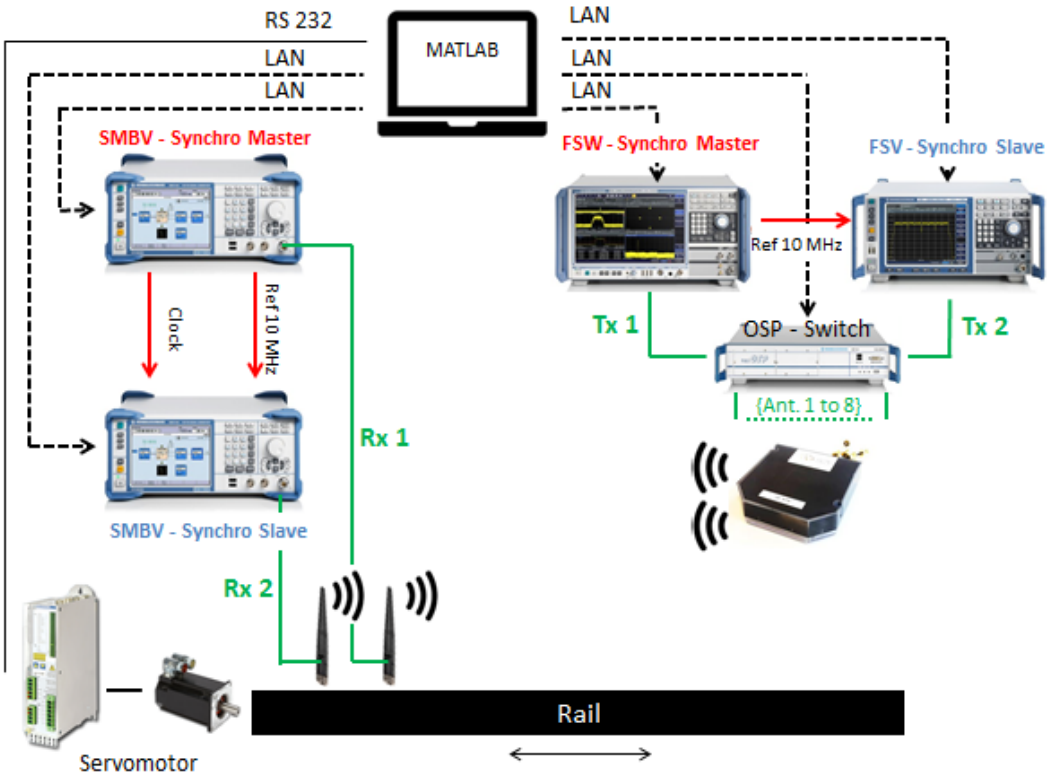

Figure 2-5: Overview of the R&S measurement setup.

On the transmission side, the MIMO 2x2 setup consists of two vector signal generator synchronized in a master/slave configuration. The generators synchronization is crucial for spatial multiplexing transmission. Each generator is connected to one Rx antenna embedded on a 4 meters long rail. This rail allows moving the transmissions antennas and thus analyzing different propagations channels.

On the other hand, the reception is ensured by two signal and spectrum analyzers. The two instruments are also synchronized in a master/slave configuration. The RF outputs of each spectrum analyzer are connected to a switch itself connected to an 8-antenna MIMO prototype. This setup aims to test all the possible MIMO 2x2 configurations available with the 8-antenna prototype. Each antenna can be paired with any other antenna to ensure the reception. In other terms with 8 antennas on the prototype, we can create 28 different configurations for the transmission.

All the instruments are remotely controlled via a simple laptop and the Matlab software. The computer is connected to the rail via an RS322 output. Every R&S instruments are also connected to the laptop via LAN cables. The program developed on Matlab automatically manages the transmission on the signal generators, the reception and the acquisition on the spectrum analyzer, and the movement of the two transmission antennas on the rail. This automation allows performing a great number of measurements to get statistically reliable results.

(a) (b) (c)

Figure 2-6: Pictures of (a) the rail, (b) the two Vector Signal generators and (c) the two Spectrum Analyzers.

2.2.2. System Configuration

The measurement method is based on the demodulation of an 802.11.AC signal with 2 TX antennas 2 Rx antennas chosen among 8. As we intend to extract data on the MIMO performance, the received signal level won't be sufficient to characterize the quality of the MIMO transmission. In this measuring method, demodulation and quantification of the system's performance are performed. The Error Vector Magnitude (EVM) criterion is studied as a performance indicator for spatial multiplexing.

Error vector magnitude (EVM) is a measure of modulation quality and accuracy as well as a performance criterion for wireless systems. It provides a good picture of the modulation as well as an evaluation of the performance of both transmitter and receiver. It also is often used as an alternative to bit error rate (BER) which is the percentage of bit errors that occur for a given number of bits transmitted. EVM measurements are used with modulation methods like QPSK and QAM, widely used in WLAN and LTE systems.

EVM take into account all the phase and amplitude errors as well as noise. Widely represented in the I/Q plane, EVM illustrates the ideal symbol vector location and size compared to the actually measured vector such as presented in the figure 2-7. The difference between the two is the EVM, which can be measured on transmitter modulator or receiver demodulator.

Mathematically EVM is the ratio of the average error vector power (P_{error}) to the average ideal reference vector power (P_{ideal}) expressed in decibels, as presented in the equation [2-1]. The averages are taken over multiple symbol periods.

$$EVM_{dB} = 10\ log\left(\frac{P_{error}}{P_{ideal}}\right) \qquad \text{eq. [2-1]}$$

The measured signal is demodulated and compared to the ideal signal that is produced mathematically from the received signal. The difference between the reference signal and the demodulated signal is the error. The vector signal analyzer displays a constellation diagram of the modulation. The ideal case is a single point, but in practice, there is a cluster of measured points around the ideal point. The more spread the points are, the poorer the EVM is. In concrete terms, a very low decibel value (for example - 40 dB) express a very low error on the modulation.

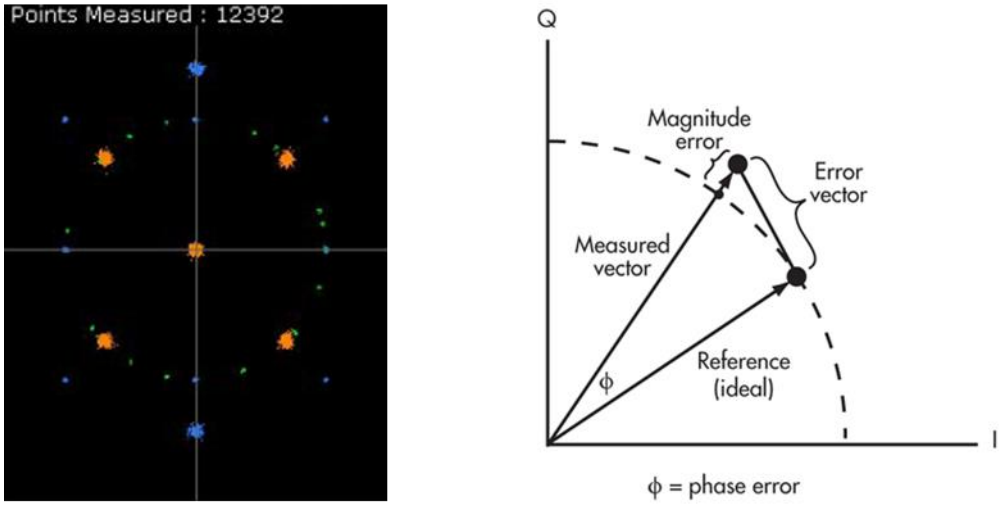

(a) (b)

Figure 2-7: (a) Example of a constellation for LTE QPSK modulation and (b) Schema of the EVM represented by the difference between the positions of the ideal signal and the actual received signal.

MIMO performance relies and depends on the propagation channel. In our situation, we want to develop a measurement method in a real environment, without the help of a reverberation chamber neither an anechoic chamber. The main problem is to control the environment in order to keep a propagation channel stable during the measurement phase. The setup was installed in a large room, naturally isolated from external radiation, especially in the Wi-Fi band where the tests were conducted. The configuration of the room is presented in the figure 2-8. The transmitter was at around 5 meters from the receivers in a line of sight (LOS) configuration.

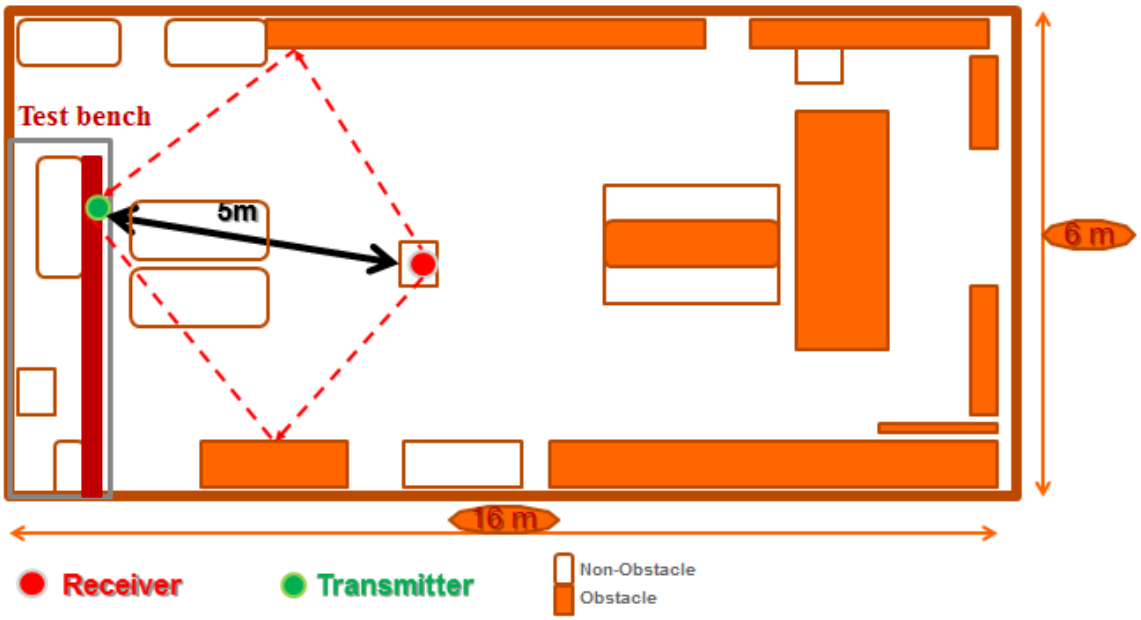

Figure 2-8: Schema of the top view of the measurement room.

2.2.3. Validation of the Measurement Setup

In order to validate the measurement setup and the methodology, we wanted to evaluate the reproducibility of the measurement. We performed three times the test with an identical configuration to estimate the average dispersion between several measurements. This experiment focuses on the acquisition of the EVM in a MIMO 2x2 configuration. We use an 8-antenna terminal at the receivers where all the possible antenna pairs are tested (28 pairs) over 200 positions of the transmitter.

The results for the three runs are presented in figure 2-9 and 2-10. Figure 2-9 presents the EVM per position on the rail for one set of antennas (Antenna set n°5 arbitrary selected among the 28 set available) and the EVM minimum acquired on the 28 antenna pairs. The 200 points measured are presented and correspond to one point every 1.5 cm. We can observe that the results are very similar for each run as much for one antenna set as for the EVM minimum. Moreover we observe that the antenna set n°5 achieve the best performances in several positions (14 positions). It is interesting to notice that the measured EVM can vary significantly between two adjacent positions. For instance the EVM change from -8 dB on the position 128 to -25 dB on the position 126. We observe a maximum dispersion of 8 dB measured at the position n° 5 of the antenna set 5. This result shows the importance to acquire a large number of point to insure the reliability of the measurement.

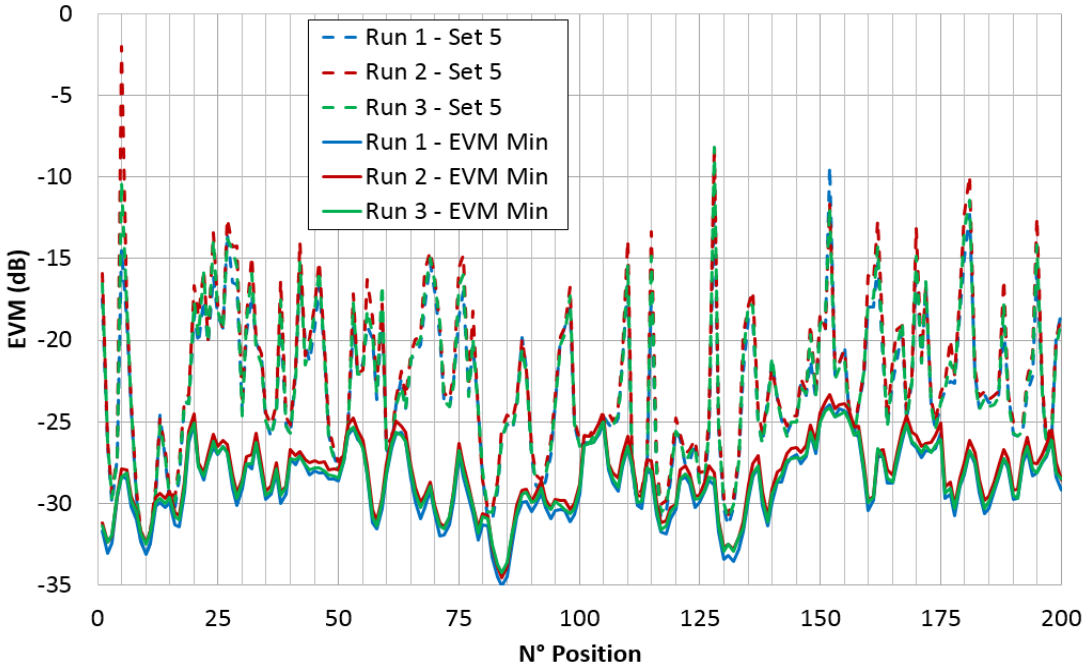

Figure 2-9: Dispersion among 3 identical EVM measurements for the antenna set 5 and the minimum EVM among all antennas sets.

The figure 2-10 presents the cumulative distributed function (CDF) for the full 200 points on the rail. To plot this graph, the measured value are sorted by ascending order and are traced in ordinate between 0 and 1, with the 1 representing 100 % of the sample. Thus we can observe than in 50 % of the measured situations, the EVM can be increased by at least 4.5 dB. We also observe a good fit among the three measurements.

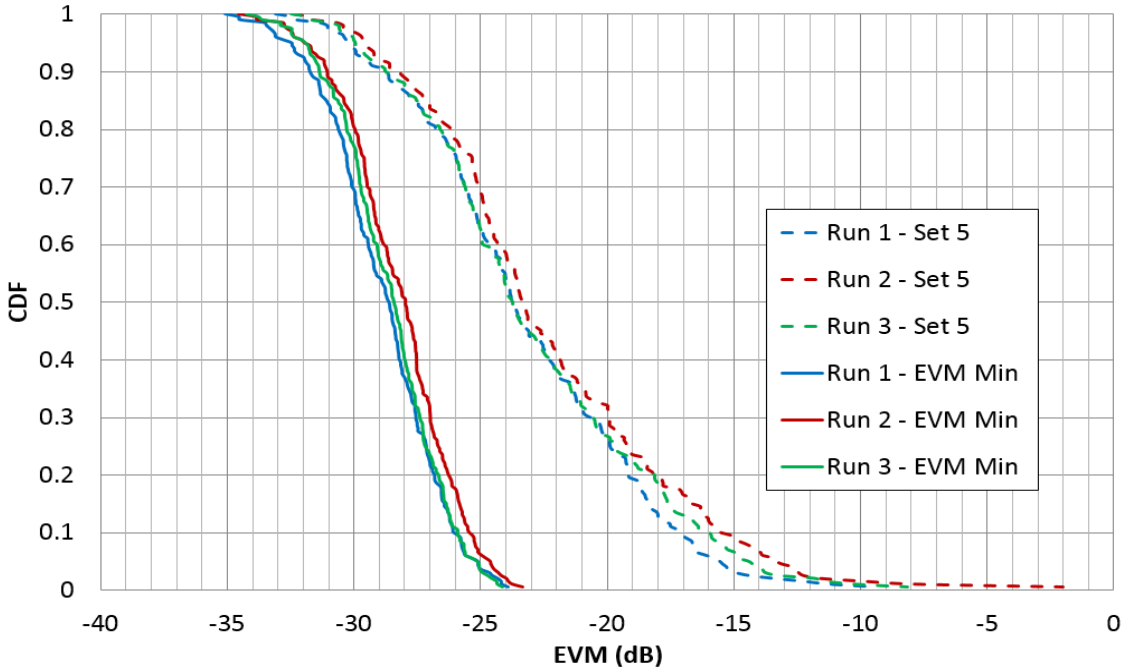

Figure 2-10: CDF of the dispersion among three identical for antennas set 5 and the minimum EVM among all antennas sets.

To determine the dispersion among the measurements, we calculate the difference between the EVM maximum and minimum measured on each position within the three runs. Then we average the dispersion over the 200 measurements. The average dispersion is calculated and presented in table 2-1 for the antenna set 5, the EVM minimum and finally for the whole measurement. The average dispersion is +/- 1.3 dB. The validation result shows a good accuracy of the measurement setup and confirms the reproducibility of the method.

Table 2-1: Average dispersion calculated on the EVM for the R&S measurement setup.

Antenna Configuration	Average Dispersion
Antenna Set n°5 (figure 2-9 and 2-10)	+/- 0.85 dB
EVM Min (figure 2-9 and 2-10)	+/- 0.96 dB
Average on 28 Antenna Sets	+/- 1.3 dB

Despite the good accuracy demonstrated above the measurement setup suffers from several constraints. The instruments used to design the testbed are very expensive. Testing all the possible configuration through the OSP switch requires a very long acquisition time. The sequential characteristics of the acquisition require a very stable propagation channel to ensure accurate measurements. Working on a higher MIMO scale (4x4, 8x8) would require additional generators and analyzers increasing substantially the cost and the complexity of the installation.

Having the opportunity to start a collaboration with EURECOM who develop an open-source implementation of the 4G standard, we decided to investigate the OpenAirInterface. By leveraging both OAI software and low-cost RF front-end to create another MIMO OTA measurement system. The systems provide the ability to perform synchronous 8 channel acquisitions.

2.3. MIMO OTA Measurements with OpenAirInterface

In this part, we describe the design of a custom testbed using existing Software Defined Radio (SDR) boards. The general purpose of this work is to develop an Over-The-Air (OTA) measurement system to characterize a MIMO access point. The main idea is to leverage the OpenAirInterface (OAI) platform developed by EURECOM [II-15], interfaced with ExpressMIMO2 PCI Express (PCIe) boards, which are the default software radio frontends for OAI. This "soft-emulator" runs on a simple Linux machine allowing for a strong cost reduction. The effectiveness of the system is confirmed by the reproducibility of the measurements, which have been obtained using a plastronic gateway with eight antennas.

2.3.1. OpenAirInterface

EURECOM has created OpenAirInterface Software Alliance (OSA), a non-profit consortium to develop an ecosystem for open source software/hardware development for the core network (EPC) and access-network (EUTRAN) of 3GPP cellular networks. OAI is now a very interesting tool used by both industry and academia. The alliance is positioning itself as a communication mechanism between the two to bring academia closer to complex real-world systems controlled by major industrial players of the wireless industry. In the actual telecommunication context OAI answers to the need of an open-source tool to help along research and development, prototyping and rapid proof-of-concept designs. A great number of industrial and academics are currently using OAI for diverse collaborative projects.

OAI can be used to build and customize an LTE base station and core network on a standard PC. It allows connecting a commercial UE to test different configurations and network setups and monitoring the network and mobile device in real-time. With OAI, the transceiver functionality is realized via a software radio frontend connected to a host computer for processing. The software can be used with standard RF laboratory equipment available in many labs in addition to custom RF hardware provided by EURECOM. Currently, the OAI platform includes a full software implementation of the 3GPP LTE protocol stack, both for the RAN and the EPC.

The RF frontend designed by EURECOM named EXPRESSMIMO2 is presented in the figure 2-11. The board features 4 parallel RF chains with bandwidths up to 20 MHz (4x5 MHz, 2x10 MHz, and 1x20 MHz) per chain covering a very large part of the RF spectrum in the range of 350-3800 MHz. It interconnects with a baseband computing engine using Gen1 1-way PCI-express. The latest version of the ExpressMIMO2 board has also built-in amplifiers, LNAs, and switches for FDD and TDD operations. Each transceiver is controlled individually.

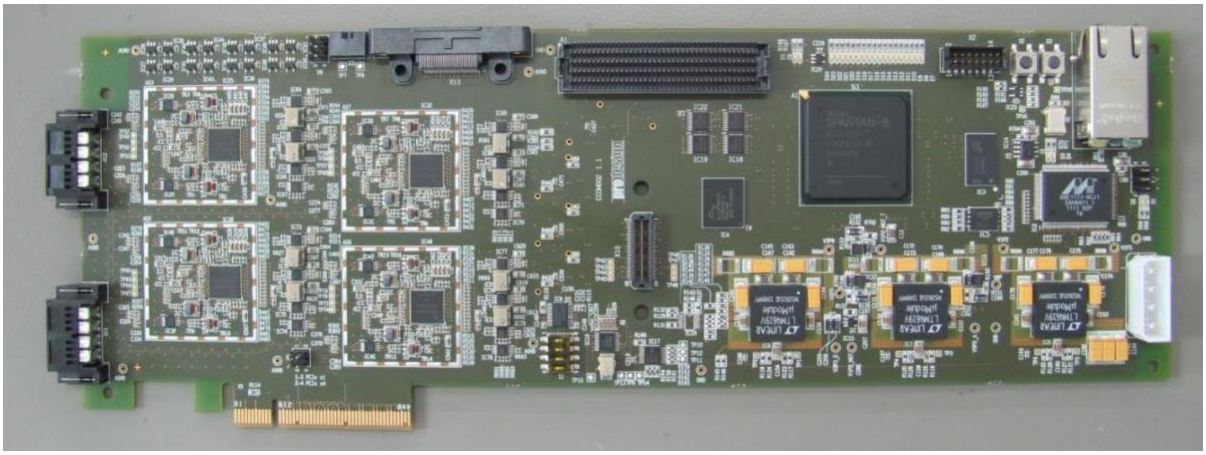

Figure 2-11: picture of the EXPRESSMIMO2 board [II-15].

For now, only LTE have been developed on OAI, but the implementation of Wi-Fi protocols are under investigation. In this work, we decided to consider our 8-antenna prototype as an LTE femtocell and not as a router anymore.

2.3.2. Testbed Overview

In this section, we present the overview of the low-cost measurement method for MIMO antenna performance assessment based on the open-source OAI initiative. The measurement setup aims to characterize various antenna configurations for MIMO application in a beamforming configuration. We intend to get the statistical result by performing a great number of measurements. The figure 2-12 presents the architecture of the measurement system.

The system consists of three ExpressMIMO2 boards running on common Linux machines with two acting as Evolved Node B (eNB) and one as User Equipment (UE). The computer also controls the movement of the rail. The eNB is in a static position at 4 meters from the center of the rail. On the transmission side (eNB) a prototype with 8 antennas at 2.6 GHz integrated into a 135x135x35mm femtocell is used. For the receiving part (UE) we use a simple monopole antenna at 2.6 GHz embedded on an automated 4 meters long rail to perform statistic measurements in different propagation channels.

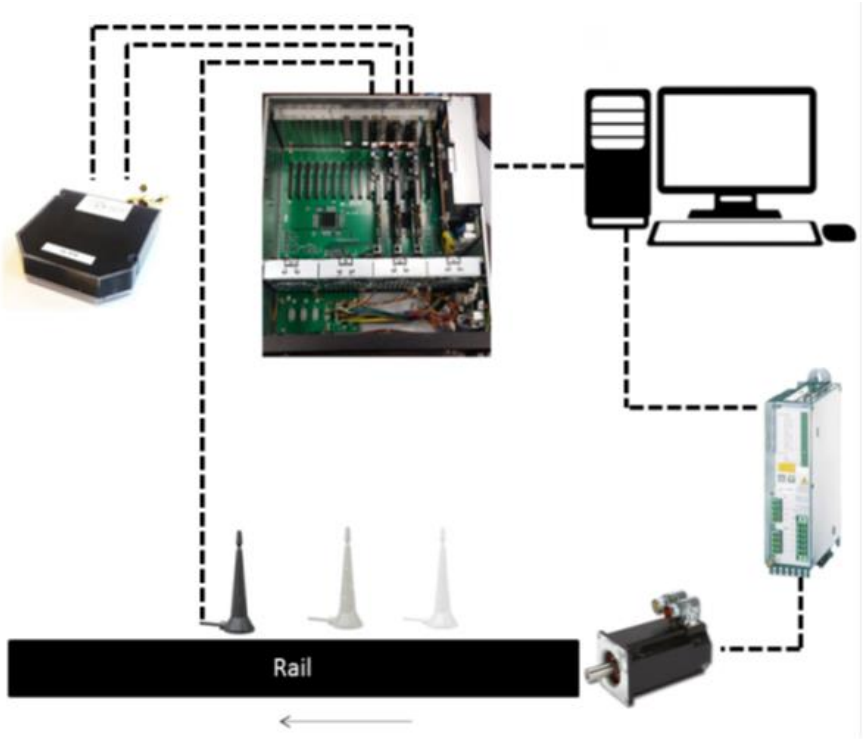

Figure 2-12: Overview of the OAI measurement setup.

2.3.3. System Configuration

The proposed setup is configured to operate in Time Division Duplexing (TDD) mode in an 8x1 MISO and 1x1 SISO communications at 2.6 GHz. The program switches between each configuration for each position of the monopole on the rail. Measurements are performed in a LOS configuration with the transmitter at around 4 meters from the receiver. The testbed works in simulation mode with the platform Octave to test the signal processing algorithms before integrating them into the OAI real-time environment. In this setup, the Signal to Noise Ratio (SNR) criterion is studied as a performance indicator for beamforming.

The eNB transmits 10 LTE OFDM frames with a 5 MHz bandwidth and a transmitted power of 10 dBm. The power is chosen to ensure a good level of reception in the whole room while avoiding saturation of receiving RF chains. For each position on the rail we test and retrieve the SNR for both 8x1 MISO and SISO configuration.

As we already said, MIMO performance relies and depend on the propagation channel. This measurement method is developed without any anechoic or reverberant chamber so we must control the environment to keep the propagation channel stable while measuring. The setup is installed in a simple room whose configuration is presented in figure 2-13. This time the room is subject to radiation in both Wi-Fi and LTE bands but not in the 2.6 GHz band which still is not used by commercial devices in France.

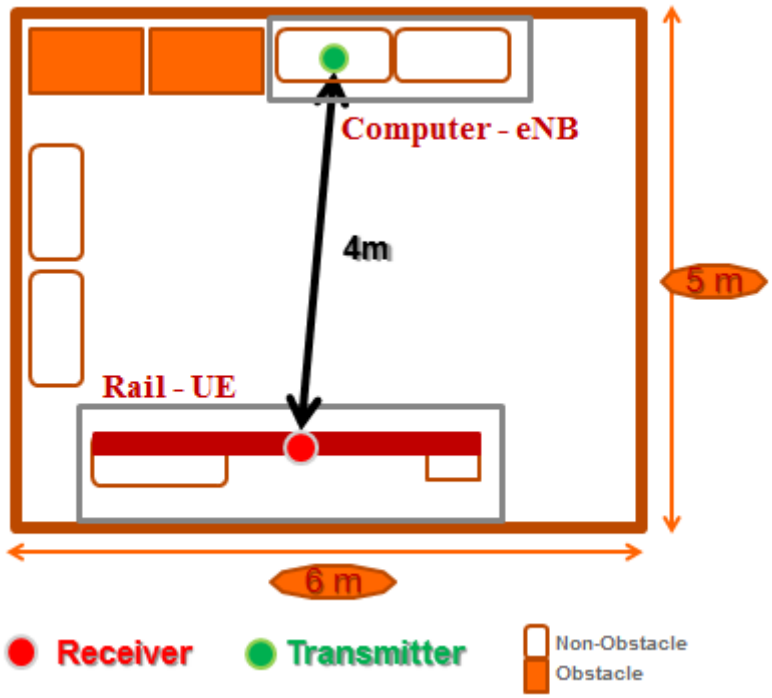

Figure 2-13: Schema of the top view of the measurement room.

2.3.4. Validation of the measurement setup

In order to determine the reproducibility of the test method, we repeated three times the same test case. These latter consists of measuring SNR values for 200 positions with a 3 cm step on the rail. The rail is going forward for the first 100 positions and backward for the last 100. At each position, we retrieve the SNR for the eight antennas in a SISO configuration as well as the SNR in a MISO 8x1 configuration.

The figure 2-14 presents the beamforming results (MISO 8x1) along with one antenna measurement (SISO antenna n°5) for the 200 positions corresponding to one point every 3 cm on the rail. We observe that whatever the case, there is a very low dispersion among the measurements. The symmetrical pattern of the curve is explained by the two-way movement on the rail. It is interesting to notice that the measured SNR can vary significantly between two adjacent positions. We observe a maximum dispersion of 30 dB measured at the position n° 94 of the antenna 5. This result shows the importance to acquire a large number of point to insure the reliability of the measurement.

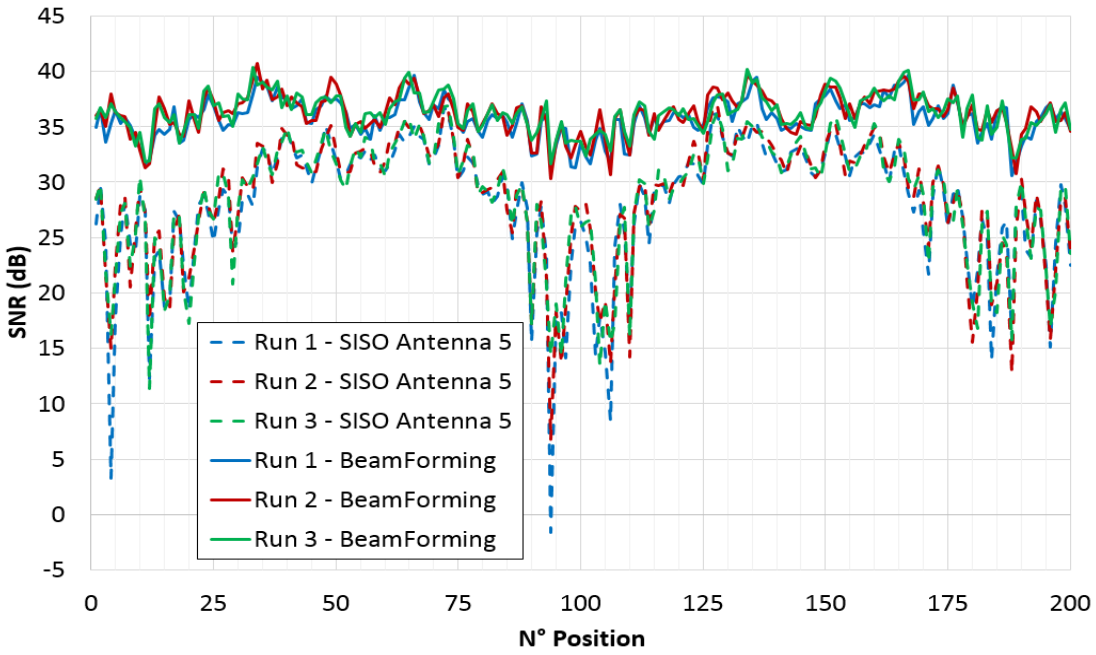

Figure 2-14: Dispersion among 3 identical MISO 8x1 and SISO SNR measurements.

Figure 2-15 presents the Cumulative Distributed Function (CDF) for the full 200 measurements. To plot this graph, the measured value are sorted by ascending order and are traced in ordinate between 0 and 1, with the 1 representing 100 % of the sample. Thus we can observe than in 50 % of the measured situations, the SNR can be increased by at least 6 dB with a beamforming configuration. We also observe that beamforming gain is very similar for the three run.

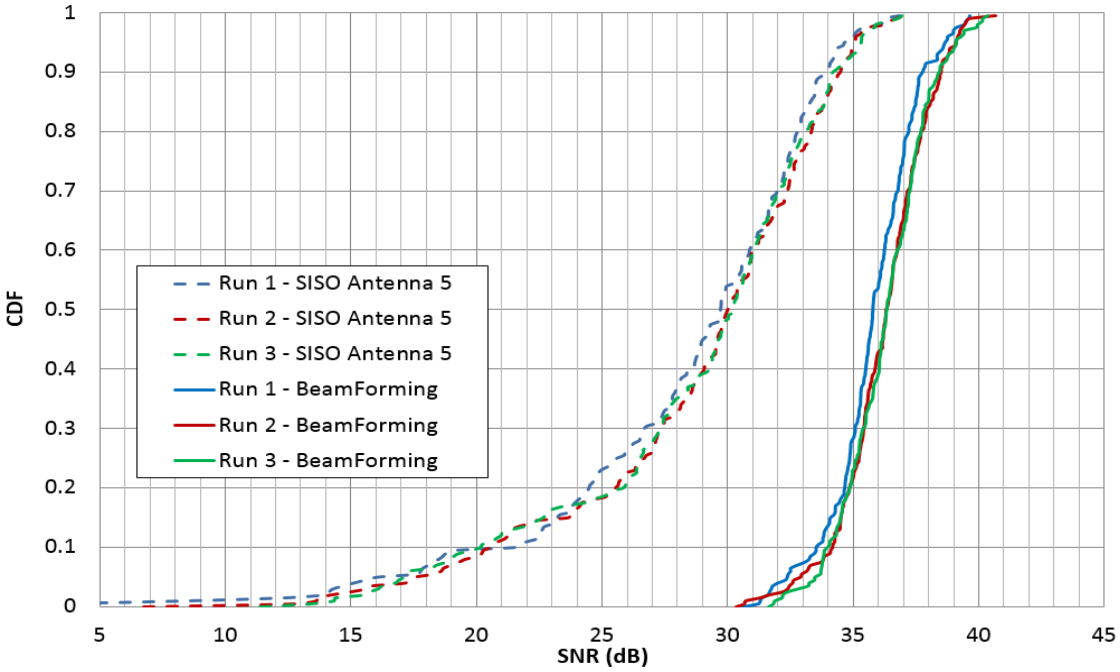

Figure 2-15: Beamforming Gain between SISO and MISO 8x1.

Finally the table 2-2 details the average dispersion calculated over the 200 positions and the three runs. To determine the dispersion among the measurements, we calculate the difference between the EVM maximum and minimum measured on each position within the three runs. The average dispersion is +/- 1.1 dB for the antenna 5 and +/- 0.67 dB for the beamforming measurement. The accuracy is satisfying compared to the level of the measured SNR. This accuracy might be improved by adding filters to the system.

Table 2-2: Average Dispersion for 8 antennas SISO and MISO 8x1 Beamforming.

Antenna Configuration	Average Dispersion
SISO - Antenna 1	+/- 1.6 dB
SISO - Antenna 2	+/- 1.6 dB
SISO - Antenna 3	+/- 1.3 dB
SISO - Antenna 4	+/- 1.3 dB
SISO - Antenna 5	+/- 1.1 dB
SISO - Antenna 6	+/- 1.5 dB
SISO - Antenna 7	+/- 1.3 dB
SISO - Antenna 8	+/- 1.2 dB
MISO 8x1 Beamforming	+/- 0.67 dB

The results show that measurements are repeatable with good accuracy of the measurement setup and validate the reproducibility of the method. The system is low-cost, very flexible and faster

than the R&S measurement setup developed in the first part. For now, we work in a simulation environment, but the setup can be extended to a real-time configuration.

2.4. Synthesis of MIMO OTA Measurement and Conclusions

The wireless industry has developed several tools to assess the Over-The-Air performance of multi-antennas systems. Unfortunately, those methods are extremely expensive while the need for low-cost experimentation is increasing especially for an academic purpose. In this chapter, we presented the experimental validation of two different measurement testbeds.

The first one has been developed through classic industrial RF instrumentation from Rhodes&Schwartz. This setup has shown a good accuracy allied with relative simplicity of use. The main problem rests the costs, increasing proportionally with the number of antennas in the MIMO system under test. The second testbed has been designed leveraging the OAI, an open-source software defined radio. The setup presents a similar accuracy, a much lower cost, and much more flexibility thanks to its open-source aspect. The table 2-3 present a comparison between all the setup discussed in this chapter in terms of complexity, flexibility, and costs.

Table 2-3: Overview of different OTA Measurement setups in terms of Cost, Complexity, and Flexibility.

Method	Complexity	Flexibility	Cost	Accuracy
Two-Stage	Medium	Medium	Medium	Medium
Reverberant Chamber	Medium	Low	Medium	High
Multi-Probes	High	Medium	Very high (>500 k€)	High (very sensitive to calibration)
Rhodes&Schwartz	Low	Low	Medium (~120 k€ for 2x2 MIMO) (~430 k€ for 8x8 MIMO)	Low (very sensitive to channel variations)
OAI	High	High	Low (~25 k€)	Medium

For the next part of the work, we choose to exploit the OAI measurements setup to test and evaluate the performance of our MIMO access points.

2.5. References

[II-1] Samsung Electronics Co., “5G vision”, White Paper, February 2015.

[II-2] T. Laitinen, J. Toivanen, P. Kyösti, J. P. Nuutinen and P. Vainikainen, "On a MIMO-OTA testing based on multi-probe technology," *2010 URSI International Symposium on Electromagnetic Theory*, Berlin, 2010, pp. 227-230.

[II-3] Rafik Addaci, Katsuyuki Haneda, Aliou Diallo, Phillipe Le Thuc, Cyril Luxey, Robert Staraj and Pertti Vainikainen, “On Dual-Band WLAN Multiantenna System and Diversity/MIMO Performance Evaluation” IEEE transactions on Antennas and Propagation, Vol. 62, No.3, March 2014.

[II-4] Agilent Technologies. Theory, “Techniques and Validation of Over-the-Air Test Methods for Evaluating the Performance of MIMO User Equipment.” Application Note.

[II-5] A. Khatun, T. Laitinen, V. M. Kolmonen, and P. Vainikainen. “Dependence of error level on the number of probes in over-the-air multiprobe test systems.” International Journal of Antennas and Propagation, 2012.

[II-6] P. Kyösti, T. Jämsä, and J. P. Nuutinen. “Channel modelling for multiprobe over-the-air MIMO testing.” International Journal of Antennas and Propagation, 2012.

[II-7] W. Fan, X. Carreño, J. Ø. Nielsen, J. Ashta, G. F. Pedersen, and M. Knudsen. Verification of Emulated Channels in Multi-Probe Based MIMO OTA Testing Setup. In Proc of Antennas and Propagation (EuCAP), 2013 7thEuropean Conference, (pp. 97 – 101). Gothenburg.

[II-8] Rhodes&Schwarz White paper, “Two-Channel Method for OTA Performance Measurements of MIMO-Enabled Devices,” 2011.

[II-9] Keysight Technologies, application note, “Theory, Techniques, and Validation of Over-the-Air Test Methods For Evaluating the Performance of MIMO User Equipment.”

[II-10]] 3GPP TR 37.976 V1.1.0 (2010-05) "Measurement of radiated performance for MIMO and multi-antenna reception for HSPA and LTE terminals" (Release 10)

[II-11] http://www.mvg-world.com/fr/products/field_product_family/antenna-measurement2.

[II-12] Tobias L. Jensen and Torben Larsen, Senior member, IEEE, “On Robust Computation of Error Vector Magnitude for Wireless Standards” IEEE transactions on Communications, Vol. 61, No 2, February 2013.

[II-13] Rene Schmogrow, Bernd Nebendahl, Marcus Winter, Arne Josten, David Hillerkuss, Swen Koenig, Joachim Meyer, Michael Dreschmann, Michael Huebner, Christian Koos, Juergen Becker, Wolfgang Freude and Juerg Leuthod, “On Error vector Magnitude as a Performance Measure for Advanced Modulation Formats” IEEE Photonics Technology Letters, Vol. 24, No.1, January 1, 2012.

[II-14] Shafik, R.A., et al., “On the Error Vector Magnitude as a Performance Metric and Comparative Analysis,” IEEE 2nd International Conference on Emerging Technologies, November 2006.

[II-15] OpenAirInterface: http://www.openairinterface.org.

3. MIMO Antenna Design for Multi-standard Gateway / Wi-Fi, LTE, 5G

Table of content Chapter 3

3.1. MULTI ANTENNA SYSTEMS 57
3.1.1. MIMO Systems and characteristics 57
3.1.2. Diversity Techniques 58
3.1.3. Spatial Multiplexing 61
3.1.4. Beamforming 62
3.1.5. Massive MIMO Systems 63
3.2. DESIGN OF 8-ANTENNA PROTOTYPES 64
3.2.1. Box Design for LDS Technology 65
3.2.2. Hook Shaped Antenna printed on a PCB substrate 68
3.2.3. Printed IFA with PCB technology 73
3.2.4. PIFA with PCB technology 77
3.2.5. Mixed prototype with hook shaped antennas, PIFA and IFA on PCB technology 82
3.2.6. Hook-shaped printed on the sides of a plastic box with LDS technology (S1) 85
3.2.7. Hook-shaped antenna printed on the top of a plastic Box with LDS technology (T2) 88
3.2.8. Summary of the different prototypes 90
3.3. MEASUREMENTS RESULTS WITH OPENAIRINTERFACE 92
3.3.1. Prototypes comparison 92
3.3.2. Antenna selection in multi-antenna devices 95
3.4. DIRECTIONAL ANTENNAS 99
3.4.1. Directivity enhancement with AMC 99
3.4.2. Directivity enhancement using a reflector 106
3.5. CONCLUSION AND PERSPECTIVES 121
3.6. REFERENCES CHAPTER 3 122

In this chapter, we present a project structured around the design of antenna systems for Wi-Fi and LTE applications. We propose to realize a router constituted of 8 dual-band antennas. Each antenna must work in two frequency bands at 2.4 - 2.7 GHz and 5.15 - 5.8 GHz to cover the WLAN 802.11n and 802.11ac standards and the LTE Time Division Duplexing (TDD) band at 2.6 GHz. The system aims to combine MIMO and diversity techniques in order to increase the performance of wireless communication in terms of signal quality, robustness, and throughput.

In a first time, we realized a set of PCB on a classic FR4 substrate with a maximum surface of 135x135 mm². We studied different types of antennas (Monopole, PIFA, and IFA) but we kept the same configuration (number of antenna and implementation) for each prototype. The second step of the project is to investigate plastronic technology to move antennas from the PCB to the plastic box. Indeed the volume occupied by the antenna is a major constraint and using the casing as support for antennas comes with several advantages (volume optimization, miniaturization, design flexibility...).

The second objective was to print the antennas directly on the plastic of the router's case in order to save space and optimizes volumes. Indeed, new technologies such as 3D printing [III-1], Laser Induced Metallization (LIM) [III-2] or Laser Direst Structuring (LDS) [III-3, III-4] open new degrees of freedom in antenna design. All along this project, we worked with Smart Plastic Product (S2P) [III-4], a technical center for plastics and composites who provides expertise and skills in terms of plastronic. Plastronic applies "to bring intelligence to plastic parts." They provide among other, skills with Laser Direct Structuring (LDS) technology which is a fast and reliable process to print RF component on various plastics. As presented in figure 3-1, plastronic is already used in several industries for different kinds of application such as antennas, sensors or LED lightning for example.

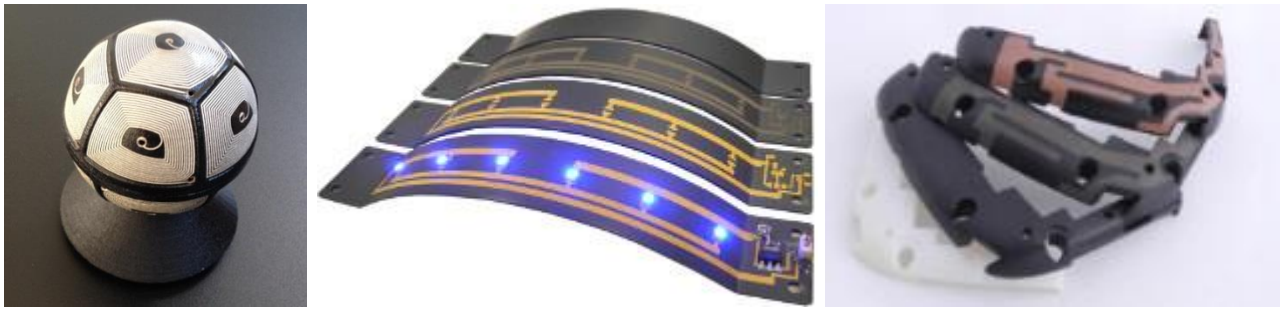

Figure 3-1: Examples of realization with LDS technology [III-4].

The interest was to test and validate the performance of the LDS technology, a metallization process on a plastic material that would allow us to print our antennas directly on the router's case. The realization of this type of part is done in three stages. First the element is injected with the

activable material in a standard mold, then a laser activates the zones which will be metallized, and finally, the metallization is done with a chemical process. To properly asses the LDS technology, we designed a box able to host antennas printed with LDS as well as the classic PCB. In order to characterize all those systems in free space, we performed S-parameters and radiation simulations on HFSS before measuring the system with a VNA and a Satimo Star Lab. To go further, we use the OAI measurement system presented in the previous chapter to study and compare systems in a realistic environment.

The last objective of this work is to use and explore the benefits of directive antennas. Indeed the system possesses more antennas than needed and we want to take advantage of this property to focus the radiation toward the user. Thus the cumulated radiation pattern must cover every direction.

3.1. Multi Antenna Systems

MIMO technology has emerged as a key technology for the high-data-rate wireless system. Many techniques have been developed to exploit multi antenna systems from the use of diversity [III-5] to more complex techniques such as spatial multiplexing or beamforming. Nowadays, several MIMO systems combine spatial multiplexing with space-time code (STC) or beamforming presented below.

3.1.1. MIMO Systems and characteristics

When it comes to MIMO systems, the usual way to characterize antennas becomes inadequate. Indeed antennas are defined by a set of parameters such as the efficiency, the matching or the radiation pattern. The emergence of multi-antenna systems requires developing new ways to characterize antennas such as correlation coefficient and multiplexing efficiency. MIMO (Multiple Input Multiple Output) techniques use antenna array at the receiver and the transmitter to increase channel capacity [III-6], the signal to noise ratio, the throughput. The increased performance compared to SISO (Single Input Single Output) system can be seen more concretely as better coverage or a reduced transmitted power. Figure 3-2 illustrates the operating principle of a MIMO system. The received signal Rx (combination of Rx1 and Rx2) can be written as follows:

$$Rx = H.Tx + n \qquad \text{eq. [3-1]} \qquad \text{with } H = \begin{bmatrix} h11 & h12 \\ h21 & h22 \end{bmatrix} \text{ and n the noise}$$

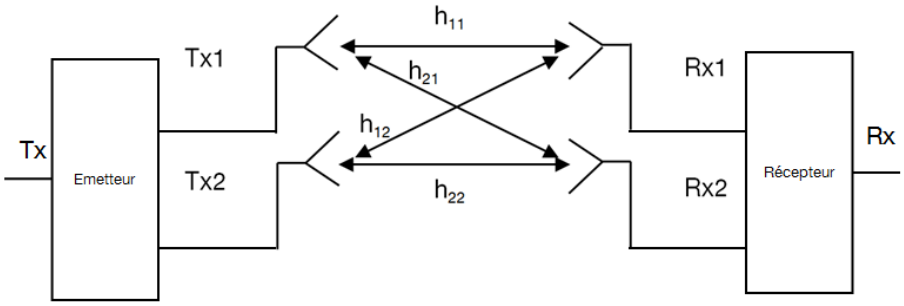

Figure 3-2: Schema of theoretical MIMO channel.

The independence of the signals received by the antennas of a system is estimated in terms of correlation coefficient or correlation envelope. The correlation envelope is the square root of the correlation coefficient. This criterion is the most used to characterize MIMO systems. The correlation between two antennas (element 1 and element 2) can be calculated according to [III-7], from S-Parameters in eq. [3-2] but it can also be calculated from measured radiated fields [III-8, III-9].

$$\rho_e = \frac{\left|S^*_{11}S_{12} + S^*_{12}S_{22}\right|^2}{\left(1-\left|S_{11}\right|^2-\left|S_{21}\right|^2\right)\left(1-\left|S_{12}\right|^2-\left|S_{22}\right|^2\right)} \qquad \text{eq. [3-2]}$$

It can be shown that the distance between antennas has a strong relationship to the overall spatial correlation [III-10, III-11]. For example, if two omnidirectional antennas with the same polarization are placed in very close one from each other, there will probably be highly correlated. Unfortunately, many portable MIMO devices are physically small, thus limiting the antenna separation to less than a wavelength. There are many solutions to achieve a low spatial correlation between two closely spaced antennas such as cross polarizing the antennas [III-12] or bringing pattern diversity between the antennas.

3.1.2. Diversity Techniques

Diversity techniques emerged to overcome the signal fading which is the main cause of a bad wireless transmission [III-13]. The global idea is to transmit the signal in several independent paths, his way if one path has a very weak signal, another path can compensate and take over the communication [III-14]. This technique can optimize the SNR by choosing the best path among all the paths. Diversity in this simple aspect is often used for MISO or SIMO systems. This diversity can be achieved with different solutions. The most spread in wireless communication is the spatial diversity, obtained by

physically spacing as much as possible antennas from each other. Another solution is the polarization diversity which makes possible to strongly decorrelate two identical signals. Finally, the pattern diversity can be used by choosing antennas with different radiation pattern. There might be other diversity techniques that are not explained here.

On the transmission side, the space-time code (STC) is a method employed to improve the reliability of the communication [III-15]. This signal processing technique consists in transmitting the same data on several antennas according to a specific repartition and repetition. This redundancy aims to exploit spatial diversity by creating independent fading conditions for each path. This method does not directly increase the throughput but allows the use of a higher modulation scheme, a better spectral efficiency or a lower transmitting power by increasing the transmission quality. The Alamouti STC is the most spread thanks to its orthogonal property [III-16].

These diversity techniques developed on antennas are used with combination techniques in the processing part of the receiver [III-17]. Each replica of the received signal is combined to improve performance. Several methods have been developed to combine the signals received. The Selection Combining (SC) method is easy to implement and very low-cost. Indeed it is the signal with the highest received power or the highest SNR which is selected among the different received signal. In the method of Maximum Ratio Combining (MRC) all received signals are weighted according to their signal-to-noise ratio and then summed. This technique allows for the optimum reception because all the received signals are used. This method can give a good SNR even if none of the paths gives a good signal, but it is complex to implement and expensive. Finally, in the Equal Gain Combing (EGC) method the branch weights are all set to unity, but the signals from each branch are co-phased to provide equal gain combining diversity. This method allows the receiver to exploit signals that are simultaneously received on each branch.

The gain in diversity is one of the most important parameters of a diversity system. It is defined as the improvement of the signal-to-noise ratio of the combined signals with respect to the signal received by an antenna alone. The diversity gain is commonly illustrated with the figure 3-3 [III-18].

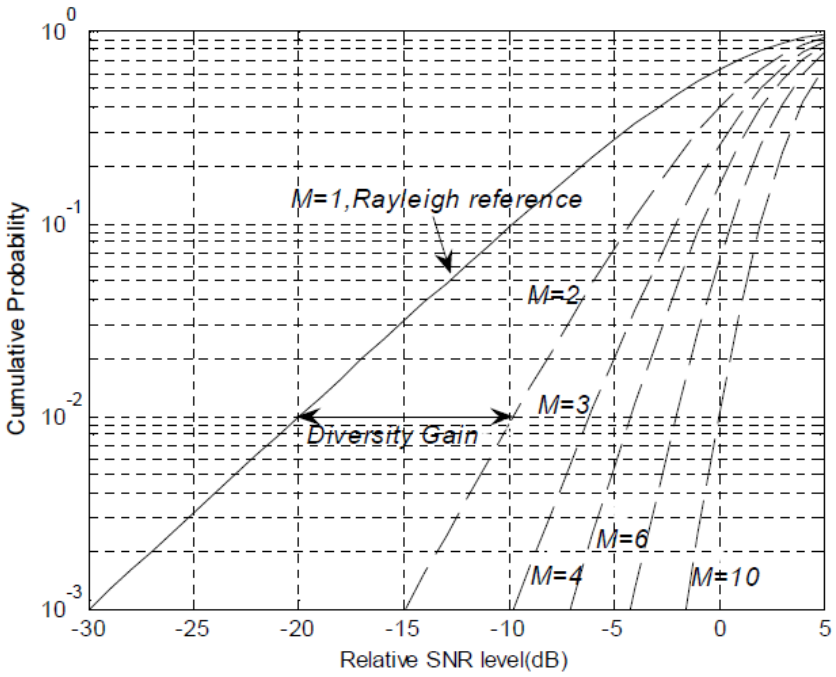

Figure 3-3: Illustration of the diversity Gain [III-18].

The correlation coefficient presented in the previous section is important because it has a direct influence on the diversity gain. Diversity techniques need to be properly implemented at the antenna level in order to have an efficient multi antenna system. The figure 3-4 [III-18] presents the diversity gain as a function of correlation coefficient when the selection combining method is applied. We can see that the diversity gain decrease when the correlation coefficient tends to one. In a classic diversity system, the objective is to achieve a correlation coefficient below 0.707 (ECC below 0.5) because the diversity gain decreases rapidly beyond this value.

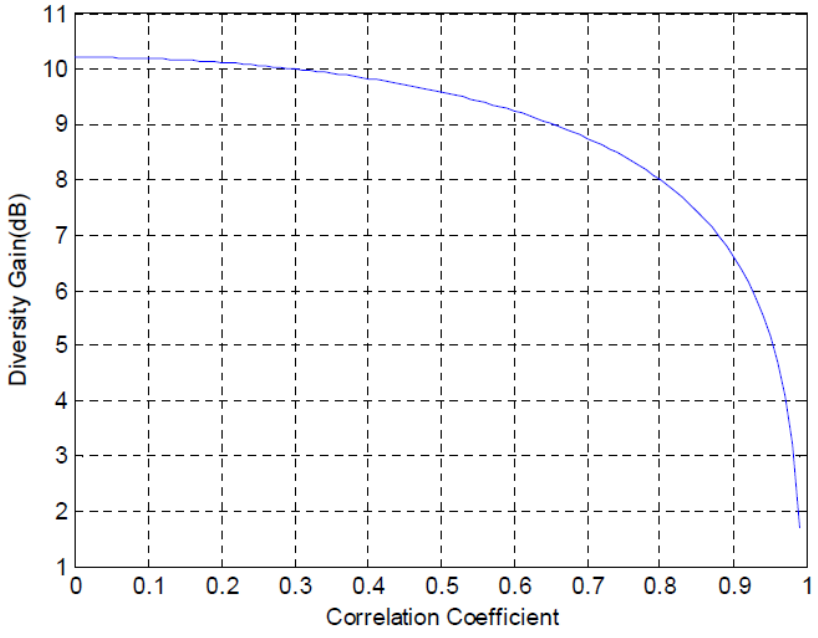

Figure 3-4: Diversity Gain as a function of correlation coefficient [III-19].

3.1.3. Spatial Multiplexing

In a MIMO system with spatial multiplexing, different data are transmitted over each antennas using the same resource in both frequency and time. The channel capacity and global throughput are then optimized and multiplied by the number of transmitting antennas. According to the Shannon capacity expression in eq. [3-1] we should have a 3 dB increase of the SNR when doubling the number of antennas at the transmitter.

$$C = \sum_{i=1}^{\min(M,N)} BW \, log_2(1 + SNRi) \qquad \text{eq. [3-3]}$$

Where BW is the bandwidth, M and N the number of antennas at the receiver and the transmitter, respectively, and SNR represents the signal to noise ratio.

This method is easy to implement at the transmitter but needs a very complex decoding system at the receiver. Indeed, each Rx antenna receives a superposition of the data transmitted by each Tx antenna. The receiver must dissociate those data to reconstruct the initial signal while suppressing interferences caused by the superposition. To achieve this reconstruction the receiver needs at least as much antenna than the transmitter. The figure 3-5 [III-19] illustrates a spatial multiplexing communication with 3 antennas at both transceiver and receiver. On the schema, each colored arrows represent a set of data simultaneously transmitted over the 3 antennas. The throughput is multiplied by three compared to a SISO system.

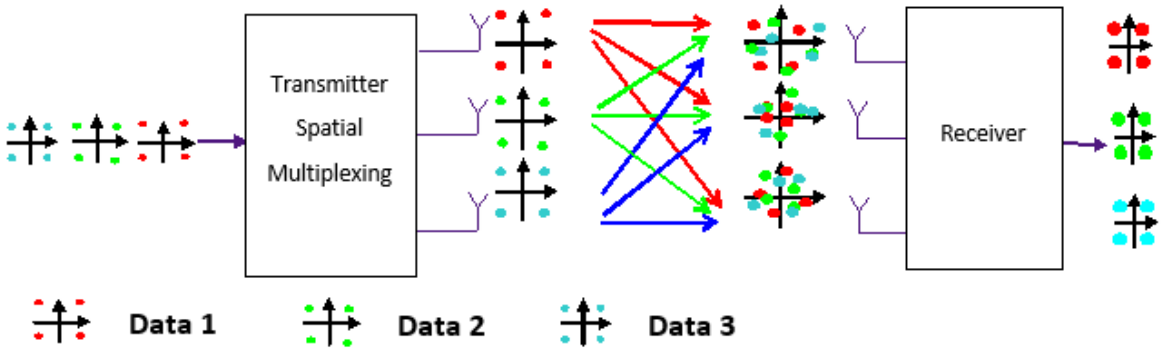

Figure 3-5: Illustration of MIMO Spatial Multiplexing with 3 antennas at the transeiver and receiver [III-19].

Spatial multiplexing can be used to communicate either with one or several users [III-20]. Single-user MIMO (SU-MIMO) requires multiple antennas both at the user equipment and the access point to spatially multiplex channels toward a single user. The main drawback is that the complex signal

processing is done on the receiver's side, limiting the benefits of the technology for small devices. Multi-user MIMO (MU-MIMO) enable a multi-antenna access point to simultaneously transmit multiple streams to different devices, instead of just one single device as in SU-MIMO. The user equipment does not need to have multiple antennas to benefits the technology. MU-MIMO does not increase peak user throughput, but it does increase average user throughput and sector capacity.

3.1.4. Beamforming

Beamforming is the ability to adapt the radiation pattern of an antenna array to a particular scenario as illustrated in the figure 3-6. In contrast with STC or spatial multiplexing, the beamforming uses the knowledge of the different channel to optimize and focus the transmission in a very specific direction [III-21]. This technique is very adapted to low mobility system such as base station to base station communication link. TDD mode is also adapted because information about the downlink channel (DL), also called Channel State Information at the Transmitter (CSIT), can be obtained thanks to an estimation of the uplink channel (UL) [III-22]. Indeed the TDD technique relies on channel reciprocity between UL and DL. Channel reciprocity means that the BS can acquire knowledge of the channel just through UL channel estimates. The beamforming method allows reducing interferences generated by other cells by focusing the transmitted power in precise directions, improving at the same time the transmission quality and robustness.

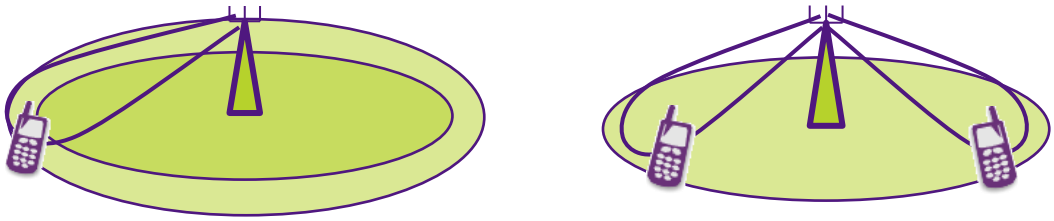

Figure 3-6: Schematic illustration of beamforming for one and two users [III-19].

Beamforming can be implemented in different ways. The beamforming is often seen as a lobe of power transmitted in a specific direction thanks to relative amplitude and phase shifts applied to each antenna. Amplitude and phase are electronically chosen to increase radiation in a particular direction while cancelling radiation in undesired directions. This solution generally doesn't consider the environment.

A second solution to implement beamforming in a multi antenna system consists of using precoding techniques. The time reversal or conjugate beamforming the simplest form of precoding

compared to Minimum Mean Square Error (MMSE) or zero-forcing beamforming (ZF). In this thesis, we will use time reversal beamforming to perform MISO measurements. This signal processing method was originally used in optic to focus waves.

3.1.5. Massive MIMO Systems

Massive MIMO refers to antennas array with tens or hundreds of antennas. The need to increase efficiency and capacity of wireless communication conducted the industry to widely study this technique for the future 5G network in [III-21] and [III-23] to [III-26]. As shown in figure 3-7, massive MIMO can be considered as a form of beamforming or an enhanced MU-MIMO connecting together tens of devices. It aims to create base stations that simultaneously communicate with a large number of users over the same frequency resource.

The design of massive MIMO systems is really challenging in many aspects. In terms of hardware implementation, the problematic is to pack as much RF chains as antennas in a small space. The temperature from the power dissipation is also a concern. A second issue is the mutual coupling among antennas of the array because antennas could be compactly arranged in such systems. Finally, the cost of such systems must be considered regarding the increased hardware and computation needed for those very large arrays.

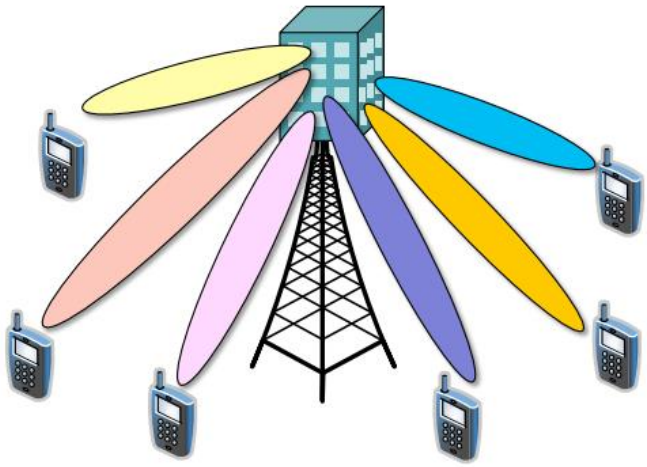

Figure 3-7: Illustration of the Massive MIMO concept [III-21].

Different structures have been proposed for massive MIMO system. The figure 3-8 (a) presents a 2D T-shaped antenna array [III-23] with 160 dual polarized λ/2 patch elements. Figure 3-8 (b) shows a 128-antenna base station consisting of four stacked double polarized 16 element circular patch arrays [III-22].

(a) (b)

Figure 3-8: Examples of (a) T-shaped [III-23] and (b) circular [III-22] Massive MIMO antenna structures.

3.2. Design of 8-Antenna Prototypes

The original idea was to improve the RF systems integrated into the Orange Livebox after receiving several negative customers' feedbacks regarding the coverage and the throughput of their equipment. By looking into the last version of the Livebox, we were able to notice a few flaws in the current system and extracting some research and development axis around MIMO antennas system for this type of device and application. Along the month we extended our work to routers, extenders, and small cell applications. Livebox 2 being our starting point we challenged ourselves by thinking about of new Livebox concept, smaller and integrating the maximum number of antenna defined in the WLAN standard.

The first problem raised by those constraints was to optimize the volume of the system. To reduce the volume of the RF system, we choose to test the LDS technology which allows printing antennas directly on the plastic box containing the system. The first step was to design a box adapted to the Laser Direct Structuring (LDS) technology. We wanted to realize a compact box but with dimensions realistic and sufficient to integrate 8 antennas. We arbitrarily opted for maximum dimensions of 135x135x35 mm^3. These dimensions are significantly smaller than the Livebox Orange currently on the market (240x170x40 mm^3) as we can see in the picture 3-9.

The main objective of this study is to design a system for dual-band WIFI. The target bands are 2.4-2.48 GHz (3.3% relative bandwidth) for the low band and 5.15-5.725 GHz (10% relative bandwidth) for the high band. Our antenna structure must have a correct level of performance (total efficiency higher

than 50%), very compact size and a low cost. We focus our design on a planar FR4 antenna to fulfill all these criteria. We studied two low-cost radiating elements printed on the PCB and their implementation on a gateway PCB. In the same way, we studied a 3D dual-band PIFA antenna. The position and interaction between 8 elements are studied and characterized. Each antenna needs to operate in two frequency bands at 2.4GHz and 5GHz to comply with the IEEE802.11n and IEEE802.11ac standard. When multiple antennas are placed together on a printed circuit board (PCB), the coupling effects and the antenna correlation have an important impact on the system performance.

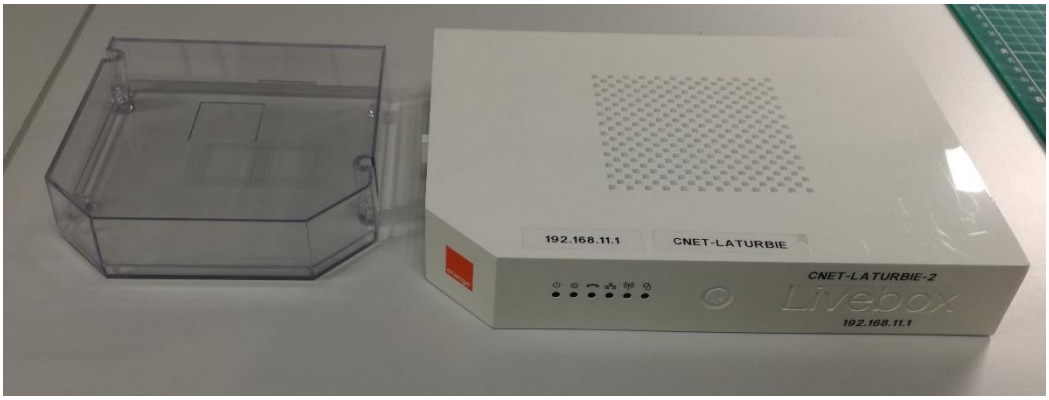

Figure 3-9: Box prototype (left) and actual Livebox from Orange (right).

3.2.1. Box Design for LDS Technology

We decided to set the size of the box to 135x135 mm² to impose volume constraints to our design. We realized two chamfers at 45° on each front corner of the box for aesthetic purpose and to provide an additional orientation to support the antennas. The box is constituted of two part (top and bottom) fixed together via plastic screws. The top has been designed to host up to eight printed antennas while the bottom has been designed to support a classic PCB. Following the first exchanges by mail and telephone with an S2P engineer, we were able to understand some constraints related to the Laser Direct Structuring (LDS) method. The main problem was whether connectors (WFL or UFL) could be welded on the plastics used. Some materials offered us this possibility in return for a rougher surface and a less aesthetic general rendering.

The first version of the prototype is presented in figure 3-10. We designed this first box with three sides tilted. By using tilted sides, we intended to create more surfaces to print antennas with LDS technology, and it was supposed to facilitate laser activation. The back side of the box has been kept straight to fit with the current design of the Livebox where this face is dedicated to the different connectors (Alimentation, Ethernet, USB, ADSL, On/Off switch...).

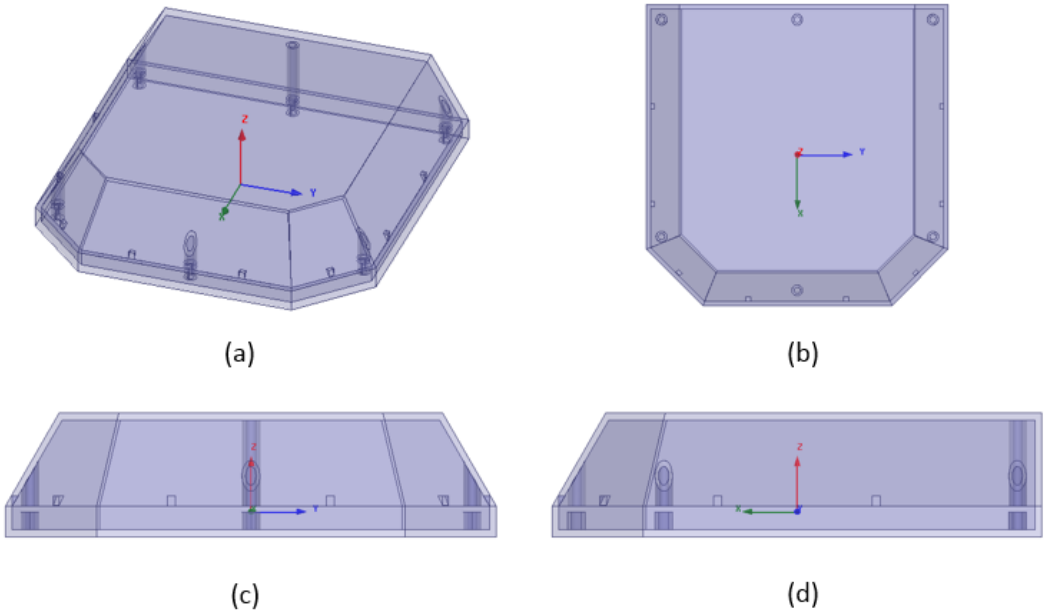

Figure 3-10: First version of the box prototype: (a) trimetric view, (b) top view, (c) front view and (d) side view.

After the first discussion with S2P in charge of the realization of the prototype, we designed the second version of the box according to the various constraints of the technology. The main modification was to straighten the sides of the box as presented in figure 3-11,

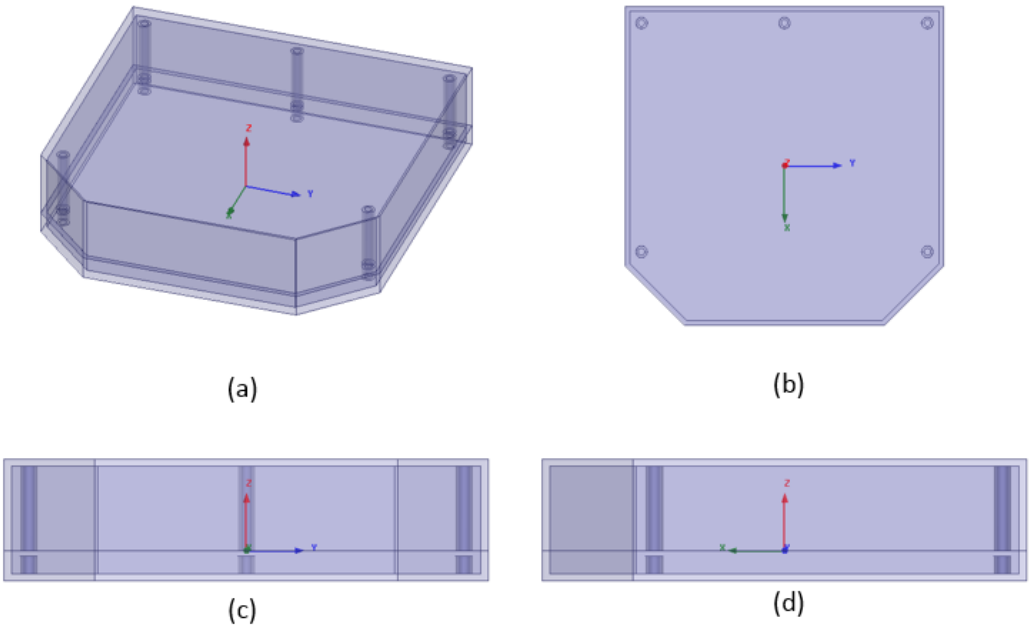

Figure 3-11: Second version of the box prototype: (a) trimetric view, (b) top view, (c) front view and (d) side view.

Finally, with the help and expertise of S2P engineers, we compromise on a definitive design for the box presented in figure 3-12. The sides are slightly tilted to ease the laser activation of surfaces. Final touches were added for the sake of esthetics. Figure 3-13 shows pictures of the simple, transparent prototype and the black prototype covered with the conductive paint.

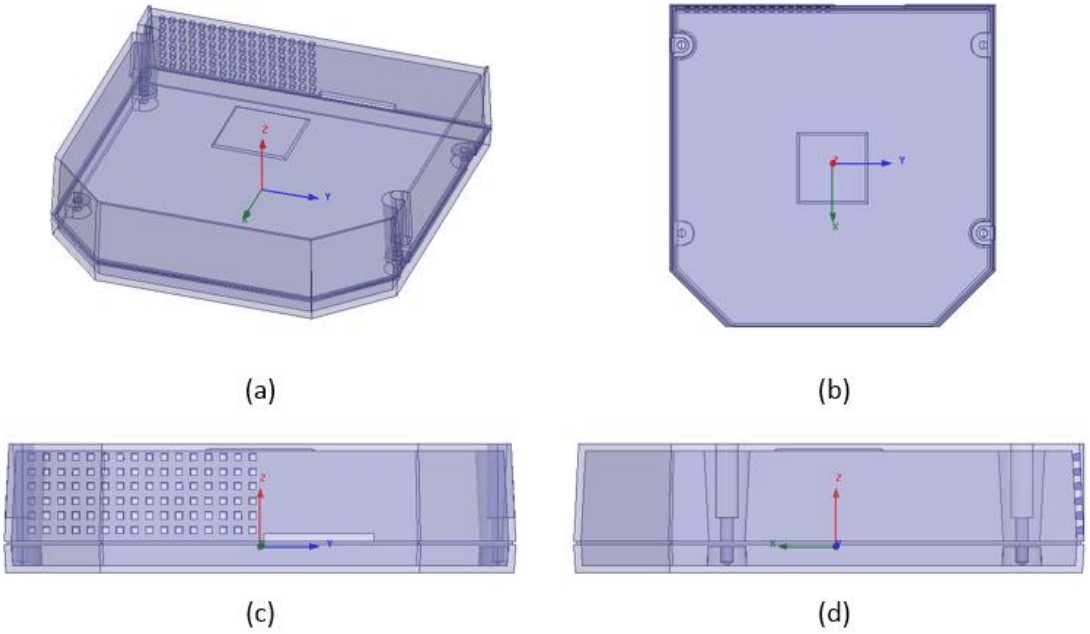

Figure 3-12: Final version of the box prototype: (a) trimetric view, (b) top view, (c) front view and (d) side view.

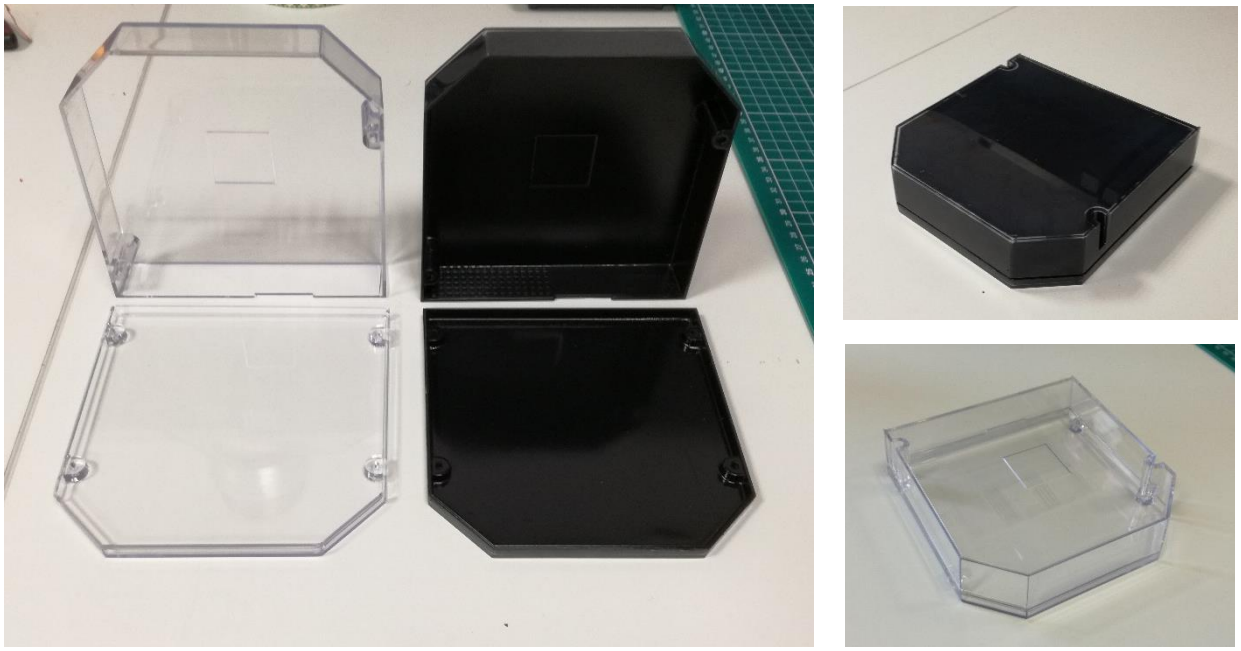

Figure 3-13: Pictures of the prototype with and without the black conductive paint.

3.2.2. Hook Shaped Antenna printed on a PCB substrate

The first 8-antenna prototype has been realized with a hook shaped antenna. The layout of the studied antenna is presented in Fig. 3-14. This antenna is a monopole printed on an FR4 substrate of thickness h = 1.6 mm, relative dielectric permittivity ε_r = 4.4 and dielectric loss tangent tanδ = 0.02. The structure is fed by a coplanar waveguide grounded (CPWG) 50 Ω line. The fed line is 1.4 mm wide and 11.5 mm long, the gap is 0.3mm width and grounded via holes are placed all along the line. The dual-band effect is obtained thanks to the two branch of this antenna. The upper branch is 2 mm wide and controls the resonance at 2.4 GHz, whereas the lower one is 1 mm wide and determines the higher frequency band at 5GHz. Each branch is folded in order to reduce the global size of the antenna. In the end, it is a compact device of 12.1x8.5mm^2 ($\lambda_0/10*\lambda_0/14$ at 2.4GHz). The matching can be improved by tuning the width of each monopole. Both resonances can be adjusted independently, by changing the length of the monopoles L_1 = 5.2 mm for the low-band and L_2 = 4.9 mm for the high-band.

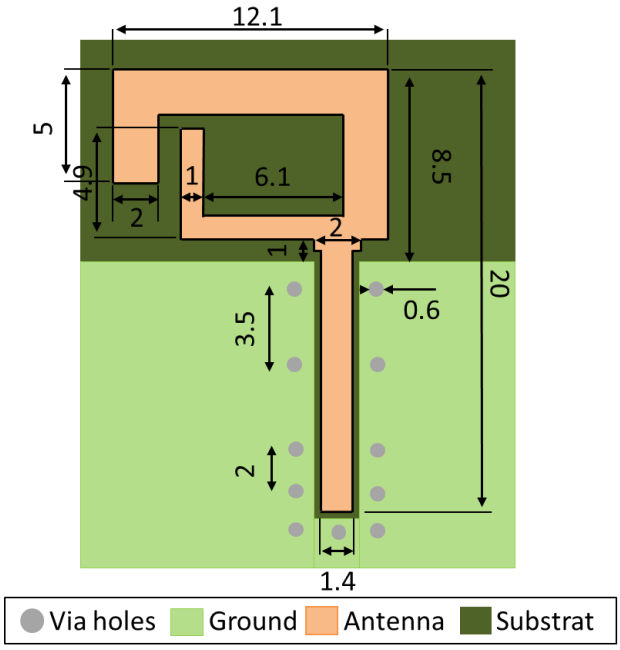

Figure 3-14: Layout of the hook shaped antenna (Dimensions in mm).

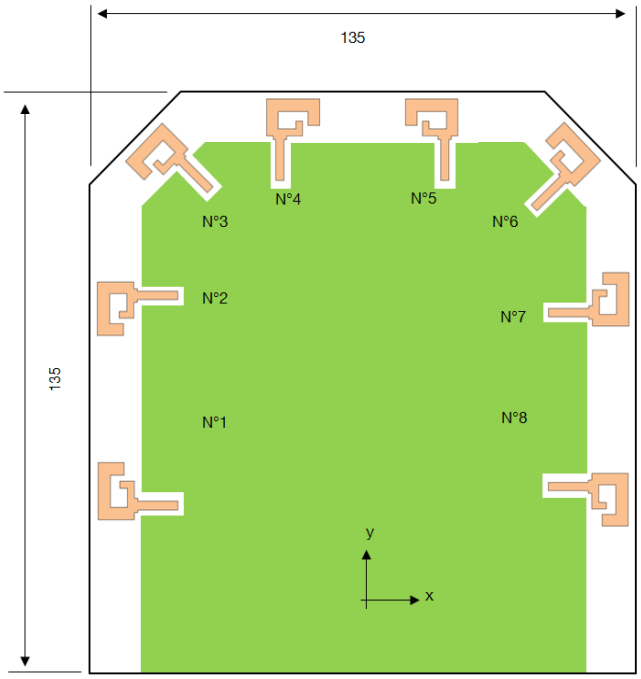

Figure 3-15: Layout of the 8 antenna gateway (Dimensions in mm).

As presented in figure 3-16, the simulation of the antenna matched the two WLAN band with a -6 dB criteria. The simulated radiation patterns of the hook antenna presented in figure 3-17 show a realized gain of 1 dB at 2.4 GHz and 2.3 dB at 5.15 GHz. The total simulated efficiency is 67% in the low band and 89% in the high band. This structure fulfills our specification regarding performance and size.

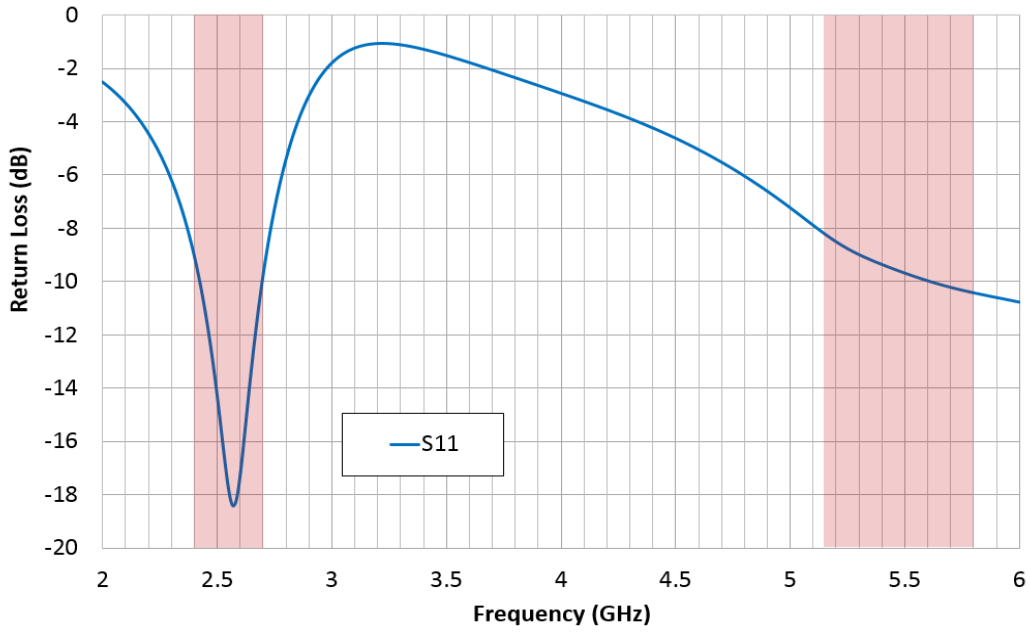

Figure 3-16: Simulated reflection coefficient for the hook antenna alone.

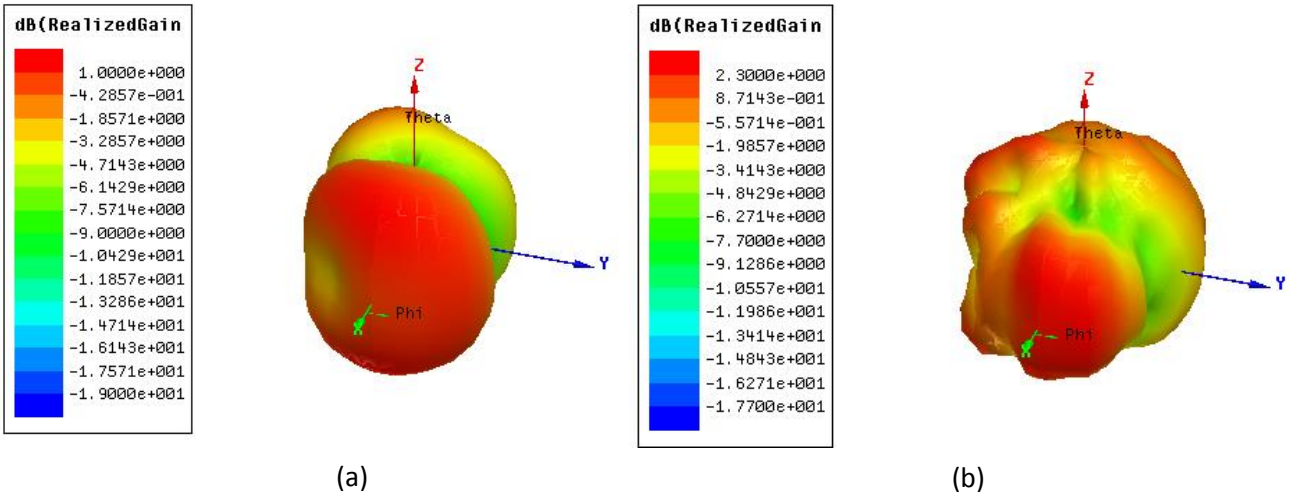

(a) (b)

Figure 3-17: Hook antenna simulated 3D radiation pattern at (a) 2.4 GHz and (b) 5.15 GHz.

The single structure presented has been duplicated to design a system with 8 antennas. The form factors of the WIFI gateway imply that the overall size of the PCB is 135x135 mm². As shown in figure 3-15, different antennas orientations are chosen to optimize S-parameters and particularly the isolation between each element. The PCB is not symmetrical toward y-axis in order to find the best configuration considering matching and isolation of each antenna. Simulation presented in Figure 3-18 shows that each antenna is matched on the target bands with a -6 dB criteria.

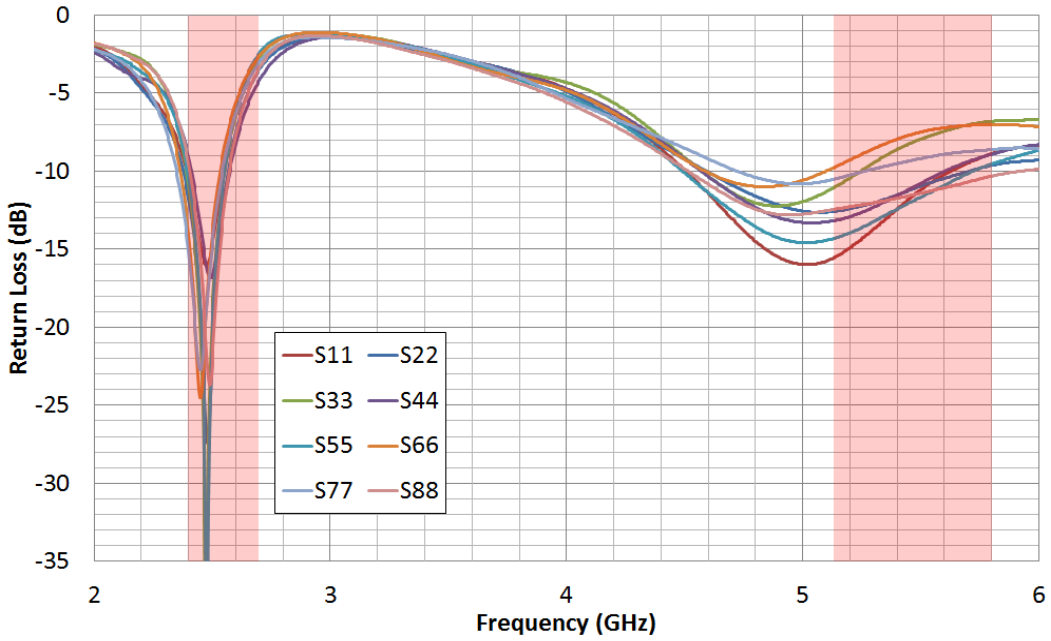

Figure 3-18: Simulated reflection coefficient of the 8 hook shaped antennas.

The prototype presented in figure 3-19 has been realized on an FR4 epoxy substrate. This prototype will be referred as “PCB 1”. Each antenna is fed using U-FL connector. A 20cm cable is clipped at each connector. A VNA is used to measure the S-Parameters at the output of the cables. Antennas 1 to 4 is measured first as we used 4 ports VNA, while the other 4 are connected with a 50 Ω load. Then antennas 5 to 8 are measured using the same procedure.

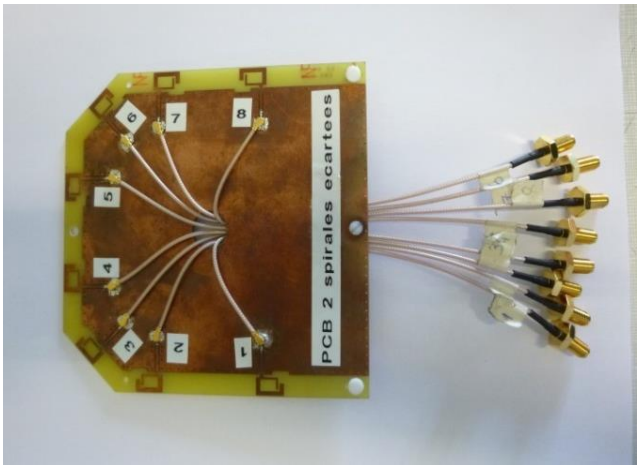

Figure 3-19: Picture of the realized 8 hook antenna prototype.

From Figure 3-20, we observed that the measurement shows better results than the simulated one in figure 3-18. In the lower frequency band, the reflection coefficients of each antenna match the simulation. Moreover, in the higher frequency band, the reflection coefficient are shifted to higher frequency and all 8 antennas have a much better matching than the ones simulated. These results

could be explained by the additional loss resulting from the U-FL cables and the FR4 substrate's electromagnetic characteristics. Indeed the dielectric permittivity can vary with frequency, thus the permittivity around 5 GHz must be lower than the permittivity used in simulation. Oscillations observed in the higher band are due to the cables. Those cables were not includes in the simulation.

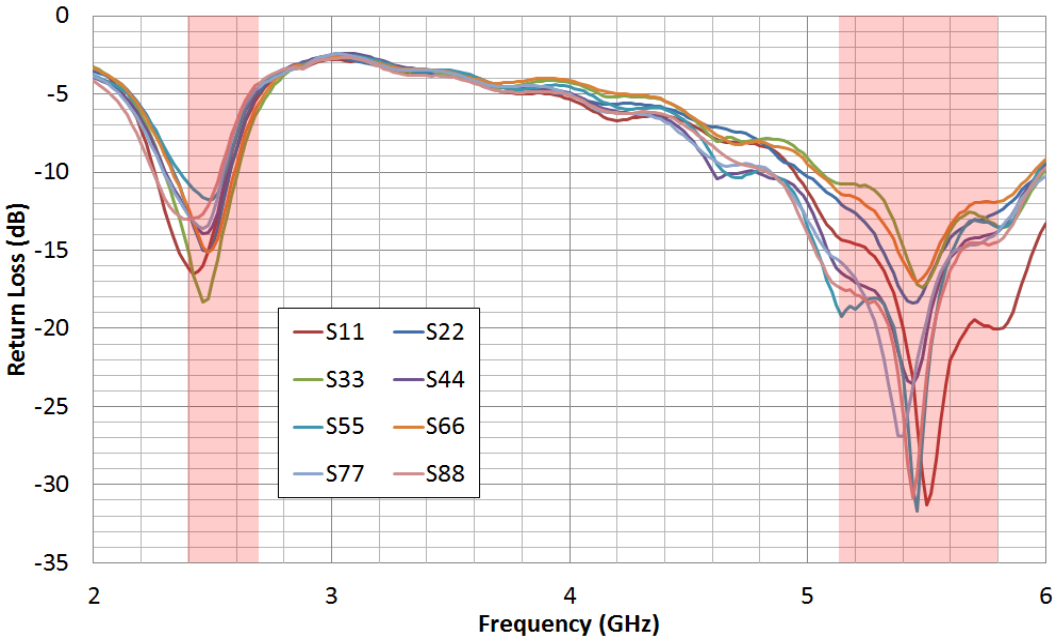

Figure 3-20: Measured reflection coefficient of the 8 hook shaped antennas.

Coupling and ECC between all antennas are shown in table 3-1. The transmission coefficient is always higher than 12 dB in the 5 GHz band while there is a minimum of isolation of 8.4 dB between antennas 1 and 2 in the low band. This table highlights the influence of the different antenna orientations presented in the figure 3-15. Antennas n°1 and n°2 are separated by the same distance than antenna n°7 and n°8 but the isolation between them is 2 dB higher in the 2.4 GHz band. The measured worst coupling are a bit high due to the lack of space available in the terminal.

The ECC, calculated with the equation [3-2], are always below 0.5 in both bands with a maximum of 0.343 between antennas 7 and 8 in the low band and a maximum of 0.312 between antennas 6 and 7 in the high band. The measured values of coupling and correlation are suitable for our application. Despite the high worst measured coupling, the calculated ECC is always under the 0.5 threshold

Table 3-1: Measured worst coupling and worst ECC for the 8 hook shaped antennas.

Antenna	Low band (2.4GHz)		High band (5GHz)	
	Worst Coupling	Worst ECC	Worst Coupling	Worst ECC
N°1	-8.6 dB (N°2)	0.091 (N°2)	-15.2 dB (N°2)	0.158 (N°2)
N°2	-8.6 dB (N°1)	0.275 (N°3)	-12.5 dB (N°3)	0.279 (N°3)
N°3	-11.3 dB (N°4)	0.275 (N°2)	-12.5 dB (N°2)	0.309 (N°4)
N°4	-10.8 dB (N°5)	0.330 (N°5)	-15.4 dB (N°3)	0.309 (N°3)
N°5	-10.8 dB (N°4)	0.330 (N°4)	-12.2 dB (N°6)	0.175 (N°6)
N°6	-10 dB (N°7)	0.269 (N°7)	-12.2 dB (N°5)	0.312 (N°7)
N°7	-10 dB (N°6)	0.343 (N°8)	- 13.9 dB (N°6)	0.312 (N°6)
N°8	-11.8 dB (N°7)	0.343 (N°7)	-15.9 dB (N°7)	0.211 (N°7)

In order to verify the radiation performance of our system, we measure it using a Satimo Starlab station. The efficiency values and the radiation diagram of the 8 antennas are collected. The table 3-2 below shows the total efficiency and gain for each antenna in both bands. Average efficiency of 45 % (-3.44 dB) and 55 % (-2.63 dB) are obtained in the low and high band.

Table 3-2: Gain and efficiency for the 8 hook shaped antennas in the lower and upper band.

Antenna	2,4 GHz		5,15 GHz	
	Gain (dB)	Efficiency (%)	Gain (dB)	Efficiency (%)
N°1	2.45	51.8	2.97	57.1
N°2	0.88	41.6	2.22	51.1
N°3	1.01	44.9	1.51	48.0
N°4	0.67	41.7	2.01	61.2
N°5	1.30	42.0	2.68	61.0
N°6	0.91	47.3	0.75	43.6
N°7	1.78	45.5	1.48	50.7
N°8	1.74	47.3	6.19	64.4
Average	1.38	45.3	2.80	54.6

Radiation patterns give interesting information on the radiation diversity of our system. Intuitively, we are looking for our 8 antennas to radiate as much as possible in different directions with different polarizations. Ideally, combining their different contributions, we would like to avoid any deep null in every direction. The radiation patterns measured are omnidirectional but with random variations in

every direction and thus are not presented because they offer very limited information regarding the gateway performance.

3.2.3. Printed IFA with PCB technology

The second prototype was realized with eight dual-bands planar IFA. The layout of the antenna is presented in the figure 3-21. Antennas are printed on the same FR4 substrate (h = 1.6 mm, ε_r = 4.4, tanδ = 0.02) than the previous prototype. This planar IFA is fed by a CPWG 50 Ω line. The fed line is 1.4 mm wide and 11.5 mm long, the gap is 0.3mm width and grounded via holes are placed all along the line. The antenna has a compact size of 16x9 mm² ($\lambda_0/8*\lambda_0/14$ at 2.4GHz). The upper branch controlling the lower frequency at 2.4 GHz is folded to keep a compact size. The second resonance at 5 GHz is obtained thanks to the matching line and its coupling with the main radiator. The matching can be improved by tuning the width (2 mm in this design) of the line. The lower resonance can easily be tune by changing the length of the higher branch. The second resonance can be adjusted by changing the distance between the matching line and the upper branch or the feeding line.

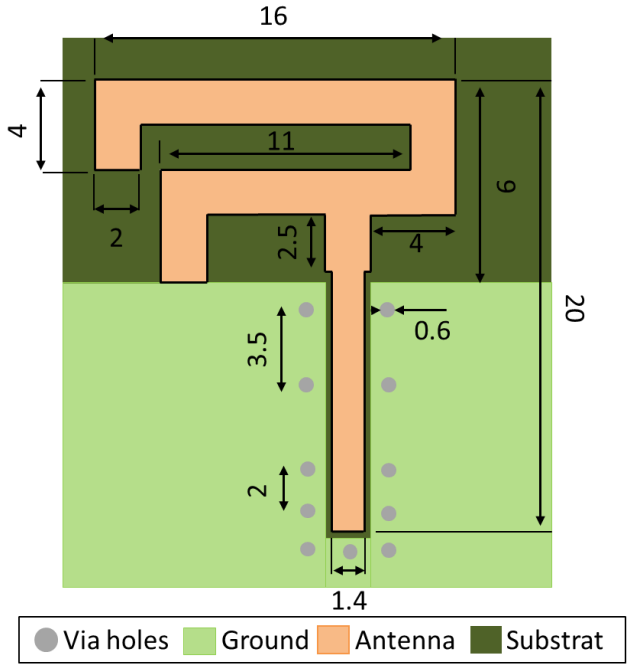

Figure 3-21: Layout of the Printed Inverted F Antenna.

As presented in figure 3-22, the simulation of the antenna matched the low band with a -6 dB criteria and the high band with a -6 dB criteria. The simulated radiation patterns of the IFA are presented in figure 3-23 show a realized gain of 2.3 dB at 2.4 GHz and 3.7 dB at 5.15 GHz. The total simulated efficiency is around 90 % in both bands. This structure fulfills our specification regarding performance and size.

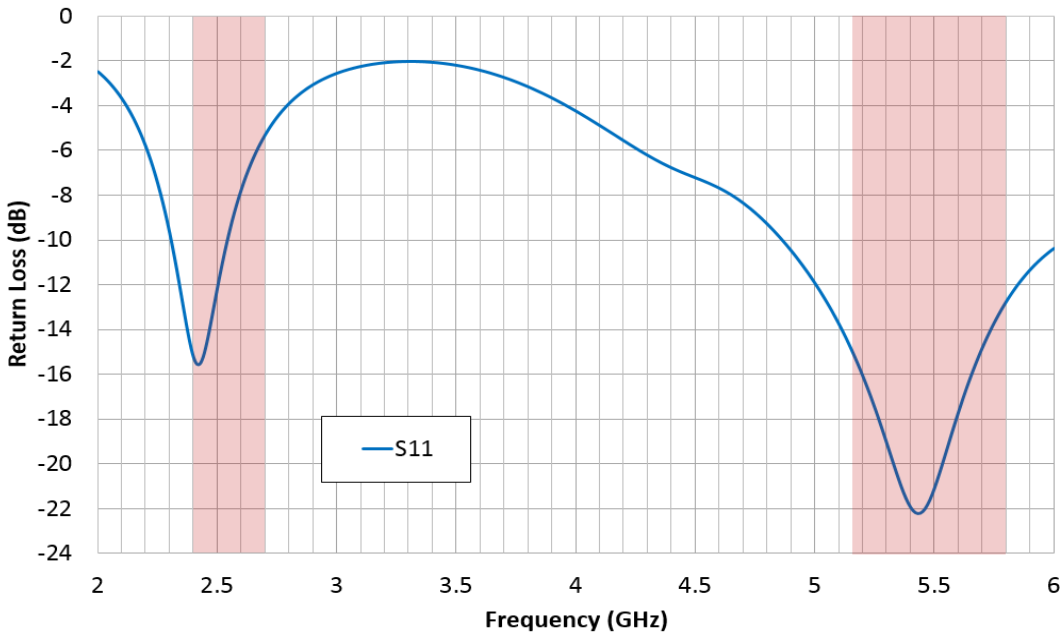

Figure 3-22: Simulated reflection coefficient for the IFA alone.

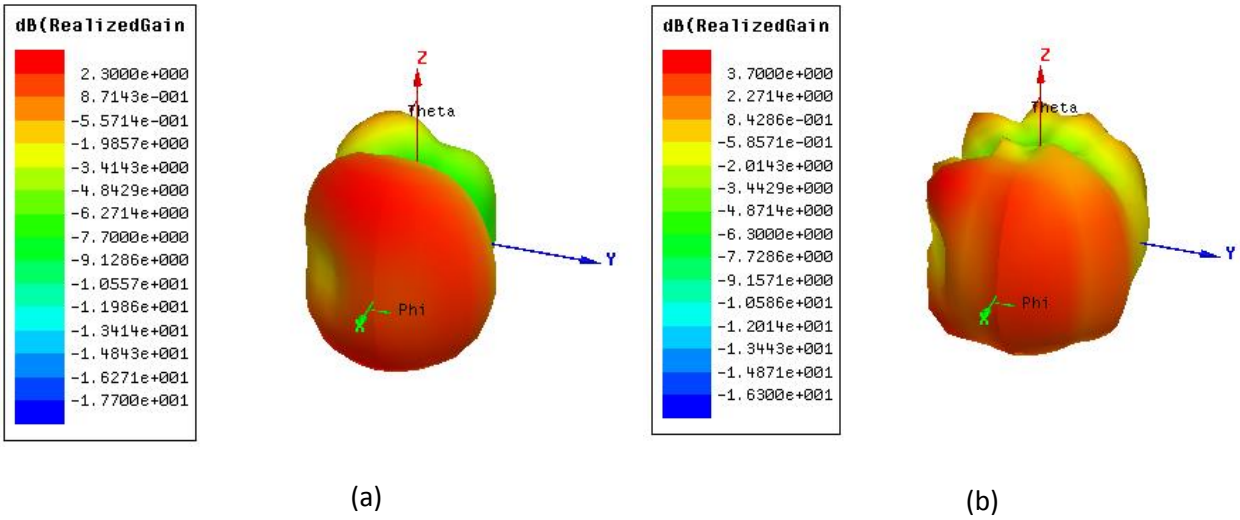

(a) (b)

Figure 3-23: IFA simulated 3D radiation pattern at (a) 2.4 GHz and (b) 5.15 GHz.

The single structure presented above, has been duplicated to design a system with 8 antennas with the same form factors and dimension (135x135 mm²) than the last PCB. This prototype will be referred as “PCB 2”. As shown in figure 3-24, the prototype has been realized on an FR4 epoxy substrate with each antenna fed using U-FL connector toward a 20 cm cable clipped at each connector. Once again, different antennas orientations are chosen to optimize S-parameters, and the same antenna implementation has been used to have an accurate comparison between prototypes.

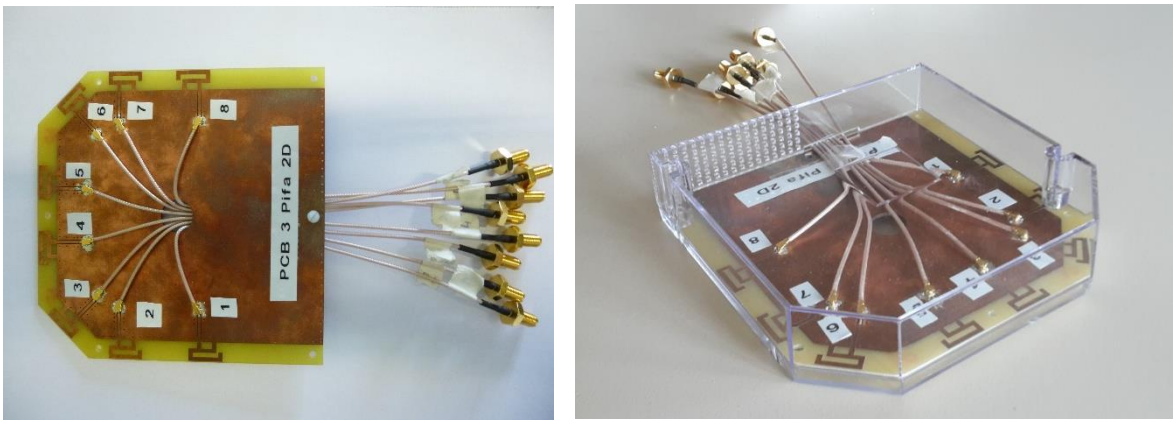

Figure 3-24: Pictures of the realized 8 planar IFA prototype.

Simulation presented in Figure 3-25 shows that each antenna is matched on the target bands with a -6 dB criteria in the low band and a -6 dB criteria in the higher band. Measurement presented in figure 3-26 match the simulation with a good agreement.

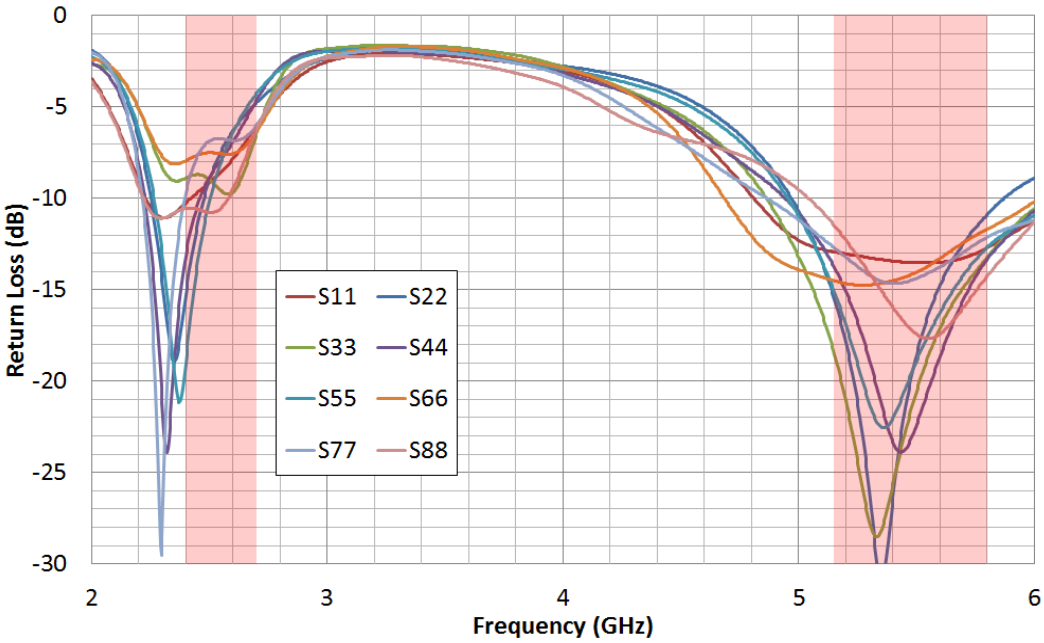

Figure 3-25: Simulated reflection coefficient for the 8 planar IFA.

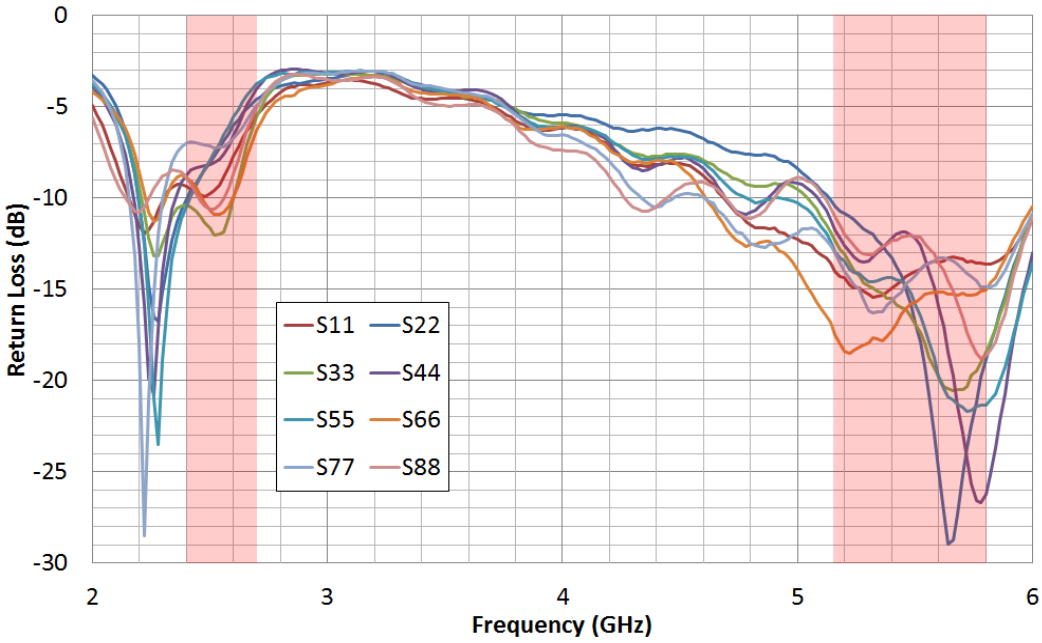

Figure 3-26: Measured reflection coefficient for the 8 planar IFA.

Coupling between antennas presented in table 3-3 shown that isolation is always higher than 10 dB in the 5 GHz band, with a minimum of isolation of 8.8 dB between antennas 5 and 6 in the low band. The measured worst coupling are a bit high due to the lack of space available in the terminal. The worst ECC presented in the same table is always lower than 0.5 with a maximum of 0.402 between antennas 3 and 4 in the low band and a maximum of 0.253 between antennas 1 and 2 in the 5 GHz band. The measured values of coupling and correlation are suitable for our application. Despite the high worst measured coupling, the calculated ECC is always under the 0.5 threshold

Table 3-3: Measured worst coupling and worst ECC for the 8 planar IFA.

Antenna	Low band (2.4GHz)		High band (5GHz)	
	Worst Coupling	Worst ECC	Worst Coupling	Worst ECC
N°1	-12.4 dB (N°2)	0.115 (N°2)	-12.4 dB (N°2)	0.253 (N°2)
N°2	-12.1 dB (N°3)	0.171 (N°3)	-24.4 dB (N°3)	0.253 (N°1)
N°3	-9.6 dB (N°4)	0.402 (N°4)	-19.5 dB (N°4)	0.089 (N°1)
N°4	-9.6 dB (N°3)	0.402 (N°3)	-19.5 dB (N°3)	0.049 (N°3)
N°5	-8.8 dB (N°6)	0.330 (N°6)	-10.9 dB (N°6)	0.107 (N°6)
N°6	-12.2 dB (N°7)	0.330 (N°5)	-18.4 dB (N°7)	0.107 (N°5)
N°7	-15.8 dB (N°8)	0.224 (N°6)	-33.7 dB (N°8)	0.037 (N°5)
N°8	-15.8 dB (N°7)	0.146 (N°7)	-33.7 dB (N°7)	0.024 (N°7)

Radiation measurements are performed for each antenna of this prototype. The table 3-4 below presents the total efficiency and gain for each antenna in both bands. Average efficiency of 51% (-2.88 dB) and 62% (-2.07 dB) are obtained in the low and high band.

Table 3-4: Gain and efficiency for the 8 planar IFA in the lower and upper band.

Antenna	2,4 GHz		5,15 GHz	
	Gain (dB)	Efficiency (%)	Gain (dB)	Efficiency (%)
N°1	1.78	54.0	3.40	74.1
N°2	2.50	58.3	0.88	52.7
N°3	2.01	61.7	1.81	55.2
N°4	2.60	60.0	2.98	61.5
N°5	0.61	41.4	2.30	54.0
N°6	1.24	44.7	3.39	65.8
N°7	1.41	38.2	3.46	69.5
N°8	2.21	53.6	3.83	63.8
Average	1.84	51.5	2.85	62.1

3.2.4. PIFA with PCB technology

The third prototype is realized with eight dual-bands 3D PIFA. The design of the antenna is presented in figure 3-27. The antenna consists of patch plane, a shorting plate connected to the ground plane and feeding plate connected to a CPWG line. The dimensions of the PIFA are 20×8 mm with the patch located 8 mm above PCB. The antenna is cut out of copper, fold at the good dimension and then welded on the ground plane. The L-shaped slot is introduced on the patch plane in order to get dual resonance. The patch and the shorting pin dimensions determine the lower frequency at 2.4 GHz. The second resonance at 5 GHz is controlled with the L-shaped slot. The matching can be improved by changing the position of the shorting pin and the height of the gap between the patch and the ground plane.

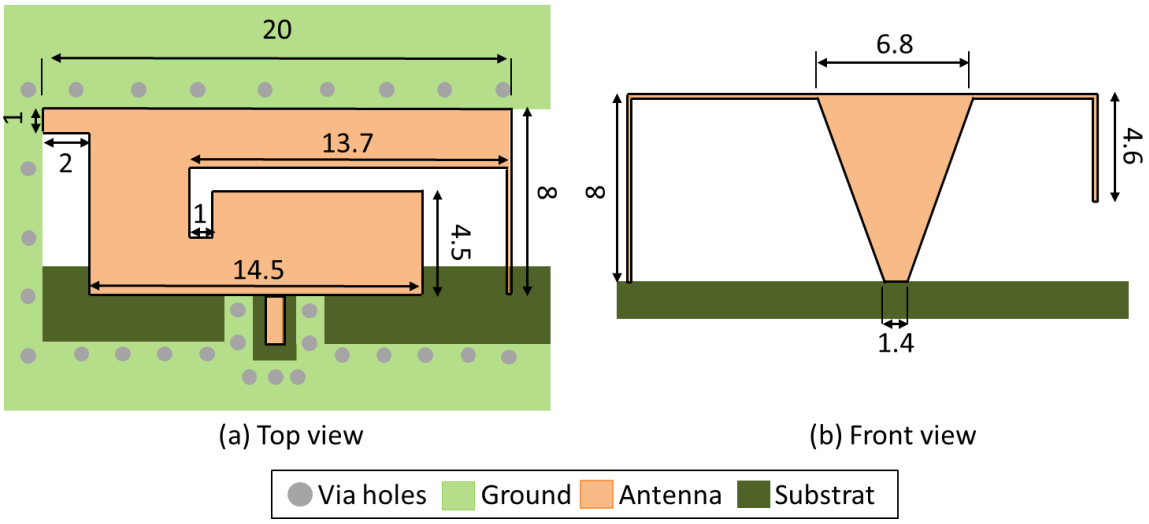

Figure 3-27: Layout of the PIFA in (a) top view and (b) front view.

As shown in figure 3-28, the simulation of the antenna matched the low band with a -6 dB criteria and the high band with a -6 dB criteria. The simulated radiation patterns of the PIFA are presented in figure 3-29 show a realized gain of 3.9 dB at 2.4 GHz and 5.5 dB at 5.15 GHz. The total simulated efficiency is around 95 % in both bands. This structure fulfills our specification regarding performance and size.

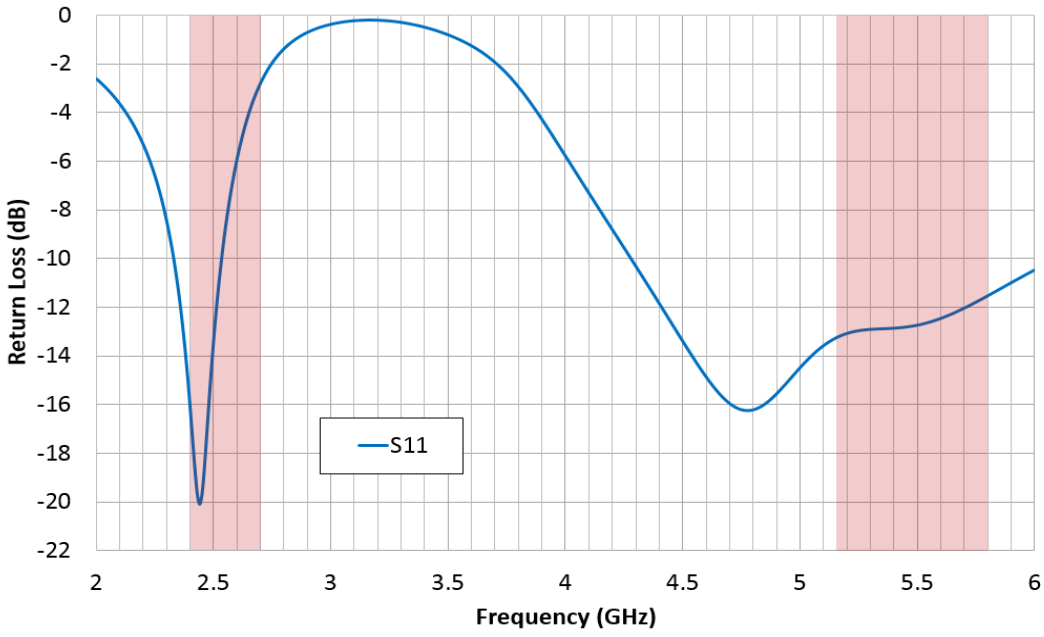

Figure 3-28: Simulated reflection coefficient for the PIFA alone.

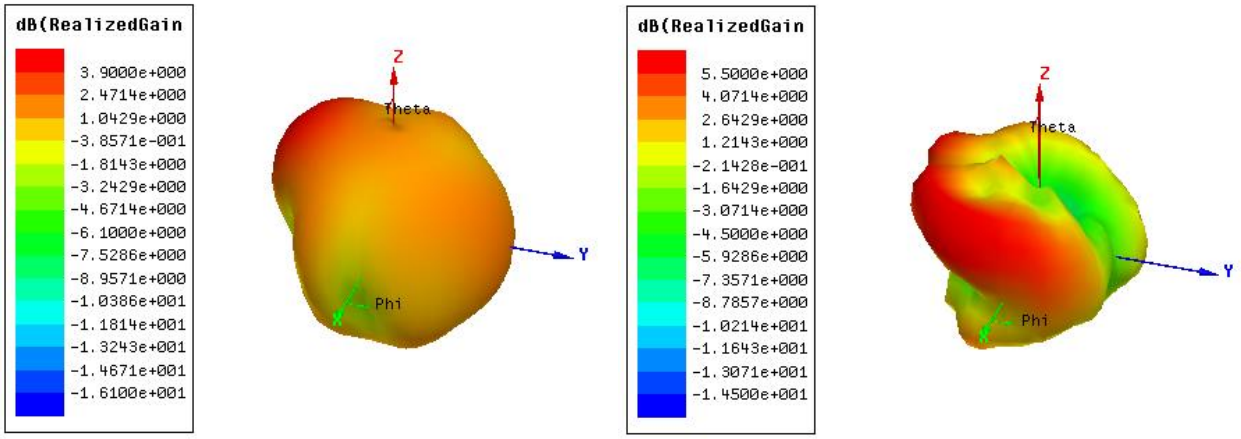

(a) (b)

Figure 3-29: PIFA simulated 3D radiation pattern at (a) 2.4 GHz and (b) 5.15 GHz.

The single structure has been duplicated to design a system with 8 antennas with the same form factors and dimension (135x135 mm²) than the two prototype presented above. This prototype will be referred as "PCB 3". As shown in figure 3-30, the prototype has been realized on an FR4 epoxy substrate with each antenna fed using U-FL connector toward a 20 cm cable clipped at each connector. Once again, different antennas orientations are chosen to optimize S-parameters, and the same antenna implementation has been used to have an accurate comparison between prototypes.

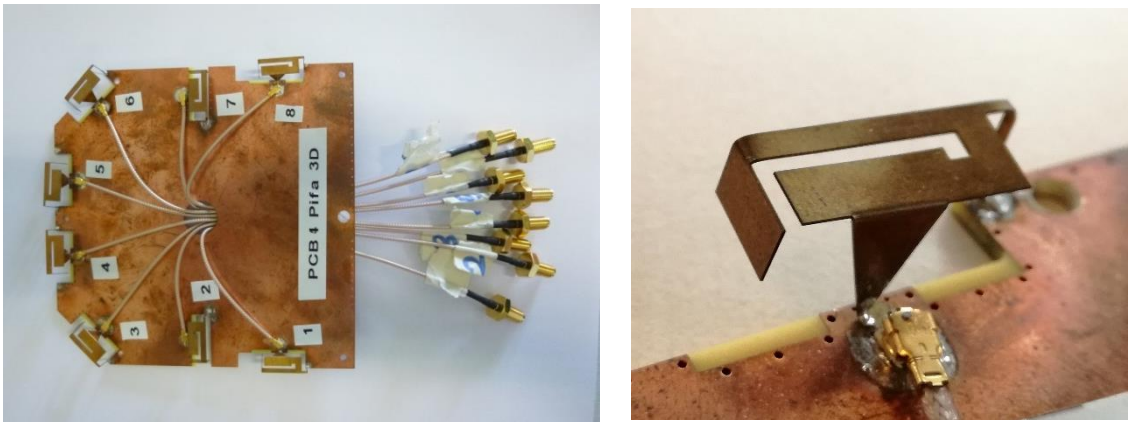

Figure 3-30: Picture of the 8 PIFA prototype.

Simulation presented in Figure 3-31 shows that each antenna is matched on the target bands with a -6 dB criteria in the low band and a -6 dB criteria in the higher band. We notice that the symmetrical characteristic of this prototype is seen is the reflection coefficient simulation. Indeed, S_{11} and S_{88} are identical as well as S_{22} with S_{77}, S_{33} with S_{66} and S_{44} with S_{55}. Measurement presented in figure 3-32 match the simulation with a good agreement.

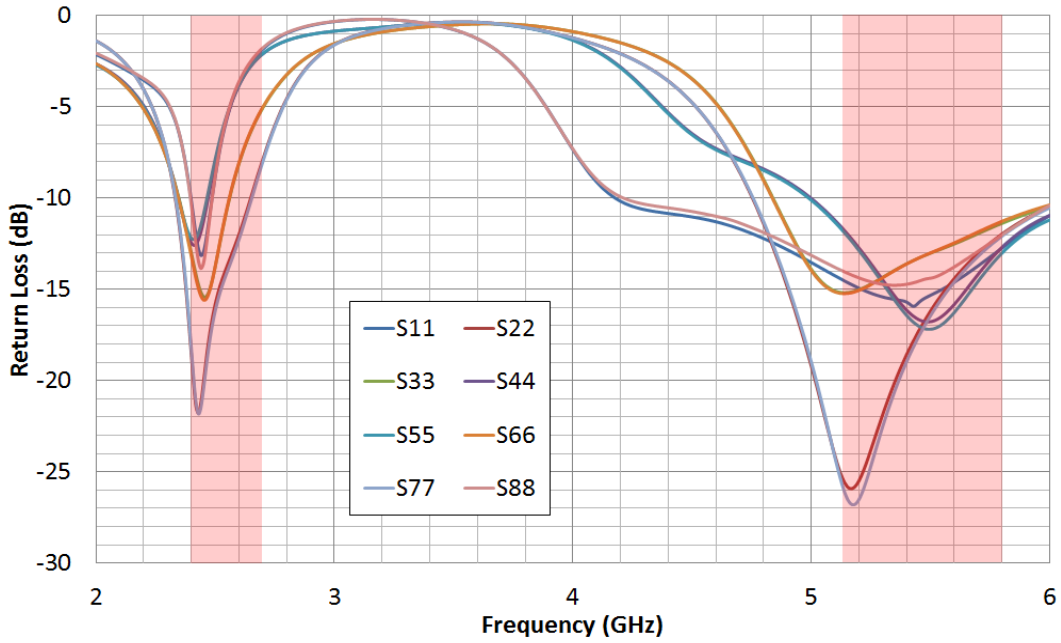

Figure 3-31: Simulated reflection coefficient for the 8 PIFA.

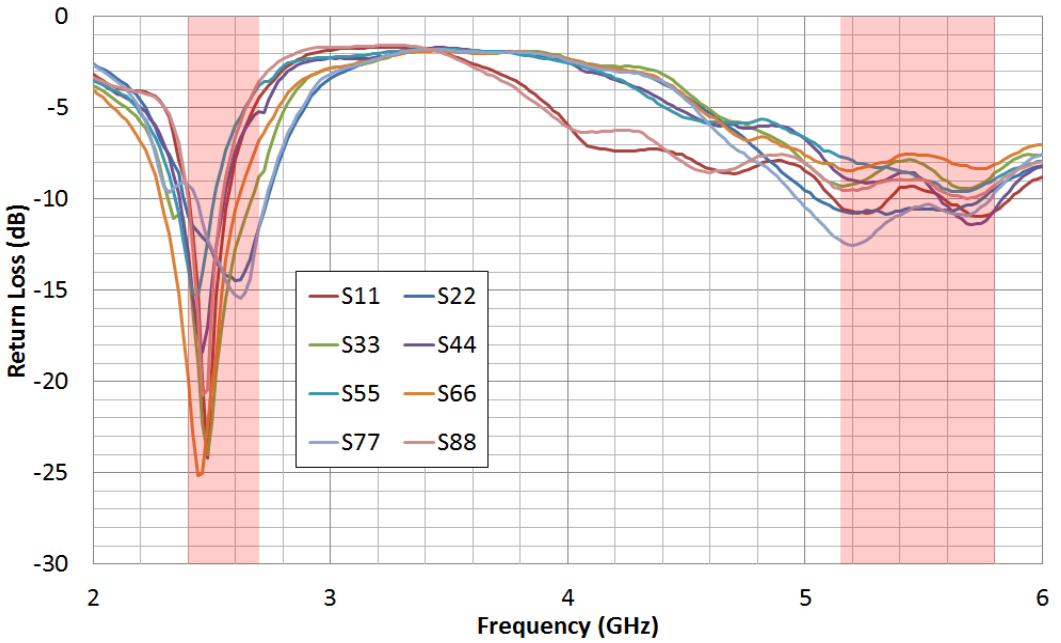

Figure 3-32: Measured reflection coefficient for the 8 PIFA.

Coupling between antennas presented in table 3-5 shown that isolation is always higher than 10 dB in the 5 GHz band, with a minimum of isolation of 7.5 dB between antennas 3 and 4 as well as antennas 5 and 6 in the low band. The measured worst coupling are a bit high due to the lack of space available in the terminal. The worst ECC presented in the same table is always lower than 0.5 with a maximum of 0.337 between antennas 5 and 6 in the low band and a maximum of 0.130 between antennas 4 and 5 in the 5 GHz band. The measured values of coupling and correlation are suitable for our application.

Table 3-5: Measured worst isolation and worst ECC for the 8 PIFA.

Antenna	Low band (2.4GHz)		High band (5GHz)	
	Worst Coupling	Worst ECC	Worst Coupling	Worst ECC
N°1	-14.7 dB (N°2)	0.145 (N°2)	-16.7 dB (N°2)	0.058 (N°2)
N°2	-11.0 dB (N°3)	0.145 (N°1)	-14.7 dB (N°3)	0.058 (N°1)
N°3	-7.5 dB (N°4)	0.310 (N°4)	-14.7 dB (N°2)	0.034 (N°4)
N°4	-7.5 dB (N°3)	0.310 (N°3)	-13.8 dB (N°5)	0.130 (N°5)
N°5	-7.5 dB (N°6)	0.337 (N°6)	-13.8 dB (N°4)	0.130 (N°4)
N°6	-7.5 dB (N°5)	0.337 (N°5)	-14.8 dB (N°7)	0.071 (N°7)
N°7	-11.0 dB (N°6)	0.154 (N°6)	-14.8 dB (N°6)	0.071 (N°6)
N°8	-14.6 dB (N°7)	0.061 (N°7)	-16.7 dB (N°7)	0.029 (N°6)

Radiation measurements are performed for each antenna of this prototype. The table 3-6 below presents the total efficiency and gain for each antenna in both bands. Average efficiency of 52 % (-2.86 dB) and 54 % (-2.70 dB) are obtained in the low and high band.

Table 3-6: Gain and efficiency for the 8 PIFA in the lower and upper band.

Antenna	2,4 GHz		5,15 GHz	
	Gain (dB)	Efficiency (%)	Gain (dB)	Efficiency (%)
N°1	3.01	67.8	4.08	61.7
N°2	2.30	55.0	2.85	56.1
N°3	1.52	48.2	3.27	54.1
N°4	1.77	49.4	4.89	54.3
N°5	2.40	49.8	4.48	52.4
N°6	1.45	49.3	3.28	51.5
N°7	1.71	56.6	3.14	60.8
N°8	2.46	38.0	3.12	38.5
Average	2.11	51.8	3.70	53.7

3.2.5. Mixed prototype with hook shaped antennas, PIFA and IFA on PCB technology

The next prototype presented in figure 3-33 is a combination of the first three realizations. The idea is to get a maximum of diversity in the antenna system by using different kind of antenna: 3 hook-shaped antennas, 3 PIFA and 2 IFA. This prototype represents the ideal system for mainstream routers, and it will be used as a reference for the performance assessment of LDS prototypes. This prototype has been designed to work with Wi-Fi bandwidth as well as in the 2.6 GHz LTE TDD bandwidth.

The figure 3-33 presents the realized prototype on an FR4 epoxy substrate with each antenna fed using U-FL connector toward a 30 cm cable clipped at each connector. This prototype will be referred as “PCB 4”. Once again, different antennas orientations are chosen to optimize S-parameters, and the same antenna implementation has been used to have an accurate comparison between prototypes.

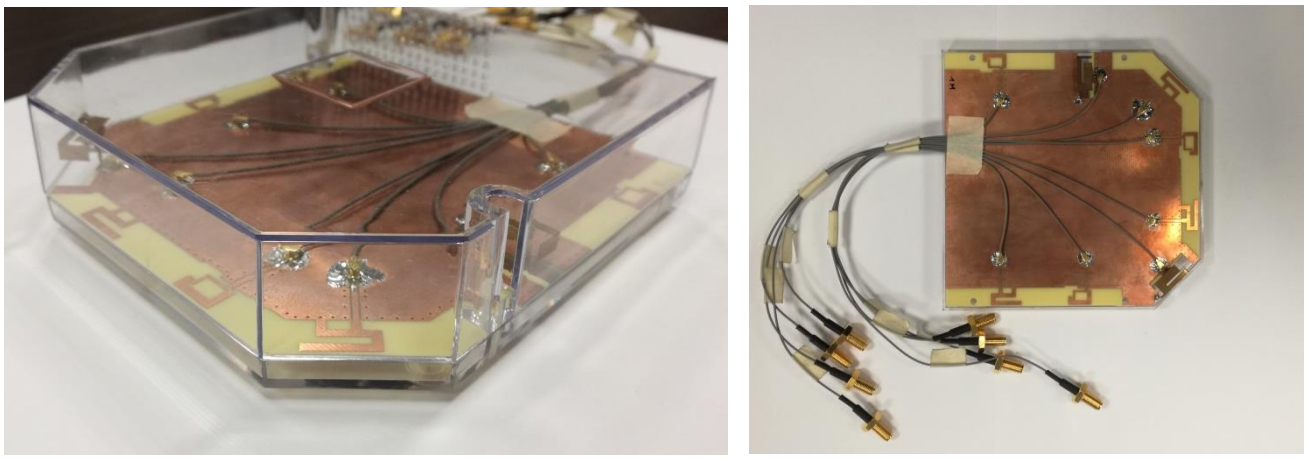

Figure 3-33: Pictures of the mixed prototype.

Simulation presented in Figure 3-34 shows that each antenna is matched on the target bands with a -6 dB criteria in the low band whereas antennas 1, 3, 4 and 5 shows a mismatch in the higher band. The antennas 2, 6, 7 and 8 match The 5 GHz band with a -6 dB criteria. We observe similarities in the reflection coefficient for antennas of the same type. Indeed, the three hook antennas (1, 4 and 7) present equivalent return loss as well as the three printed IFA (3, 5 and 8). Finally the two PIFA present similar reflection coefficient in the low band but a significant difference in the 5 GHz band. This difference can be explain by the position of the two antennas regarding the ground plane and the other antennas.

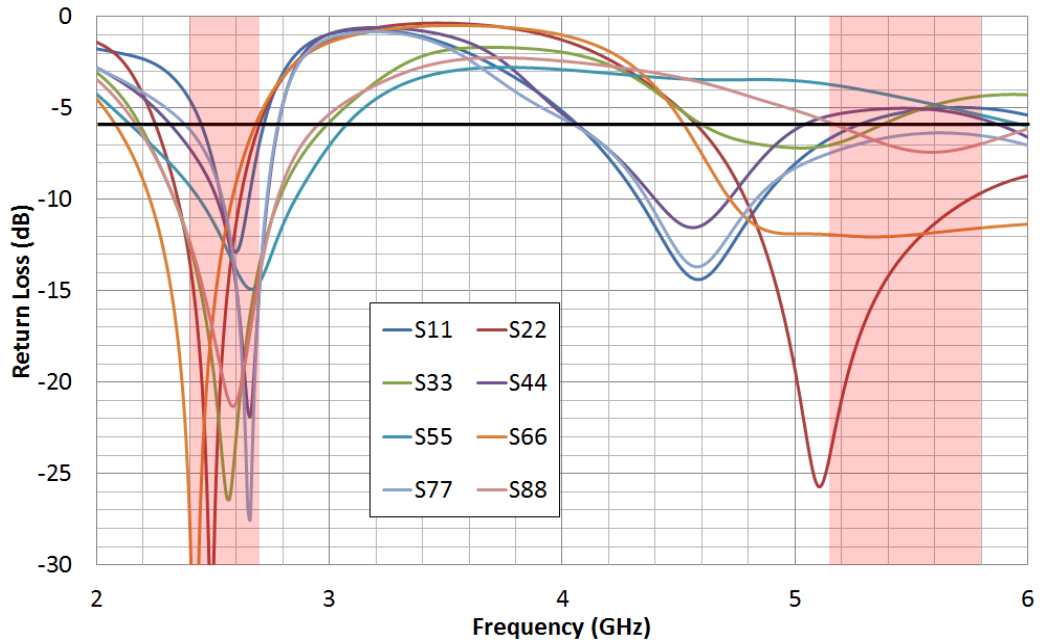

Figure 3-34: Simulated reflection coefficient for the 8 antennas of the mixed prototype.

The measured matching presented in figure 3-35 is better than the simulated one. The additional losses in the cables along with the variations of the substrate dielectric characteristics might explain the differences between simulation and measurement.

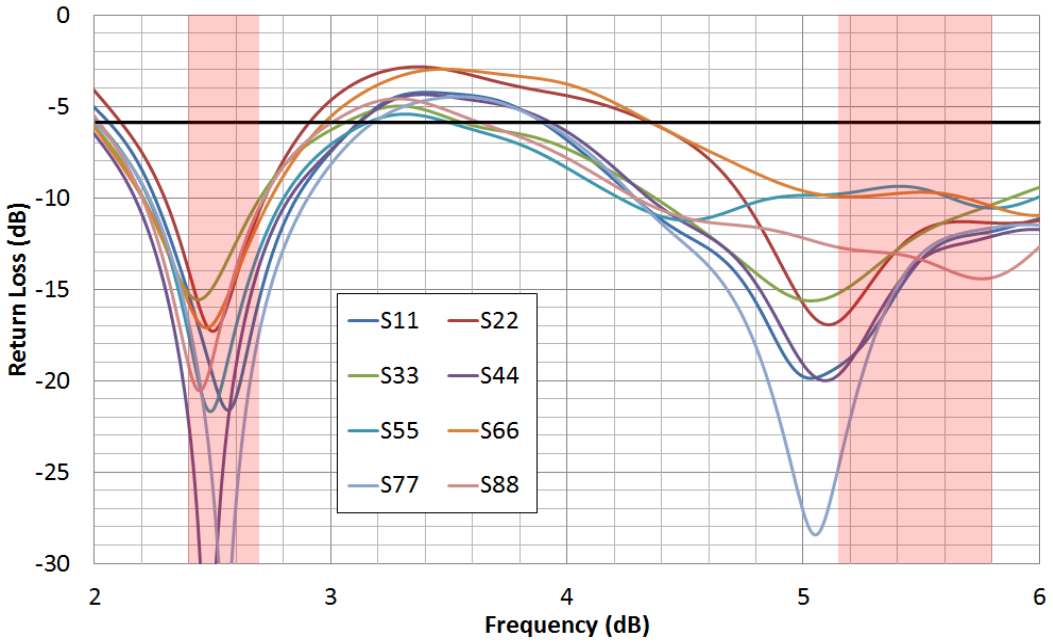

Figure 3-35: Measured reflection coefficient for the 8 antennas of the mixed prototype.

Coupling between antennas presented in table 3-7 shown that isolation is always higher than 18 dB in the 5 GHz band, with a minimum of isolation of 10 dB between antennas 5 and 6 in the low band. The measured worst coupling are a bit high due to the lack of space available in the terminal. The ECC is always below 0.5 in both bands with a maximum of 0.484 between antennas 5 and 6 in the low band

and a maximum of 0.300 between antennas 4 and 5 in the high band. The measured values of coupling and correlation are suitable for our application.

Table 3-7: Measured worst isolation and worst ECC for the 8 antennas of the mixed prototype.

Antenna	Low band (2.4GHz)		High band (5GHz)	
	Worst Coupling	Worst ECC	Worst Coupling	Worst ECC
N°1	-24.3 dB (N°2)	0.042 (N°2)	-25.0 dB (N°2)	0.081 (N°5)
N°2	-9.8 dB (N°3)	0.201 (N°3)	-21.8 dB (N°3)	0.064 (N°1)
N°3	-9.8 dB (N°2)	0.201 (N°4)	-18.9 dB (N°4)	0.176 (N°4)
N°4	-12.1 dB (N°5)	0.134 (N°5)	-18.9 dB (N°3)	0.300 (N°5)
N°5	-10.1 dB (N°6)	0.484 (N°6)	-20.8 dB (N°4)	0.300 (N°4)
N°6	-10.1 dB (N°5)	0.484 (N°5)	-19.7 dB (N°7)	0.163 (N°5)
N°7	-12.6 dB (N°8)	0.146 (N°8)	-19.7 dB (N°6)	0.130 (N°8)
N°8	-12.6 dB (N°7)	0.146 (N°7)	-27.8 dB (N°7)	0.130 (N°7)

Radiation measurements are performed for each antenna of this prototype. The table 3-8 below presents the total efficiency and gain for each antenna in both bands. Average efficiency of 50 % (-3.04 dB) and 50 % (-3.07 dB) are obtained in the low and high band.

Table 3-8: Gain and efficiency for the 8 antennas of the mixed prototype in the lower and upper band.

Antenna	2,4 GHz		5,15 GHz	
	Gain (dB)	Efficiency (%)	Gain (dB)	Efficiency (%)
N°1	2.85	56.8	3.64	44.9
N°2	1.81	44.7	4.01	62.5
N°3	1.41	42.3	2.21	51.3
N°4	2.46	51.5	3.33	45.0
N°5	2.49	51.5	1.78	43.1
N°6	1.32	54.2	3.73	50.6
N°7	3.36	49.3	4.20	48.3
N°8	3.33	47.1	2.82	48.8
Average	2.44	49.7	3.29	49.3

3.2.6. Hook-shaped printed on the sides of a plastic box with LDS technology (S1)

This prototype introduces the LDS technology presented in the introduction of this chapter. The box designed in the section 3.2.1 is now used as a support to print antennas. The first design we realized with LDS uses the hook-shaped antenna presented in figure 3-15. Dimensions of the antennas have been slightly adjusted to the permittivity of the polycarbonate substrate ($\varepsilon_r = 2.7$, $\tan\delta = 0.013$). The positions and orientations of antennas on the box match the first prototypes in order to have an accurate comparison between classic PCB technology and LDS technology. Antennas have been printed on the side of the gateway to favor vertical polarization which is known to be better for indoor communications.

Figure 3-36 shows the prototype of a plastronic gateway fabricated with LDS technology, with 8 hook-shaped dual-band antennas. This prototype will be referred as “Box Side.” The 2.4 GHz band includes a Wi-Fi and an LTE band (TDD). Antennas are connected with 17 cm coaxial cables. The main drawback of this design is the need to transfer a piece of the ground plane on the plastic box for each antenna. Indeed the cost of such technology has a strong dependence on the amount of surface metallized.

Figure 3-36: Pictures of the realized prototype with 8 hook-shaped antennas printed on the side of the box.

Simulation presented in Figure 3-37 shows that each antenna is matched on the target bands with a -6 dB criteria in the low band and a -6 dB criteria in the higher band. The matching is decrease

compare to the hook antenna printed on FR4 substrate because of the smaller ground plane printed on the polycarbonate box. Measurement presented in figure 3-38 match the simulation with a good agreement. Oscillations are due to the cables 17 cm coaxial cables connected to each antenna.

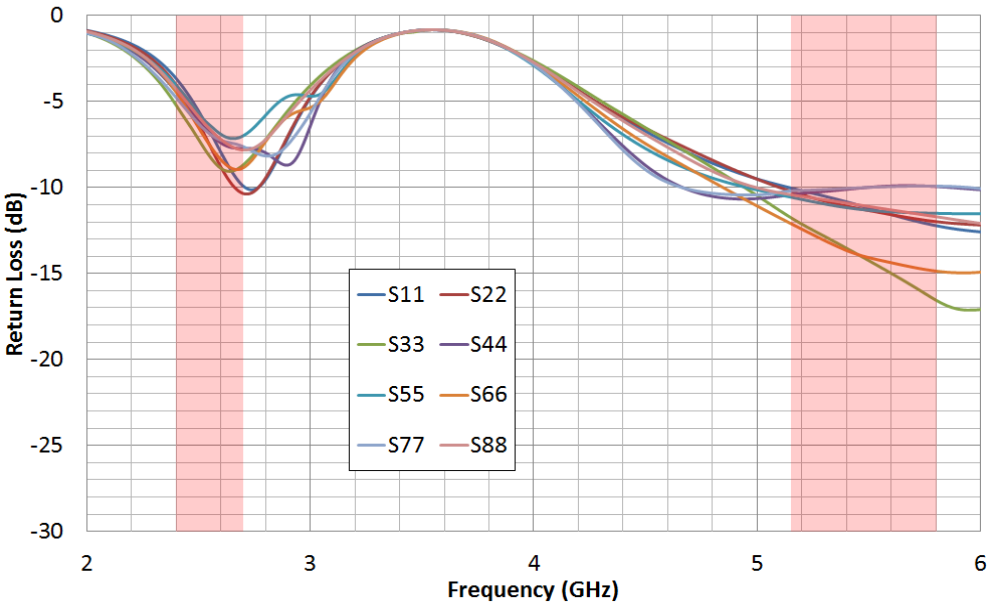

Figure 3-37: Simulated reflection coefficient for the 8 hook shaped antennas printed on the side of the plastic box.

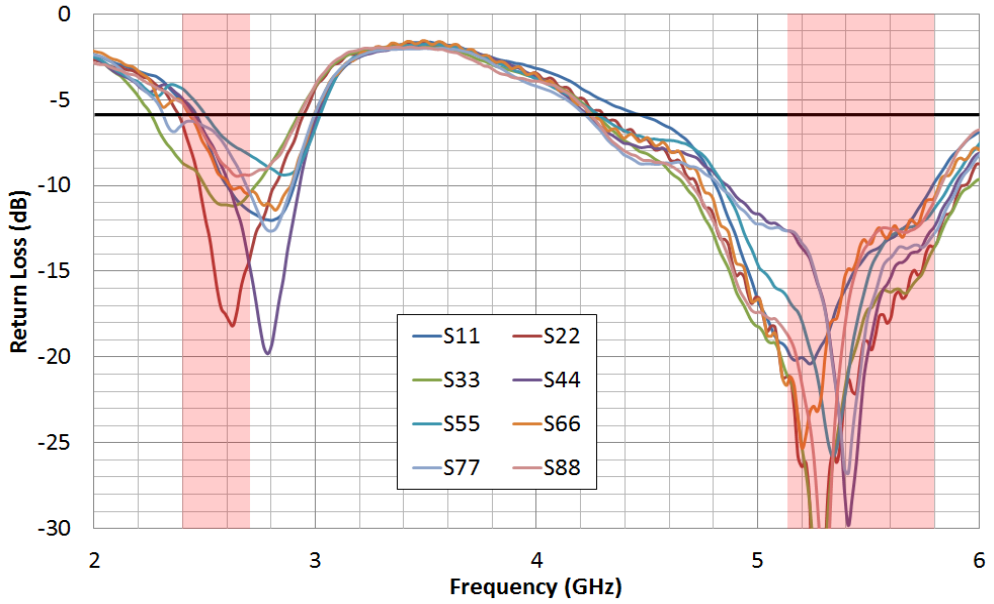

Figure 3-38: Measured reflection coefficient for the 8 hook shaped antennas printed on the side of the plastic box.

Coupling between antennas presented in table 3-9 shown that isolation is always higher than 13 dB in the 5 GHz band, with a minimum of isolation of 11 dB between antennas 5 and 6 in the low band. The measured worst coupling are a bit high due to the lack of space available in the terminal. The ECC is always below 0.5 in both bands with a maximum of 0.355 between antennas 5 and 6 in the low band

and a maximum of 0.107 between antennas 1 and 2 in the high band. The measured values of coupling and correlation are suitable for our application.

Table 3-9: Measured worst isolation and worst ECC for the 8 Hook-shaped antennas printed on the side of the plastic box.

Antenna	Low band (2.4GHz)		High band (5GHz)	
	Worst Coupling	Worst ECC	Worst Coupling	Worst ECC
N°1	-12.0 dB (N°2)	0.198 (N°2)	-14.4 dB (N°2)	0.107 (N°2)
N°2	-12.0 dB (N°1)	0.198 (N°1)	-14.4 dB (N°3)	0.107 (N°1)
N°3	-15.2 dB (N°4)	0.158 (N°4)	-13.8 dB (N°4)	0.083 (N°4)
N°4	-15.2 dB (N°3)	0.324 (N°5)	-13.8 dB (N°3)	0.083 (N°3)
N°5	-11.2 dB (N°6)	0.355 (N°6)	-13.2 dB (N°6)	0.102 (N°6)
N°6	-11.2 dB (N°5)	0.355 (N°5)	-13.2 dB (N°5)	0.102 (N°5)
N°7	-13.0 dB (N°6)	0.245 (N°8)	-14.4 dB (N°6)	0.053 (N°6)
N°8	-19.1 dB (N°7)	0.245 (N°7)	-18.6 dB (N°7)	0.049 (N°7)

Radiation measurements are performed for each antenna of this prototype. Table 3-10 below presents the total efficiency and gain for each antenna in both bands. Average efficiency of 58 % (-2.40 dB) and 65 % (-1.87 dB) are obtained in the low and high band. Efficiency is increased by 10 %, and gain is 2 dB better than the prototype realized with PCB technology.

Table 3-10: Gain and efficiency for the 8 hook-shaped antennas printed of the side of the plastic box in the lower and upper band.

Antenna	2,4 GHz		5,15 GHz	
	Gain (dB)	Efficiency (%)	Gain (dB)	Efficiency (%)
N°1	4.4	75.0	5.49	70.0
N°2	4.72	70.0	4.84	71.0
N°3	3.93	49.0	3.83	65.0
N°4	2.31	51.1	5.33	61.9
N°5	2.61	50.0	3.50	60.0
N°6	3.08	55.0	4.50	63.0
N°7	2.62	61.9	4.01	67.0
N°8	1.83	49.0	4.44	61.9
Average	3.30	57.5	4.54	65.0

3.2.7. Hook-shaped antenna printed on the top of a plastic Box with LDS technology (T2)

The second prototype realized with the LDS technology uses the same hook-shaped antenna. The positions and orientations of antennas on the box match the first prototypes in order to have an accurate comparison between classic PCB technology and LDS technology. Antennas have been printed on the top of the gateway. Figure 3-39 shows the prototype of a plastronic gateway fabricated with LDS technology, with 8 hook-shaped dual-band antennas. This prototype will be referred as “Box Top.” The 2.4 GHz band includes a Wi-Fi and an LTE band (TDD). Antennas are connected with 17 cm coaxial cables. Once again, we had to transfer a piece of the ground plane on the plastic box for each antenna.

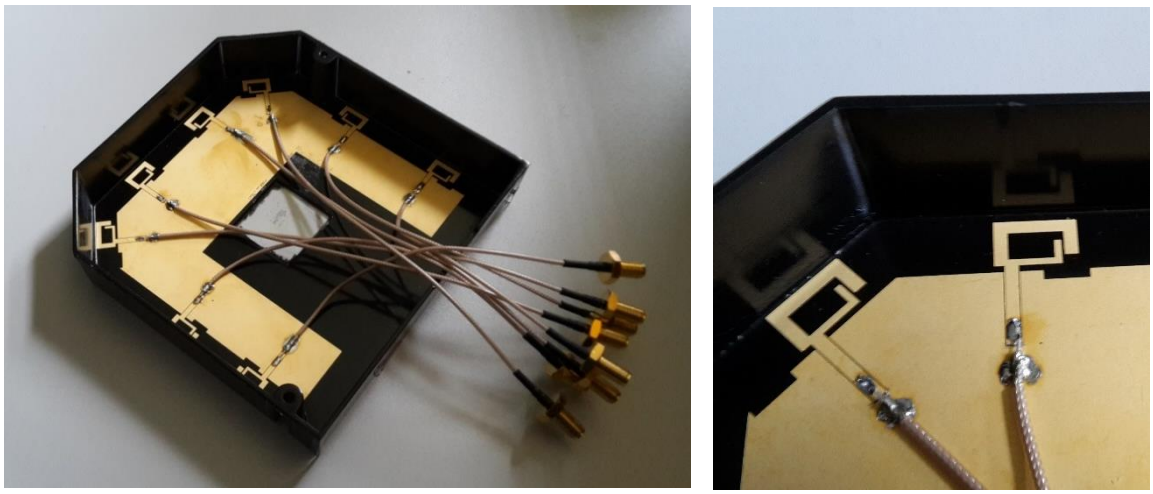

Figure 3-39: Pictures of the prototype with 8 hook-shaped antennas printed on the top of the plastic box.

Simulation presented in Figure 3-40 shows that each antenna is matched on the target bands with a -6 dB criteria in the low band and a -6 dB criteria in the higher band. Measurement presented in figure 3-41 match the simulation with a good agreement.

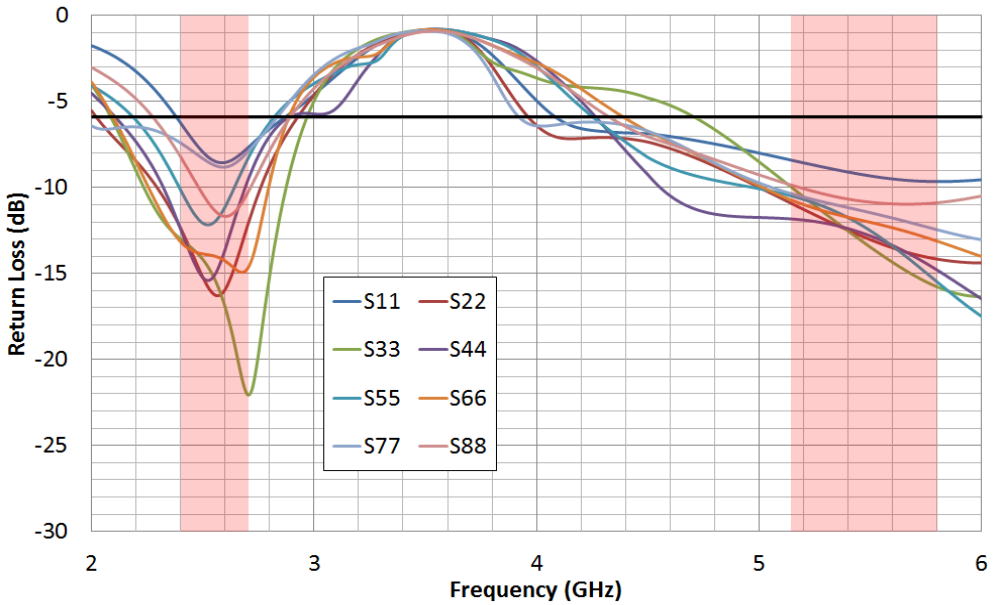

Figure 3-40: Simulated reflection coefficient for the 8 hook shaped antennas printed on the top of the plastic box.

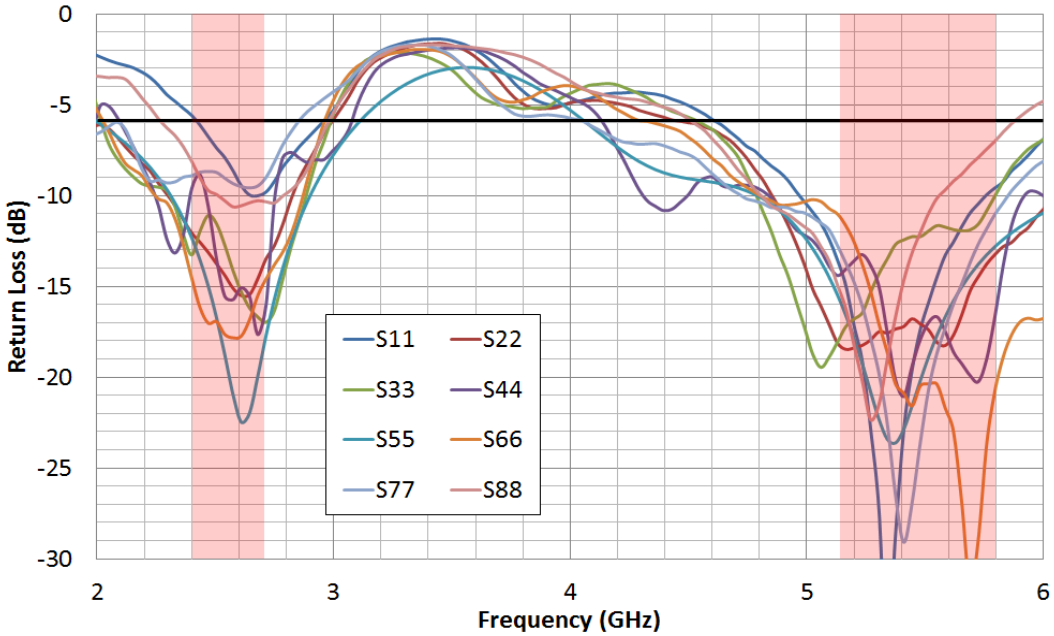

Figure 3-41: Measured reflection coefficient for the 8 hook shaped antennas printed on the top of the plastic box.

Coupling between antennas presented in table 3-11 shown that isolation is always higher than 11 dB in the 5 GHz band, with a minimum of isolation of 10 dB between antennas 4 and 5 in the low band. The measured worst coupling are a bit high due to the lack of space available in the terminal. The ECC is always below 0.5 in both bands with a maximum of 0.205 between antennas 4 and 5 in the low band and a maximum of 0.293 between antennas 1 and 2 in the high band. The measured values of coupling and correlation are suitable for our application.

Table 3-11: Measured worst isolation for the 8 Hook-shaped antennas printed on the top of the plastic box.

Antenna	**Low band (2.4GHz)**		**High band (5GHz)**	
	Worst Coupling	**Worst ECC**	**Worst Coupling**	**Worst ECC**
N°1	-11.6 dB (N°2)	0.201 (N°2)	-11.3 dB (N°2)	0.293 (N°2)
N°2	-11.6 dB (N°1)	0.201 (N°1)	-11.3 dB (N°1)	0.293 (N°1)
N°3	-11.7 dB (N°2)	0.111 (N°4)	-12.2 dB (N°4)	0.137 (N°4)
N°4	-9.9 dB (N°5)	0.205 (N°5)	-12.4 dB (N°3)	0.137 (N°3)
N°5	-9.9 dB (N°4)	0.205 (N°4)	-13.9 dB (N°6)	0.236 (N°6)
N°6	-14.3 dB (N°7)	0.158 (N°5)	-13.9 dB (N°5)	0.236 (N°5)
N°7	-11.9 dB (N°8)	0.165 (N°8)	-14.9 dB (N°8)	0.057 (N°6)
N°8	-11.9 dB (N°7)	0.165 (N°7)	-14.9 dB (N°7)	0.056 (N°7)

Radiation measurements are performed for each antenna of this prototype. The table 3-12 below presents the total efficiency and gain for each antenna in both bands. Average efficiency of 58 % (-2.82 dB) and 45 (-3.41 dB) are obtained in the low and high band. Efficiency and gain are similar to the previous prototype.

Table 3-12: Gain and efficiency for the 8 hook-shaped antennas printed of the top of the plastic box in the lower and upper band.

Antenna	2,4 GHz		5,15 GHz	
	Gain (dB)	Efficiency (%)	Gain (dB)	Efficiency (%)
N°1	3.48	50.6	3.06	41.5
N°2	3.85	59.6	4.94	49.4
N°3	1.80	54.0	4.38	49.7
N°4	3.56	49.3	3.39	47.2
N°5	4.26	51.3	5.64	49.5
N°6	2.15	42.9	1.01	22.5
N°7	2.12	48.2	6.7	52.8
N°8	5.56	62.2	4.33	52.4
Average	3.52	52.2	4.47	45.6

3.2.8. Summary of the different prototypes

Six prototypes with 8 dual-band antennas have been realized. The different realizations illustration the progression from classic solution with PCB technology to an innovative solution with LDS technology. PCB1 to PCB 2 has been realized with printed antennas which are easy to manufacture and very low-cost elements. Printed antennas are suitable for Wi-Fi application but are characterized by low efficiency and gain. PCB 3 has been designed with PIFA antennas, known to have good efficiency and gain but a higher cost than printed antennas. PCB 4 is a compromise between the three previous realizations. This solution allows increasing diversity between antennas while maintaining good performance in terms of efficiency and gain. Finally, the solutions presented with LDS technology come with a high cost but presents enhanced performance thanks to low losses in the substrate. Moreover, this solution allows to optimize significantly the volume occupied by antennas.

The table 3-13 sums up the main characteristics measured in free space for each prototype. We can see the difficulty to improve isolation and correlation between antennas is such a small terminal no matter what technology is used. Nevertheless, the mixed prototype presents the lowest correlation in the low band among the prototypes realized with PCB technology. The gain and efficiency of antennas printed on the plastic box are slightly better than antennas printed on PCB technology. Unfortunately, the performance of LDS prototypes is degraded by the handmaid weld of the coaxial cable of the fed lines and ground plane.

Table 3-13: Summary of the main characteristics measured for each prototype

Prototype	2.4 GHz			5 GHz		
	Mean Gain (dB)	Mean Efficiency (%)	Mean ECC	Mean Gain (dB)	Mean Efficiency (%)	Mean ECC
PCB 1 - Hook	1.38	45.3	0.101	2.80	54.6	0.111
PCB 2 - IFA	1.84	51.5	0.083	2.85	62.1	0.034
PCB 3 - PIFA	2.11	51.8	0.069	3.70	53.7	0.029
PCB 4 - Mix	2.44	49.7	0.058	3.29	49.3	0.060
Box Side	3.30	57.5	0.096	4.54	65.0	0.025
Box Top	3.52	52.2	0.062	4.47	45.6	0.042

Each prototype achieves the performance required for Wi-Fi gateway applications regarding the free space results measured on antennas. In the next step of the study, the prototypes will be evaluated as a complete system and not as simple radiating elements. The objective is to see if the improvements in antennas performance bring by LDS technology will be perceptible when the gateway is used in a beamforming configuration.

3.3. Measurements Results with OpenAirInterface

In this section, the measurement setup developed with OpenAirInterface and presented in chapter 2 is used to test the different prototype in a realistic environment.

The first part of the study aims to compare the performance between prototypes. Only four prototypes have been tested: PCB 1 (hook antenna), PCB 4 (mixed prototype), Box Side (hook antenna printed on the side of the plastic box) and finally the Box Top (hook antenna printed on the top of the plastic box). PCB 1 is used as a pure reference for comparison with the Box Side and the Box Top because the same antennas, orientation, and implementation have been used for the design of those prototypes. The PCB 4 is considered as an "ideal" case for PCB technology. For that study, PCB 2 (IFA) and PCB 3 (PIFA) doesn't bring any value in terms of performance comparison.

The second part of the study proposes to investigate antenna selection within multi-antennas devices. Based on an SNR measurement, this method allows choosing the best set of antennas among the 8 antennas to perform a MISO 2x1 or MISO 4x1 communication. The point is to evaluate if all antennas are needed to establish a strong link between transmission and reception.

3.3.1. Prototypes comparison

In order to compare the performance of the four prototypes, we performed a set of measurement with OAI. Figure 3-42 shows pictures of the measurement setup. On the left picture, we can see a commercial monopole antenna acting as the user equipment and embedded on the top of the pole mounted on the rail. The right picture shows the computer controlling the whole setup, the PCI express frame supporting the three expressMIMO2 boards and an 8 antenna gateway connected to the RF front-ends.

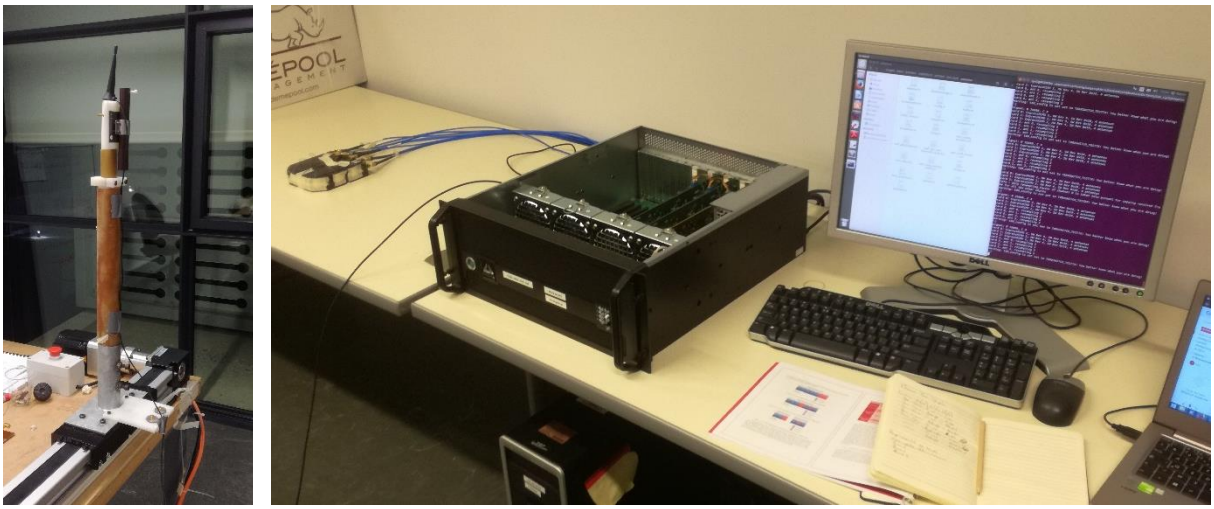

Figure 3-42: Pictures of the antenna embedded on the rail and the OAI testbed connected to an 8 antenna prototype.

The proposed setup is configured to operate in Time Division Duplexing (TDD) mode in an 8x1 MISO configuration at 2.6 GHz. The testbed aims to characterize beamforming gain through SNR measurements. The gateway transmits 10 LTE OFDM frames with a 5 MHz bandwidth and a transmitted power of 10 dBm. The power is chosen to insure a good level of reception in the whole room while avoiding saturation of receiving RF chains. Measurements are performed in a line of sight configuration.

For each prototype, the measurement process consists of measuring SNR values for 200 positions with a 3 cm step on the rail. The rail is going forward for the first 100 positions and backward for the last 100. At each position, we perform SNR measurement in a MISO 8x1 configuration as well as retrieve the SNR in a SISO configuration for the eight antennas of the prototype. The figure 3-43 presents the Cumulative Distributed Function (CDF) for the 200 SNR measurements for the 8 antennas (solid lines) as well as the measured SNR in the MISO 8x1 beamforming configuration (dotted line) for the PCB 4.

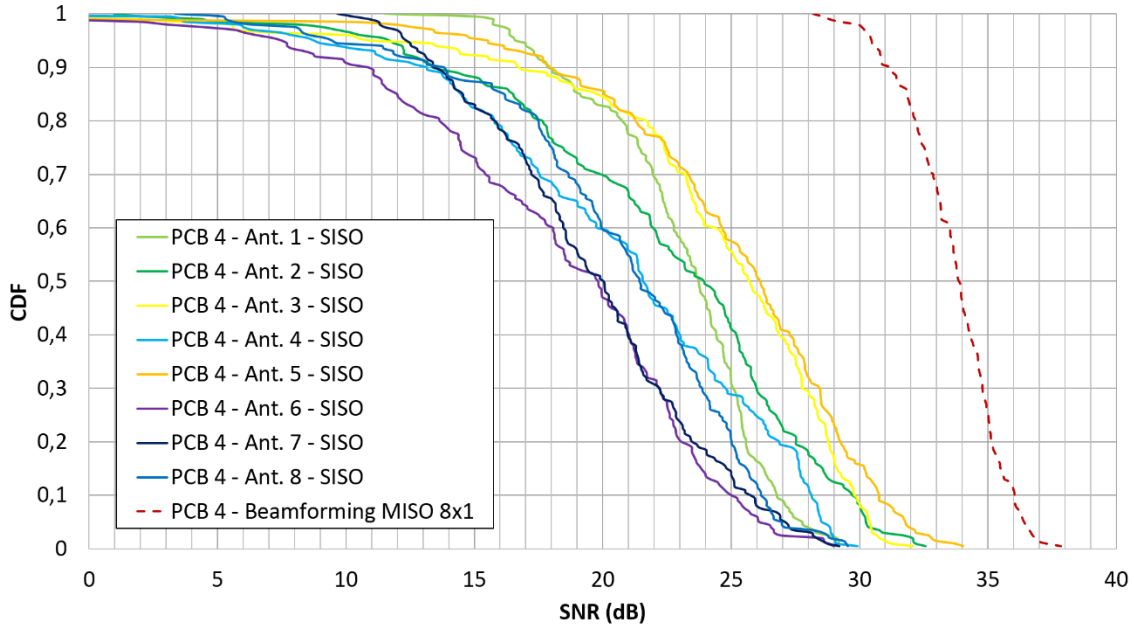

Figure 3-43: CDF of the measured SNR in SISO configuration for the 8 antennas and MISO 8x1 configuration for the PCB 4.

For a matter of visibility, we decided to average the SNR value measured on the 8 antennas for every position. Figure 3-45 presents the CDF for the average SNR measured in SISO configuration as well as the SNR measured in 8x1 MISO configuration. The graph illustrates the 9 dB increase on the SNR for the 8x1 MISO case compared to the SISO one.

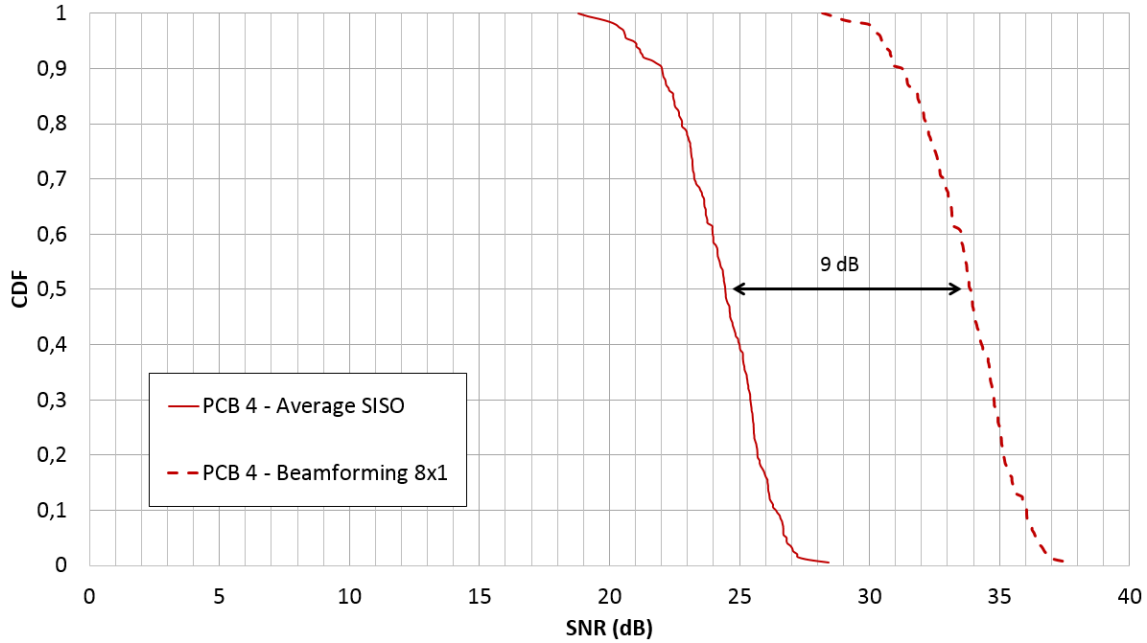

Figure 3-44: CDF of the average SNR in SISO configuration and MISO 8x1 configuration for the PCB 4.

The same measurement process has been performed for the three other prototypes (PCB 1, Box Side and Box Top). SNR in SISO configuration have been averaged for the 8 antennas at each position and beamforming MISO 8x1 have been performed in the same conditions for each prototype. Figure 3-45 presents the results of the four prototype in the form of CDF. The figure highlights the different performance of each prototype. PCB 1 offers the lowest SNR, followed by the PCB 4, the Box Top and finally the box Side. We notice a 4 dB increase between the PCB 1 and its equivalent in LDS technology, the Box Side. This difference is higher than expected regarding the gain improvement of 2 dB obtained with the LDS prototype.

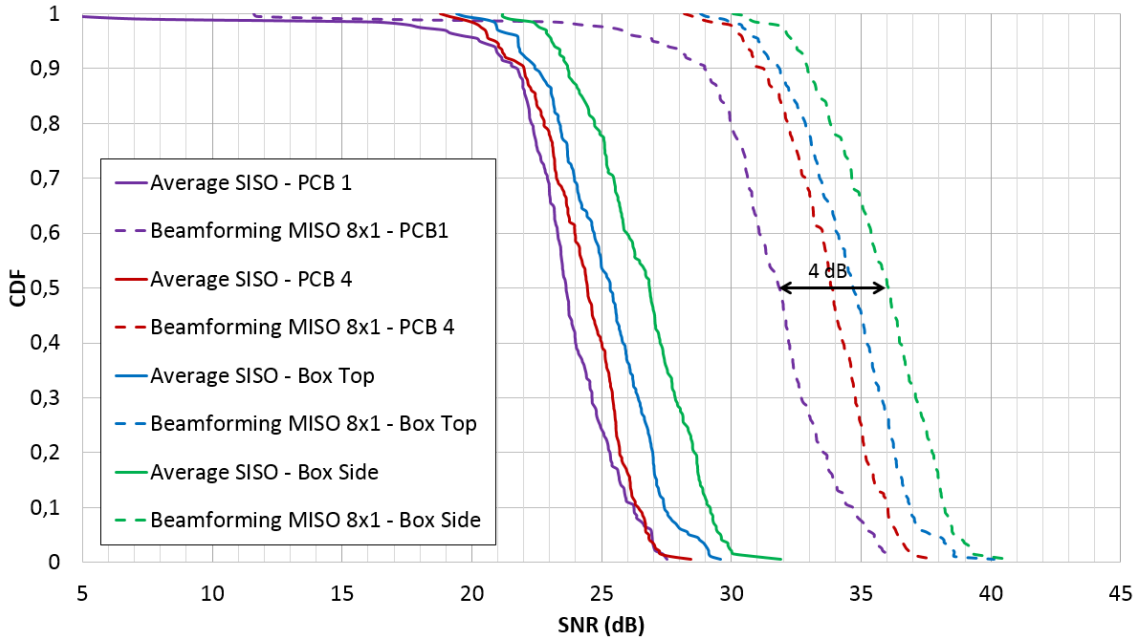

Figure 3-45: CDF of the average SNR in SISO configuration and MISO 8x1 configuration for the PCB 1, PCB 4, Box Side and Box Top.

Several conclusions on antenna designs can be extracted from those results. Regarding the PCB 1 and PCB 4, we could say that antenna diversity plays an important role in the beamforming performance. Indeed the average SISO seems quite similar between PCB 1 and PCB 4, but the MISO 8x1 offers performance higher of 2 dB with the PCB 4. Moreover the Box side and box Top presents equivalent free space characteristics, but the Box Side seems to improve the beamforming efficiency significantly. This difference might be explained by the polarization involved in the two designs, mainly vertical for the Box Side and mainly horizontal for the Box Top.

The set of measurements performed with OAI gives interesting information about antenna performance within a multi-antenna gateway. Indeed it appears that antenna free space characteristics have a major impact on the gateway performance as a system.

3.3.2. Antenna selection in multi-antenna devices

Antenna selection within multi-antenna systems has been studied in the literature regarding channel capacity [III-27]. The optimization of the number of antennas in multi-antenna devices has also been studied in [III-28] and [III-29] in order to reduce the rank of the channel matrix [III-30]. In this section, we wanted to explore antenna selection in terms of SNR. Such techniques can be very interesting for the management of the energy consumption. Indeed the use of a high number of antennas at the transmitter implies a high consumption.

In our experiment, the so-called adaptive beamforming aims to select the best set of antennas among the 8 antennas to perform a Beamforming MISO 2x1 or MISO 4x1 communications. The objective is to know the achievable performance with 2 or 4 antennas at the transmitter. For this purpose, we developed an algorithm on OAI able to select for each position on the rail, the 2 or the 4 best antennas and used them for a MISO 2x1 and a MISO 4x1 beamforming communication. In order to evaluate the interest of this technique, we compare this adaptive scheme to a fixed scheme where a MISO 2x1 and MISO 4x1 beamforming communication are performed always using the same antennas for each position of the transmitter on the rail. We conduct this experiment with the best prototype measured in the previous section, the Box Side. Figure 3-46 presents which antennas have been chosen for the fixed scheme of beamforming. We decided to use the front antennas because they are facing the reception antenna in the LOS configuration of our measurement setup. Antennas 4 and 5 are chosen for the MISO 2x1 communication and antennas 3, 4, 5 and 6 for the MISO 4x1.

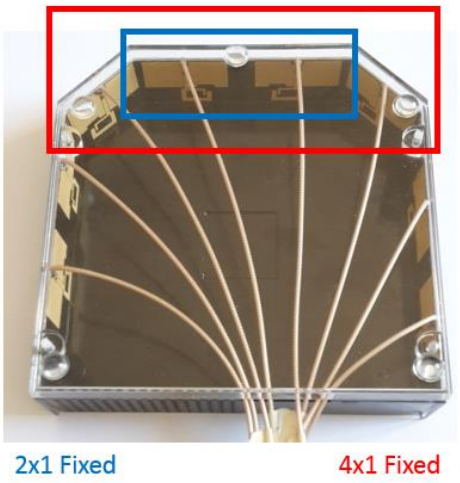

Figure 3-46: Antennas chosen for the MISO 2x1 (blue) and 4x1 (red) beamforming fixed scheme

The results of this experiment are presented in figure 3-47 in the form of a CDF. The blue lines present MISO 2x1 beamforming, the red lines presents MISO 4x1 beamforming, the green line presents the full 8x1 beamforming, the dotted lines present the adaptive scheme while the solid lines present the fixed beamforming scheme. We observe an average 3 dB increase on the SNR for the adaptive scheme for the MISO 2x1 and 4x1 beamforming compare to the fixed scheme. A second interesting observation is a very low gap (less than 1 dB) between the adaptive MISO 4x1 and the full MISO 8x1. This could be explained by the use of antennas providing a very weak signal in the MISO 8x1 configuration, which penalizes the global performance of the system.

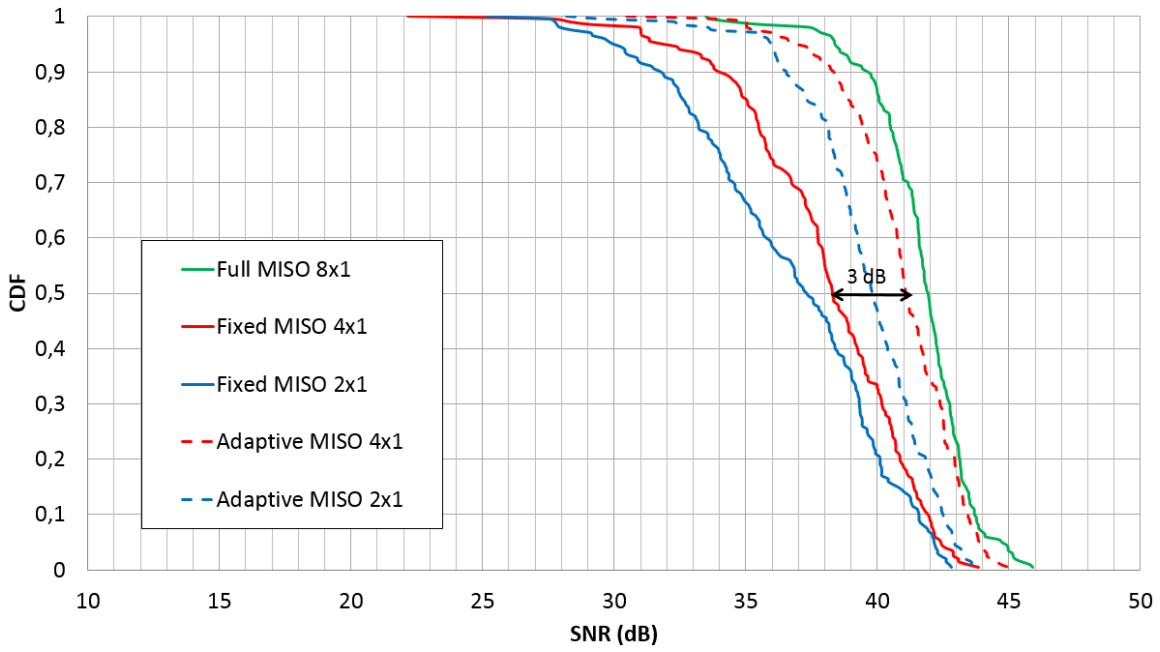

Figure 3-47: CDF of the SNR measured in MISO 2x1, 4x1 and 8x1 for a fixed and adaptive beamforming scheme with the Box Side prototype in LOS.

To strengthen those conclusions we decided to realize the same measurement but in a Non Line-Of-Sight configuration (NLOS). To obstruct the direct view between transmitter and receivers we installed a metallic closet in the middle of the room. Consequently, the path loss is increased and the propagation channel modified. The results of the measurement in NLOS are presented in figure 3-48 in the form of a CDF. The first observation is that the SNR measured values are 10 dB lower than in LOS. Secondly, we find the same gap between the adaptive MISO 4x1 scheme and the full MISO 8x1 than in the LOS configuration again. Finally, we observe that fixed MISO 4x1 comes closer to the adaptive MISO 4x1 with an average gap of 2 dB, while the fixed MISO 2x1 is way less performant than the adaptive MISO 2x1 with an average gap of 6 dB. As is, it is very difficult to explain this last observation.

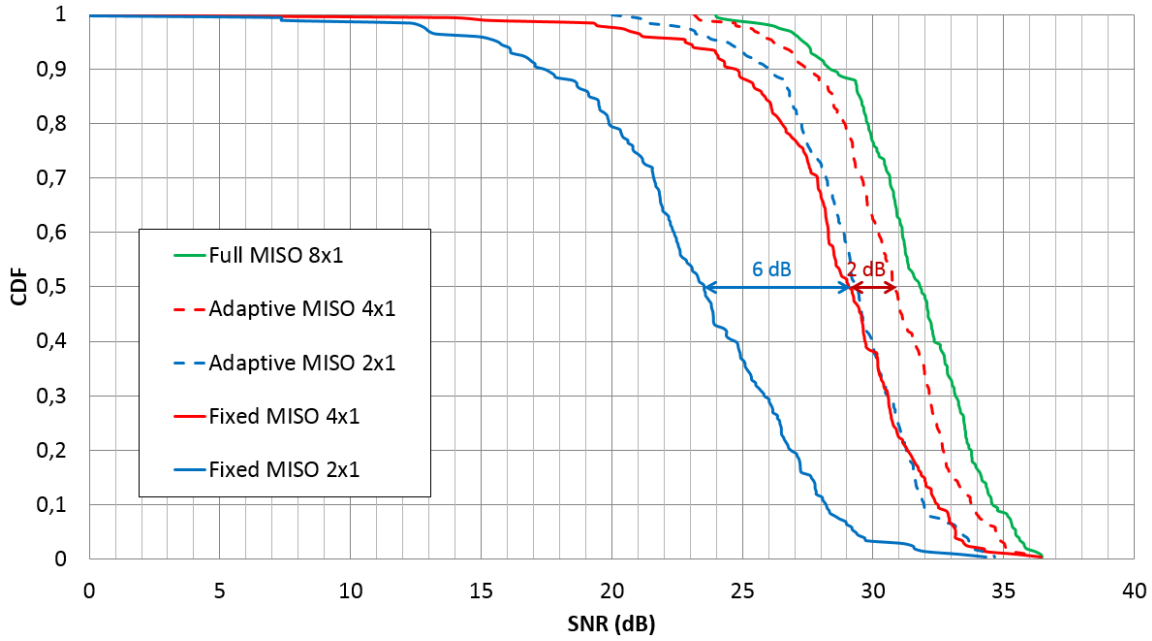

Figure 3-48: CDF of the SNR measured in MISO 2x1, 4x1 and 8x1 for a fixed and adaptive beamforming scheme with the Box Side prototype in NLOS.

In order to provide more insight into the measurement results, we retrieved the number of usage for each antenna in the adaptive beamforming scheme. Indeed, for each position, the algorithm selects the best antennas in terms of SNR, so it is interesting to observe which antennas have been chosen all along the 200 positions of the Rx antenna on the rail. The figure 3-49 presents in a stick diagram how many times each antenna has been used during the 200 measurements for the adaptive beamforming in each configuration (LOS MISO 2x1, LOS MISO 4x1, NLOS MISO 2x1 and NLOS MISO 4x1). The hatched and solid sticks present the respectively NLOS and LOS configuration while blue and red sticks present MISO 4x1 and MISO 2x1 scheme respectively.

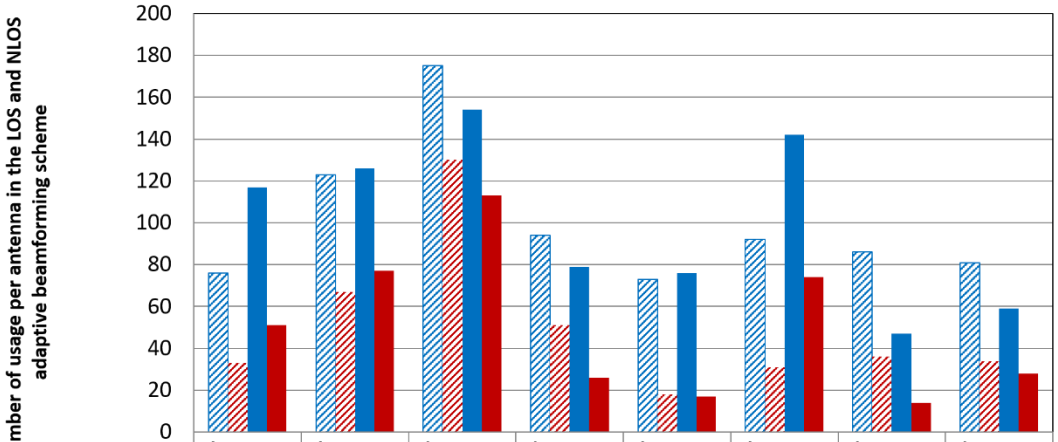

	Antenna 1	Antenna 2	Antenna 3	Antenna 4	Antenna 5	Antenna 6	Antenna 7	Antenna 8
Index NLOS - MISO 4x1	76	123	175	94	73	92	86	81
Index NLOS - MISO 2x1	33	67	130	51	18	31	36	34
Index LOS - MISO 4x1	117	126	154	79	76	142	47	59
Index LOS - MISO 2x1	51	77	113	26	17	74	14	28

Figure 3-49: Number of usage per antenna and per configuration within the Box Side prototype.

From those results, we observe that every antenna is not used as much as other. For example antenna 3 has been the most used in every configuration even thought this element doesn't provide the higher gain and efficiency among other antennas of the prototype. In LOS Antennas 3 and 6, placed in the two corner of the box, have been widely used. Their favorable positions regarding the receiver could explain the amount of usage of those two elements but the very low usage of elements 4 and 5, place in front of the box, and refute this hypothesis.

The radiation pattern of those antennas has been left aside during this study. This parameter could bring more insight into the system performance with antenna selection. Unfortunately, the antennas designed in the six prototypes doesn't present significant omnidirectional or directive pattern. Conclusions about the best pattern configuration can't be established with those prototypes. In the next part, we will study with the same measurement setup, two prototypes presenting omnidirectional and directional radiation patterns.

As a conclusion, the measurements setup developed with OAI shown its capabilities to compare various antenna designs and to implement and tests new functionalities. Indeed the results highlighted the improved performance of the LDS method compared to the PCB technology. Moreover, antenna selection within multi-antenna gateway has shown promising results to optimize energy consumption and to address users intelligently. One perspective of this work would be to test antenna selection in MU-MIMO configuration.

3.4. Directional antennas

In this section, we want to evaluate the influence of antenna radiation pattern on the performance of the multi-antenna gateway. In this context, we kept working with the box designed in the previous section. The objective is to compare the performance of 8 omnidirectional antennas with 8 directional antennas. We aim to design antennas radiating in half a sphere in order to obtain spatial filtering of the receive signals. For this purpose, we explored two solutions.

The first solution was to exploit Artificial Magnetic Conductors (AMC) as a reflector to modify and focus the radiation pattern of the hook-shaped antenna realized in the Box Side in a specific direction. The main advantage of this solution is that the AMC can be located very close to the antenna and thus allows keeping a very low volume occupied by antennas.

The second solution consisted of designing a new dipole antenna and a reflector based on the layout of this antenna. The main advantage of this solution is that the dipole presents a clean omnidirectional pattern. When adding a reflector behind the antenna, the antenna radiate in half a sphere which allows a reliable and accurate comparison between an omnidirectional and a directive pattern.

3.4.1. Directivity enhancement with AMC

AMC Artificial Magnetic Conductors are structures with periodic metallic patterns printed on a dielectric substrate. Generally used as a reflector plane, they possess the very interesting property of having the phase of the reflection coefficient varying from -180 ° to 180 ° by passing through 0 °, in contrast to a conventional ground plane which allows a reflection of 180 °. This phase reflection property is very important because it makes it possible to reduce the size of the antenna compared to a conventional ground plane.

The most basic AMCs are therefore networks of square conductive elements. The patch dimensions fix the resonance frequency. Other parameters intervene in the design of an AMC including the spacing between each cell as well as the height and permittivity of the substrate.

In the perspective of focusing the radiation towards the user, we envisaged integrating artificial magnetic conductors into the router. These structures are simulated under HFSS with a Floquet port and periodic conditions at the boundaries of the radiation box.

3.4.1.1. Design of a dual-band AMC

According to the studies carried out on this type of structure, it is possible to create a dual-band AMC consisting of a central patch resonating at the high frequency and an external ring resonating at the low frequency. We, therefore, study in a first time single-band cells at 2.4 GHz and 5 GHz realized on a substrate FR4 of permittivity ε_r = 4.6 and thickness h=1.6 mm. We began by realizing the ring structure operating at 2.4 GHz and the patch resonating at 5 GHz as presented respectively in figure 3-50(a) and 3-50(b). Then we combined the two structures to form the dual-band AMC is shown in Figure 3-50(c). The gap between the patch and the ring plays an important role in the design of the AMC. In this design, the gap is fixed at 0.45 mm. The dimensions of each structure are presented in figure 3-51.

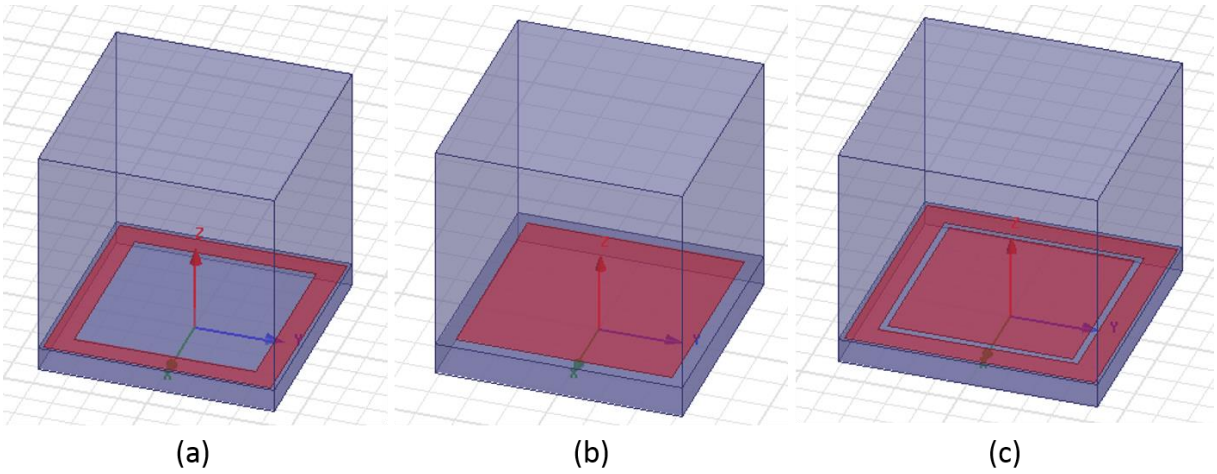

Figure 3-50: Simulated view of the (a) 2.4 GHz mono-band ring structure, (b) 5 GHz mono-band patch structure and (c) combined ring and patch dual-band structure.

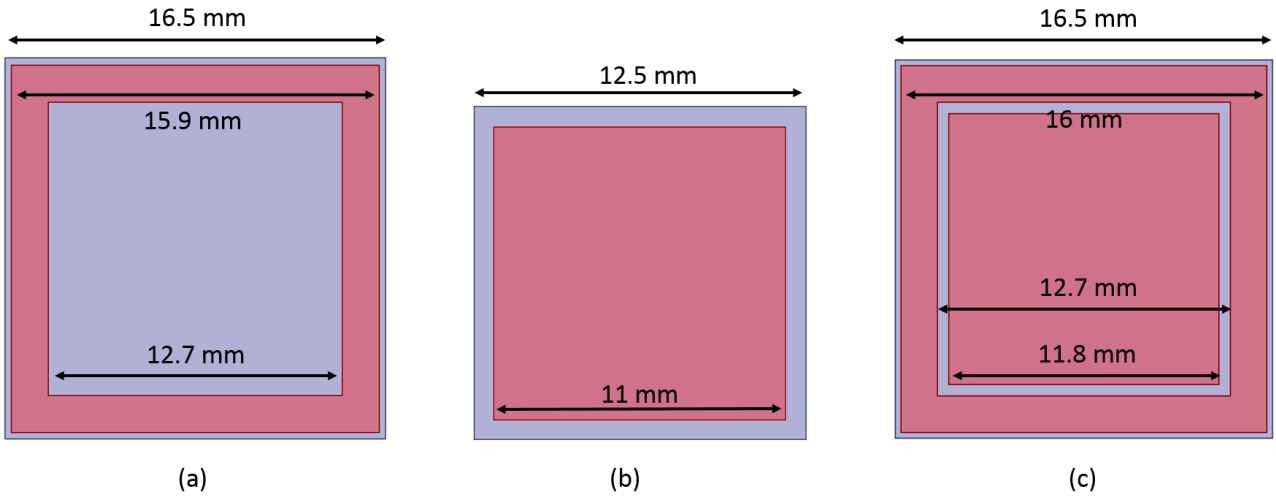

Figure 3-51: Dimensions of the (a) 2.4 GHz mono-band ring structure, (b) 5 GHz mono-band patch structure and (c) combined ring and patch dual-band structure.

By convention, we observe the phase of the reflection coefficient (the coefficient of the plane wave sent on the structure is observed) between 90 ° and -90 to evaluate the functioning of the AMC. Figure 3-52 presents the phase of the reflection coefficient for each structure. We observe that the phase of the reflection coefficient passes through 0 ° in the useful frequency bands (red rectangle on the graph). The role of the reflecting plane of the structure is thus ensured in these two bands.

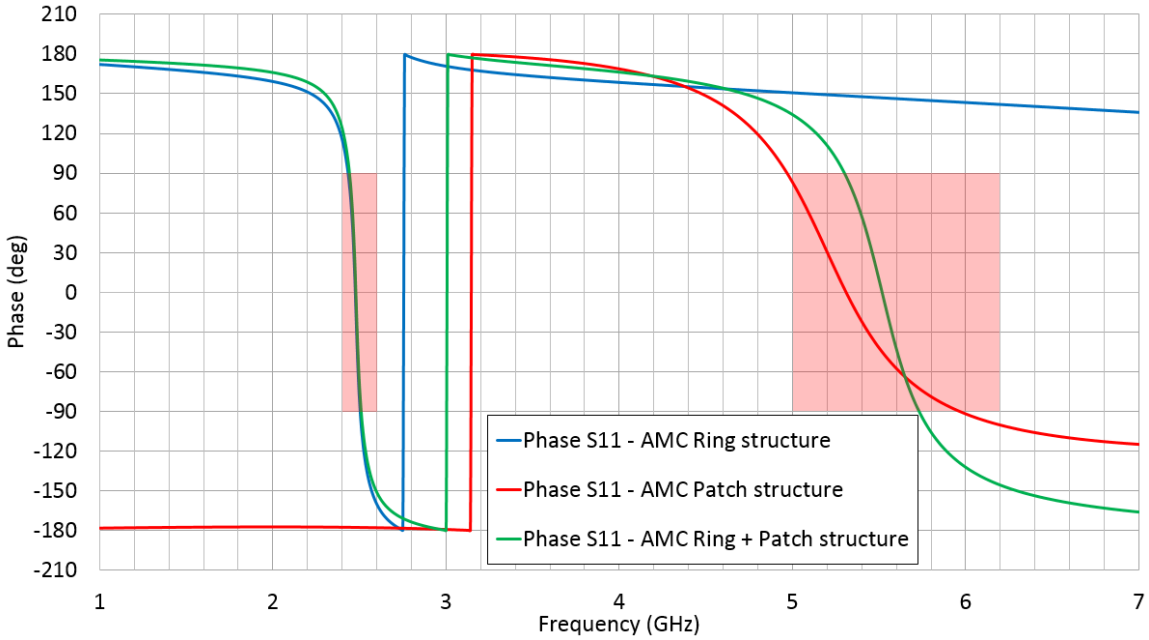

Figure 3-52: Simulated phase of the coefficient reflection for the three structures.

3.4.1.2. AMC Array with hook-shaped antenna

The previous results presented the cells alone in which the network effect was simulated by the Floquet port and the periodic conditions at the boundaries of the radiation box. The more complete the cell structure, the more effective the reflective plane effect will be. Thus we realize a 4x4 network presented in figure 3-53, integrating the hook-antenna over the structure with is a 1 mm air gap between the antenna and the AMC.

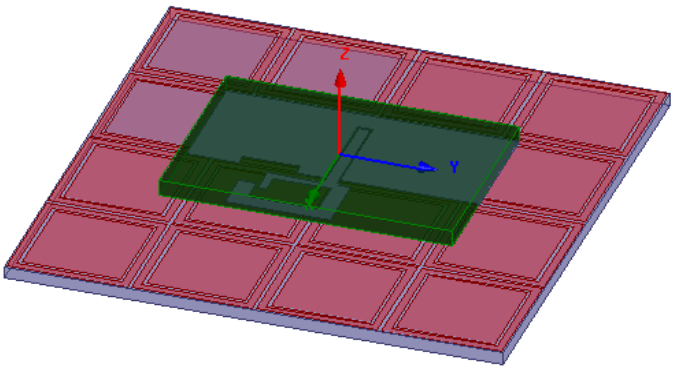

Figure 3-53: Simulated 4x4 AMC with hook shaped antenna.

Figure 3-54 presents the simulated 3D radiation pattern of the hook-antenna for the 2.4 GHz and 5 GHz frequency. We observe that in both frequencies, the hook-antenna forms a radiation pattern focus toward the z axis. The antenna has a maximum simulated gain of 4.26 dB at 2.4 GHz and 5.3 dB at 5 GHz.

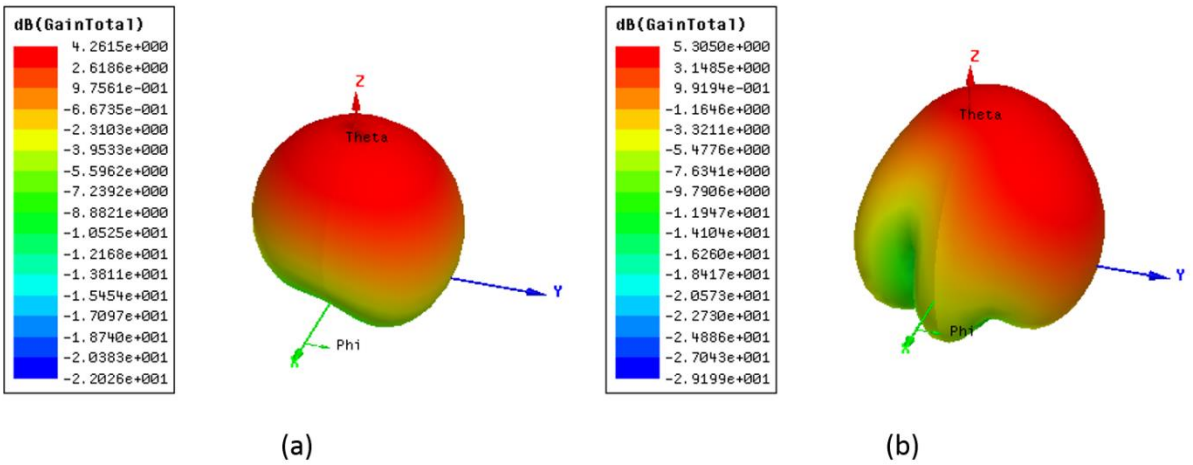

(a) (b)

Figure 3-54: 3D radiation patterns of the simulated hook antenna over a 4x4 AMC at (a) 2.4 GHz and (b) 5.15 GHz.

This step becomes very complex in terms of the adaptation of the antenna. Indeed these parameters S are modified in contact with the AMC, and all the dimensions (antennas and AMC) comes into play to re-adapt the antenna. The position of the antenna with respect to the AMC remains the major parameter. Therefore, we decided to concentrate our study on the radiation pattern obtained.

Moreover, our housing having fixed dimensions, we cannot integrate a 4x4 cell network into the prototype of the router (the box has a height of 35 mm). We studied a technique of miniaturization of AMC. This method consists of making a spiral patch that resonates at 2.4 GHz and then adds a resonant ring at 5 GHz. We tested several topologies of spirals. The realization of this type of structure is very complex under HFSS because each dimension has to be parameterized in order to carry out parametric studies (variations of the dimensions). We managed to realize a 13.1x13.1 mm AMC structure, reducing the size of the initial square patch by nearly 20%. Despite this significant size reduction, it was not small enough to fit the plastic box.

To further reduce the size of the AMCs, it is possible to increase the height of the substrate. The increase in height has the effect of shifting the frequency of operation towards the low frequencies. Thus we can reduce the dimensions of the structure to go back to the operating frequency of 2.4 GHz. We chose not to increase the height of the substrate to retain a small structure. So we explored another option, which is to create a flexible horizontal AMC network.

3.4.1.3. Specific AMC Design for Box

As the technique of miniaturization has not succeeded, we turn to another option. We had the idea to realize a horizontal network with the dual band cell presented previously. The idea is to create a flexible band that will come to rest on the walls of the box and thus directs the antenna radiation to the outside of the box.

In order to obtain a flexible structure, we propose to print the square patterns on a layer of Duroïd of thickness h = 0.254 mm and of permittivity εr = 2.2. The ground plane of the AMC will be printed on FR4 and will be added by pieces into the box. Figure 3-55 presents a schematic of the structure.

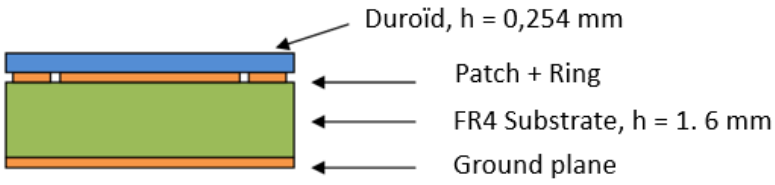

Figure 3-55: Schema of the AMC structure with a thin duroïd layer.

We studied the effect of the Duroïd layer on the dual band AMC cell already realized. In Figure 3-56 we notice that the reflection coefficient undergoes a slight shift towards the low frequencies when adding a layer of Duroïd. In spite of all, the reflection coefficient remains adapted in the useful bands. This shift is explained by the permittivity of this material which is higher than that of the vacuum.

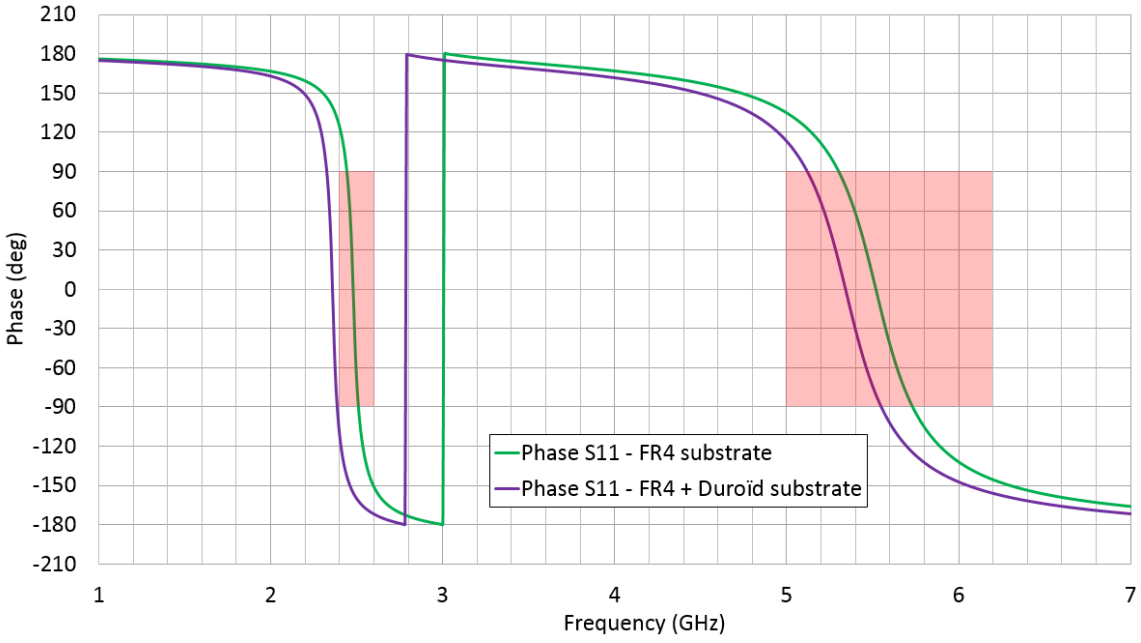

Figure 3-56: Phase of the reflection coefficient for the AMC structure with and without the duroïd layer.

To validate the hypothesis of operation of a horizontal network we realize a simulation of the antenna on a network of 2x6 elements presented in figure 3-57. We can see in Figure 3-58 that the hook-antenna radiation is focused in the vertical plane for both 2.4 GHz and 5 GHz frequencies. This type of radiation is suitable for our application. Indeed, considering the positioning of the antennas on the router, we will be able to cover all directions.

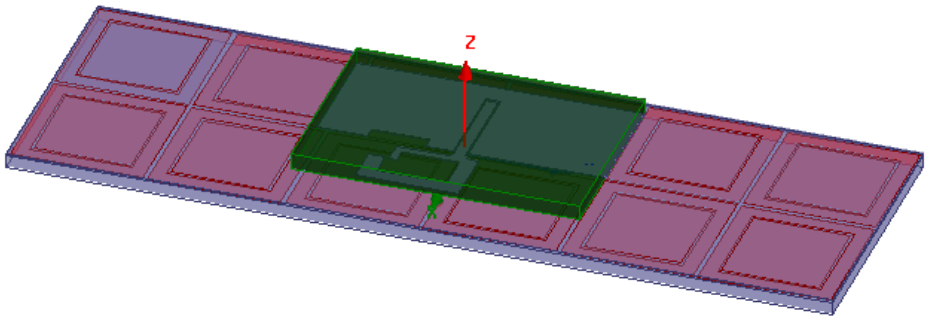

Figure 3-57: Simulated hook antenna over a 2x6 elements AMC dual-band AMC.

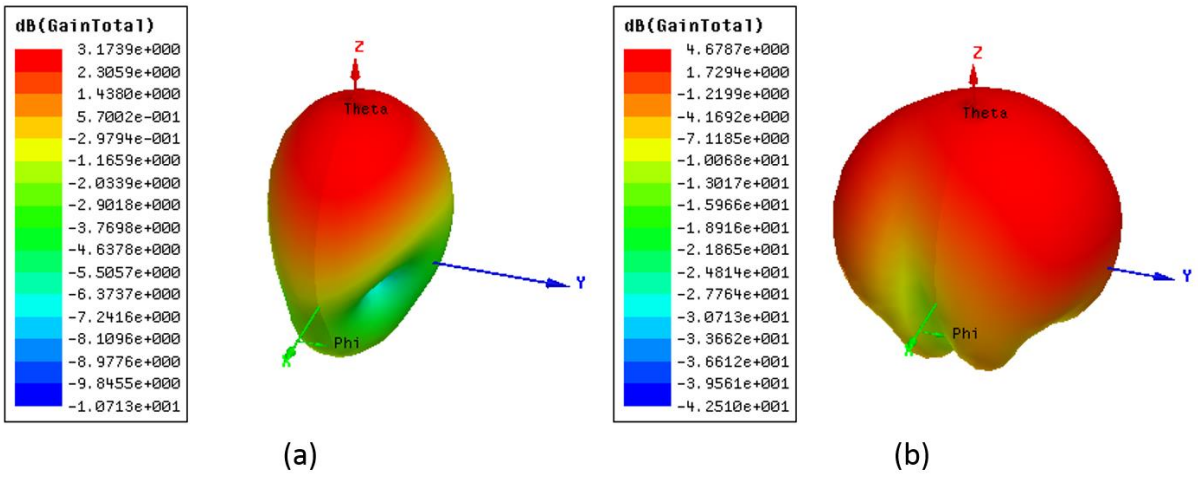

Figure 3-58: 3D radiation patterns of the simulated hook antenna over a 2x6 elements AMC on duroïd substrate at (a) 2.4 GHz and (b) 5.15 GHz.

We printed the 2x27 elements dual-band AMC on the duroïd substrate. Figure 3-59 presents the structure which has a dimension of 32x432 mm to fulfill the whole contour of the plastic box. The AMC has been embedded in the Box Side prototype with a 2 mm gap from antennas maintained thanks to a layer of foam material of permittivity $\varepsilon_r = 1$.

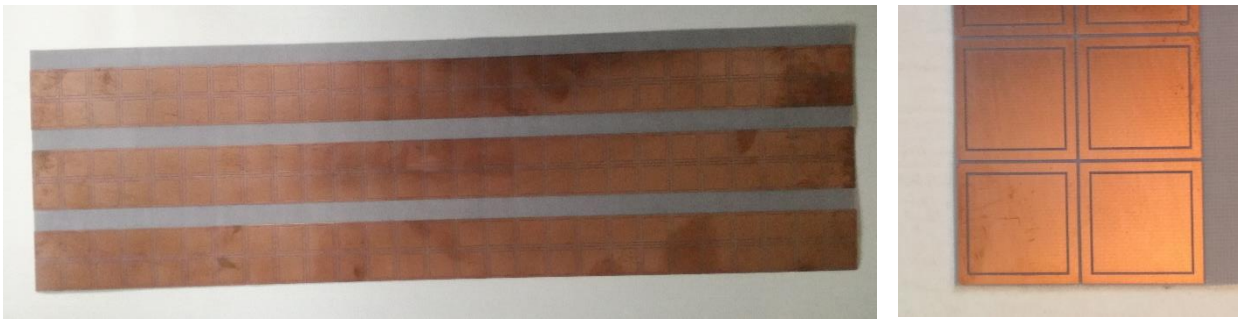

Figure 3-59: Pictures of the 2x27 elements AMC.

The radiation pattern and S-parameter of the prototype have been measured respectively on a Satimo Starlab and a VNA. Unfortunately, measurements where not conclusive and thus are not presented here. Antenna matching was not achieved as well as the expected radiation pattern.

Several parameters can explain this failure. Indeed the alignment between AMC and antennas couldn't be realized the same way than in simulation. Secondly, the whole shape of the box introduces some perturbations that destroy the radiation pattern. The last explanation is the lack of elements in the vertical dimension of the AMC. Only two element over the vertical axis was not enough to create the reflector effect of the AMC.

To validate this last hypothesis we realized a 5 GHz AMC on a Neltec NY9220 substrate of permittivity $\varepsilon_r = 2.2$ and thickness h = 3.175 mm. By increasing the thickness of the substrate, we were able to significantly reduce the single element dimensions to a square of 3.2x3.2 mm. Then we realized an AMC prototype constituted of 8x10 elements for a total dimension of 25.6x32 mm. The realized prototype is presented in figure 3-60. AMCs were added to the Box Side behind every antenna with a 1 mm gap realized with a layer of foam material.

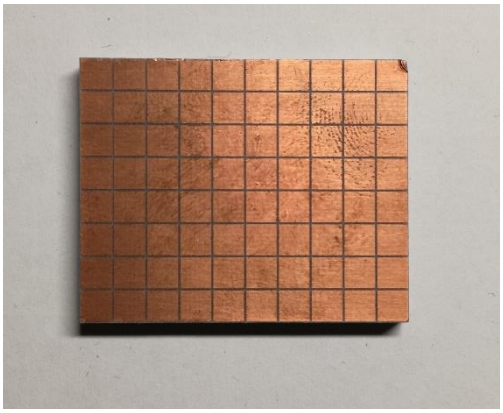

Figure 3-60: Picture of the 8x10 elements AMC at 5 GHz.

Radiations measurements at 5 GHz indeed focused the radiation pattern of the antennas in the expected direction. This experiment validates the fact that the AMC needs a dense network of the patch to operate as a reflector. Unfortunately, the final objective is to measure the directional prototype with OAI which only operate between 350 MHz and 3800 MHz. Thus we need a prototype working with directional antennas in this frequency range.

3.4.2. Directivity enhancement using a reflector

In this study, the main point is to explore the impact of antenna directivity in a multi-antenna gateway. In order to measure the system with the OAI measurement setup, we decided to work with a mono-band antenna targeting the 2.6 GHz band. We design a dipole antenna able to be printed on the side of the plastic box presented above in this chapter. Then the same dipole is shunted and placed behind the original dipole to act as a reflector.

3.4.2.1. Omnidirectional Dipole Design

In order to reduce the fabrication cost of the gateway antenna, a printed version of a dipole is studied with the major advantage of integrating a balun inside the dipole structure itself. This antenna design is very suitable for LDS technology because it presents a very low metallization surface compares to the previous studies antennas which need a ground plane transferred on the plastic.

The layout of the dipole antenna is presented in figure 3-61. The antenna is printed on the polycarbonate substrate of thickness 2 mm, permittivity ε_r = 2.7 and loss tangent tanδ = 0,013. The antenna has a compact size of 25.5x12 mm^2 (λ_0/4xλ_0/10 at 2.6 GHz). The structure is fed by a 50 Ω coaxial cable. The coaxial cable has to be modeled with a sufficient length in order to obtain an accurate result and to stabilize the input impedance around the resonance.

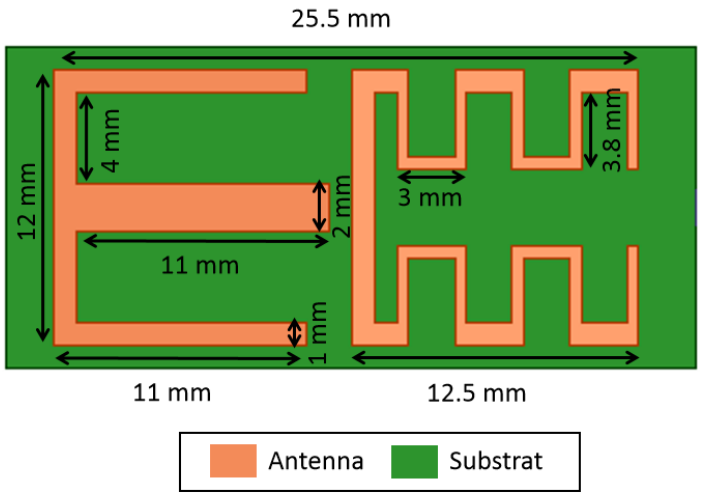

Figure 3-61: Layout of the dipole antenna.

When the correct resonance is identified in the simulation, the structure can be tuned with 2 main parameters. The left arm dipole length is slightly tuning the frequency resonance and the matching. The right arm dipole length has a very large influence on the frequency resonance with a limited impact on the matching. However, considering the small size of the antenna, it needed to be matched with an LC circuit. The matching of the antenna is improved thanks to an inductor and a capacitor welded on the antenna such as presented in figure 3-62. The serial capacitor is represented by the red rectangle while the shunt inductor is represented by the blue rectangle.

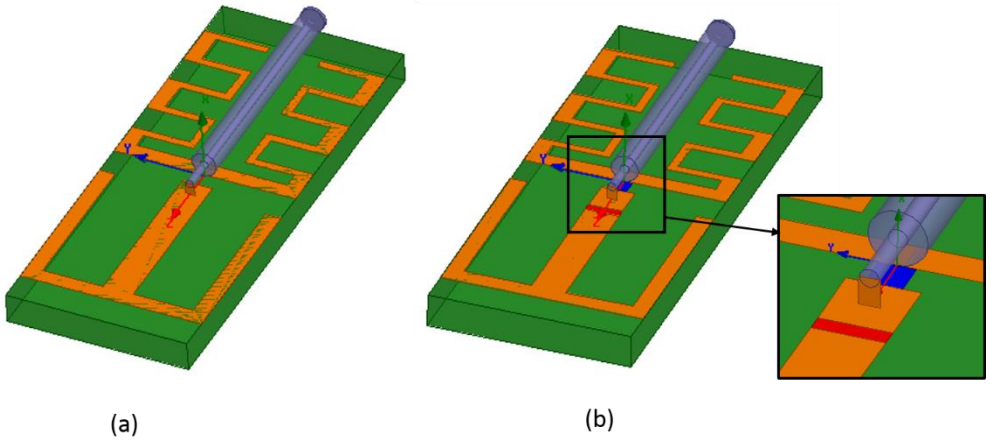

Figure 3-62: Simulated dipole (a) alone and (b) with matching components.

Figure 3-63 presents a smith chart of the reflection coefficient for the antenna alone (blue) and the antenna with the matching circuit (red). The figure also presents the schema of the matching circuit realized to match the antenna. We observe the matching improvement realized thanks to the LC circuit.

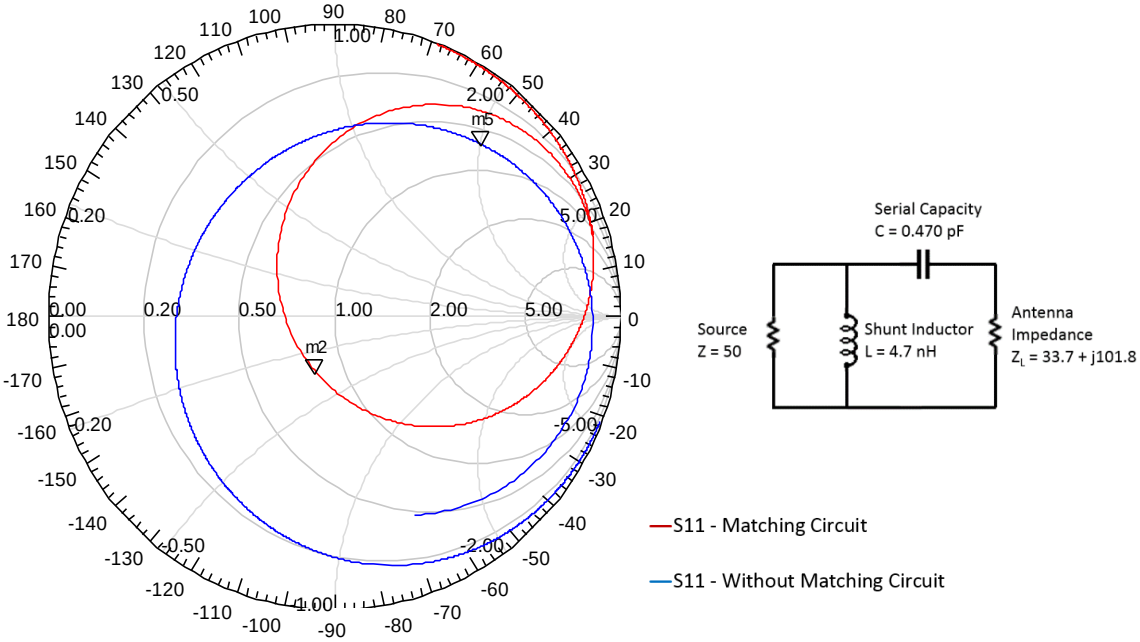

Figure 3-63: Smith chart of the reflection coefficient of the dipole with and without matching circuit.

The return loss of the matched and unmatched configuration of the dipole is presented in figure 3-64. We observe that the dipole is matched at 2.8 GHz. Even if the frequency is a bit higher than the 2.6 GHz targeted frequency, we decided to continue the study with this dipole. Indeed we would need to increase the size of the antenna to get the 2.6 GHz operating frequency.

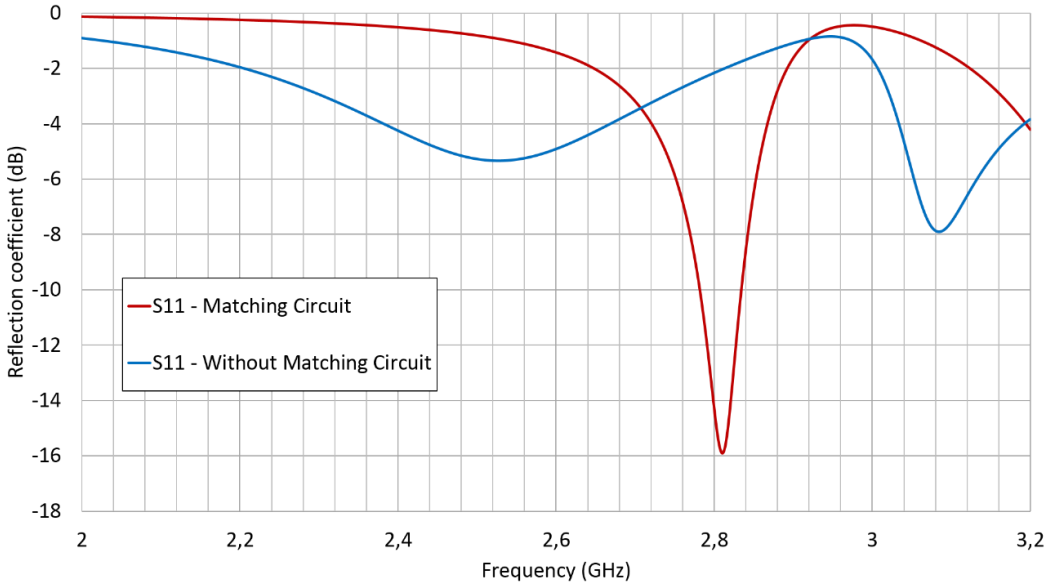

Figure 3-64: Reflection coefficient for the dipole alone and the dipole with matching components.

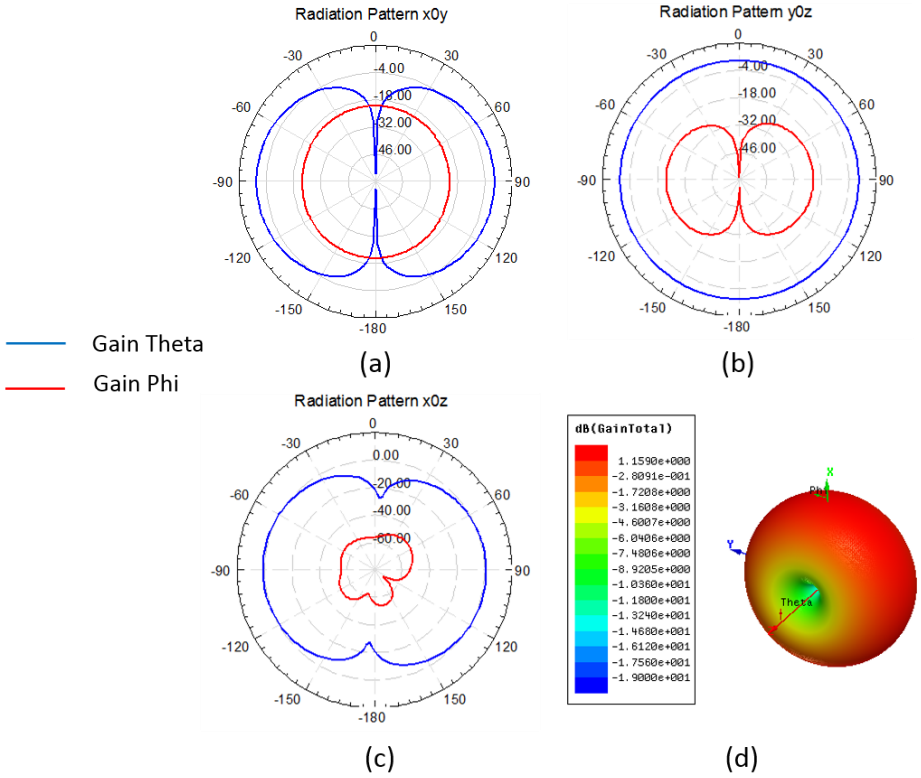

Figure 3-65: Radiation pattern of the dipole antenna in (a) x0y plane for θ = 90°, (b) y0z plane θ = 0°, (c) x0z ϕ = 0° plane and (d) in 3 dimensions.

The simulated radiation pattern is presented in figure 3-65. The figure shows the Gain Theta and Gain Phi in three in the x0y, y0z and x0z plane of the antenna as well as the total gain 3D radiation pattern. We observe that the antenna has a clear omnidirectional radiation pattern with a total gain of 1.1 dB. The simulated Front-to-Back ratio is 0.2 dB.

3.4.2.2. Directive Dipole Design

In order to obatin a directional antenna, we use a reflector located 10 mm behind the antenna. The reflector is design with the same layout than the origanal antenna, but the two branch of the dipole are shunted as presented in the figure 3-66 below. The shunted dipole printed on a thin layer of duroïd(h=0.1 mm), act as a resonnator to focus radiation toward x axis.

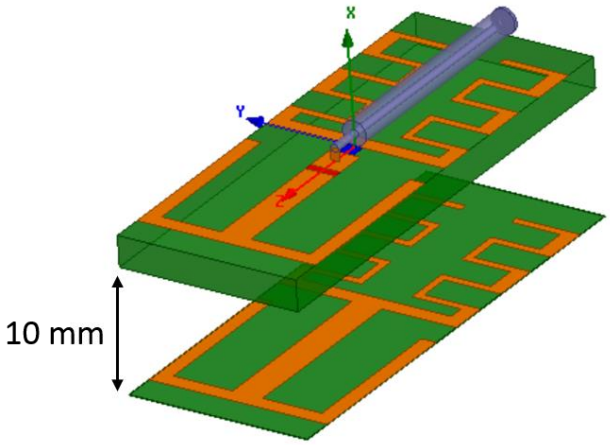

Figure 3-66: Simulated dipole with reflector.

The reflection coefficient presented in figure 3-67 shows a slight mismatch of the antenna. Despite this perturbation, the antenna is matched with a -5 dB criteria at 2.8 GHz.

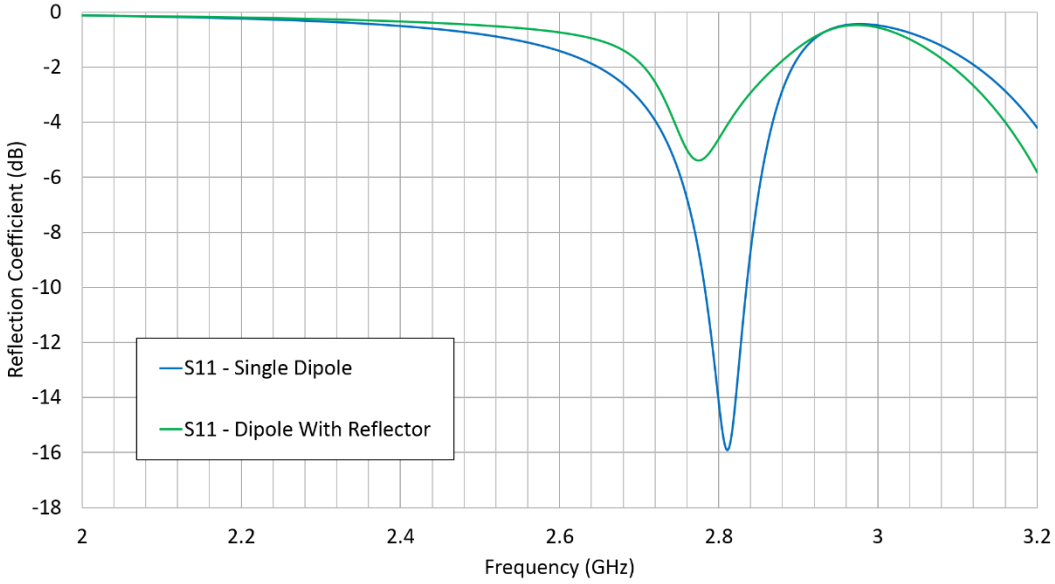

Figure 3-67: Simulated coefficient reflection of the dipole and reflector.

The simulated radiation pattern is presented in figure 3-68. The figure shows the Gain Theta and Gain Phi in three in the x0y, y0z and x0z plane of the antenna as well as the total gain 3D radiation pattern. We observe that the antenna is focused toward the x axis with a total gain of 2.8 dB. The simulated Front-to-Back ratio is 13 dB.

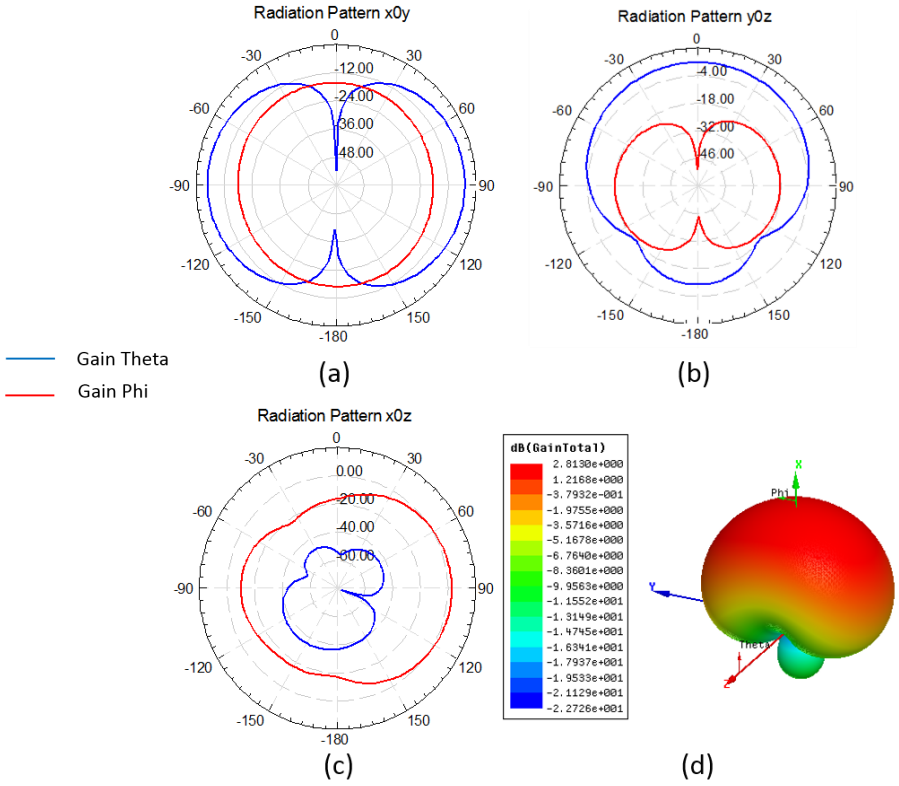

Figure 3-68: Radiation pattern of the dipole antenna in (a) x0y plane for θ = 90°, (b) y0z plane θ = 0°, (c) x0z ϕ = 0° plane and (d) in 3 dimensions.

3.4.2.3. Realization of the 8 dipole antenna prototype

In order to gain some time in the realization of the prototype, we printed 8 antennas on a very thin duroïd substrate. Then we welded the matching components and finally, we connected a 15 cm coaxial cable with each antenna as presented in figure 3-69.

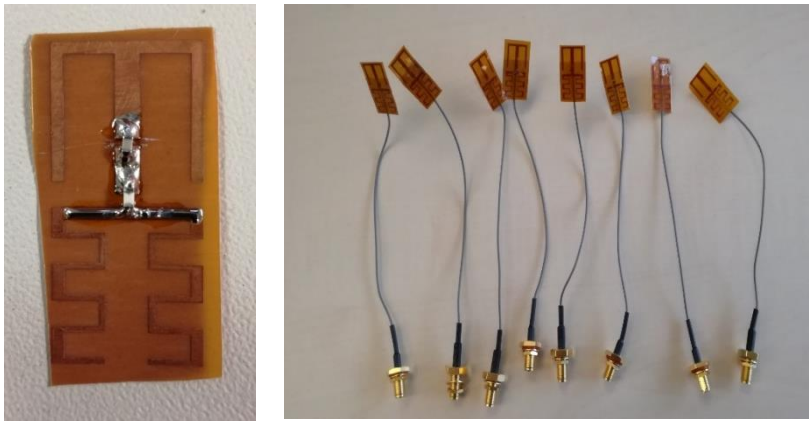

Figure 3-69: Pictures of the antennas realized on the duroïd substrate.

Then we placed the antennas on the external face on the box, fixed with paper adhesive tape. The duroïd layer used to print the antennas is so thin regarding the thickness of the box that it becomes quasi transparent. The figure 3-70 shows a picture of the final realization.

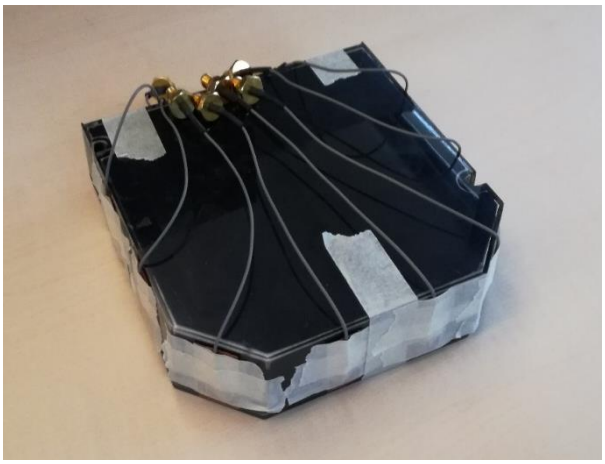

Figure 3-70: Picture of the realized prototype with 8 omnidirectional antennas.

To realize the 8 antenna gateway, we printed 8 resonators shunted with a strip of copper welded on each arm of the dipole. As presented o figure 3-71, a reflector is placed within the box behind each antenna and maintained in position with a 10 mm foam cube and paper adhesive tape. Reflectors are located such as each antenna radiates toward the outside of the box.

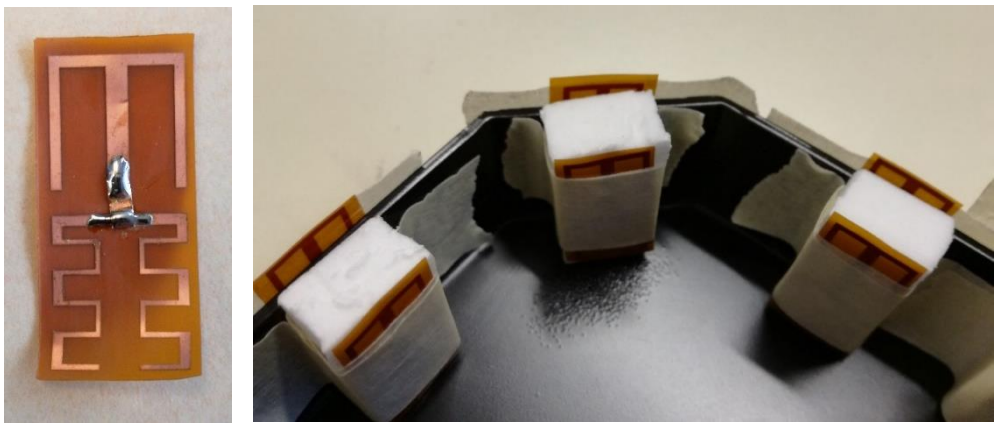

Figure 3-71: Pictures of the reflector placed behind the antenna.

The final realization is presented in figure 3-72. The advantage of this method is that we can easily assemble or disassemble the reflector to switch from an omnidirectional configuration to a directional configuration.

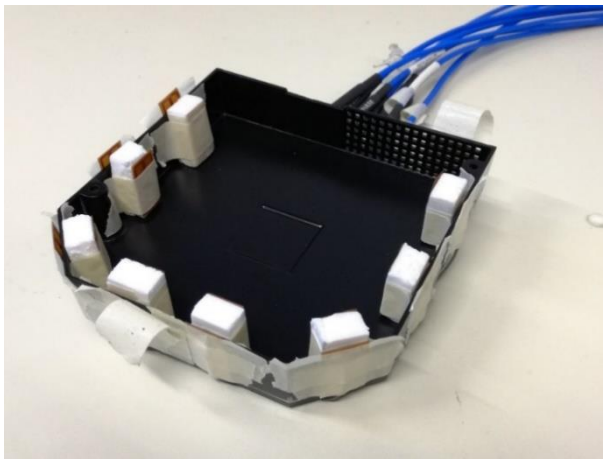

Figure 3-72: Picture of the realized prototype with 8 directional antennas.

The measured reflection coefficient is presented in Figure 3-73 for the omnidirectional configuration and in figure 3-74 for the directional configuration. Both measurements show that each antenna is matched at 2.8 GHz. Return loss for the 8 directional antennas is significantly better than expected in the simulation.

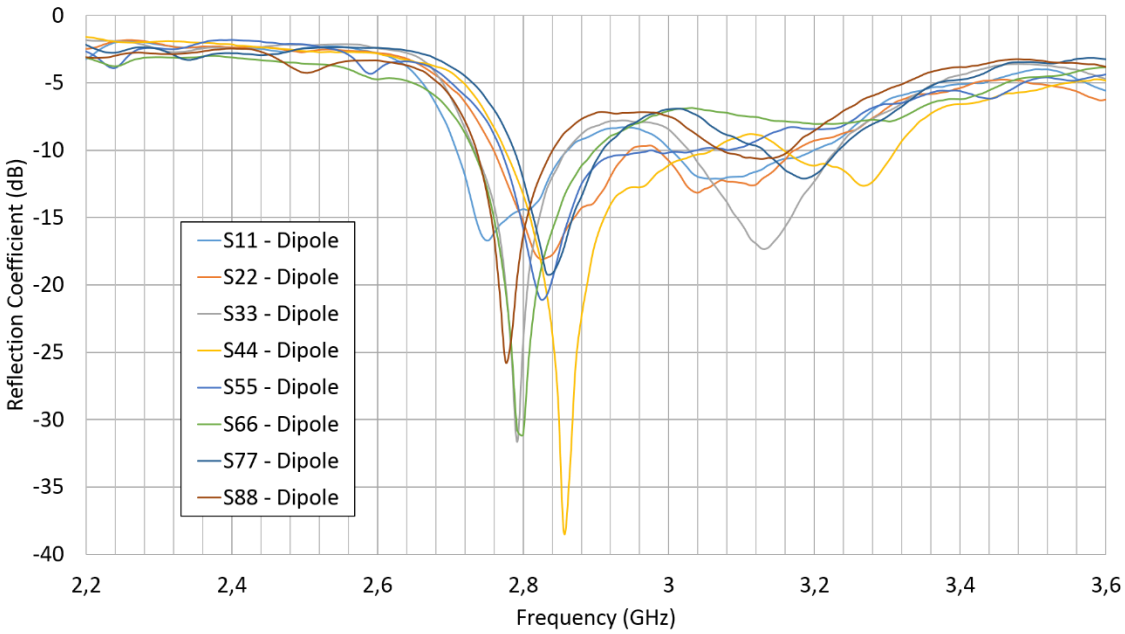

Figure 3-73: Measured reflection coefficient for the 8 omnidirectional antennas.

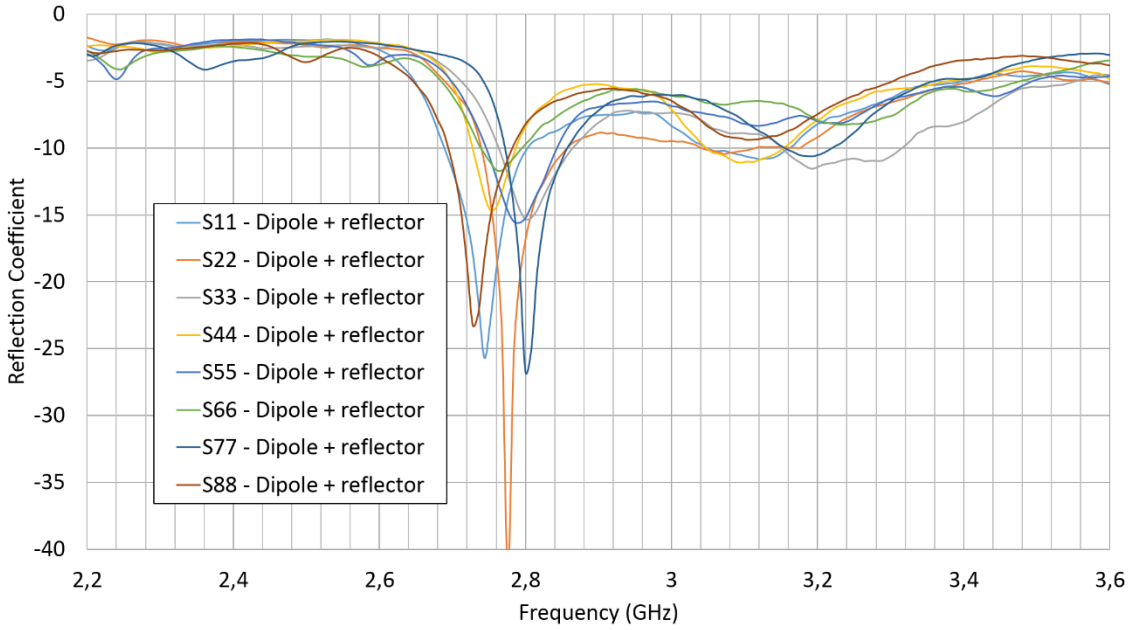

Figure 3-74: Measured reflection coefficient for the 8 directional antennas.

Coupling and ECC between antennas are presented in table 3-14. The table shows that isolation is always higher than 21 dB (antennas 3 and 4) for the omnidirectional dipoles. We measured a minimum of isolation of 27 dB between antennas 3 and 5 for the directional configuration. We notice that the measured isolation for the two configurations is significantly higher than the previously realized prototypes in PCB or LDS technology. The ECC is always below 0.5 in both omnidirectional and directional configuration, with a maximum of 0.252 between antennas 4 and 5 for the single dipole and a maximum of 0.165 between antennas 3 and 5 for the dipole plus reflector configuration. The dipole present an average correlation of 0.059 while the configuration with reflector has an average correlation of 0.025. The correlation is decreased by a factor two when adding the reflector. The measured values of coupling and correlation are suitable for our application.

Table 3-14: Measured worst coupling for the 8 dipole antennas in both configurations.

Antenna	**Single Dipole**		**Dipole + Reflector**	
	Worst Coupling	**Worst ECC**	**Worst Coupling**	**Worst ECC**
N°1	-23.9 (N°2)	0.057	-35.3 (N°4)	0.072
N°2	-23.9 (N°1)	0.128	-39.3 (N°3)	0.072
N°3	-21.9 (N°4)	0.100	-27.6 (N°5)	0.165
N°4	-21.9 (N°3)	0.252	-34.2 (N°3)	0.069
N°5	-23.7 (N°4)	0.252	-27.6 (N°3)	0.165
N°6	-24.2 (N°7)	0.165	-29.4 (N°7)	0.058
N°7	-24.2 (N°6)	0.149	-29.4 (N°6)	0.119
N°8	-25.5 (N°7)	0.149	-30.0 (N°8)	0.119

Radiation measurements are performed for each antenna of the prototype. The table 3-15 below presents the total efficiency and gain for each antenna for both omnidirectional and directional configuration. An average efficiency of -1.51 dB (70%) and -1.90 dB (65%) are obtained respectively in omnidirectional and directional configuration. Each antenna presents an omnidirectional pattern when used alone and a directional pattern matching the simulated one when used with the reflector.

Table 3-15: Gain and efficiency for the 8 dipole antennas in both omnidirectional and directional configurations.

Antenna	Single Dipole		Dipole + Reflector	
	Gain (dB)	Efficiency (dB)	Gain (dB)	Efficiency (dB)
N°1	2.38	-1.16	3.00	-1.68
N°2	2.78	-1.34	4.57	-1.79
N°3	4.12	-1.33	4.75	-1.85
N°4	3.95	-1.19	5.17	-2.16
N°5	3.62	-1.37	4.27	-2.23
N°6	3.76	-1.51	3.60	-1.67
N°7	3.49	-1.44	5.17	-1.36
N°8	3.05	-1.21	3.67	-1.22
Average	3.30	-1.51	4.20	-1.90

Figure 3-75 presents the measured radiation pattern of the antenna 1 in the omnidirectional and directional configuration. We observe that the radiation pattern is indeed focused in half a sphere. The same results are observed for each antenna but are not presented here. The directional antenna presents a Front-To-Back ration of 13 dB.

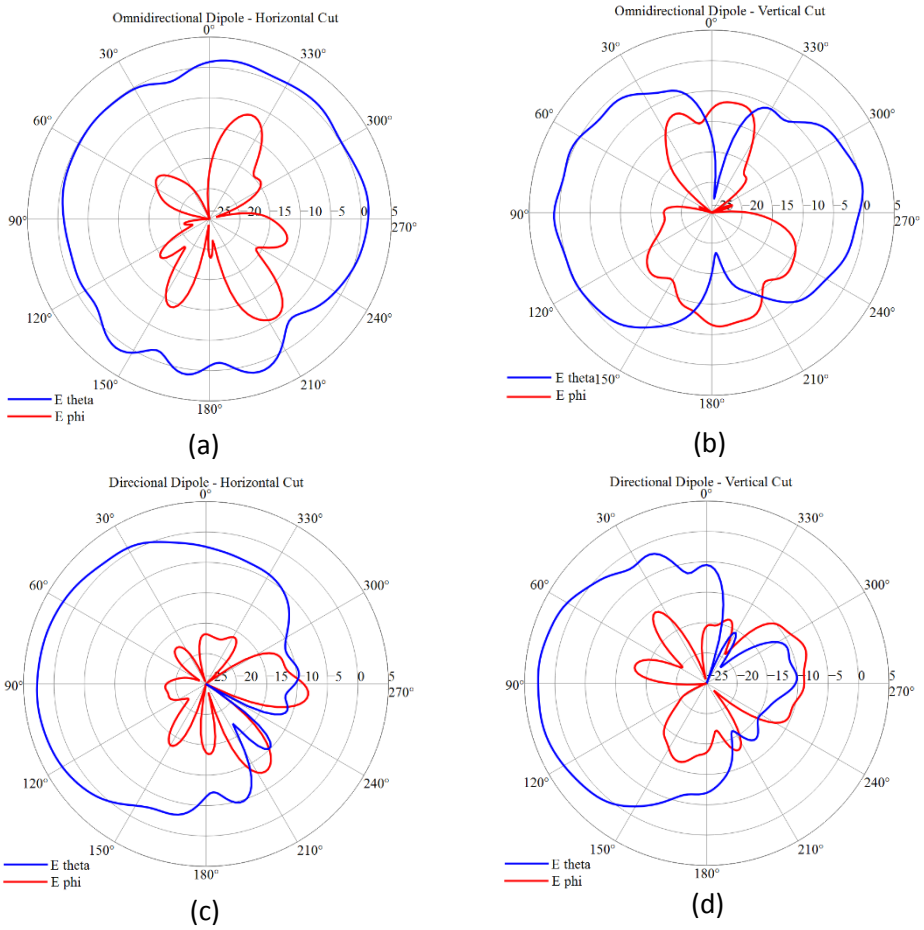

Figure 3-75: Measured radiation pattern for (a), (b) the omnidirectional and (c), (d) directional configuration of the antenna 1 in (a), (c) Horizontal plane theta = 90°, (b), (d) vertical plane phi = 90°.

3.4.2.4. Measurement with OpenAirInterface

In order to investigate the influence of the radiation pattern on the global performance of the multi-antenna system, we tested the prototype with the OAI measurement setup. For this measurement campaign, we use the same configuration previously described. We performed the measurement MISO 8x1 beamforming as well as MISO 4x1 and MISO 2x1 in both adaptive and fixed scheme in LOS and NLOS configurations for 200 positions of the receiver antenna on the rail.

To observe if antennas effectively filter spatially the received signal we tested three positions of the box regarding the Rx antenna. The three positions are illustrated in the figure 3-76. In position 1 antennas n°3, 4, 5 and 6 are facing the receiver while in position 2 it is antennas n°1, 2 and 3 and antennas n°8, 7 and 6 in position 3. Logically, when using the adaptive beamforming scheme in LOS, the antenna selection should favor the use of antennas facing the receiver.

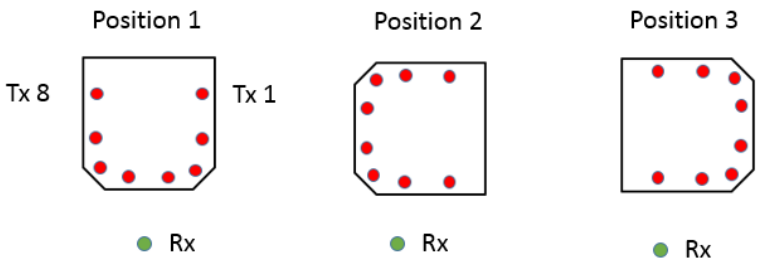

Figure 3-76: Schematic representation of the three tested orientations of the box.

Measurement results are presented in the form of CDF. In the figure 7-77 to 7-82, we compare the performance of the omnidirectional and directional prototype in different measurement configurations. In those figures, the measurements retrieved with the omnidirectional prototype are presented with solid lines while the ones retrieved with the directional prototypes are presented with dotted lines. In each figure, the MISO 8x1 beamforming is presented with green lines, the MISO 4x1 with red lines and the MISO 2x1 with red lines. In the legend of each figure the prototype and position used are referred as “O” for omnidirectional and “D” for directional followed by the prototype position 1, 2 or 3. For example, the adaptive MISO 8x1 beamforming realized with the omnidirectional prototype in position 1 in a LOS configuration is referred as “O1 – LOS – Adapt MISO 8x1”.

Figures 3-77 to 3-79 present the measurement results respectively for position 1, 2 and 3 in a LOS configuration. In positions 1 and 3 we observe that both prototypes achieve the same level of performance while the omnidirectional prototype achieves better performance in the position 2 with an average 5 dB increase on the measured SNR. The measurement results for position 1, 2 and 3 in an NLOS configuration are presented respectively in figure 3-80, 3-81 and 3-82. In positions 1, the omnidirectional prototype tends to be better with an average increase of 2 dB on the SNR. The results retrieved in position 2 tend to confirm the last observation with an average increase of 5 dB on the SNR measured with the omnidirectional prototype. Finally, in position 3, we observe that both prototypes achieve almost the same level of performance. However, the directional prototype which presents slightly better results with around 1 dB increase on the measured SNR In MISO 8x1 and MISO 4x1 configuration.

From those results, it seems difficult to draw a clear conclusion. The propagation conditions might be favorable for the omnidirectional prototype in position 2 whereas they seem more favorable to the directional prototype in position 3. In order to bring more insight to the analysis, we observed the measurements results obtained with a fixed beamforming scheme. In this configuration, antenna 4 and 5 are used for MISO 2x1 and antennas 3, 4, 5 and 6 for MISO 4x1 no matter what configuration or

orientation of the box. The results are not presented here. Nevertheless, both prototypes present exactly the same behavior than with adaptive beamforming for each position. Indeed both prototypes achieve similar results in position 1 with only a 2 dB increase for the MISO 8x1 with the omnidirectional prototype in NLOS. In position 2, the omnidirectional prototype is significantly better with 5 dB increase in LOS and 6 dB in NLOS. The directional prototype works better is position 3 with a 2 dB increase in NLOS.

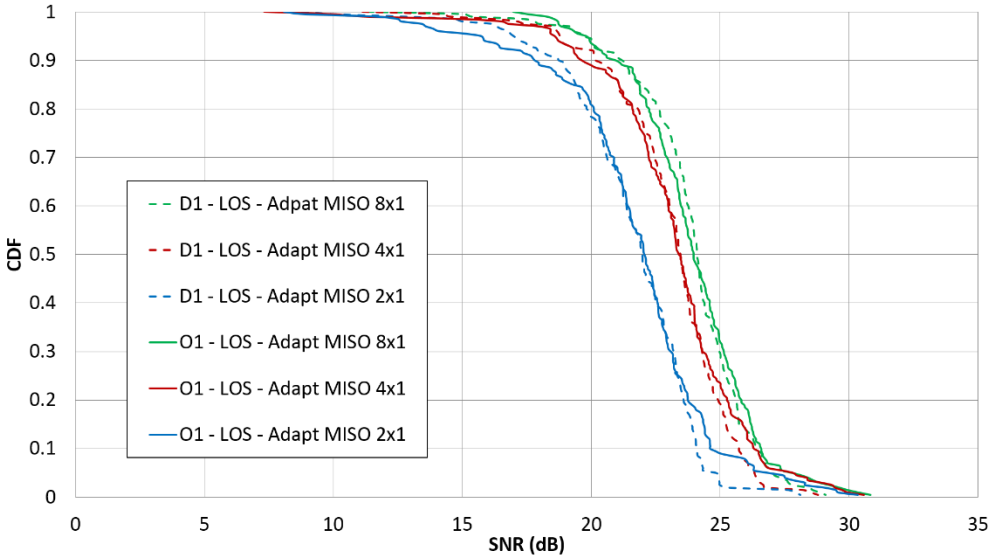

Figure 3-77: CDF of the measured SNR on the directional and omnidirectional prototypes in position 1 for a LOS configuration.

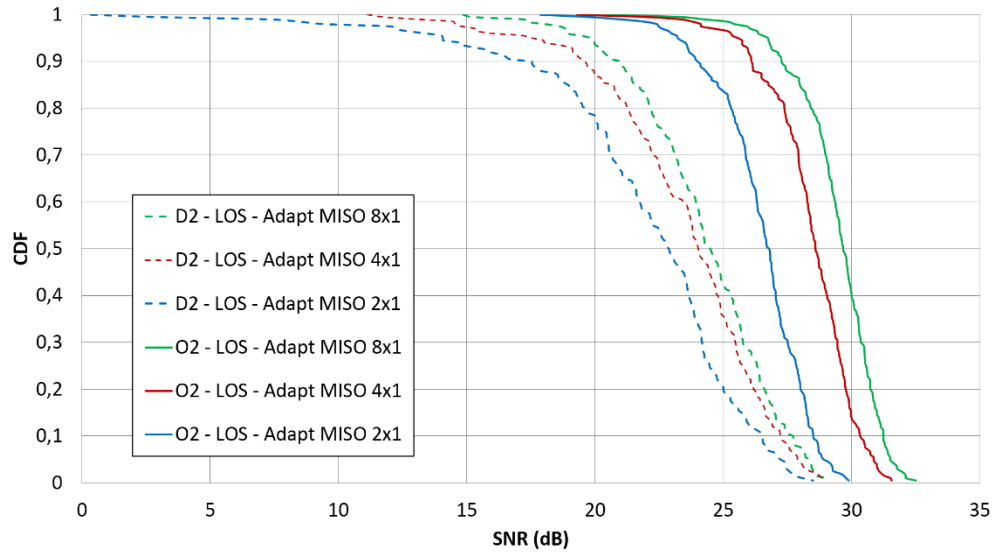

Figure 3-78: CDF of the measured SNR on the directional and omnidirectional prototypes in position 2 for a LOS configuration.

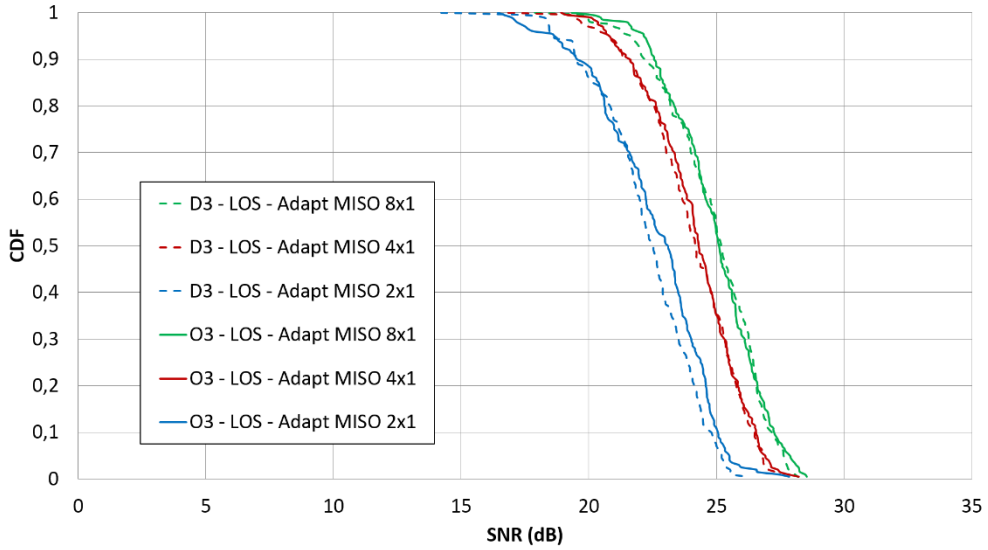

Figure 3-79: CDF of the measured SNR on the directional and omnidirectional prototypes in position 3 for a LOS configuration.

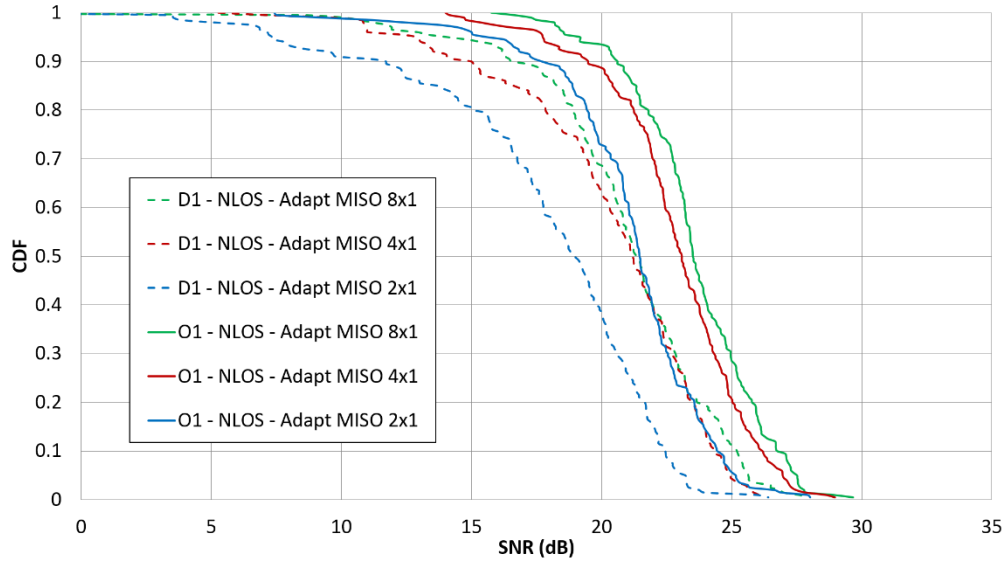

Figure 3-80: CDF of the measured SNR on the directional and omnidirectional prototypes in position 1 for a NLOS configuration.

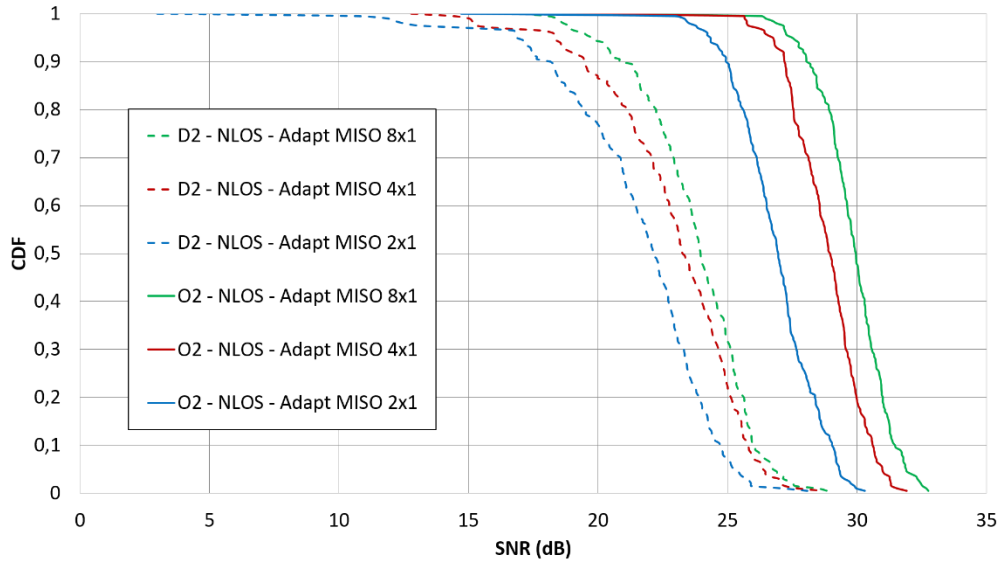

Figure 3-81: CDF of the measured SNR on the directional and omnidirectional prototypes in position 2 for a NLOS configuration.

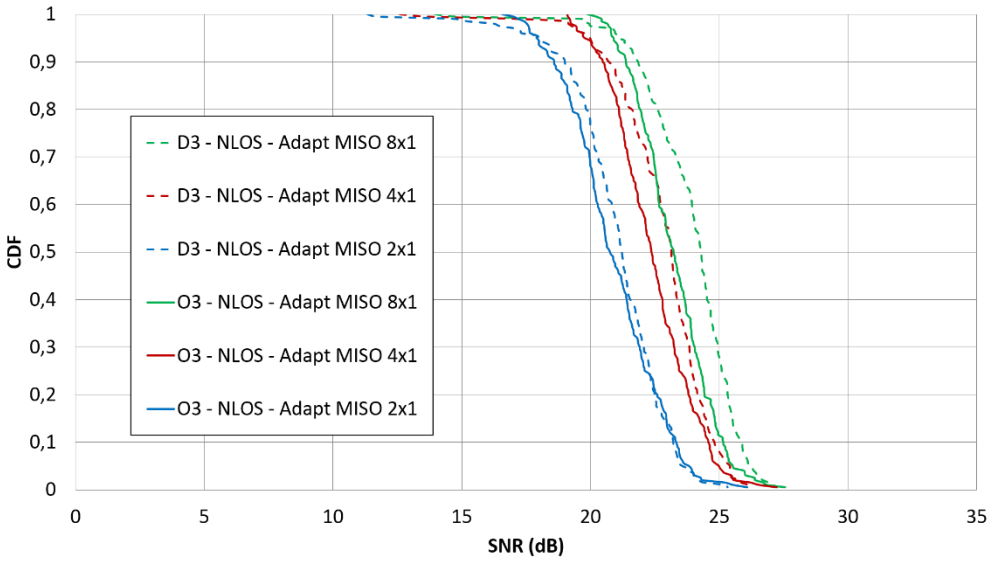

Figure 3-82: CDF of the measured SNR on the directional and omnidirectional prototypes in position 3 for a NLOS configuration.

In order to observe if a form of spatial filtering is achieved with the directive prototype, we observe which antennas have been selected with the adaptive beamforming scheme in each position. The figure 3-83 summarize the number of utilization for each antenna for the MISO 4x1 beamforming in every tested configuration. The position 1 in presented in green, the 2 in blue and the 3 in red while the LOS is presented with solid sticks and the NLOS with hatched sticks. Unfortunately, we can't notice a pattern regarding the antenna selection. The adaptive beamforming doesn't seem to favor the transmitting antennas facing the receiving antenna.

Number of usage per antenna in the LOS and NLOS configuration with the adaptive beamforming scheme.

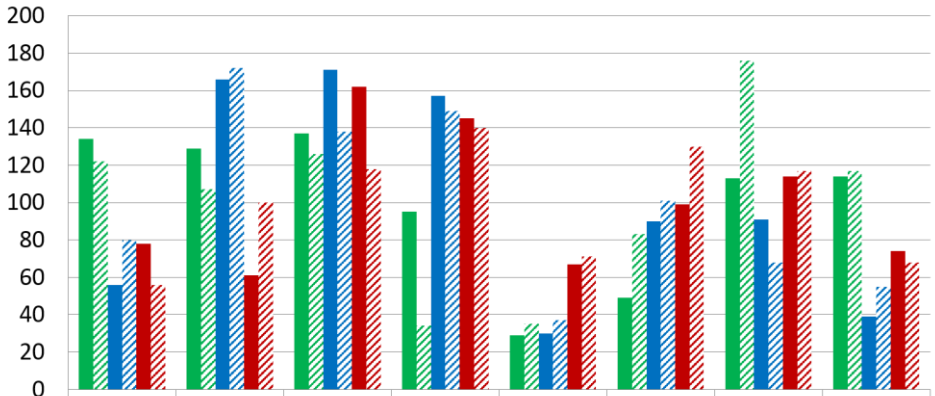

	Antenna 1	Antenna 2	Antenna 3	Antenna 4	Antenna 5	Antenna 6	Antenna 7	Antenna 8
D1 - LOS - Index MISO 4x1	134	129	137	95	29	49	113	114
D1 - NLOS - Index MISO 4x1	122	107	126	34	35	83	176	117
D2 - LOS - Index MISO 4x1	56	166	171	157	30	90	91	39
D2 - NLOS - Index MISO 4x1	80	172	138	149	37	101	68	55
D3 - LOS - Index MISO 4x1	78	61	162	145	67	99	114	74
D3 - NLOS - Index MISO 4x1	56	100	118	140	71	130	117	68

Figure 3-83: Number of usage per antenna in MISO 4x1 configuration in both LOS and NLOS with the directional prototype.

In the last attempt to extract reliable conclusions, we performed on more set of measurement in a fourth position. For this experiment, we located the gateway outside the room, with the same orientation than in position 1 but with a 20 cm wall between transmitting and receiving antenna. We performed measurement with both prototypes with the fixed and adaptive beamforming scheme.

Figure 3-84 presents the results for the adaptive beamforming and figure 3-85 for the fixed beamforming scheme. In both configurations, the directional prototype presents the better performance.

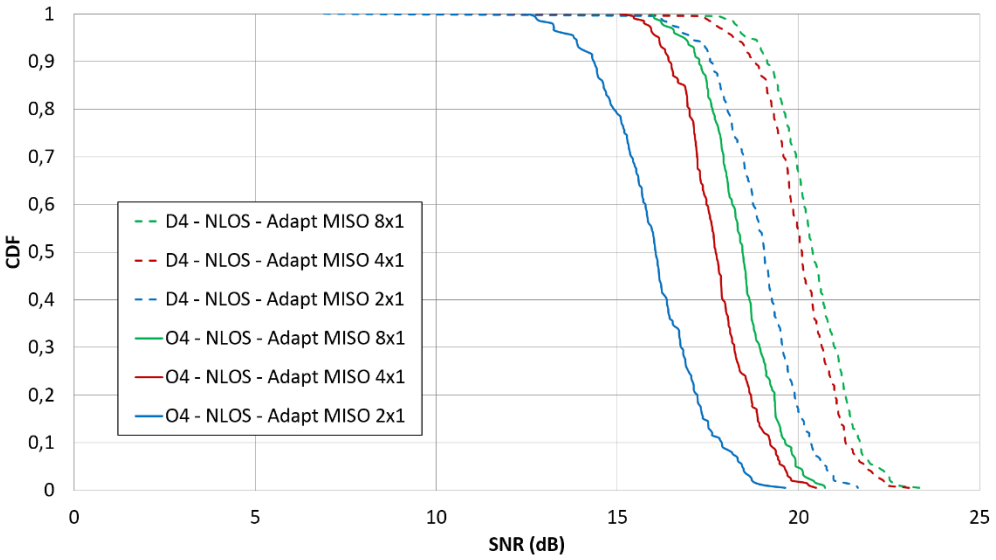

Figure 3-84: CDF of the measured SNR on the directional and omnidirectional prototypes in position 4 for the adaptive beamforming scheme.

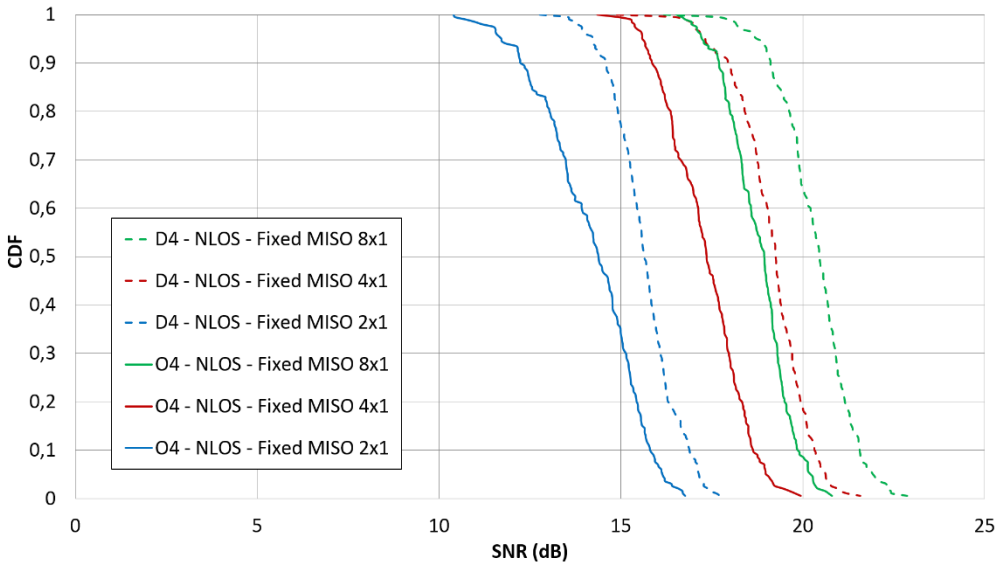

Figure 3-85: CDF of the measured SNR on the directional and omnidirectional prototypes in position 4 for the fixed beamforming scheme.

Regarding the whole results of this study, it is still difficult to draw a clear conclusion. However, the directivity improvement on antennas has shown some interesting capabilities to enhance the performance of the multi-antenna gateway. In order to bring more clarity to the study, much more measurements should be realized, especially with different location of the gateway. The reliability of the prototype might be improved by definitely printing antennas on the box with LDS technology. Moreover, a more controlled environment could improve the method accuracy.

3.5. Conclusion and perspectives

In this chapter, we studied different antenna configuration and implementation within a multi-antenna gateway. In a first time, we design a set of 8-antenna prototypes on PCB technology and LDS technology. We compared the antenna performance by performing a set of free-space measurement with a VNA and a Satimo StarLab. The performance of the gateways has been studied as a system thanks to the OAI measurement setup. The results have shown the benefits of LDS technology thanks to the improvement brought on antennas efficiency and gain. Moreover, antenna selection has been implemented in the OAI setup and has shown interesting results. Indeed we demonstrated that a MISO 4x1 beamforming performed with antenna selection achieve quasi equivalent performance than a MISO 8x1.

In a second time, we explore directional antenna and their influence on the performance of multi-antenna gateway. We realized an omnidirectional dipole convertible to a directional dipole thanks to a reflector. Free-space measurement has shown good results in gain and efficiency. Both omnidirectional and directional prototype have been measured with OAI setup. Despite a high number of measurement, we were not able to draw a very clear conclusion on any improvement brought by the antenna directivity. More experiments should be conducted to sharpen the conclusions. Nevertheless, an important point to observe is that depending on the gateway orientation we often observe that one configuration provides better performance than the other. An interesting perspective would be to test a hybrid configuration mixing omnidirectional and directional antenna.

To go further, we intend to use a commercial smartphone as UE, since OpenAirInterface is a 3GPP LTE compliant platform. Moreover, the open-source aspect of OAI allows the development of various algorithms to test more scenarios such as MU-MIMO or carrier aggregation. OAI will be capable of accommodating various communication protocols without additional hardware.

3.6. References

[III-1] J.-M. Floch, B. El Jaafari, and A. E. S. Ahmed, "New Compact Broadband GSM/UMTS/LTE Antenna Realised by 3D Printing," 9th European Conf. Antennas Propag. (EuCAP), Lisbon, Portugal, May 13-17, 2015.

[III-2] W. Y. Li, W. Chung, T. H. Kao, M. C. Huang and M. T. Hong, "Novel 11 GHz 2-port antenna array integrated at a corner of mobile phone casing by LIM technologies of ITRI with diverse end-fire radiation patterns," 2015 IEEE International Symposium on Antennas and Propagation & USNC/URSI National Radio Science Meeting, Vancouver, BC, 2015, pp. 1530-1531.

[III-3] F. Sonnerat, R. Pilard, F. Gianesello, F. Le Pennec, C. Person and D. Gloria, "Innovative LDS antenna for 4G applications," Antennas and Propagation (EuCAP), 2013 7th European Conference on, Gothenburg, 2013, pp. 2773-2776.

[III-4] http://www.s-2p.com/temp/fr/technologies/laser-direct-structuring-lds/.

[III-5] L. Zheng and D. Tse, "Diversity and multiplexing: A fundamental tradeoff in multiple-antenna channels," IEEE Trans. Inf. Theory, vol. 49, no. 5, pp. 1073-1096, May 2003.

[III-6] I. E. Telatar, "Capacity of multi-antenna gaussian channels," *Europ. Trans. Telecommu.*, vol. 10, pp. 585-595, Nov./Dec. 1999.

[III-7] I. Salonen I. and P. Vainikainen, "Estimation of Signal Correlation in Antenna Arrays," JINA Int. Symp. Antennas, Vol. 2,2002, pp. 383-386.

[III-8] Diallo, Aliou & Luxey, Cyril & Le Thuc, Philippe & Staraj, R & Kossiavas, G. (2007). Conception et analyse en diversité de systèmes multi-antennes pour téléphones mobiles UMTS.

[III-9] A. Derneryd and G. Kristensson, "Signal correlation including antenna coupling," in ***Electronics Letters***, vol. 40, no. 3, pp. 157-159, 5 Feb. 2004.

[III-10] Svantesson, T., Ranheim, A.: `Mutual coupling effects on the capacity of multielement antenna systems,' Proc. of IEEE Int. Conf. on Acoustics, Speech, and Signal Processing, 2001, Salt Lake City, UT, USA, p. 2485–2488.

[III-11] Kildal P-S.and Rosengren K., "Correlation and Capacity of MIMO Systems and Mutual Coupling, Radiation Efficiency, and Diversity Gain of their antennas: Simulations and Measurements in a Reverberation Chamber," IEEE Communications Magazine, Vol. 42, N°12, pp.104-112, Dec. 2004.

[III-12] Avendal, Johan; Ying, Zhinong; Lau, Buon Kiong, " Multiband diversity antenna performance study for mobile phones" in International Workshop on Antenna Technology: Small and Smart Antennas Metamaterials and Applications, 2007. IWAT '07.

[III-13] D. Tse et P. Viswanath, Fundamentals of Wireless Communication. Cambridge University Press, 2005.

[III-14] C. C. Chiau, «Study of the diversity antenna array for the MIMO wireless communication systems,» Department of Electronic Engineering Queen Mary, University of London United Kingdom, 2006.

[III-15] P. F. R. Piechocki, «Performance of space-time coding with HIPERLAN/2 and IEEE 802.11a WLAN standards on real channels », p. 848 - 852 vol.2, 2001.

[III-16] S. Alamouti, « A simple transmit diversity technique for wireless communications,» IEEE Journal on Selected Areas in Communications, vol. 16, no. 8, p. 1451-1458, 1998.

[III-17] Petri Isomäki, Jouni Isoaho, « On diversity combining,» TUCS Technical Report No 884, April 2008.

[III-18] Bin Guo, “Antenna Diversity in Mobile Phones,” Antenna Group, Department of signals and systems, Chalmers University of Technology. Gothenburg, Sweden. January 2008.

[III-19] M. Hélard, E. Hardouin, T. Sälzer, “White Paper MIMO.” Orange. 2013.

[III-20] Commscope, White Paper “What base station antenna configuration is best for LTE-Advanced?” 2012.

[III-21] E. G. Larsson, O. Edfors, F. Tufvesson, and T. L. Marzetta, "Massive MIMO for next generation wireless systems," in ***IEEE Communications Magazine***, vol. 52, no. 2, pp. 186-195, February 2014.

[III-22] X. Jiang, M. Cirkic, F. Kaltenberger, E. G. Larsson, L. Deneire and R. Knopp, "MIMO-TDD reciprocity under hardware imbalances: Experimental results," 2015 IEEE International Conference on Communications (ICC), London, 2015, pp. 4949-4953.

[III-23] F. Rusek, D. Persson, B. K. Lau, E. G. Larsson, T. L. Marzetta, O. Edfors, and F. Tufvesson, “Scaling up MIMO: Opportunities and challenges with very large arrays” IEEE Signal Process. Mag., vol. 30, no. 1, pp. 4046, Jan. 2013.

[III-24] S. Malkowsky ***et al.***, "The World’s First Real-Time Testbed for Massive MIMO: Design, Implementation, and Validation," in ***IEEE Access***, vol. 5, pp. 9073-9088, 2017.

[III-25] H. Yang and T. L. Marzetta, “Performance of conjugate and zero-forcing beamforming in large-scale antenna systems,” IEEE J. Sel. Areas Commun., vol. 31, no. 2, pp. 172–179, Feb. 2013.

[III-26] H. Q. Ngo, E. G. Larsson, and T. L. Marzetta, “Energy and Spectral Efficiency of Very Large Multiuser MIMO Systems,” IEEE Transactions on Communications, vol. 61, no. 4, pp. 1436–1449, Apr 2013

[III-27] A. F. Molisch, « MIMO systems with antenna selection - an overview », in Radio and Wireless Conference, 2003. RAWCON ’03. Proceedings, 2003, p. 167-170.

[III-28] Andreas F.Molish, Neelesh B.Mehta, Hongyuan Zhang, Peter Almers and Jinyun Zhang, “On Implemetation Aspects of Antenna Selection for MIMO Systems” IEEE Invited Paper

[III-29] R.Nabar, D.Gore, and A.Paulraj, “Selection and use of optimal transmit antennas in wireless systems” in Proc. Int. Con5 Telecomtn. (ICT), (Acapulco), IEEE, 2000.

[III-30] D.Gore, R.Nabar, and A.Paulraj, “Selection of an optimal set of transmit antennas for a low rank matrix channel,” in ICASSP 2000.

4. MIMO Antenna Design beyond 6 GHz for Hand effect Investigation on Handset Devices

Table of content Chapter 4

4.1. Evolution and Challenges for mobile devices toward 5G 126
4.1.1. Millimeter-Wave Antenna for 5G Handset Devices 126
4.1.2. User Effect and Body Loss below 6 GHz 128
4.1.3. User Effect and body Loss beyond 6 GHz 129
4.2. Measurement Setup for hand effect investigation 130
4.3. Preliminary study a with 11 GHz Prototype 131
4.3.1. Single Antenna structure and dimensions 132
4.3.2. Mobile Phone Prototype at 11 GHz 133
4.3.3. Hand effect Measurement 133
4.3.4. Conclusion of the study at 11 GHz 137
4.4. Advanced study with a 15 GHz Prototype 138
4.4.1. Single Antenna structure and dimensions 138
4.4.2. Mobile Phone Prototype at 15 GHz 139
4.4.3. Free Space Measurement 141
4.4.4. Beamforming Computation 147
4.4.5. Measurement with hand effect 153
4.4.6. Beamforming Computation with Hand Effect 160
4.4.7. Conclusion of the study at 15 GHz 165
4.5. Conclusion and Perspectives 165
4.6. References for chapter 4 167

This chapter presents the assessment of the hand effect on high frequency antennas for future 5G mobile phones. The study aims to evaluate the negative impact on beamforming capabilities due to user's hand for frequencies above 10 GHz. A 3D spherical near field scanner with a fixed AUT is leveraged to measure the 3D radiation pattern with a real human hand impact. Antenna performance in term of S-parameters, radiation pattern and efficiency are presented.

As a preliminary study, we designed the first prototype at 11 GHz to measure the impact of a real human hand on a single antenna. This band was chosen according to several studies on handset devices at 11 GHz. We also investigate the liability of a phantom hand in those frequencies. Then to deal with this topic in depth, we designed a second prototype at 15 GHz enabling to perform beamforming measurements. We couldn't perform measurements at 28 GHz because we didn't possess the suitable equipment for this frequency. The main originality of our approach lays in the fact that we can use a real hand for the measurement of the amplitude and phase of the radiating fields.

4.1. Evolution and Challenges for mobile devices toward 5G

4.1.1. Millimeter-Wave Antenna for 5G Handset Devices

The fast increase of the telecommunication traffic nowadays and for the years to come drives the industry to investigate new solutions to improve network capacity. The future 5G network aims to provide a solution to the ten time increase prediction of the mobile data traffic [IV-1]. The network capacity can be raised by increasing the network density, the spectral efficiency and the spectrum bandwidth [IV-2], [IV-3]. To address these issues, at the antenna level the two main technologies that are investigated are Multiple Input Multiple Output (MIMO) techniques and centimeter and millimeter waves (mmWave) antennas. Indeed it is known that centimeters and millimeters wave antennas offer larger bandwidth compared to the crowded sub-6GHz spectrum, which makes them good candidates for future networks. An important benefit dealing with high frequency antennas is the miniaturization, which allows easier integration of multiple antennas in a terminal. However, mmWave antennas come with higher path loss in the channel as can be seen in the well-known Friis' formula:

$$P_R = P_T + G_T + G_R + 20\log\left(\frac{c}{4\pi R f}\right). \qquad \text{eq. [4-1]}$$

In this equation, $P_{R,T}$ and $G_{R,T}$ are respectively the power and gain for receiving and transmitting antenna, c the speed of light, R the distance between the receiver and transmitter and f the carrier frequency. In order to balance this higher path loss without increasing P_T, the antenna gains in handset terminals and base stations need to be much higher than in current sub-6 GHz mobile phones. Achieving a higher gain and reaching a higher range can be realized by using antenna array and beamforming technique. The narrowed beam resulting from the increased gain has to be compensated by the beam-steering algorithm introduced by the phased array configuration. Indeed the phased array allows, by controlling the phase and amplitude of each antenna, the generation of a radiation pattern pointing towards a specific direction, thus enabling the system to receive the incoming signal from different angles [IV-4].

The steering angle range being limited, it is mandatory to cleverly think the antenna implementation on the handset device in order to achieve a good complete scan pattern and good coverage efficiency [IV-5]. Several studies have presented terminal antennas designed to highlight the importance of the antenna implementation and the coverage at 11 GHz and 13 GHz bands [IV-6]. In [IV-7] different topologies of high-gain steerable antenna array at mmWave frequencies are presented along with their total scan pattern and coverage efficiency. The feasibility of a low profile 28 GHz beam steering solution with high peak gain for handset device is also demonstrated in [IV-8], [IV-9] and [IV-10] with various antenna designs. Figure 4-1 presents as an example one of those solutions.

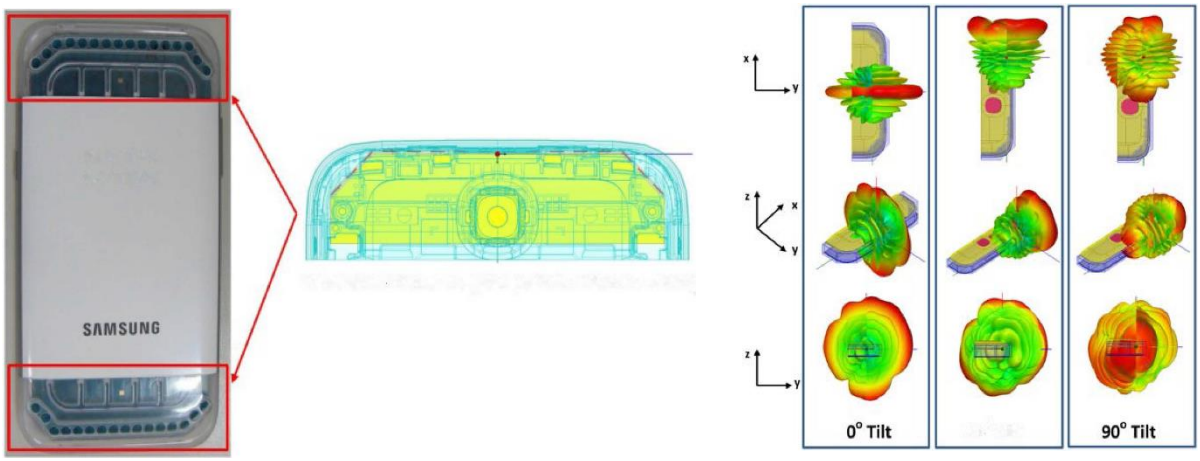

Figure 4-1: Design and analysis of a low-profile 28 GHz beam-steering antenna solution [IV-8].

4.1.2. User Effect and Body Loss below 6 GHz

It is known that handset devices are strongly impacted by user's blockage below 6 GHz. The influence of the hand depends on the antenna position in relation to user's hand and the operating frequency. For instance, in [IV-11], more than 6 dB body loss have been measured on an antenna below 1 GHz. In the sub-6GHz bands, the hand effect is mainly disturbing and absorbing the antenna near field leading to an overall decreased in the antenna efficiency that is very hard to compensate. In [IV-12] the user effect is investigated on a phased array for mobile terminals at 3.5 GHz revealing a 5 dB body loss as shown in Figure 4-2. Different phased array configurations are studied showing that antenna implementation can minimize the loss in terms of coverage efficiency and scanning angles. The interaction between the user hand and a MIMO antenna array below 6 GHz is presented for different scenarios in [IV-13] and [IV-14]. The study reveals a decrease of the total efficiency and a deterioration of the diversity gain for the higher bands at 5 GHz. However, at low frequencies, the article highlights a reduction of the envelope correlation resulting in enhancement of the diversity gain and the multiplexing efficiency. The impedance variation and efficiency reduction have been simulated in [IV-15] for different hand textures and positions. In [IV-16] and [IV-17], by studying different grip style, it is shown that human hand is the main cause for absorption and mismatch losses and that the position of the hand strongly affects radiation efficiency and causes radiation pattern deterioration.

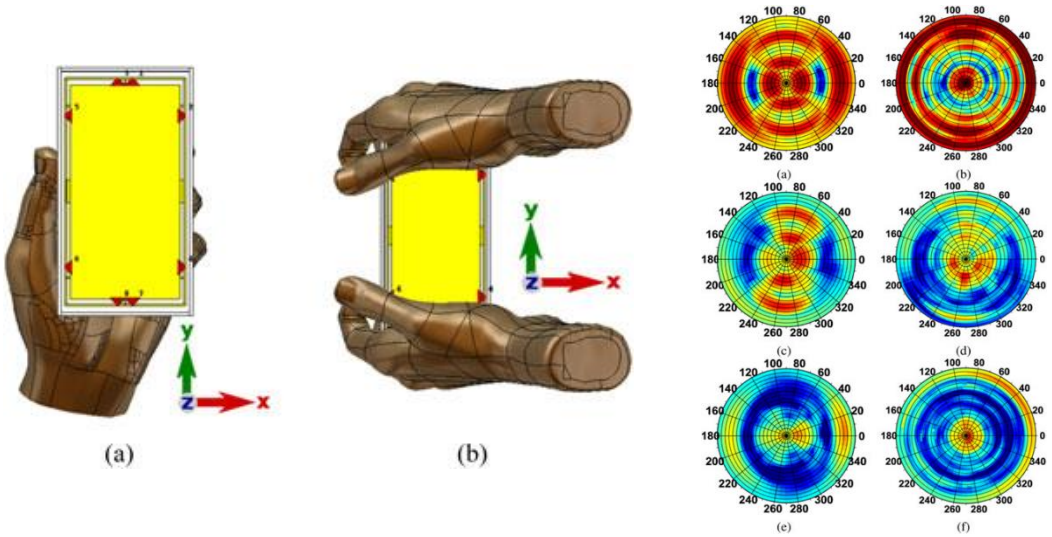

Figure 4-2: Performance investigation of a mobile terminal phased array with user effect at 3.5 GHz [IV-12].

4.1.3. User Effect and body Loss beyond 6 GHz

If the impact of the body has been deeply studied in low frequency, this topic just started being addressed at higher frequencies. This effect is quite different in centimeter and millimeter wave because of the reduced antenna size. The hand mainly masks some local areas, meaning that this effect could be mitigated with a smart positioning of the antenna. Indeed, in [IV-18] represented in the Figure 4-3, the simulated 28 GHz antenna array suffers a 9.5 dB decrease in gain when a finger is positioned above the antenna and the author claim that more losses are expected when the user's hand fully covers the antenna region. In [IV-19], a measurement campaign is performed on a 15 GHz User Equipment (UE) for 5G mm-Wave communication system. Based on measured and calculated results, they present a shadowing effect around 20 to 25 dB at 15 GHz with a decrease of the coverage efficiency around 30%. Finally, in [IV-20], a measurement campaign has been led on a 28 GHz handset terminal with 12 different users to investigate the body impact on a 5G UE statistically. The paper focuses on only one antenna, speculating that the behavior of an antenna array could be accurately predicted from the performance of one antenna element.

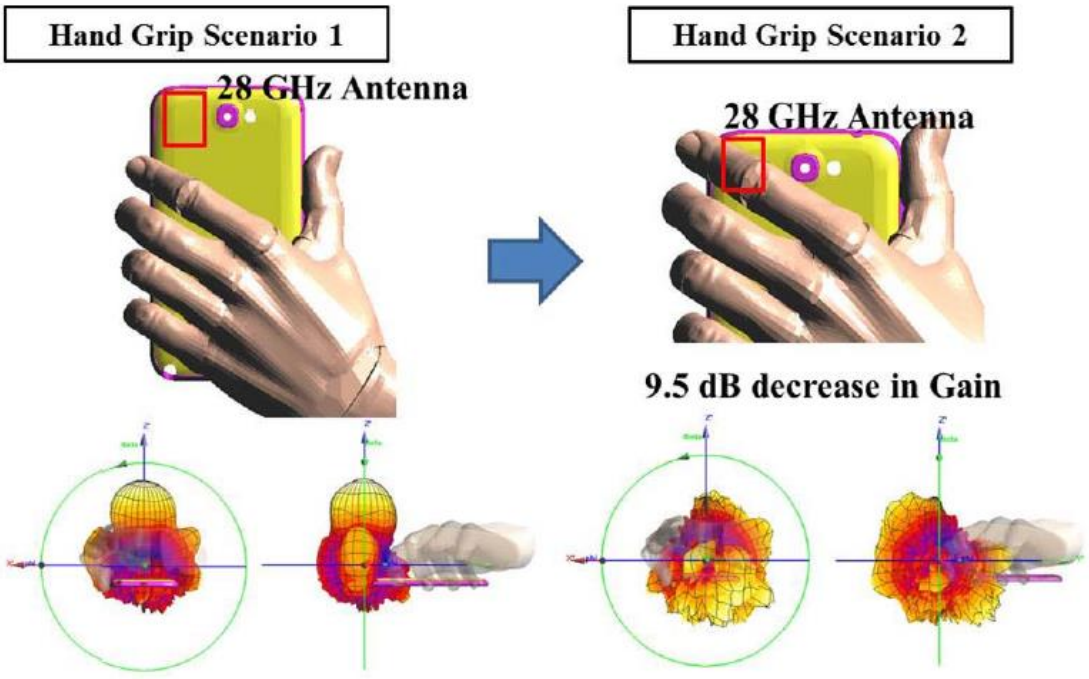

Figure 4-3: mmWave phased array for 5th generation cellular handset [IV-18].

Studies have clearly shown that human body dielectric properties vary along with frequency [IV-21]. The variations of relative permittivity and dielectric loss between 1 GHz and 20 GHz are presented in Figure 4-4 for human skin, blood, and bones. The first observation is that the dielectric

loss doubles in the high frequency bands. Secondly, we observe a 50% decrease in the permittivity value between 1 and 20 GHz. This clearly demonstrates that models used for body phantom below 3 GHz are not suitable for frequencies higher than 10 GHz.

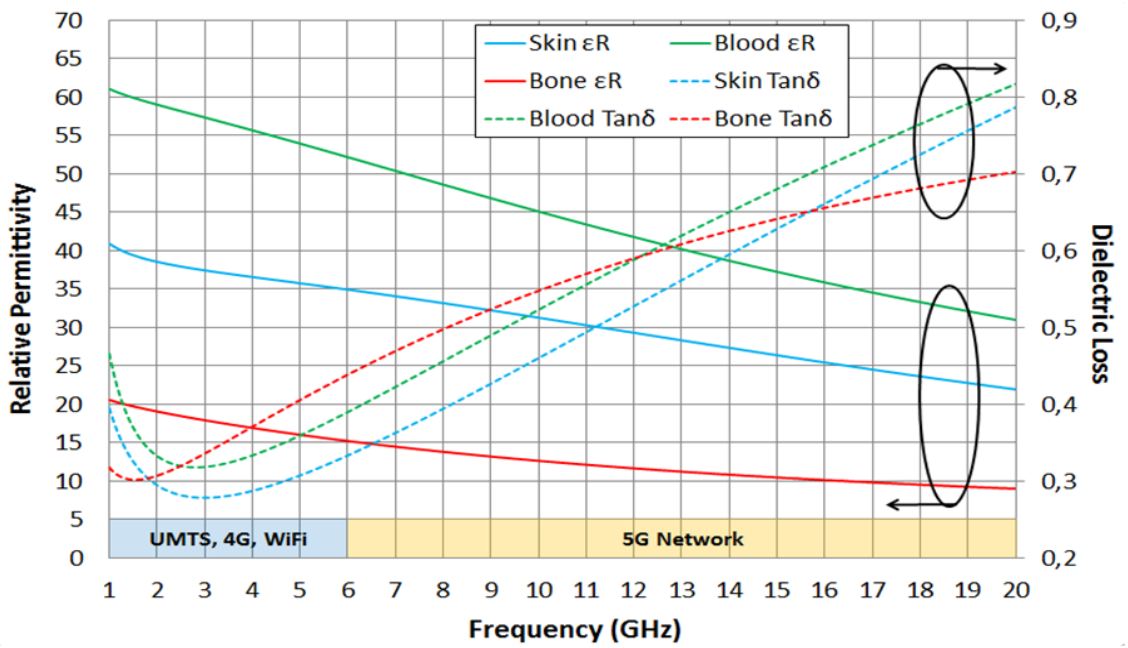

Figure 4-4: Relative permittivity and dielectric loss in skin, bones and blood.

4.2. Measurement Setup for hand effect investigation

To perform measurements, we used the 3-axis scanner with a fixed Antenna Under Test (AUT) designed by NSI and presented in Figure 4-5 [IV-22]. This robotic positioning system consists of three rotational positioners. The first one, mounted on a large floor stand, defines the horizontal ϕ-axis of rotation. The second positioner is attached to the ϕ rotation stage with a 90° angle to form the θ-axis. The last positioner is attached to the θ rotation stage forms the χ-axis and manages the polarization rotation stage. The total region of motion is practically limited to $-150° \leq \theta \leq 150°$ and $-180 \leq \phi \leq 180°$ by the AUT support stand. The main advantage of this setup is the fixed AUT which allows us to hold the device during the measurement. The main problem in experimentally characterizing the hand effect is to hold still while measuring the four antennas.

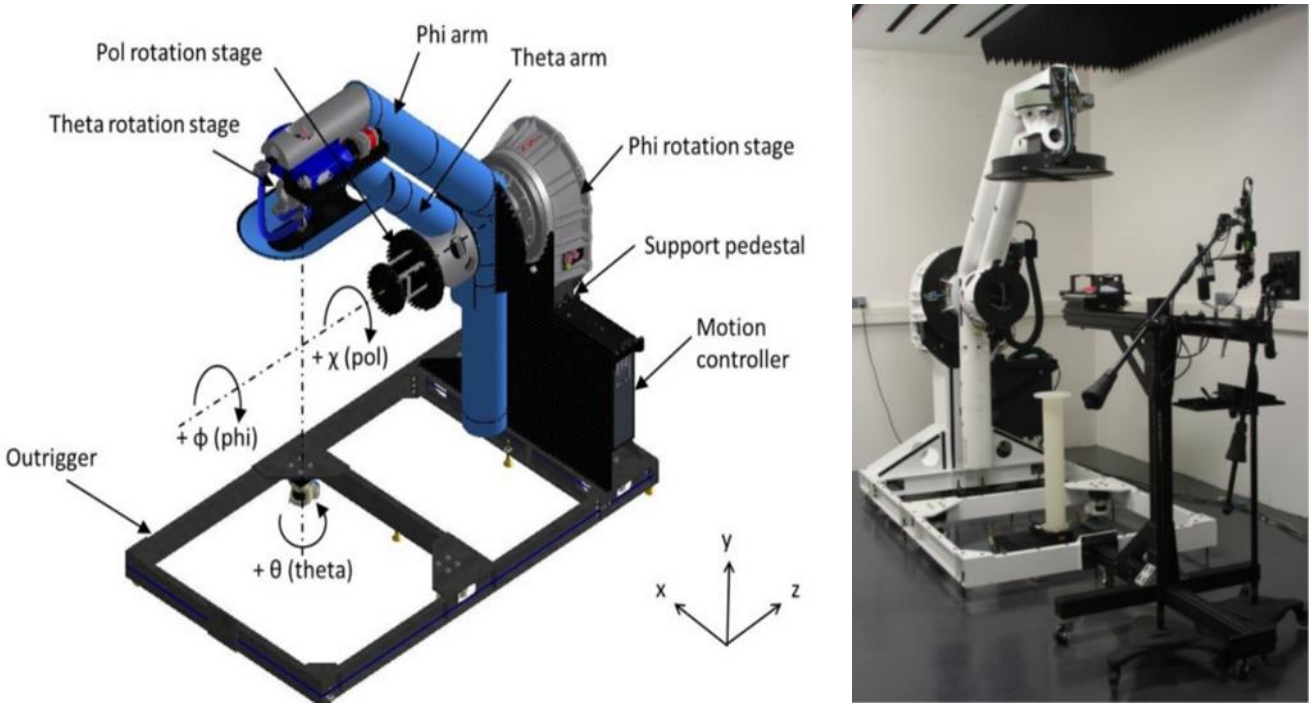

(a) (b)

Figure 4-5: schema (a) and picture (b) of the measurement setup.

For the second study at 15 GHz, we managed to reduce as much as possible the measurement time by adding a Rhodes&Schwartz OSP switch that was remotely controlled with MATLAB. The switch introduced a 2.85 dB loss which had been added to each measurement afterwards. A specific antenna holder made of low-permittivity foam material has been designed and manufactured to limit as much as possible the interaction with the AUT.

4.3. Preliminary study a with 11 GHz Prototype

In this section, a 5G MIMO mobile phone prototype including four antennas working in the 10-13.2 GHz band is designed. The objective of the study is to evaluate the negative impact due to the user's hand in frequencies higher than 10 GHz. The measurement setup presented above is leveraged in order to measure a 3D radiation pattern with a real human hand impact. The results are compared to the measurement performed with the same configuration but with a phantom hand. S-parameters, radiation pattern and efficiency are presented and discussed for one antenna only.

4.3.1. Single Antenna structure and dimensions

In this section, the design of a high frequency MIMO handheld device to use for the tests is presented. The requirements are a total efficiency above 50%, compact size to fit in a mobile phone terminal and being low cost [IV-23]. We decided to implement four dipoles antennas working at 11 GHz on a 70x140 mm² FR-4 PCB to fit with the dimension of a smartphone. The layout of the antenna is presented in the Figure 4-6. The dipole is printed on an FR-4 substrate of relative dielectric permittivity ε_r = 4.4 and thickness h = 1.6 mm. The radiating element is fed through a slot excited with a micro-strip line. It is a compact structure of 12x7.3 mm² ($\lambda_0/2.2x\lambda_0/3.7$ at 11.2 GHz, the center of the 11 GHZ band). Optimal matching is achieved by tuning two different parameters: one parallel stub (Lslot) located between the two horizontal arms of the T dipole and one serial stub set at the end of the micro-strip line (Lstub).

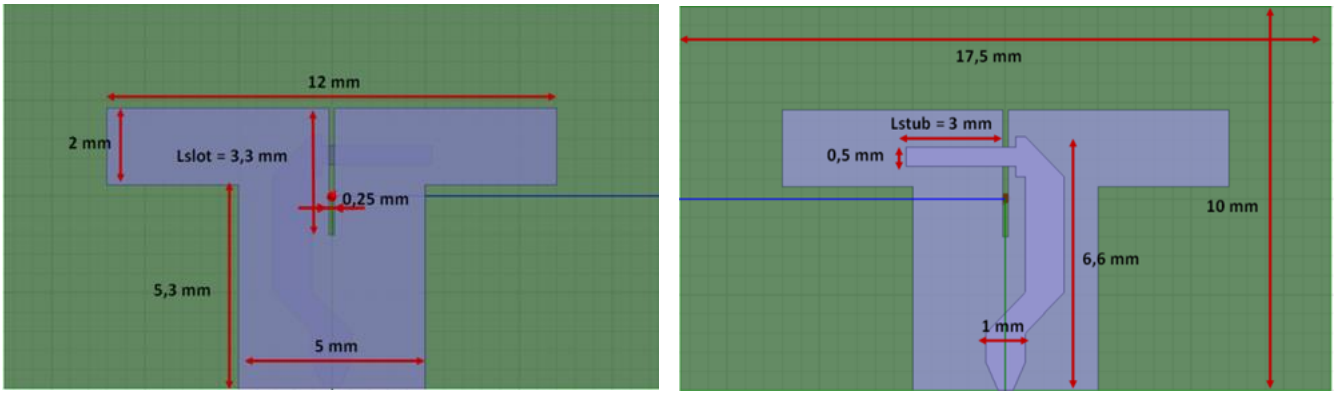

(a) (b)

Figure 4-6: Top (a) and bottom (b) view of the antenna structure at 11 GHz with dimensions.

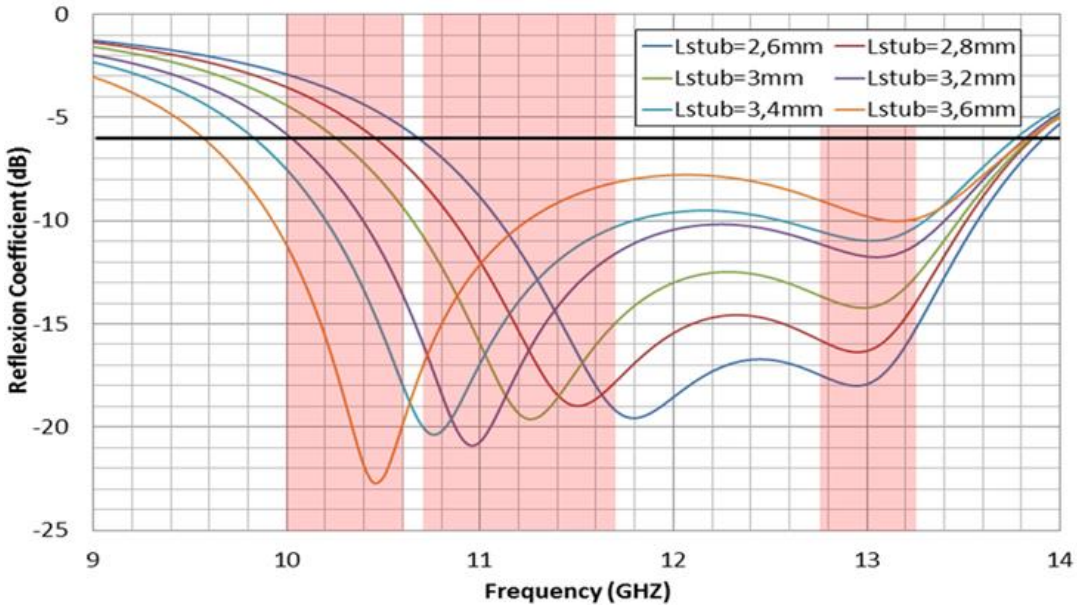

Figure 4-7: Return Loss for various Lstub values.

A parametric simulation of the reflection coefficient for different micro-strip stub lengths (Lstub) is presented in Figure 4-7. For Lstub = 3.2mm, the antenna is matched over a 3 GHz bandwidth and almost covers the 10GHz, 11 GHz and 13 GHz band with a -6dB criteria. Based on full wave HFSS simulation, the total efficiency is 89% at 11 GHz. When integrated into a 140x70mm² terminal the antenna provides a 6 dBi directional radiation pattern.

4.3.2. Mobile Phone Prototype at 11 GHz

The mobile prototype presented Figure 4-8 has been realized with a circuit board plotter (LPKF ProtoMat S63) according to the dimensions presented in Fig. 1. We decided to implement four antennas in the top-right corner of the device, where the hand effect might be smaller considering the classic way of grabbing a mobile phone. The distance between each antenna is $0.8\lambda_0$ (21.5 mm). In the first measurement campaign, only two front antennas have been connected through 130 mm rigid coaxial cables. A plastic casing was designed for this prototype and fabricated using a 3D printer with ABS material.

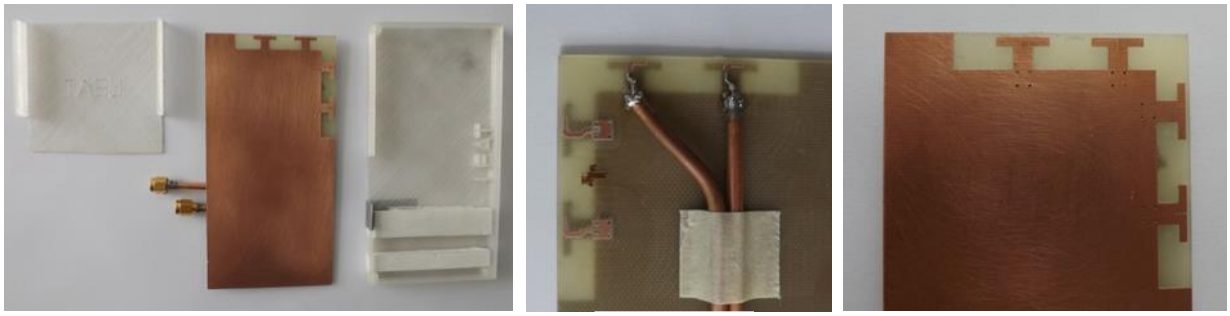

(a) (b) (c)

Figure 4-8: (a) Overview of the prototype with a 3D printed casing and the two connected antennas (b) bottom view of the prototype with the two connected coaxial cables and (c) top view zoom of the antennas.

4.3.3. Hand effect Measurement

In this second part, we aim to present measurements with real users and hand phantom interferences. Measurements with the real human model have already been proposed for lower frequency. Millimeter wave add many challenges for this type of measurement, in particular, because of the shorter wavelength, the human model has to stay as stable as possible. At the stage of the study, we will focus on a single antenna to characterize the human body impact. As shown in Figure 4-9 we chose to adopt a position which maximizes the interference with a finger very close to the antenna under test. Furthermore, we mimic hand phantom position.

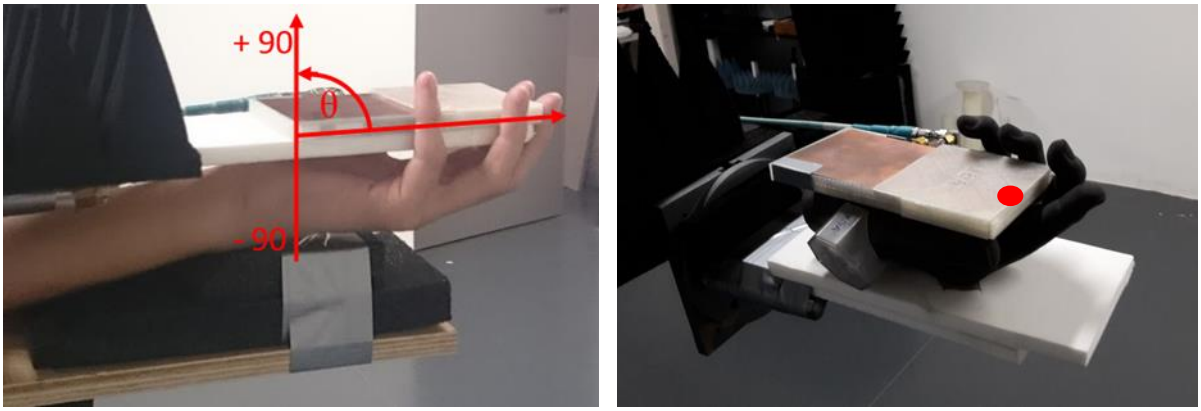

(a) (b)

Figure 4-9: Pictures of the hand (a) and the phantom (b) interacting with the prototype. The red dot mark the position of the antenna.

Reflection coefficient has been measured at the output of the 130mm cable with deembedding. Figure 4-10 presents the simulated S_{11} (dotted line) and the measured S_{11} (solid lines) of one antenna for four different configurations: the PCB in free space, the PCB with, the prototype with casing and user's hand and finally the prototype with casing and the hand phantom. Results show that casing and hands have a low influence on the antenna reflection coefficient, meaning that reactive field of the antenna is not modified by the casing and hand.

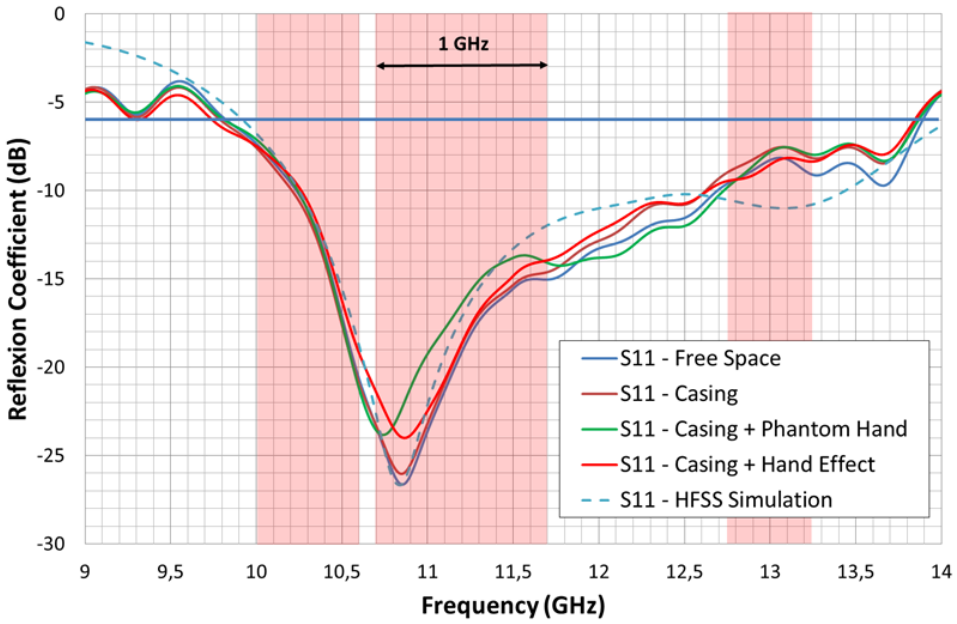

Figure 4-10: Return loss of the prototype for four different configuration and simulation.

The Figure 4-11 presents the radiation pattern for each hand in the elevation (vertical) plane. We observe that the radiation pattern tend to be lower in the region where the hand was located. We can also notice the diversity of the results of each measurement and each hand which led us to average those results.

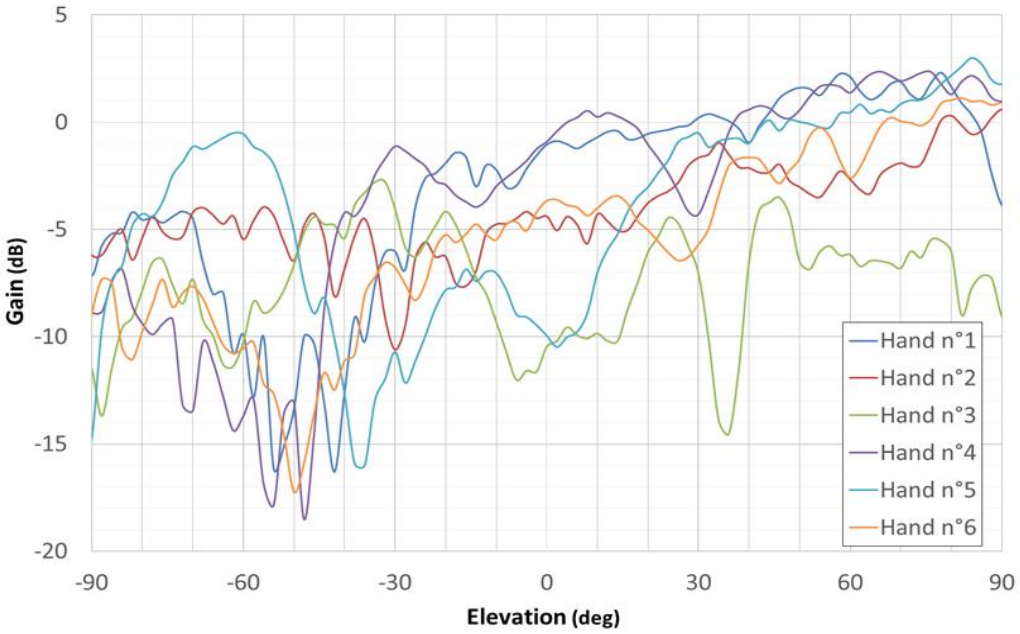

Figure 4-11: Elevation measurement with hand effect for 6 different hands.

The figure 4-12 presents the free space radiation, with the hand phantom and with the average radiation pattern of 6 different hands (different size and shape from men and women test subject). From Figure 4-12, we observe that the radiation pattern is modified when the user or the hand phantom is holding the device especially in the direction where the hand is located (-90° elevation angle). It shows a maximum decrease of about 12 dB of the total peak gain for a real hand and about 6 dB for the hand phantom. The decrease of the peak total gain for the user hand measurement is twice more than the phantom hand measurement.

We can also observe in Figures 4-13(a) and 4-13(b) that HFSS simulation fit with measurement in free space. Figure 4-13(d) shows the radiation measurement with the perturbation caused by the hand; we observe that most of the radiated power is oriented to the top. The hand absorbs all the bottom radiation. Finally, Figure 4-13(c) shows the radiation measurement with the interferences caused by the hand phantom. We observe that the phantom doesn't interact as much as a real human hand with the antenna. Table 4-1 sums up the important results and show a loss of 5.5 dB for the efficiency with the real hand and a loss of 2.3dB with the hand phantom. These results validate the need for higher frequency compatibles phantoms.

Figure 4-12: Comparison between radiation patterns in three configurations in the antenna perpendicular plane (elevation).

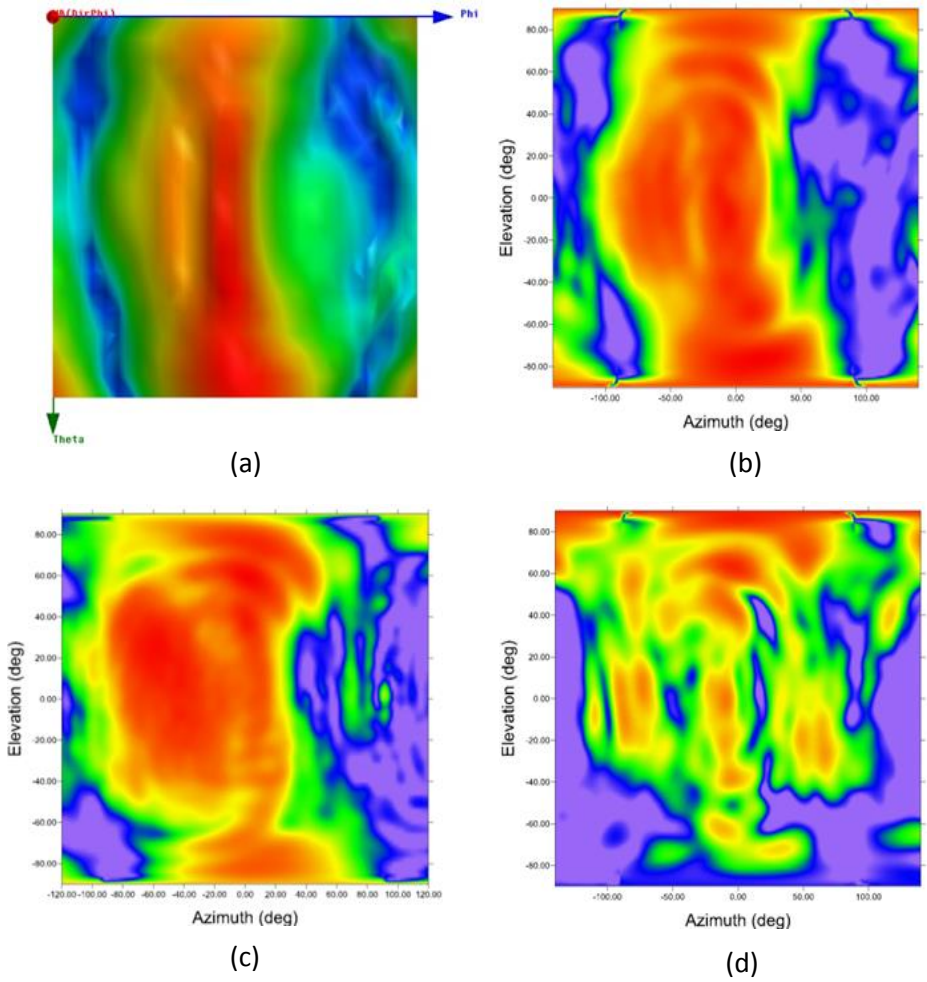

Figure 4-13: Radiation pattern: (a) 2D HFSS simulation, (b) free space 2D measurement, (c) 2D measurement with phantom hand and (d) 2D measurement including hand effect.

Table 4-1: Overview of the 3d Measurement results.

	Directivity (dB)	Peak Gain (dB)	Efficiency (dB)
Free Space Simulation	4.8	4.3	-0.5 (89%)
Free Space Measurement	5.8	4.0	-1.8 (66%)
Casing + Phantom Meas.	6.3	2.2	-4.1 (39%)
Casing + Hand Meas.	10	2.6	-7.3 (18%)

4.3.4. Conclusion of the study at 11 GHz

For this preliminary study, we designed and realized a mobile phone prototype according to future 5G requirements. We have shown that body dielectric properties versus frequency are not constant and that an important impact of the hand on millimeter wave terminal can be expected.

We studied the influence of a real user hand thanks to a spherical near-field scanner with fixed AUT. First results show a decrease of about 6 dB of the total efficiency at 11 GHz for a real human hand whereas it shows less than a 3 dB decrease for the hand phantom. Moreover, in the main lobe direction, the peak gain with hand effect is 9 dB lower than the peak gain in free space.

As a primary conclusion, considering the constraint budget link in millimeter wave communications, the hand effect on the terminal has to be carefully considered. One perspective of this work is the development of a hand phantom in millimeter wave. A second important point will be the study of innovative techniques to reduce the hand effect.

The 11 GHz prototype was not suitable enough for an advanced study because of some weaknesses in the design (antenna implementation, rigid coaxial cables...) so we decided to push the study with an upgraded new prototype at 15 GHz and using the same measurement approach.

4.4. Advanced study with a 15 GHz Prototype

For this study, we designed a low cost high frequency 4-element MIMO antenna system characterized by compact size to fit in a mobile phone terminal and with total efficiency above 50%. We implemented four T dipoles antennas [IV-23] working at 15 GHz on a 70 x 140 mm2 FR-4 PCB to fit with the dimension of a smartphone.

This study evaluates the user's impact on 4-element 15 GHz antenna array implemented on a smartphone. We consider the user's blockage not only in terms of efficiency but also on the maximum gain achievable in a beam-steering configuration with real hand measurement on the 4 antennas. The 15 GHz frequency band is the front door of the multiple band opportunities existing in the millimeters and centimeters wave. The main objective of this work is to characterize the influence of the user. The second objective is to evaluate the beamforming efficiency when the antenna array suffers from user shadowing.

4.4.1. Single Antenna structure and dimensions

Figure 4-14 presents the layout of the simulated antenna at 15 GHz. An FR-4 substrate of relative dielectric permittivity $\varepsilon_r = 5$ and thickness h = 0.8 mm is used to print the dipole. The radiating element is fed through a slot excited with a micro-strip line. We designed a compact structure of 8.5 x 5.5 mm2 (λ/2.4 x λ/3.6 at 15 GHz). The parallel stub (Lslot) located between the two horizontal arms of the T dipole and the serial stub at the end of the microstrip line (Lstub) are tuned to achieve optimal matching. Based on full wave HFSS simulation, the total efficiency is 87% (-0.6 dB) at 15 GHz. When integrated into a 140 x 70 mm2 terminal, the antenna provides a 5.5 dBi directional radiation pattern and 4.7 dB realized gain.

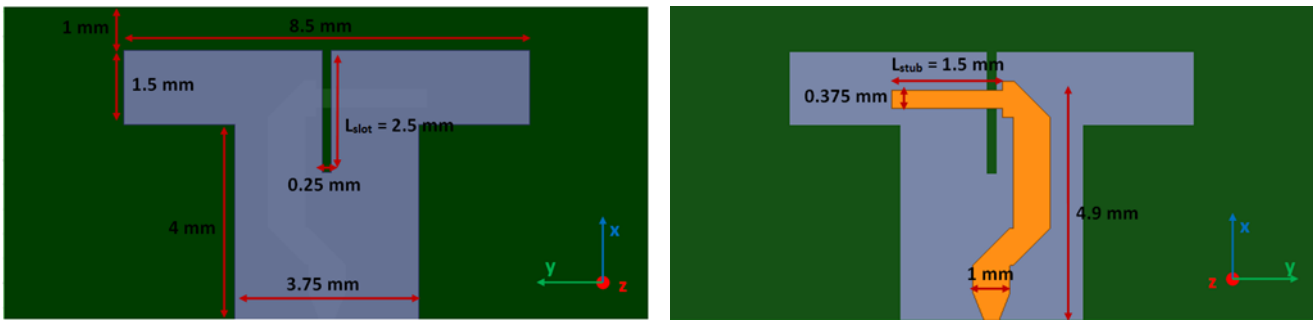

(a) (b)

Figure 4-6: Top (a) and bottom (b) view of the antenna structure at 15 GHz with dimensions.

4.4.2. Mobile Phone Prototype at 15 GHz

We realized the mobile phone prototype with 4 antennas according to the dimensions presented in Figure 4-14. We decided to implement two arrays of two antennas, one on the top and one on the left side of the mobile, where the hand effect might be minimized considering the two classic way of grabbing a smartphone (”data mode” with two hands and ”call mode” with one hand). The distance between the antennas is 0.6λ (i.e., 12 mm). Each antenna is connected through a 170 mm semi-rigid coaxial cable.

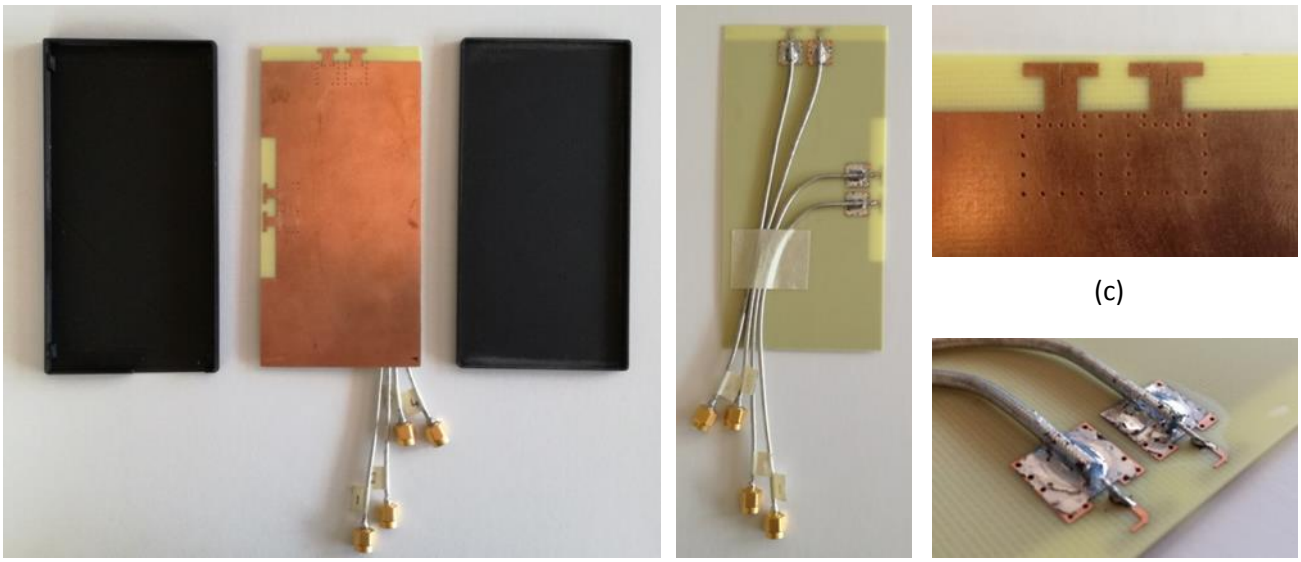

(a) (b) (c) (d)

Figure 4-15: (a) Overview of the prototype with a 3D printed casing, (b) bottom view of the prototype with the four connected coaxial cables, (c) top view zoom on two antennas and (d) bottom view zoom on two antennas.

This prototype allows the implementation of MIMO techniques and beamforming thanks to the multiple antennas. A plastic case was designed for this prototype and fabricated using a 3D printer with ABS material.

S-parameters have been measured at the output of the 170 mm cable. Deembedding is realized on a VNA by filtering the S11 parameter in the time domain. Figure 4-16(a) presents the measured versus the simulated return loss and isolation for antennas 1 and 2. The same data are presented for antennas 3 and 4 in Figure 4-16(b). Measurements (solid lines) and simulations (dotted lines) are both performed including the casing. We observe that all antennas are matched at 15 GHz even if the measured results are slightly shifted down in frequency because of the actual substrate permittivity higher than the

simulated one. We observe that all the prototype antennas offer more than 3 GHz bandwidth for an S11 < - 6 dB (Figure 4-16). Isolation better than -20 dB is obtained between antennas 1 and 2 as well as between antennas 3 and 4.

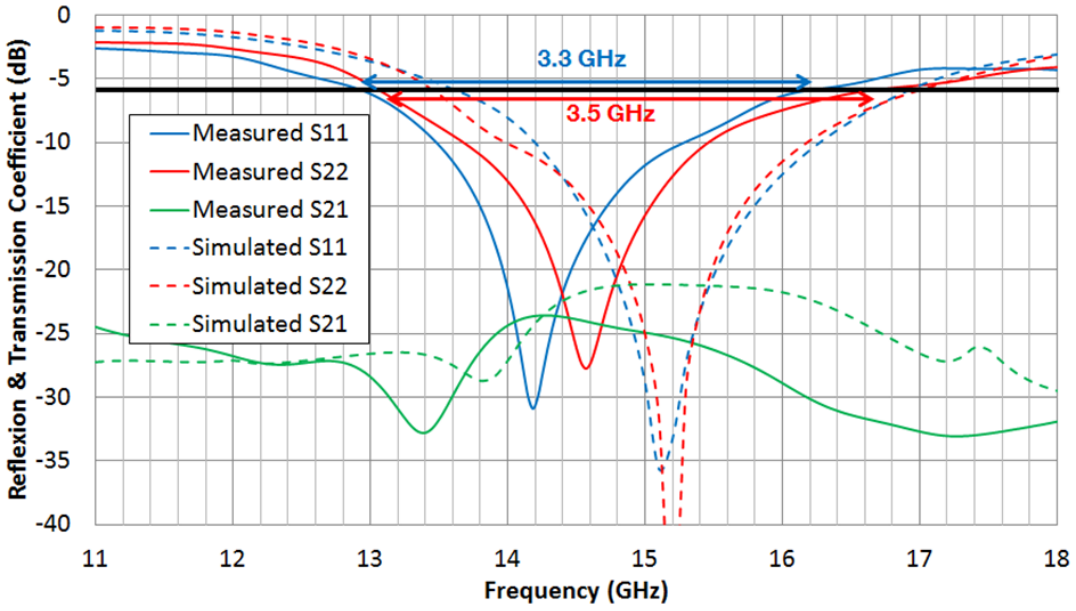

(a)

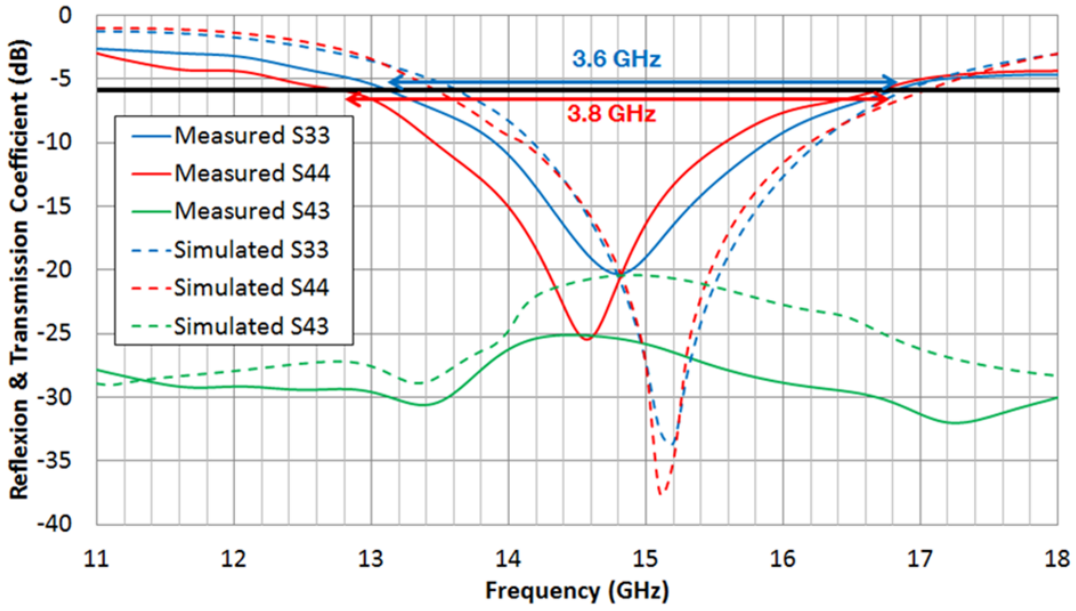

(b)

Figure 4-16: Return loss and isolation for (a) antenna 1 and 2, (b) antenna 3 and 4.

Figure 4-17 shows the top view (plane at θ = 90°) of the 3D simulated radiation pattern for each antenna. This figure highlights the end-fire characteristic of the antennas. We observe a maximum total gain of about 4 dB in the main radiating direction for each antenna.

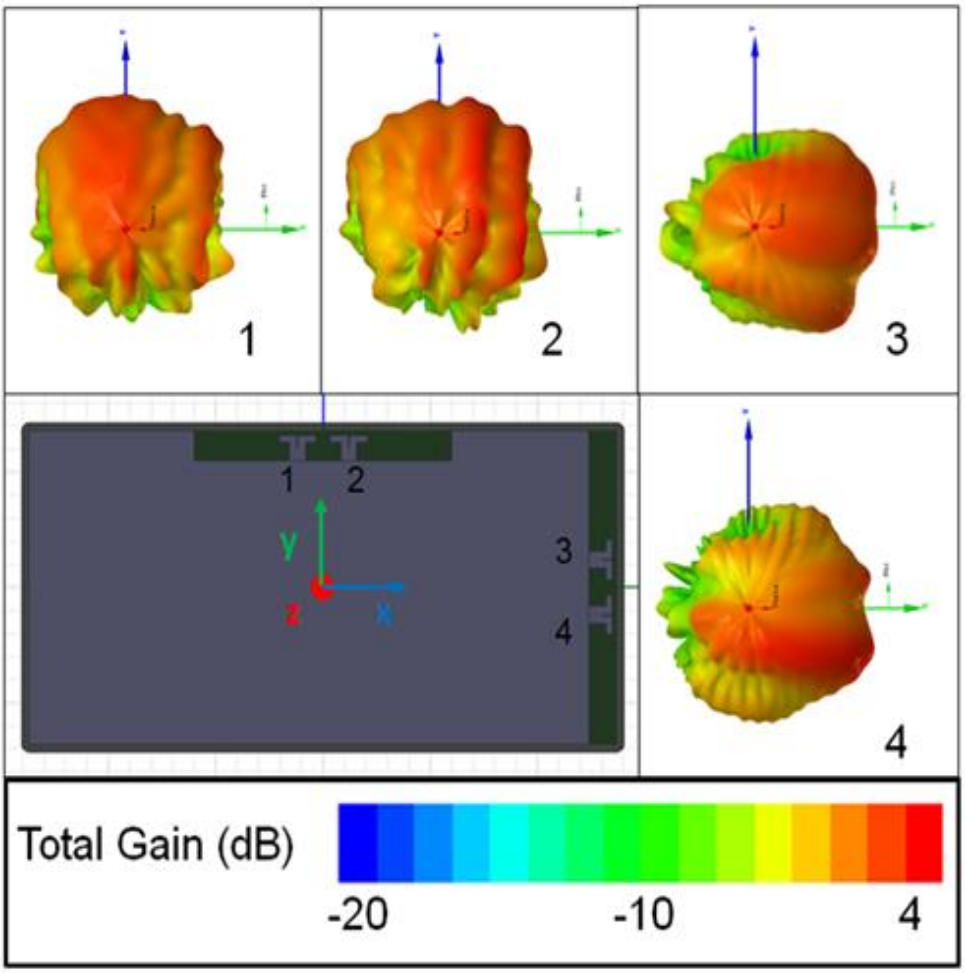

Figure 4-17: Top view of the simulated radiation pattern for each antenna.

4.4.3. Free Space Measurement

This section is aimed at validating the measurement setup with respect to simulations. Figure 4-18 shows the foam support (ε_r = 1.02) created to place and keep the device under test (DUT) in the right position. We had to create two different positions to overcome the range limitation of the positioner in the θ-axis. Indeed, we wanted to measure the radiation pattern at least from -90° to 90° around the center of the antenna in the horizontal plane. Some gaps have been dug around the two specific cavities enabling a user to grab the smartphone covering antennas 1 and 2. The Position 1 is the one presented in the figure 4-18 while in the position 2, the prototype is turned of 45° over the z axis.

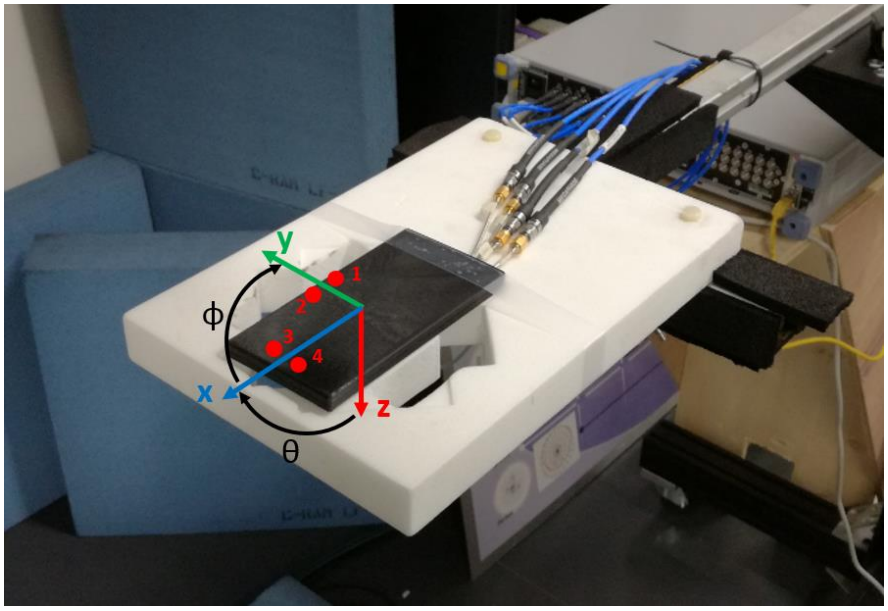

Figure 4-18: Photo of the setup with foam support and prototype.

Figures 4-19 to 4-22 present a comparison between simulated (dotted lines) and measured radiation patterns (solid lines) for all the antennas. Each figure shows the Gain-ϕ in blue and the Gain-θ in red in the planes y0z at ϕ = 90° (vertical plane for antennas 1 and 2), x0z at ϕ = 0° (vertical plane for antenna 3 and 4) and x0y at θ = 90° (horizontal plane for each antenna). Due to the mechanic constraints of the scanner, and the two position created on the support, we present measurements between θ = -50° and θ = 230° in the x0z plane and between ϕ = -10° and ϕ = 190° in the x0y plane (for antennas 1 and 2) or between ϕ = -100° and ϕ = 100° in the x0y plane (for antennas 3 and 4). All the simulated results have been transferred in the same spatial coordinates presented in figure 4-18. Simulations are presented over 360° for both vertical and horizontal planes. Moreover, we choose to center the maximum of the useful pattern (measured and simulated) on each plot.

Figure 4-19 shows a measured maximum gain of 3.5 dBi in the vertical plane (located at θ = 130°, ϕ = 90°) and 2.7 dBi maximum gain in the horizontal plane (located at θ = 90°, ϕ = 100°). Antenna 1 has an 80 % simulated total efficiency versus a 58 % measured efficiency in the Satimo StarLab.

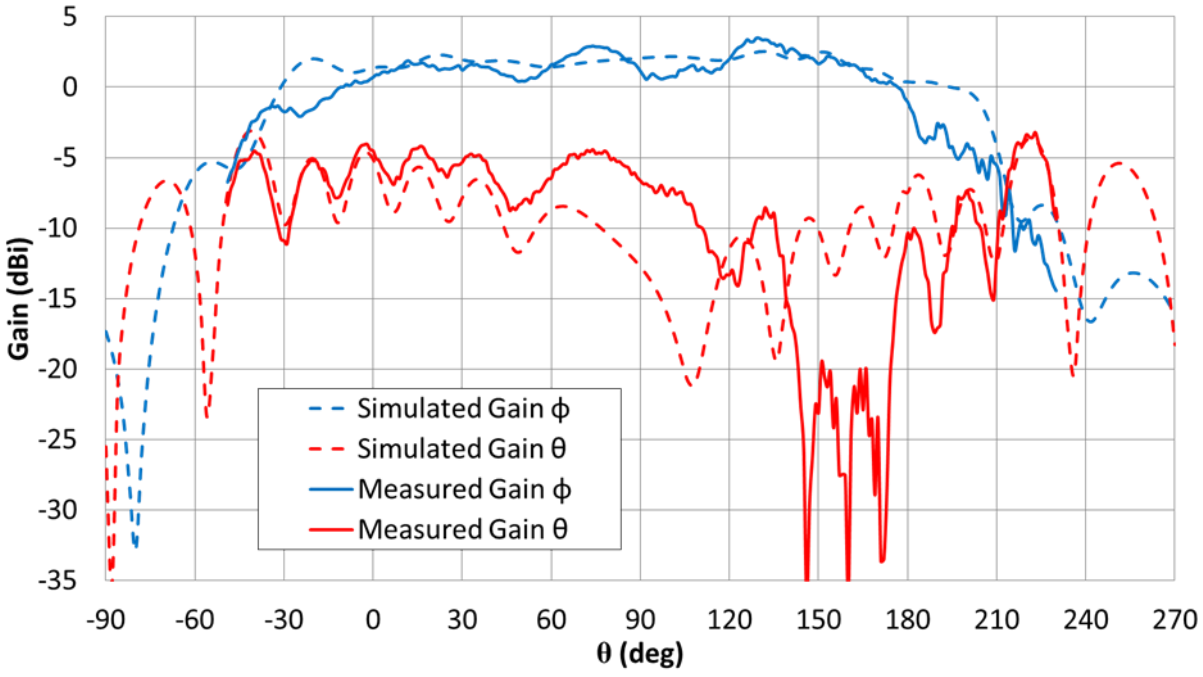

(a)

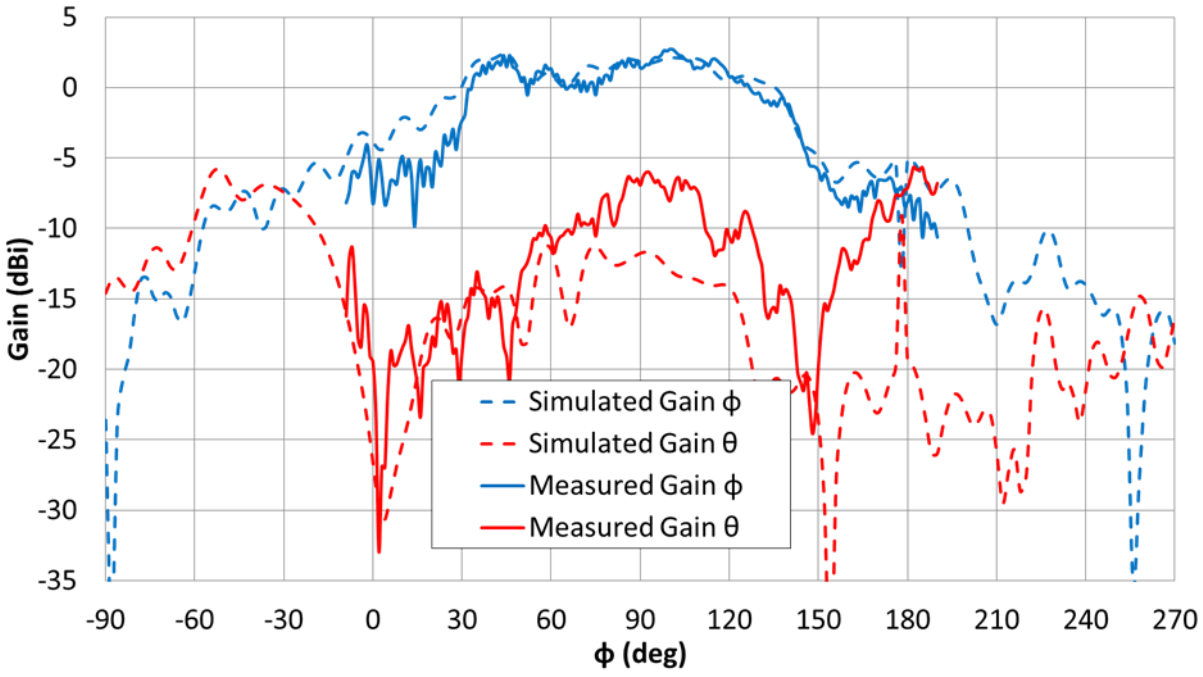

(b)

Figure 4-19: Antenna 1 simulated vs measured gain in the planes at (a) ϕ = 90° and (b) θ = 90°.

Figure 4-20 shows a measured maximum gain of 2.1 dBi in the vertical plane (located at θ = 126°, ϕ = 90°) and 2.8 dBi maximum gain in the horizontal plane (located at θ = 90°, ϕ = 72°). Antenna 2 has an 80 % simulated total efficiency versus a 56 % measured efficiency.

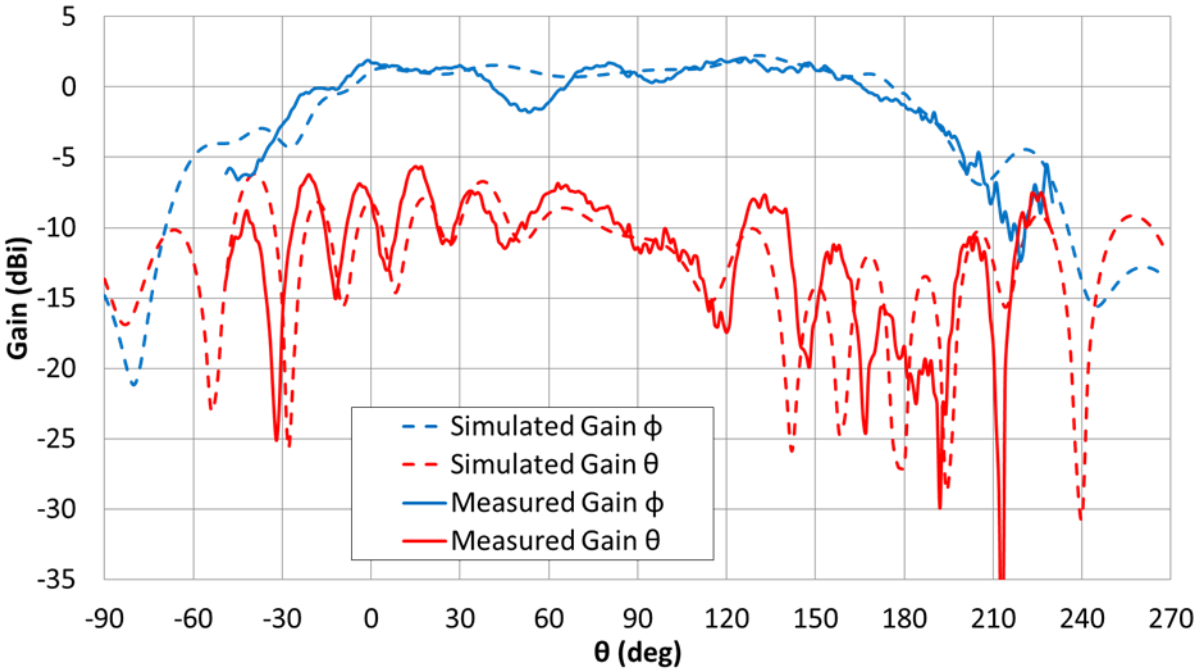

(a)

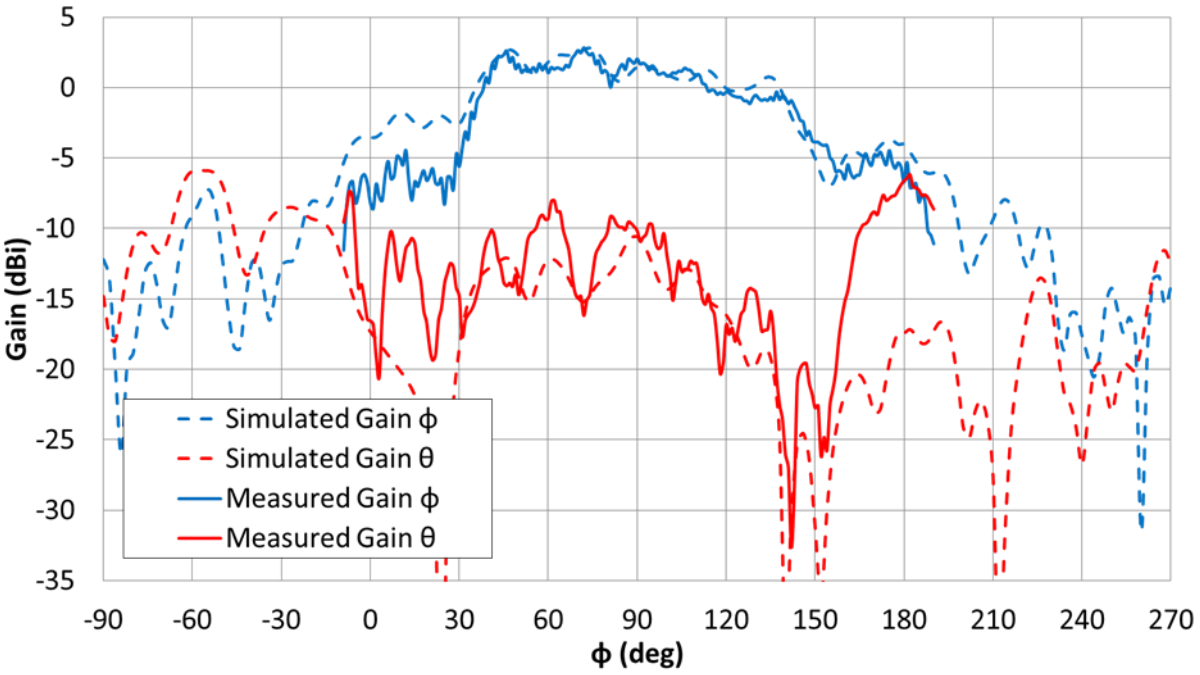

(b)

Figure 4-20: Antenna 2 simulated vs measured gain in the planes at (a) φ = 90° and (b) θ = 90°.

Figure 4-21 shows a measured maximum gain of 2.9 dBi in the vertical plane (located at θ = 119°, ϕ = 90°) and 2.9 dBi maximum gain in the horizontal plane (located at θ = 90°, ϕ = 18°). Antenna 3 has an 81 % simulated total efficiency versus a 65 % measured efficiency.

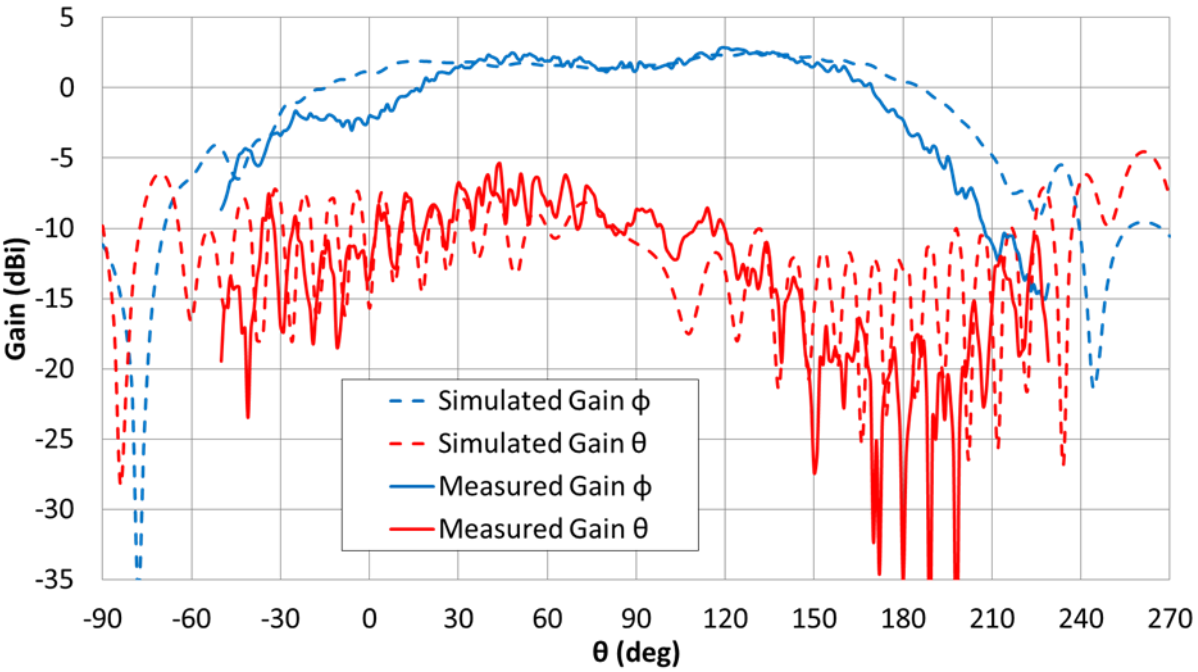

(a)

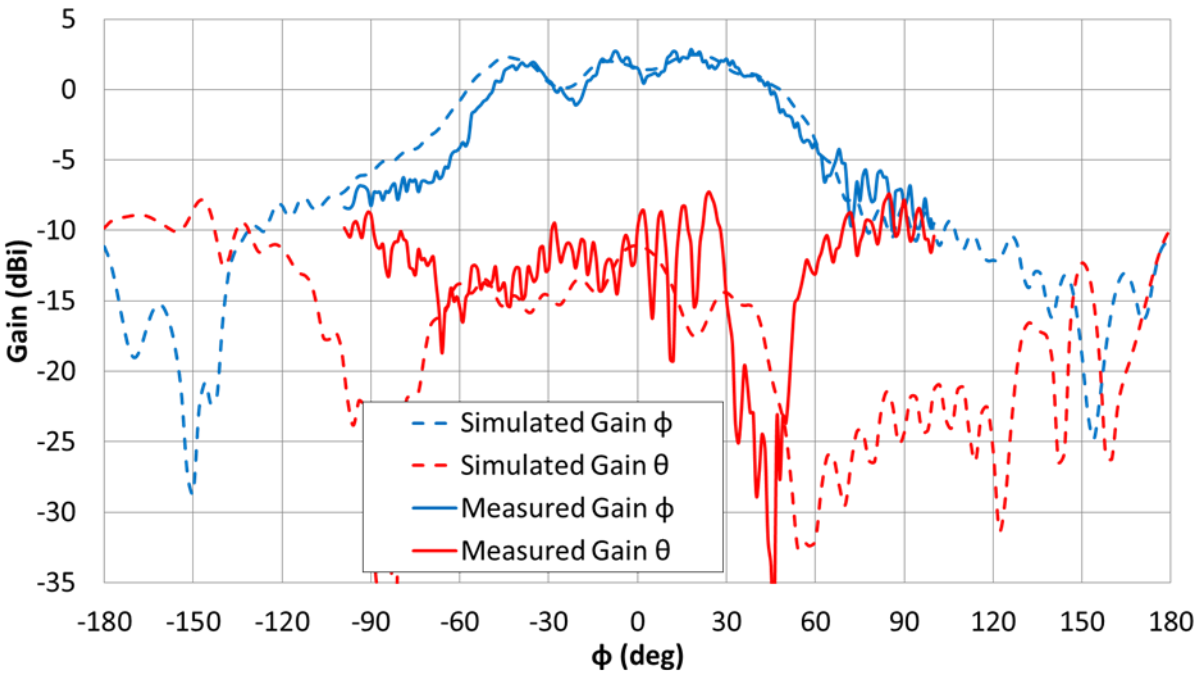

(b)

Figure 4-21: Antenna 3 simulated vs measured gain in the planes at (a) φ = 0° and (b) θ = 90°.

Figure 4-22 shows a measured maximum gain of 1.4 dBi in the vertical plane (located at θ = 60°, ϕ = 90°) and 3.9 dBi maximum gain in the horizontal plane (located at θ = 90°, ϕ = -19°). Antenna 4 has an 81 % simulated total efficiency versus a 55 % measured efficiency.

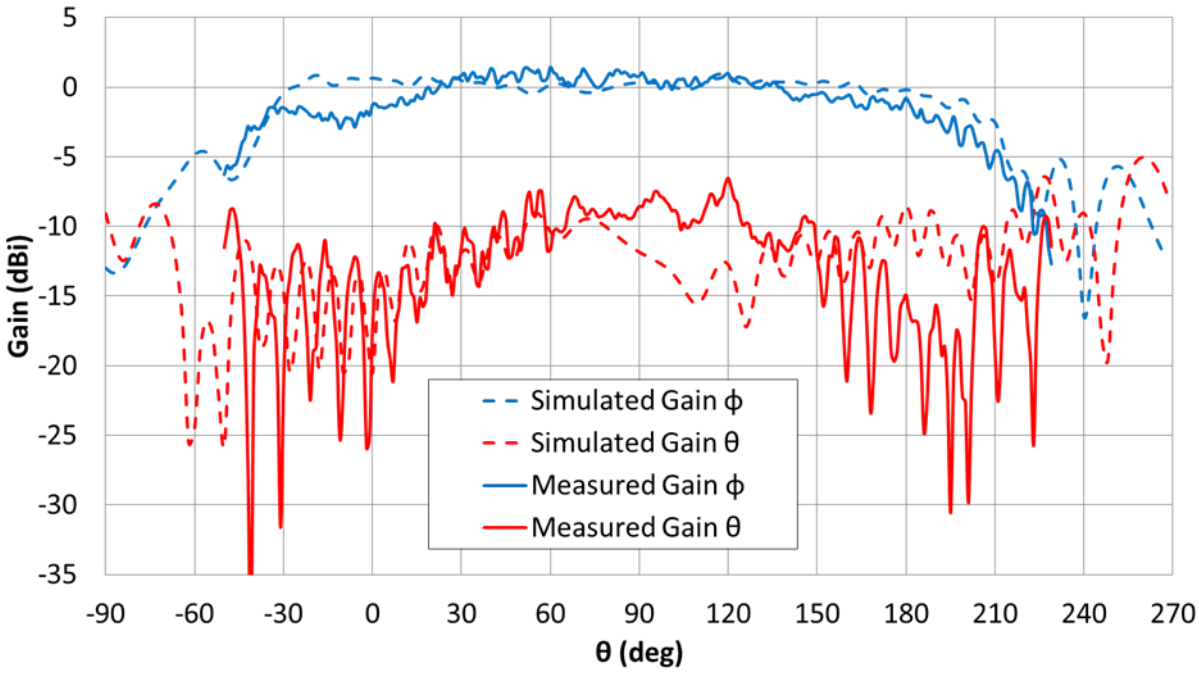

(a)

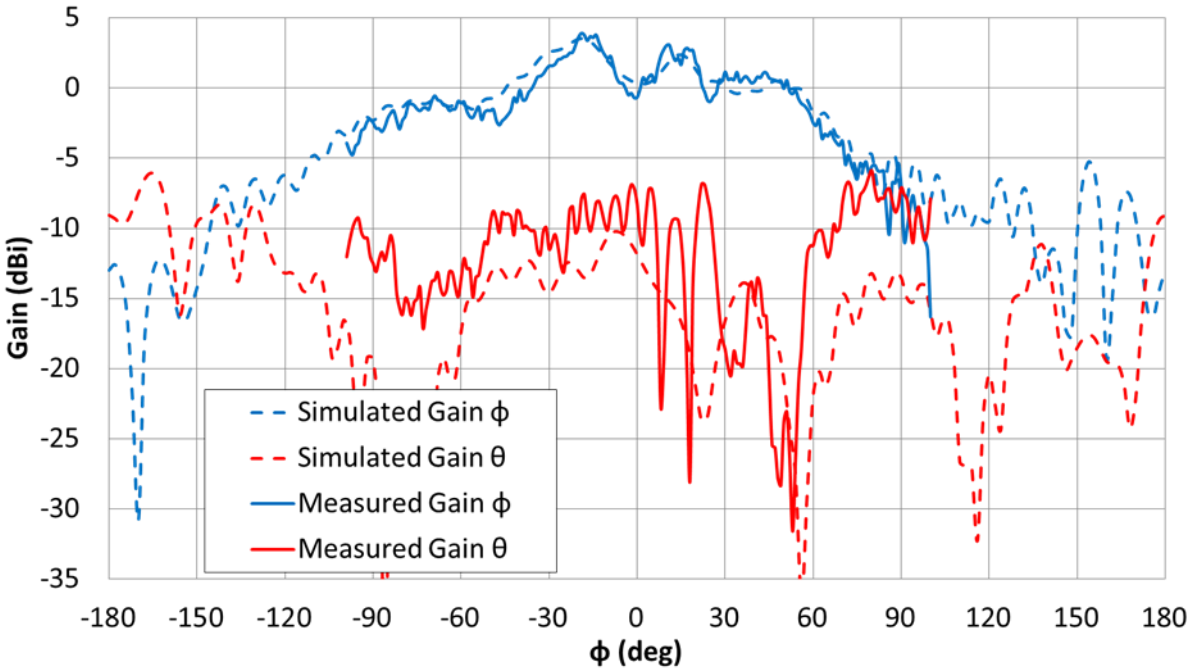

(b)

Figure 4-22: Antenna 4 simulated vs measured gain in the planes at (a) ϕ = 0° and (b) θ = 90°.

Those results are consistent with the expected antenna performance for this type of application and measurements match simulations with good accuracy. We observe a good agreement between simulations and measurements especially for the main polarization (Gain-ϕ).

4.4.4. Beamforming Computation

The terminal prototype is composed of 2 arrays of 2 antennas radiating towards the y-axis (antennas 1 and 2) and towards the x-axis (antennas 3 and 4). Each array can be used in beamforming mode to increase the gain towards a specific direction. The beamforming gain (or array gain) G_{array} for each array is obtained by computing a linear combination of the single element gains, i.e., as:

$$G_{array}(\theta;\varphi) = G_a(\theta;\varphi) + G_b(\theta;\varphi)e^{-j\gamma}. \qquad \text{eq. [4-2]}$$

where a = {1, 3} and b = {2, 4} indicate the antenna element, $G_{i,j}$ are the gain of the single elements, and γ is the phase difference that can be introduced between the 2 elements of the array (we are assuming here that no amplitude difference can be introduced). The beamforming gain can be maximized in each direction (θ,ϕ) by optimizing the phase difference γ. The result is the so-called Total Scan Pattern (TSP) gain, introduced in [IV-5], [IV-6] and [IV-19], and defined as:

$$G_{TSP}(\theta,\varphi) = \max\{G_{array}(\theta,\varphi)\}. \qquad \text{eq. [4-2]}$$

Finally, in order to highlight the improvement given by the beamforming technique, we define ΔG(θ,ϕ) as the difference between GTSP and the best gain among the two antennas used to form the beam, i.e.,

$$\Delta G(\theta,\varphi) = G_{TSP}(\theta,\varphi) - \max\{G_a(\theta,\varphi), G_b(\theta,\varphi)\}. \qquad \text{eq. [4-3]}$$

Figure 4-23 shows the comparison between the simulated and the measured beamforming gain obtained considering antennas 1 and 2 (a = 1, b = 2) and γ = 0°. The numerical data are obtained directly from the HFSS simulations, while the experimental ones are computed from the measured single element antenna patterns $G_1(\theta,\phi)$ and $G_2(\theta,\phi)$ using (2).The good agreement between the curves validates the beamforming calculations as well as demonstrates the accuracy of the measurements for both the θ and ϕ components. The beamforming gain achieves a 5.8 dBi maximum value in the vertical plane (located at θ = 280°, ϕ = 90°) and a 4.8 dBi maximum value in the horizontal plane (located at θ = 90°, ϕ = 89°).

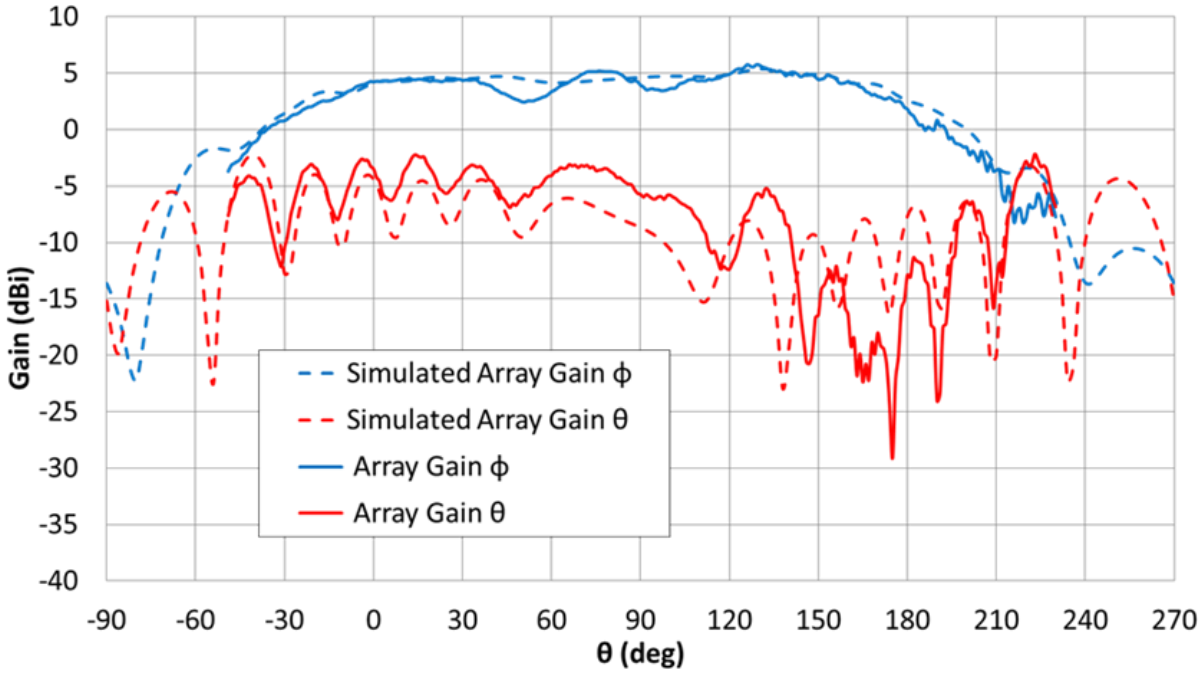

(a)

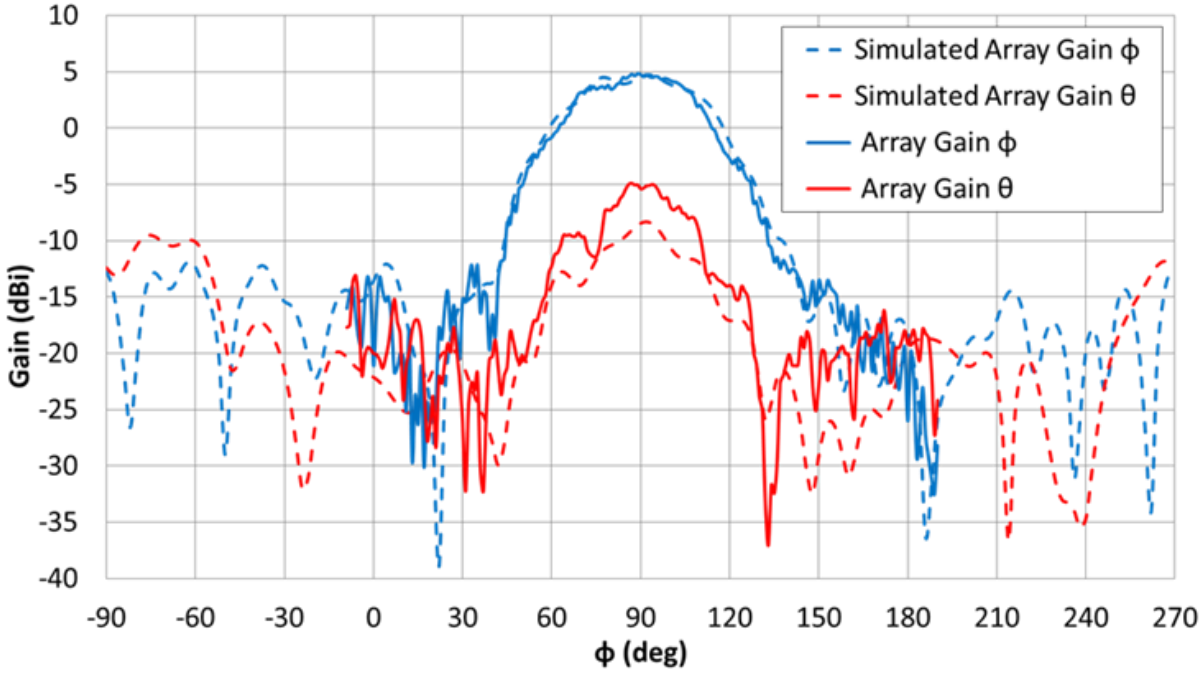

(b)

Figure 4-23: Antenna 1 and 2 simulated vs measured array gain in the planes at (a) ϕ = 90° and (b) θ = 90.

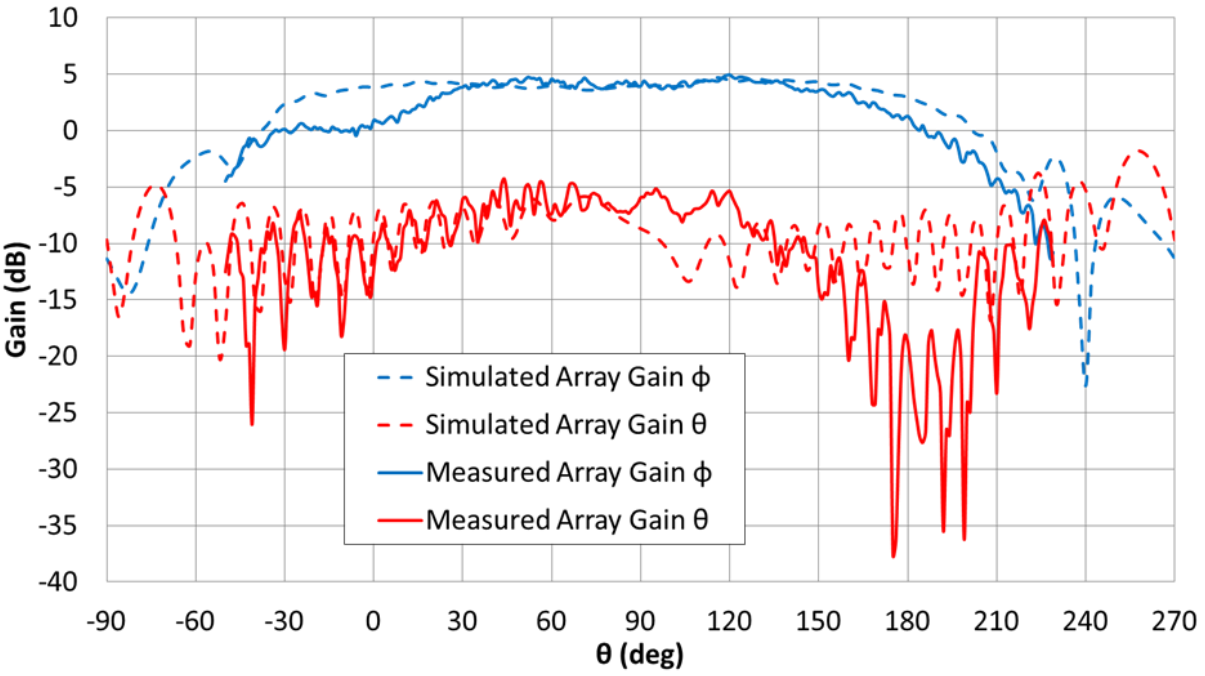

(a)

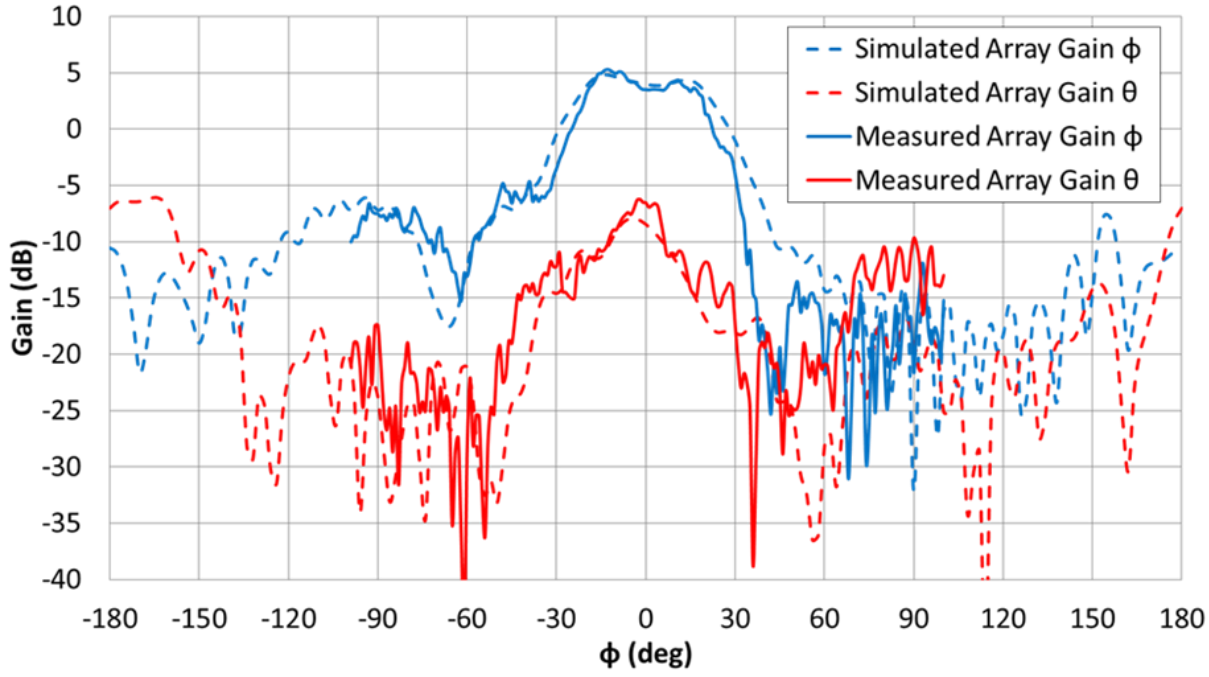

(b)

Figure 4-24: Antenna 3 and 4 simulated vs measured array gain in the planes at (a) ϕ = 0° and (b) θ = 90.

We observe similar results for the second array. Antennas 3 and 4 on Figure 4-24 achieve a 4.9 dB maximum gain in Theta plane (θ = 120°, ϕ = 90°) and a 5.3 dB maximum gain in horizontal plane (θ = 90°, ϕ= - 13°). Those two graphs show a good match between the beamforming simulated and the measured one

Figure 4-25 presents the TSP gain G_{TSP} obtained using antennas 3 and 4. The array exhibits a 5.0 dBi maximum gain in the vertical plane (at θ = 120°, ϕ = 90°) and a 5.8 dBi maximum gain in the horizontal plane (at θ = 90°, ϕ = -13°).

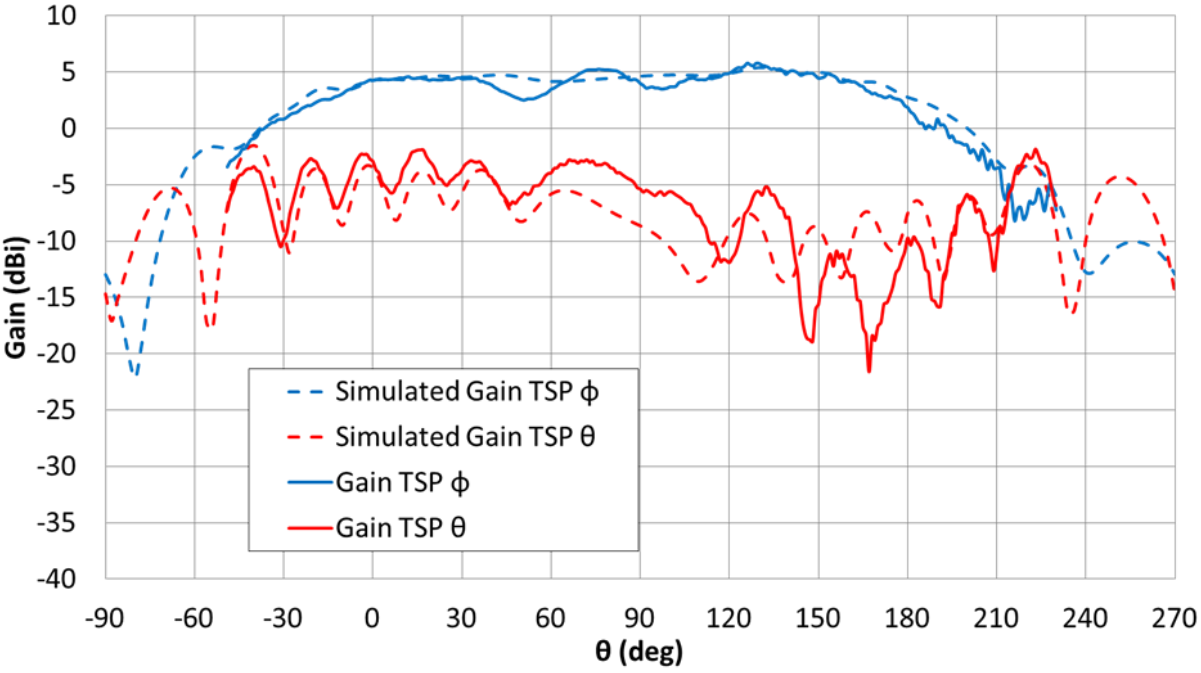

(a)

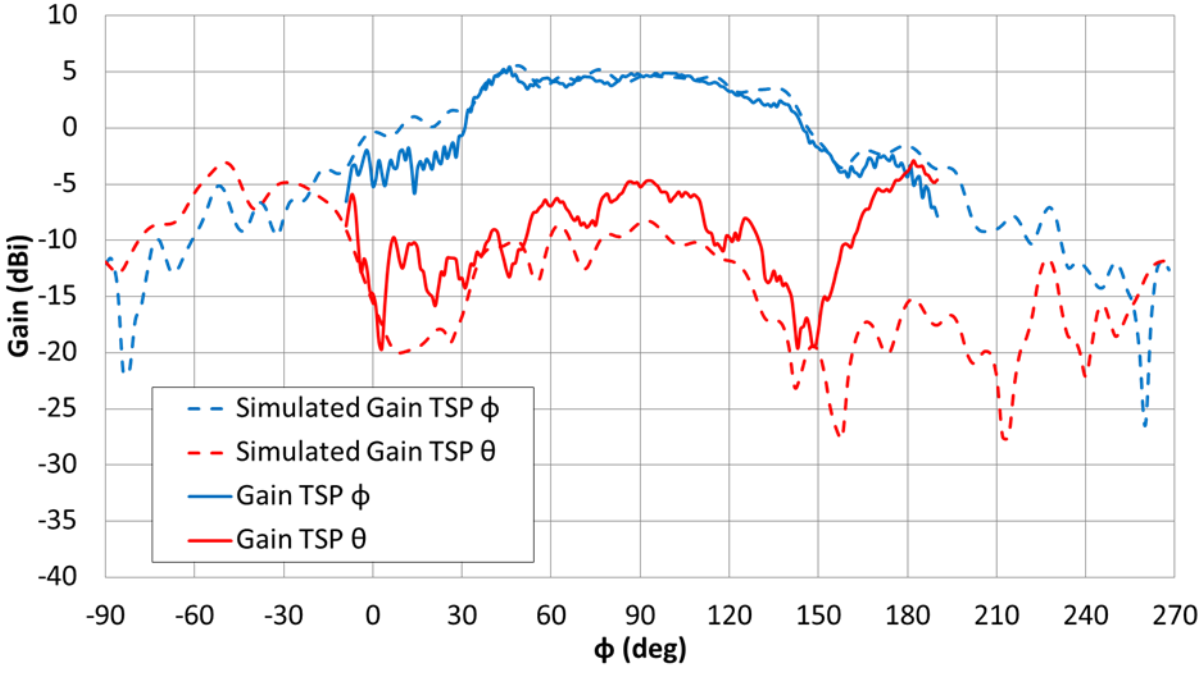

(b)

Figure 4-25: Antenna 1 and 2 Simulated vs Measured Beamforming Gain TSP in the planes at (a) ϕ = 90° and θ = 90°.

Antennas 3 and 4 on Figure 4-26 achieve a 5.0 dB maximum gain in vertical plane (θ= 120°, ϕ = 90°) and a 5.8 dB maximum gain in Phi plane (θ = 90°, ϕ = - 13°). We also observe an average 2.3 dB beamforming gain in Theta plane and a 2.1 dB beamforming gain in the Phi plane for the main polarization Phi. The good agreement between simulations and measurements further confirm the beamforming computation method and the precision of the measurement setup.

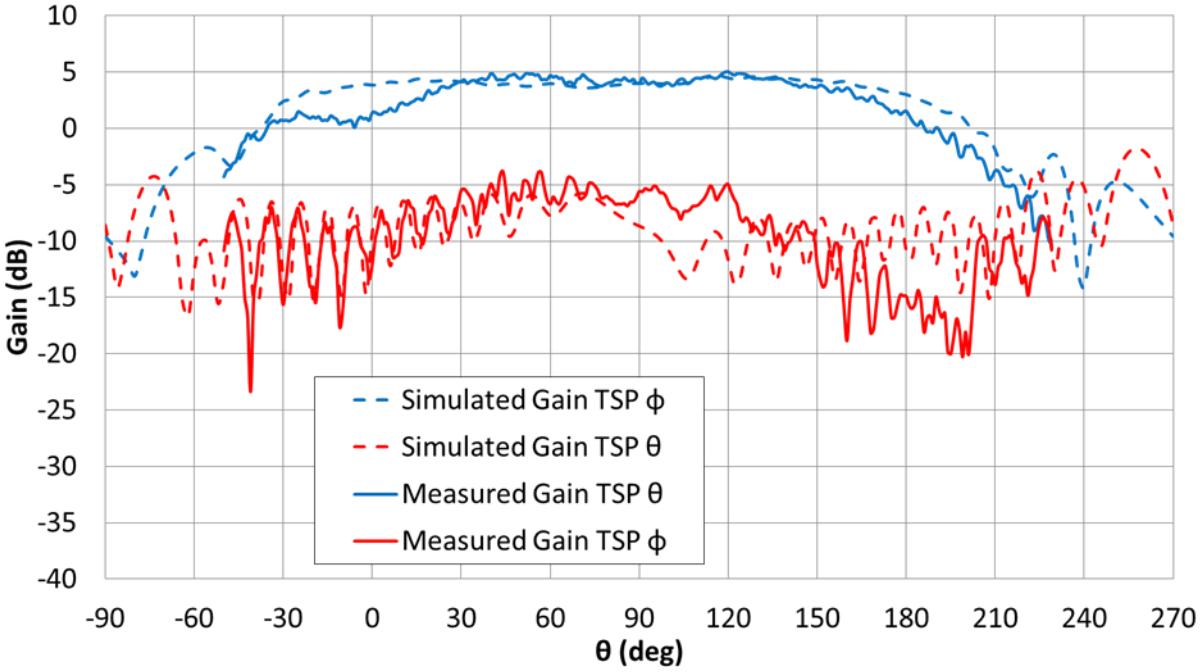

(a)

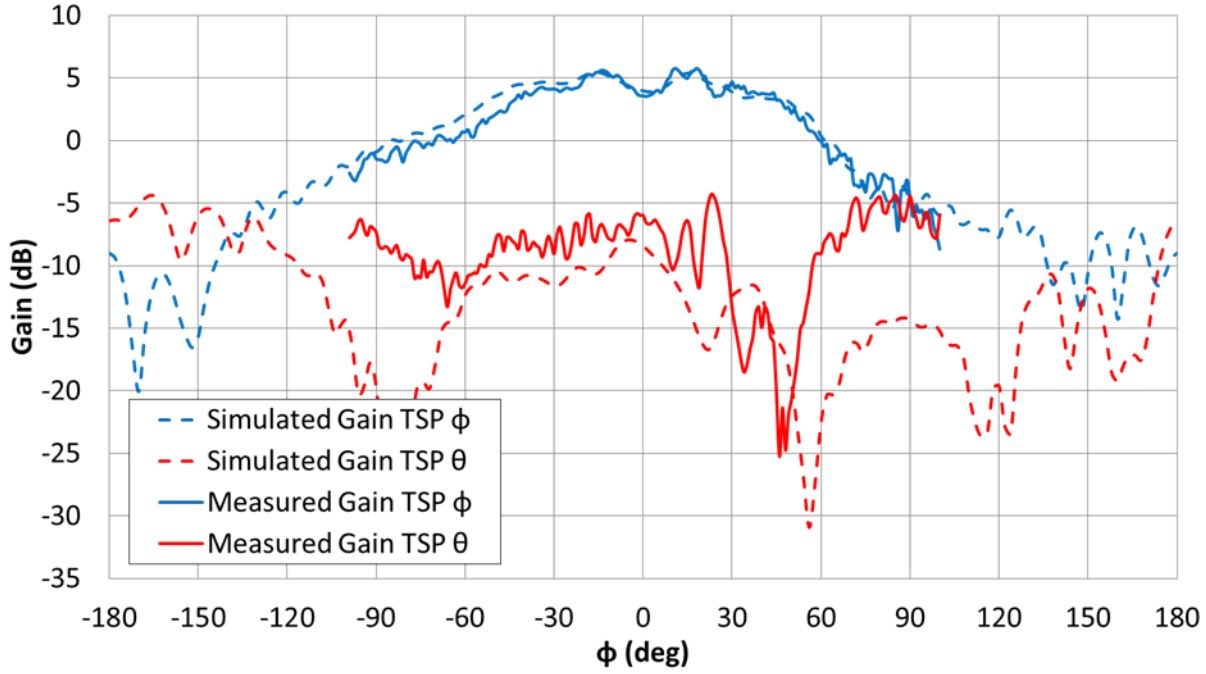

(b)

Figure 4-26: Antenna 3 and 4 Simulated vs Measured Beamforming Gain TSP in the planes at (a) ϕ = 90° and θ = 90°.

The figure 4-27 presents the gain for antenna 1 and 2 as well as the beamforming gain TSP. This figure illustrates the ΔG between the maximum gain achievable and the best gain among antenna 1 and 2. We observe that the beamforming configuration can provide a better gain in every direction of θ and ϕ.

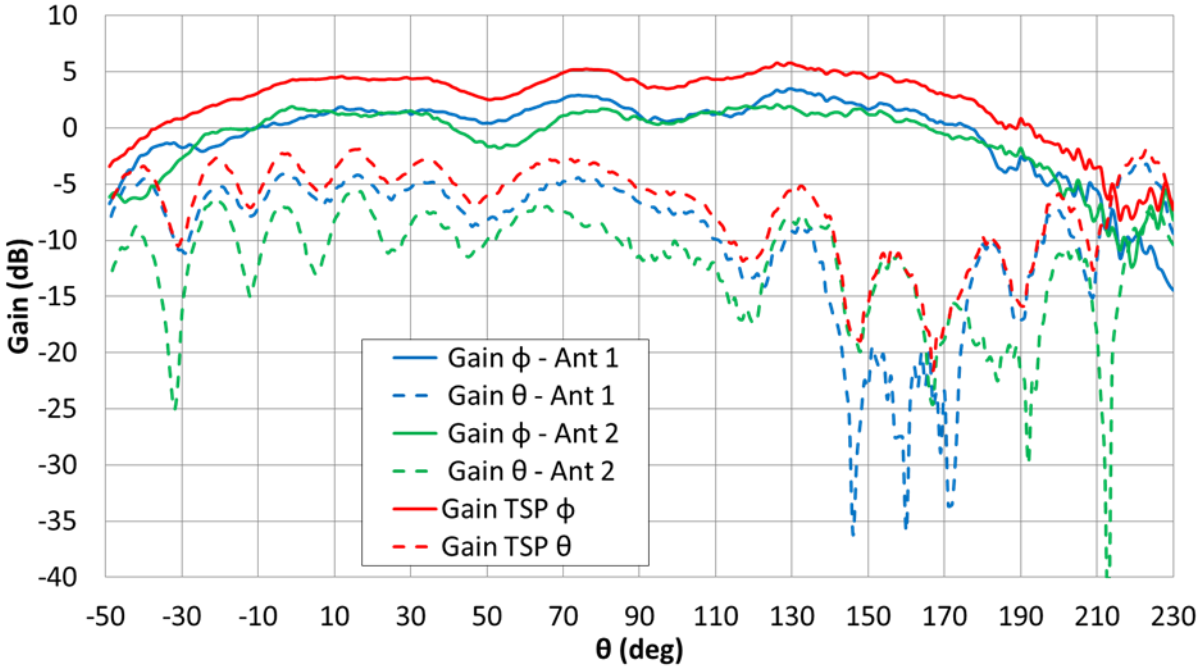

(a)

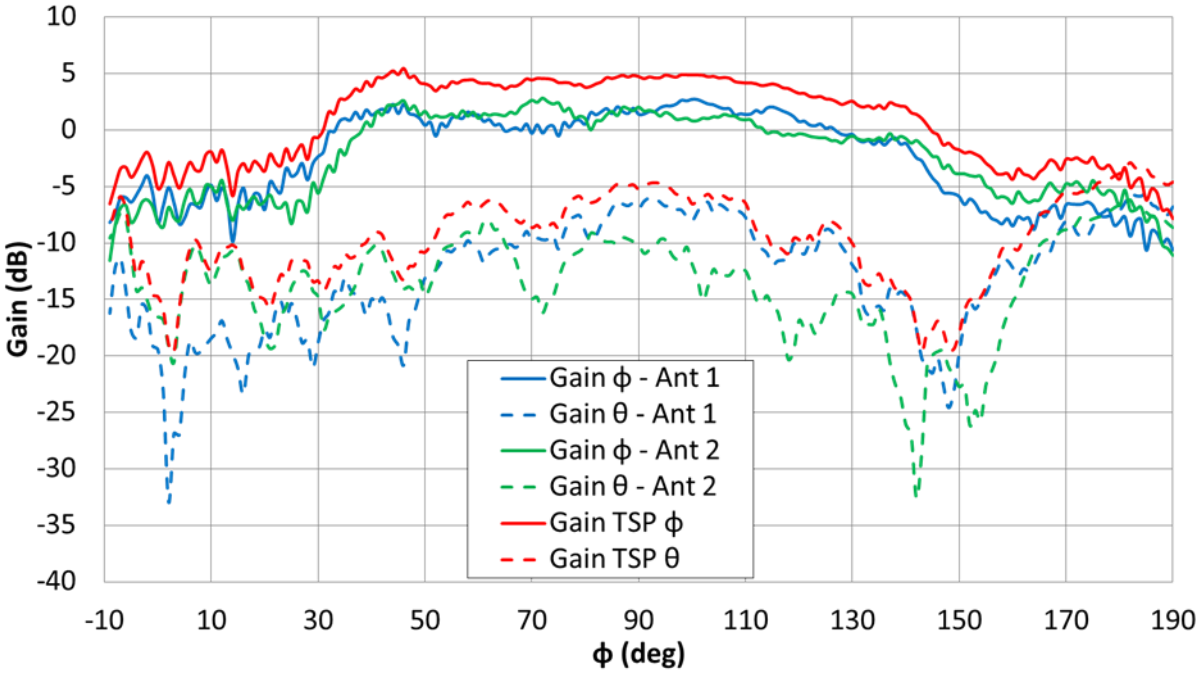

(b)

Figure 4-24-7 : Antenna 1 and 2 measured gain and beamforming Gain TSP in the planes at (a) ϕ = 90° and (b) θ = 90°.

4.4.5. Measurement of hand effect

Figure 4-29 shows the measured S-parameters of each antenna with the user effect, i.e., grabbing the smartphone as presented in Figure 4-28(a). We can observe that all the antennas still match the frequency band with good isolation between two elements of the same array. Casing and hands have a low influence on the antenna reflection coefficient, meaning that the reactive fields of the antennas are not distorted by the casing or the hand.

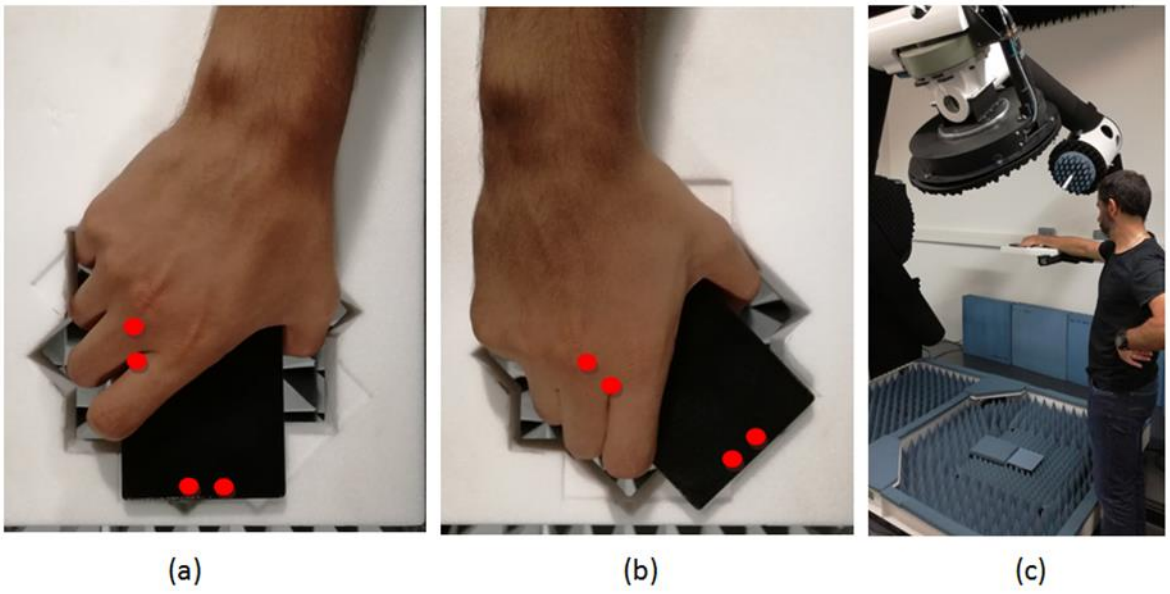

Figure 4-28: Photos of the grip in the two configurations (a) and (b) and a general view of the user holding the device.

For the radiation pattern measurement with hand effect, eight different people, men, and women volunteered in order to get results with hands of various sizes and shapes. For this experiment, we wanted to reduce the measurement time by focusing the acquisition in the antenna's region of interest. Indeed it was difficult not to move while holding the device for a long period (a full 3D radiation pattern is measured in about 20 minutes). Therefore we swept only 240° around the antenna in the vertical plane and 200° in the horizontal plane. Despite this limitation, we are able to observe the impact of the hand in a reliable way.

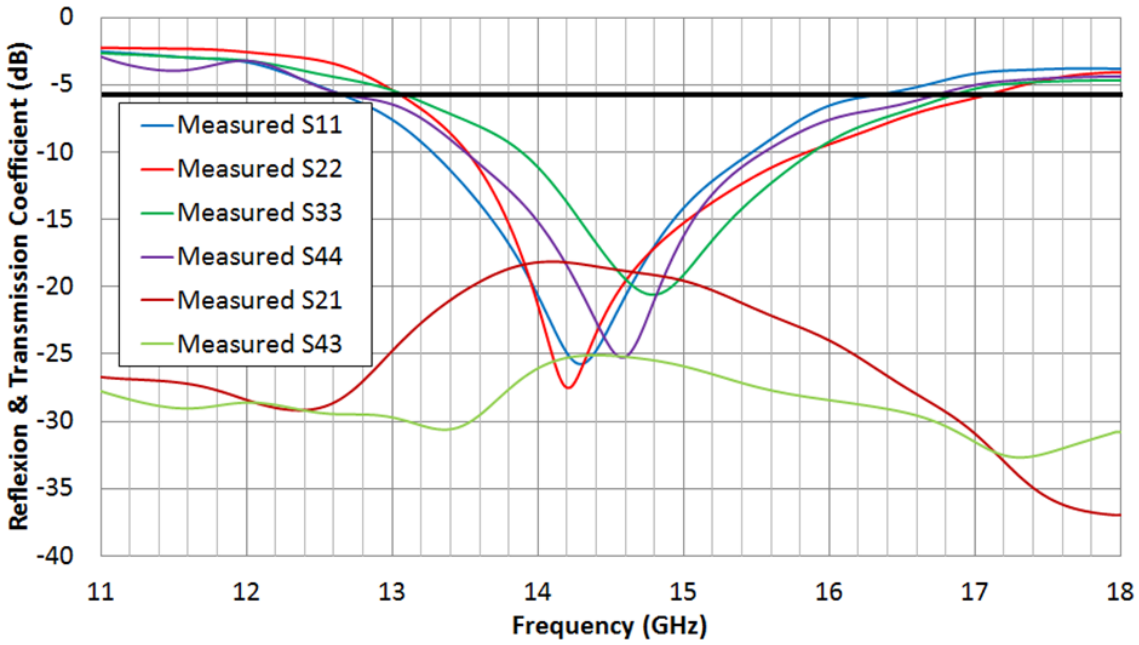

Figure 4-29: Return loss and isolation for each antenna for the measured prototype with hand effect.

Figure 4-30 presents the gain main component (Gain ϕ) of antenna 1 in both the planes at ϕ = 90° and θ = 90° for all the different user hands. The free space (FS) gain of antenna 1, already shown in Fig. 9(a), is reported for comparison. First, we observe that the radiation pattern is modified when the user's hand is holding the device especially in the direction where the hand is located, with a radiated power oriented to the top of the antenna. The hand absorbs all the bottom radiation. We also notice the variety of the results, which confirms the necessity to produce a lot of measurements to obtain statistically reliable results. Differences in the measurement results are, indeed, caused by the various sizes and shapes of hands we used as well as by slight variations in the holding position.

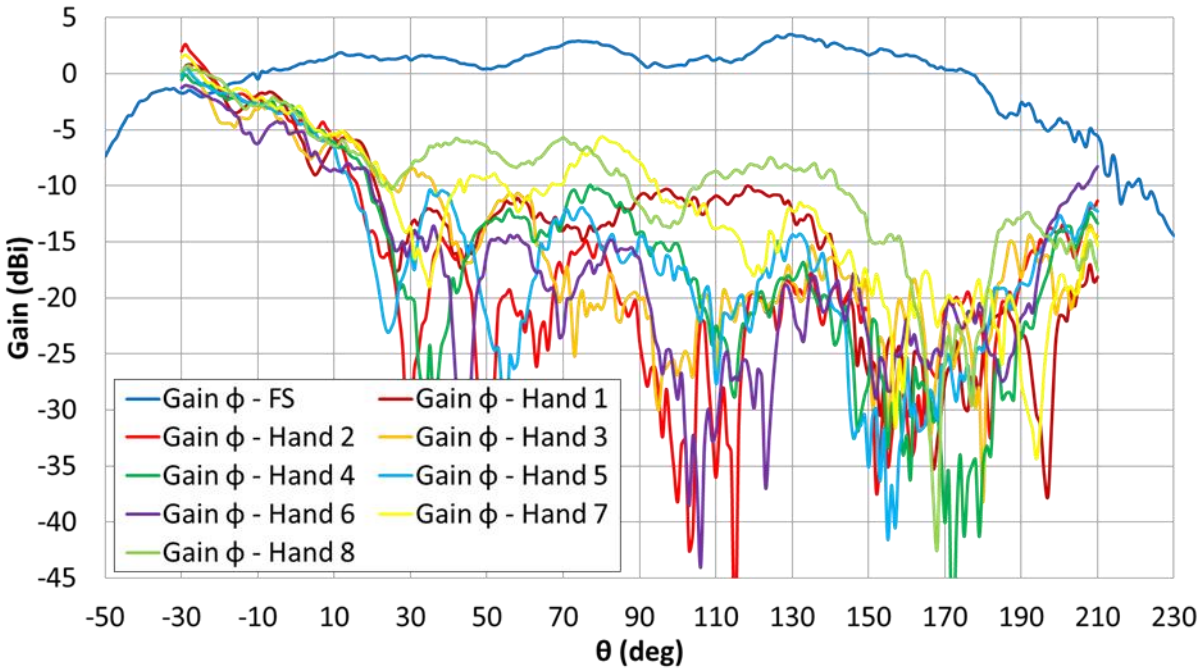

(a)

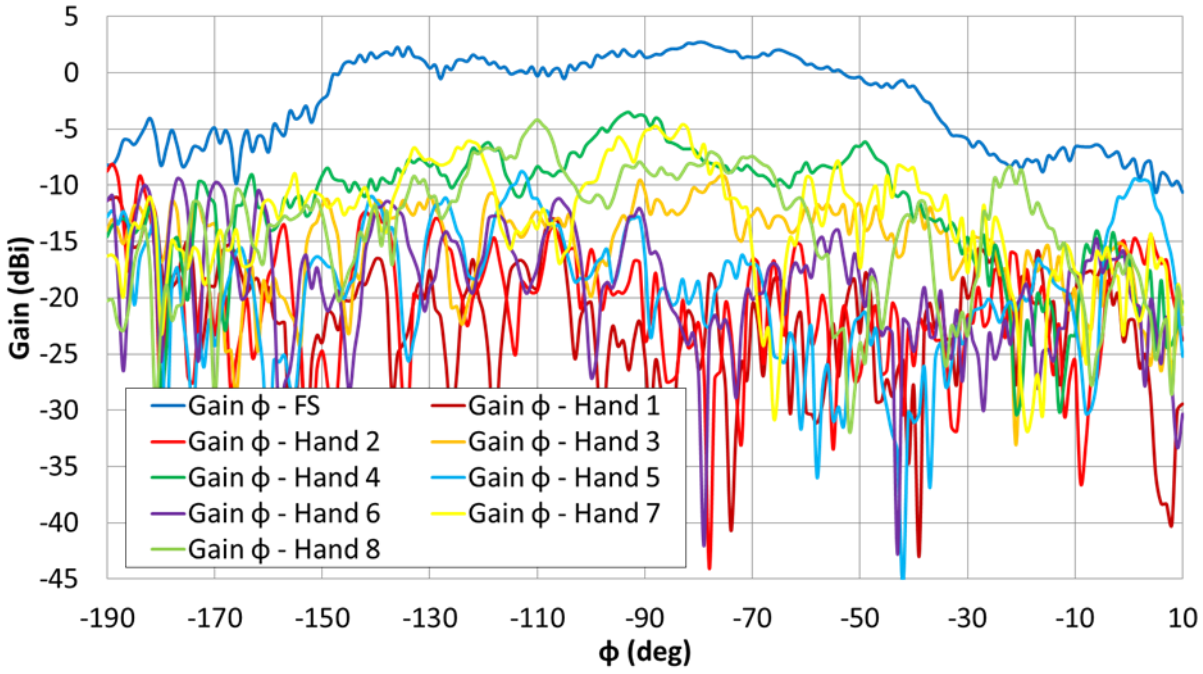

(b)

Figure 4-30: Antenna 1 free space and hand effect radiation measurement in the plane at (a) ϕ = 90° and θ = 90°.

For better visibility, we present in Figure 4-31 the average gain with hand blockage versus the free space measurements for antenna 1. Figure 4-31(a) clearly shows a decrease of the gain along the θ-axis (solid blue line) that is coherent with the holding position. We observe a maximum loss of 20 dB where the palm of the hand is entirely covering the smartphone. Figure 4-31(b) shows a quite constant 14 dB loss along the ϕ-axis.

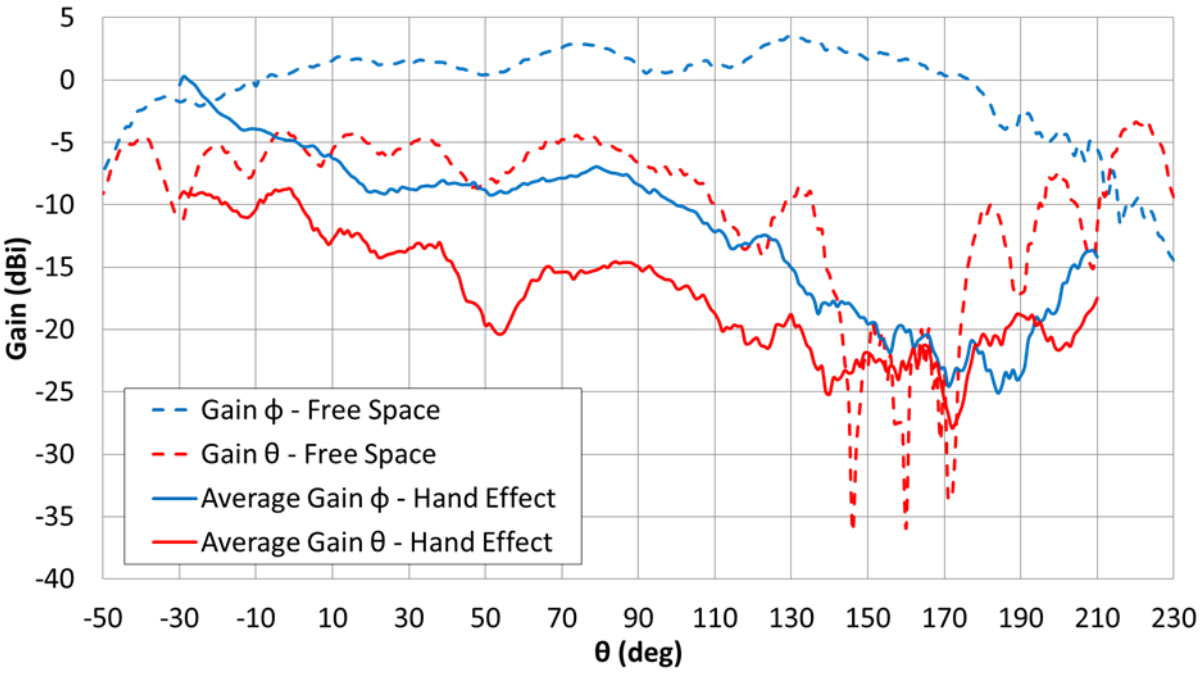

(a)

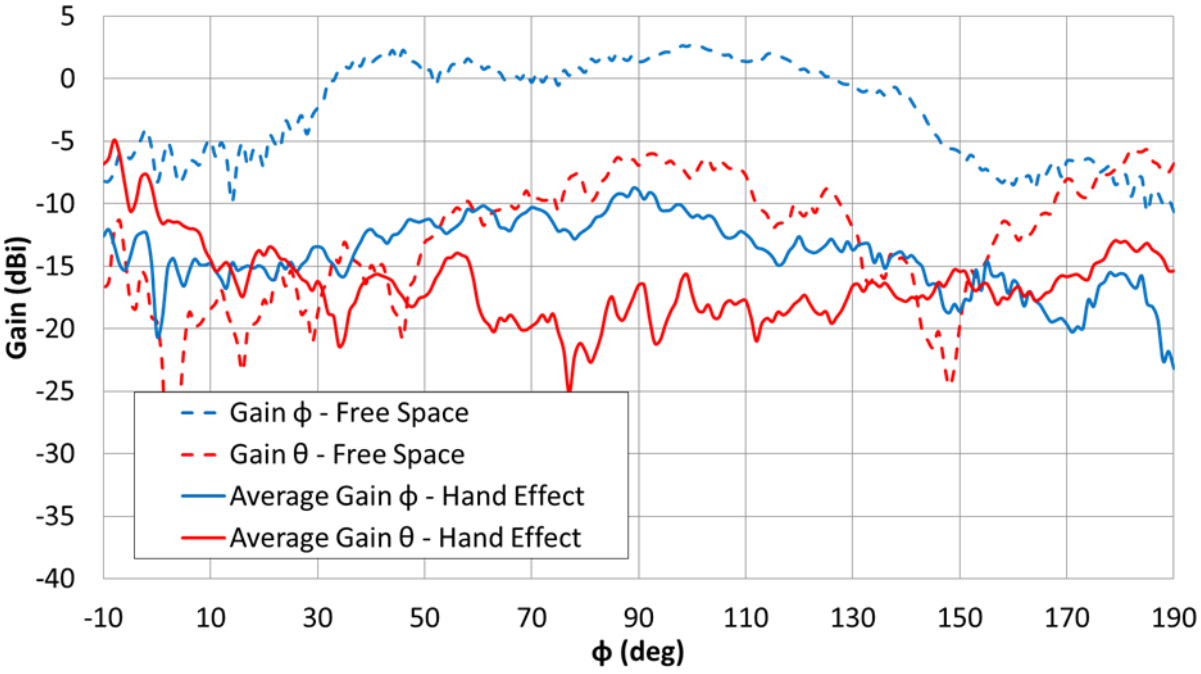

(b)

Figure 4-31: Antenna 1 free space and Average hand effect measured gain in the plane at (a) ϕ = 90° and θ = 90°.

The same behavior described above for the antenna 1 is visible in Figure 4-32, where the results for antenna 2 are reported.

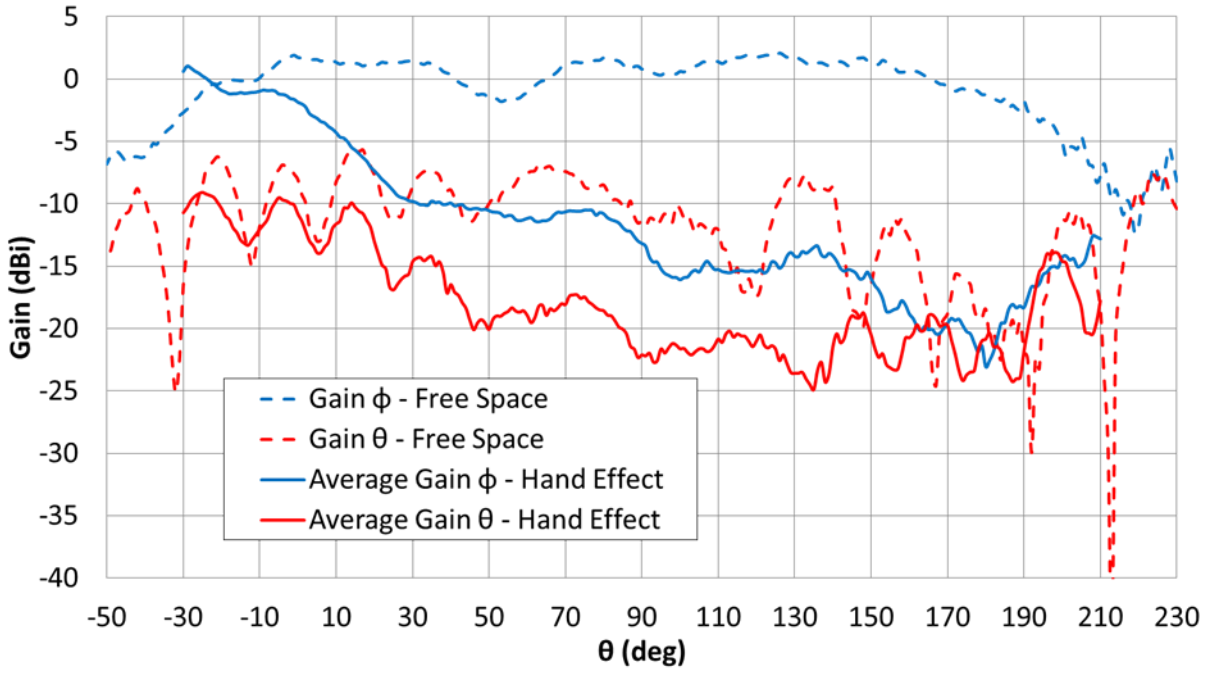

(a)

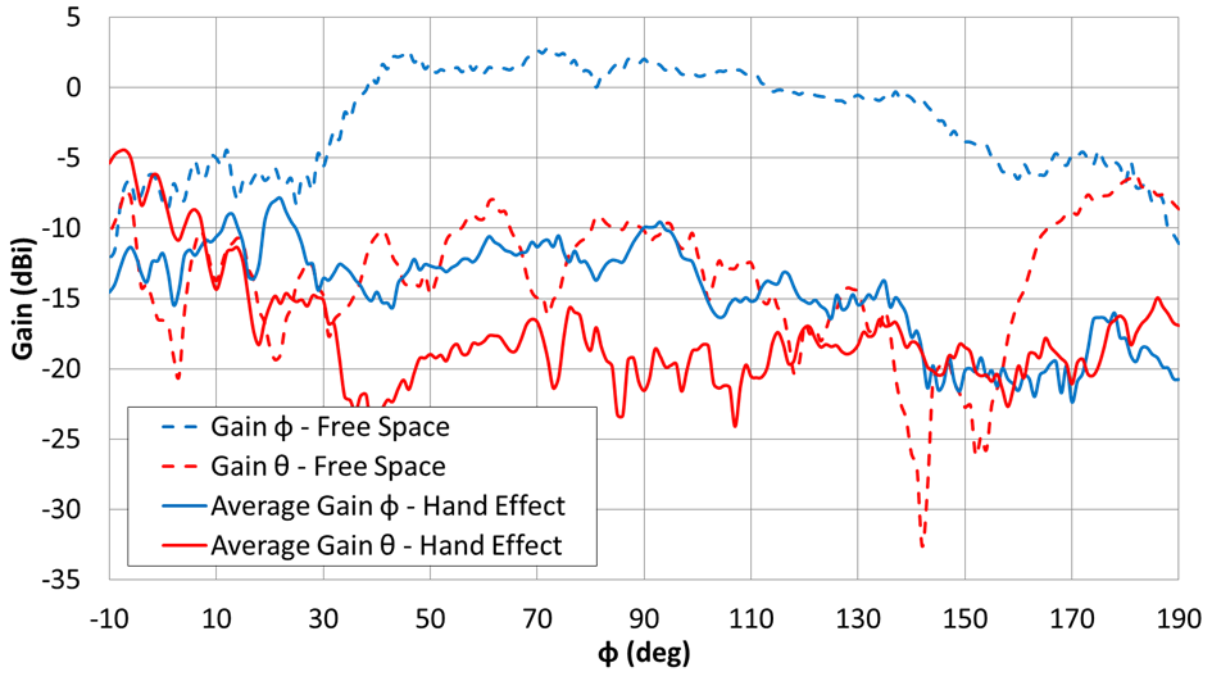

(b)

Figure 4-32: Antenna 2 free space and Average hand effect measured gain in the plane at (a) ϕ = 90° and θ = 90°.

As expected, antennas 3 and 4 are not impacted at all by the hand. The results are reported for the sake of completeness in Figures 4-33 and 4-34.

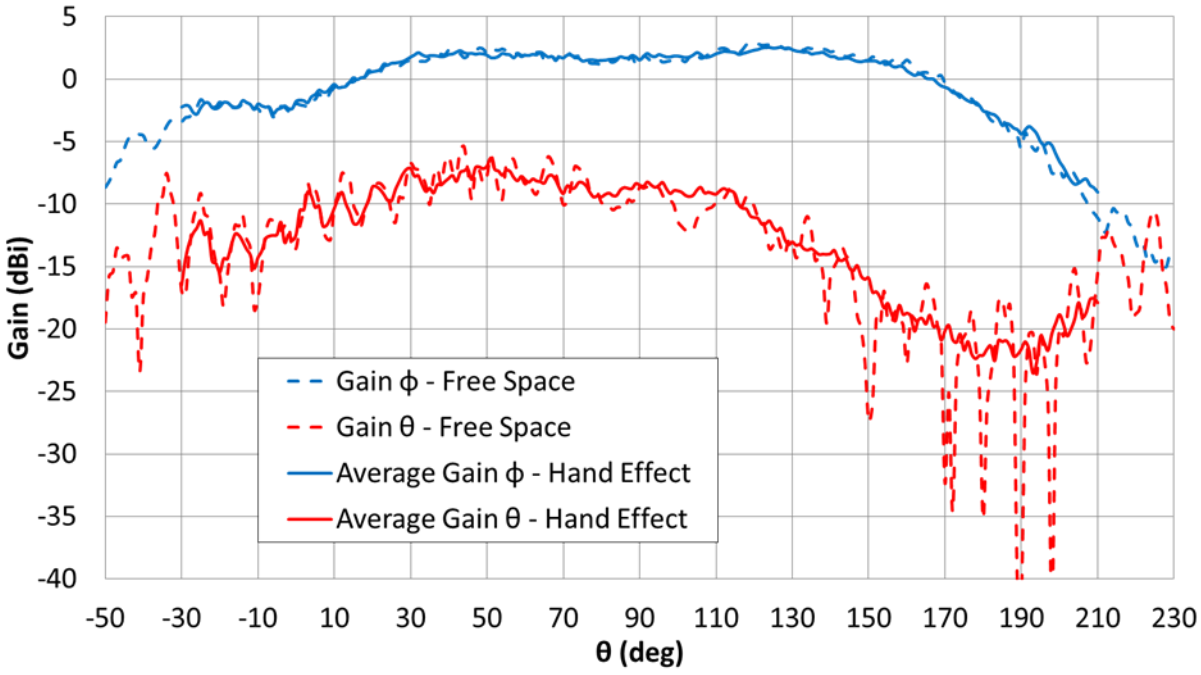

(a)

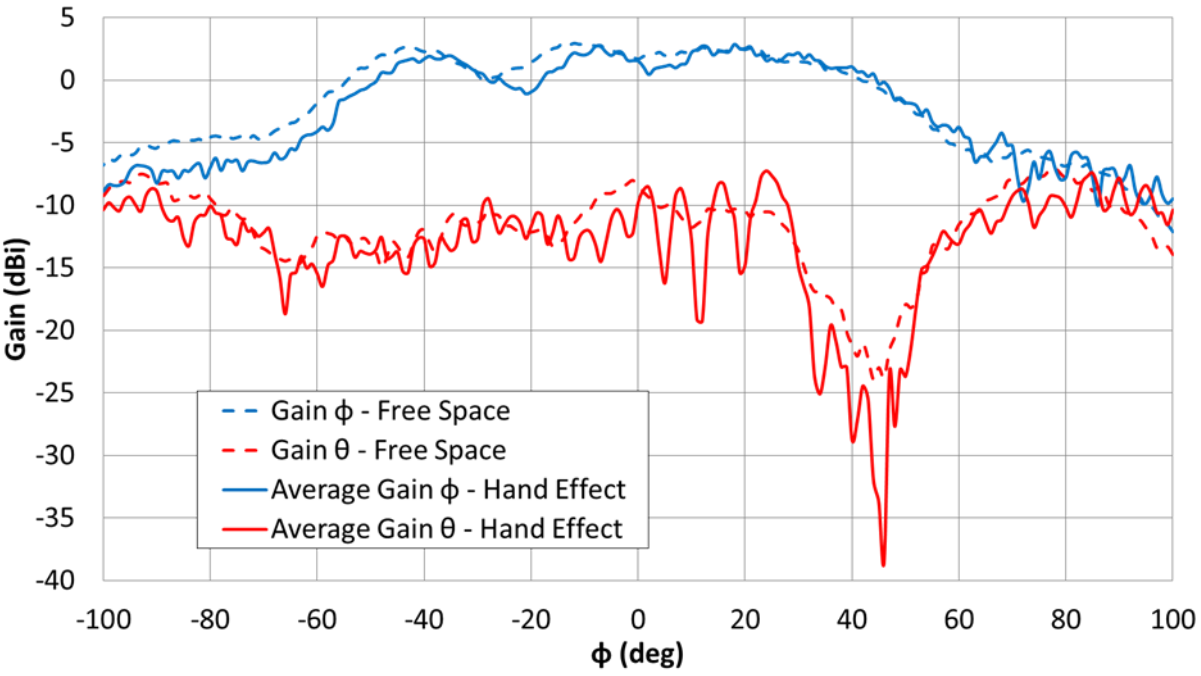

(b)

Figure 4-33: Antenna 3 free space and Average hand effect measured gain in the plane at (a) ϕ = 90° and θ = 90°.

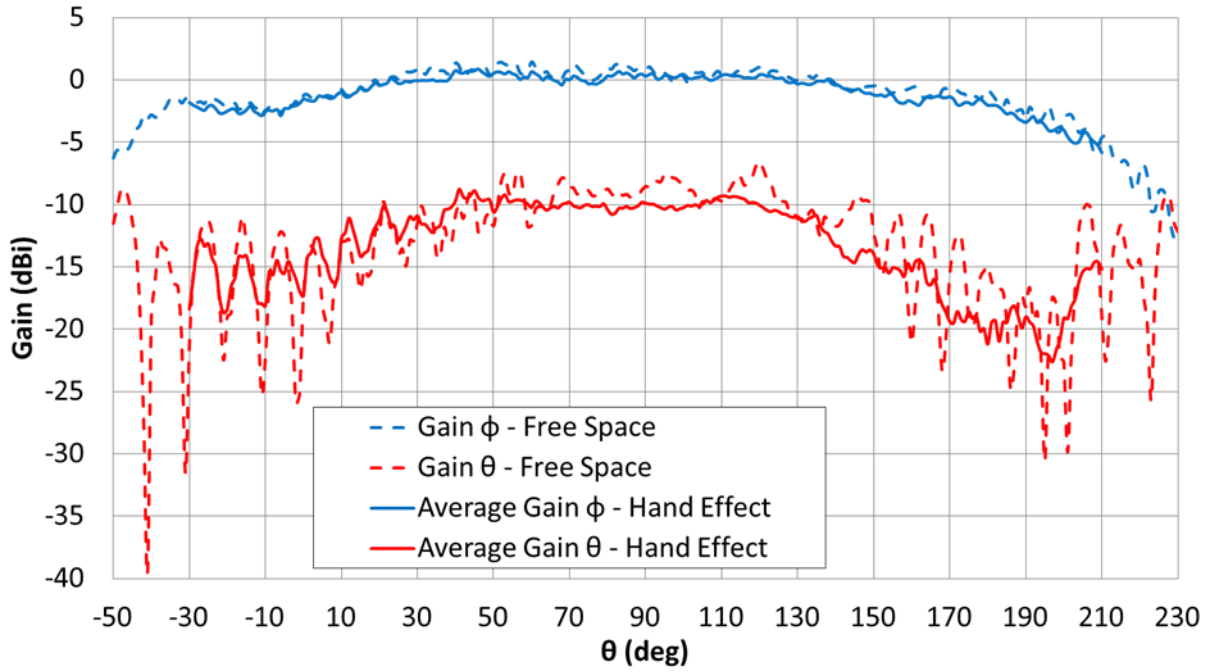

(a)

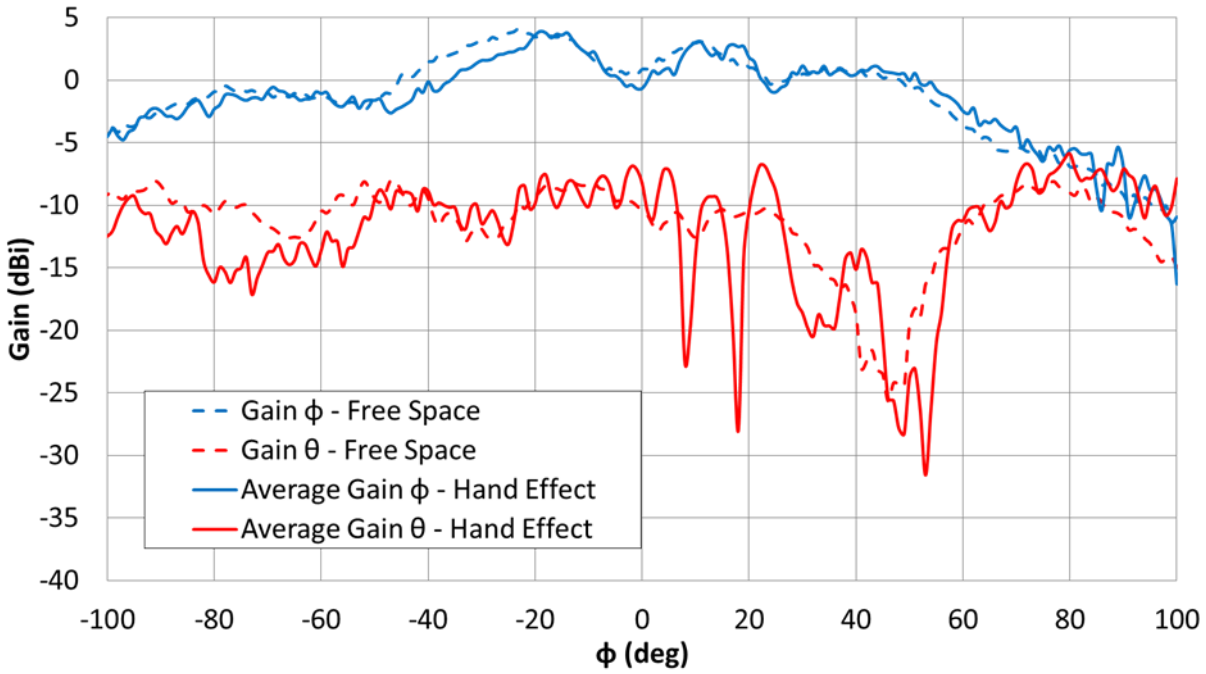

(b)

Figure 4-34: Antenna 3 free space and Average hand effect measured gain in the plane at (a) ϕ = 90° and θ = 90°.

Table 4-2 and table 4-3 present the average and maximum loss in gain caused by the user's hand on each antenna respectively for the plane at $\phi = 90°$ and $\theta = 90°$, respectively. The user's hand causes an average 14.7 dB loss in the vertical plane and 11.9 dB loss in the horizontal plane for the main polarization of antenna 1 with a maximum loss at 24.9 dB in the vertical plane. Antenna 2 is impacted the same way while antennas 3 and 4 maintain a similar gain as the one exhibited in free space.

Table 4-2: Loss with user blockage in the vertical plane θ.

Antenna n°	Avg. Loss Gain-ϕ (dB)	Avg. Loss Gain-θ (dB)	Max Loss Gain-ϕ (dB)	Max Loss Gain-θ (dB)
1	14.7	7.71	24.9	143
2	13.5	7.35	21.8	16.4
3	0.3	0.03	2.2	22.2
4	0.8	0.4	2.1	10.7

Table 4-3: Loss with user blockage in the horizontal plane ϕ.

Antenna n°	Avg. Loss Gain-ϕ (dB)	Avg. Loss Gain-θ (dB)	Max Loss Gain-ϕ (dB)	Max Loss Gain-θ (dB)
1	11.9	5.98	16.8	21.6
2	13.1	5.64	20.0	13.7
3	0.6	0.9	3.9	14.7
4	0.05	0.03	5.4	17.7

4.4.6. Beamforming Computation with Hand Effect

The beamforming computation method validated in a previous section is applied to measurements with hand effect. In this section, the analysis focuses on the array impacted by the user effect composed of antennas 1 and 2.

Table 4-4 presents the average beamforming gain achieved in free space and for the different measurement with each hand. Antennas 3 and 4 are not impacted by the user's body, so only the data for the beamforming achieved with antenna 1 and 2 are reported in this table. We observe that the beamforming is not as efficient as in free space when a user is holding the device. Indeed the best

beamforming gain achieved among the 8 measurements with the hand is 1.40 dB against 2.41 dB in free space in the vertical plane and 1.46 dB against 2.49 dB in the horizontal plane. Efficient beamforming cannot be achieved because user's interference increases the gain imbalance between the two antennas of the same array. Even if a maximum of 3 dB ΔG can be achieved, this performance cannot be controlled meaning that we cannot create a beam in a chosen direction.

Table 4-4: Beamforming gain and gain imbalance for the main polarization of antenna 1 and 2 in free space and with user blockage.

	Vertical Plane				Horizontal Plane			
	Average ΔG (dB)	**Max ΔG (dB)**	**Avg. Gain Imbalance (dB)**	**Max Gain Imbalance (dB)**	**Average ΔG (dB)**	**Max ΔG (dB)**	**Avg. Gain Imbalance (dB)**	**Max Gain Imbalance (dB)**
Free Space	2.52	3.0	1.33	7.29	2.44	3.0	1.41	3.53
Hand 1	1.61	3.0	8.72	25.1	1.27	3.0	10.6	22.7
Hand 2	1.73	3.0	5.09	13.5	1.16	3.0	13.5	27.9
Hand 3	1.62	3.0	7.12	19.4	1.47	3.0	10.4	22.7
Hand 4	1.64	3.0	11.6	26.3	1.15	3.0	11.8	25.2
Hand 5	1.29	3.0	9.67	22.6	1.05	3.0	13.4	29.9
Hand 6	1.70	3.0	10.1	23.8	1.55	3.0	9.06	21.3
Hand 7	1.60	3.0	6.04	16.8	1.74	3.0	10.5	24.8
Hand 8	1.42	3.0	19.7	25.1	1.43	3.0	14.6	30.0

Figure 4-35 presents a comparison between the TSP gain with the hand (solid lines) and in free space (dotted lines). In free space, antennas 1 and 2 achieve a 5.8 dBi maximum gain in the vertical plane (at θ = 128°, ϕ = 90°) and a 5.5 dBi maximum gain in horizontal plane (at θ = 90°, ϕ = 89°). We observe that G_{TSP} with hand effect is 25 dB lower than G_{TSP} in free space in the worst case. Around the direction at θ = -20°, G_{TSP} with the hand becomes higher than G_{TSP} in free space because the hand is not covering this area and the beamforming benefits of a small reflecting effect from the hand.

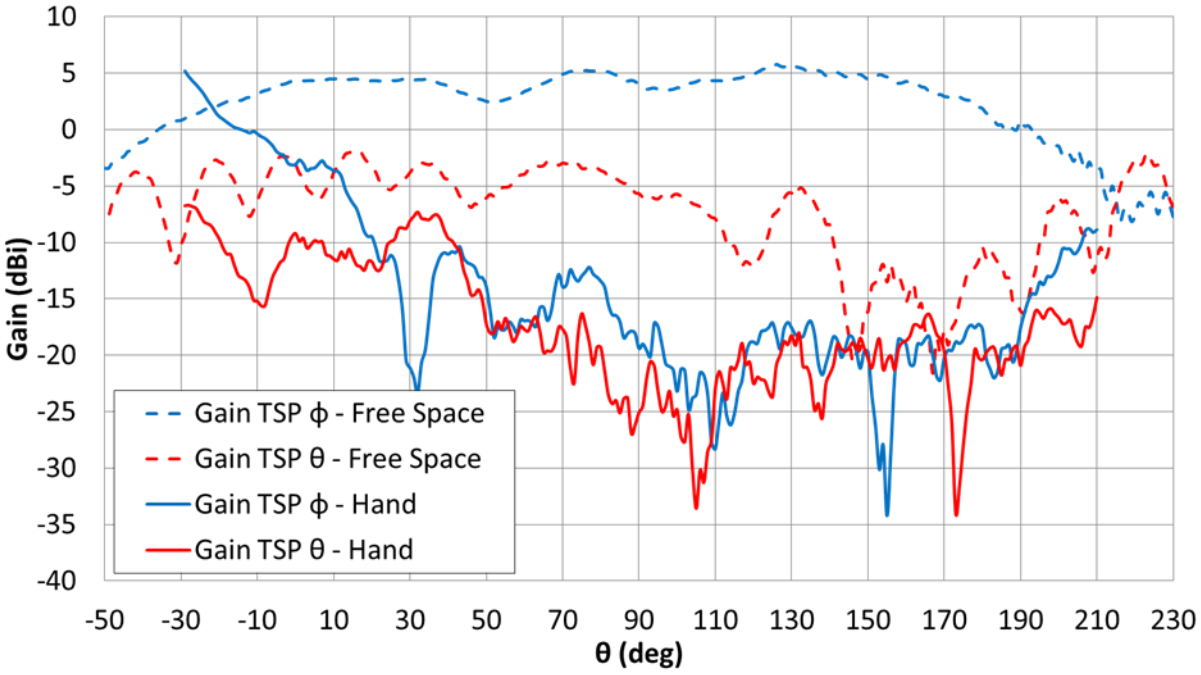

(a)

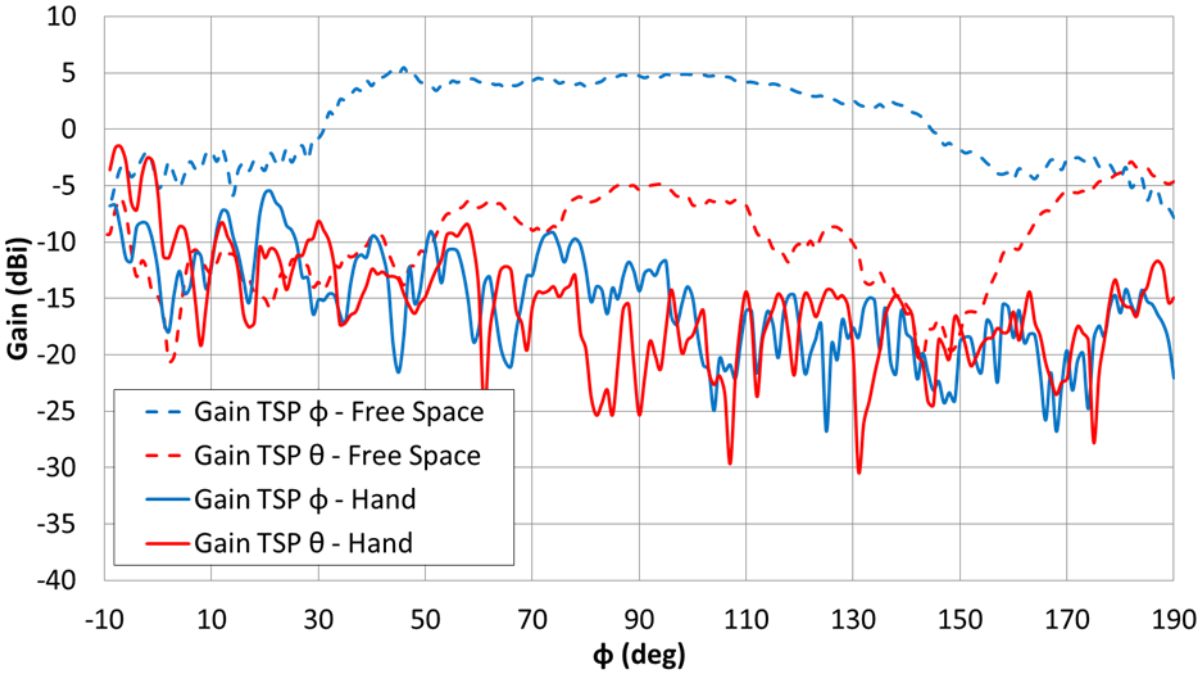

(b)

Figure 4-35 : Antenna 1 and 2 measured beamforming gains TSP in free space vs measured gain TSP with hand effect in the planes at (a) ϕ= 90° and (b) θ = 90°.

Figure 4-36 presents the beamforming gain TSP versus the gain of the two antennas composing the array. This figure aims to show that the beamforming capabilities regarding the orientation of the beam, are considerably reduced. Indeed when the user impact is too strong, it becomes impossible to choose a specific direction of transmission.

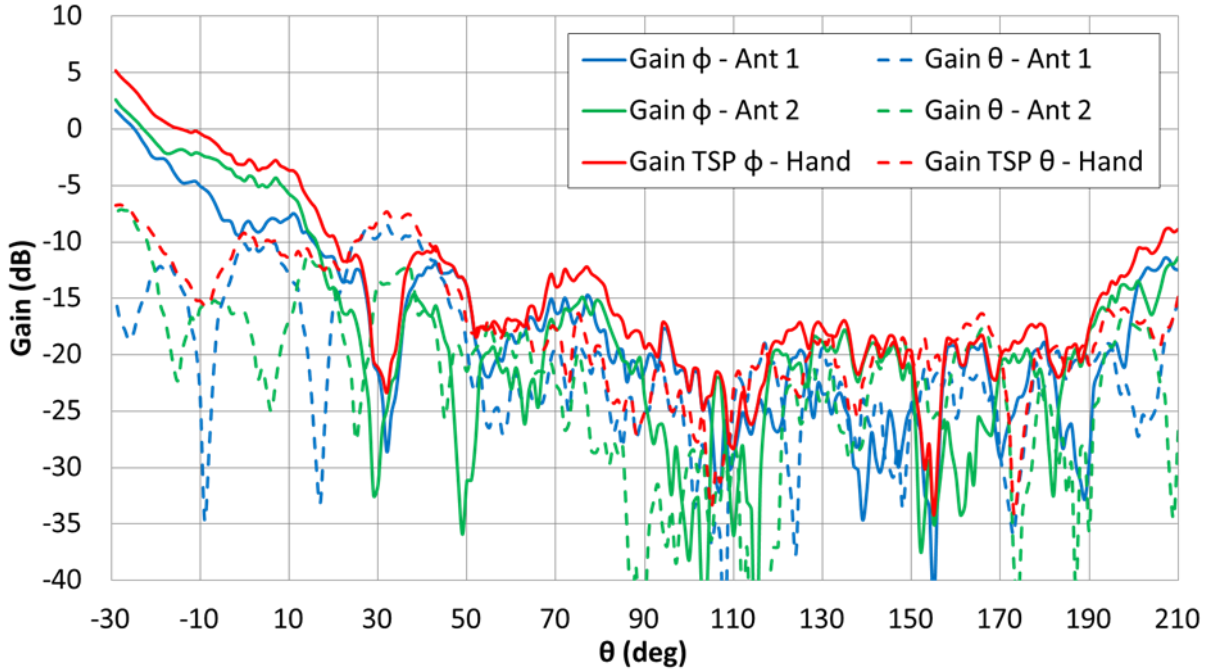

(a)

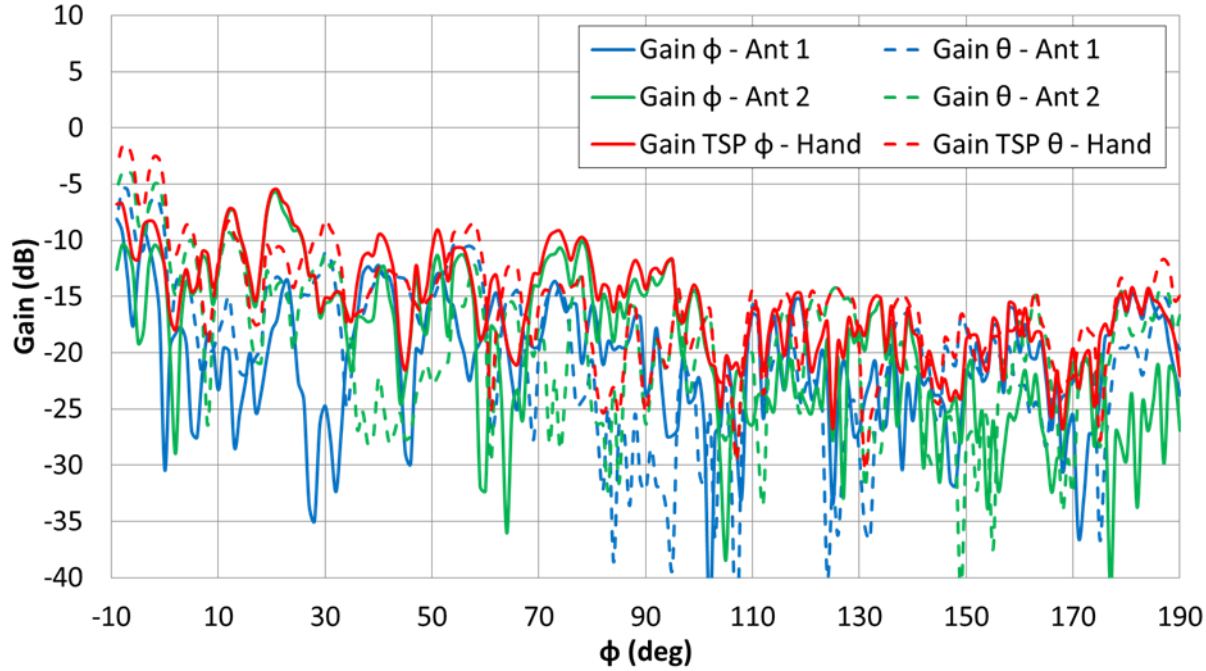

(b)

Figure 4-36: Antenna 1 and 2 measured gain and measured beamforming gain TSP with hand effect in the planes at (a) ϕ = 90° and (b) θ = 90°.

Figure 4-37 presents the cumulated distributed function (CDF) of ΔG as a function of θ and ϕ for the case in free space (dotted lines) and with the hand (solid lines). The blue lines correspond to the array with antennas 1 and 2 while the red lines are for the array with antenna 3 and 4. The main result is the difference between the blue lines, which shows the efficiency of the beamforming in both the free space and with the hand blockage configurations. It is clear that the beamforming with the hand

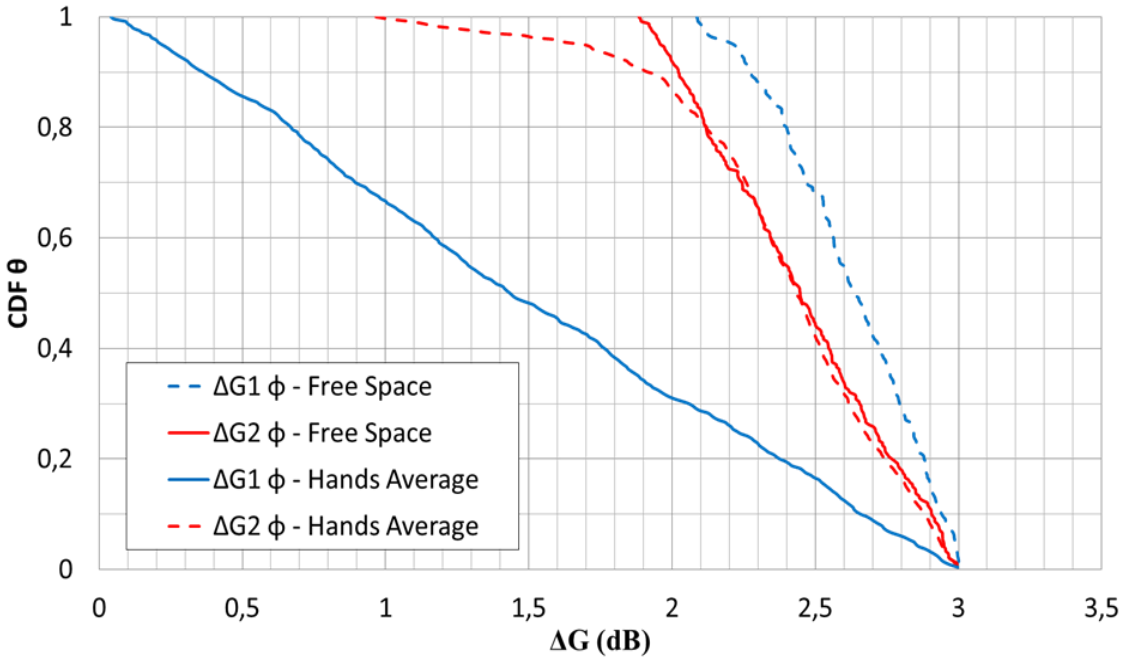

(a)

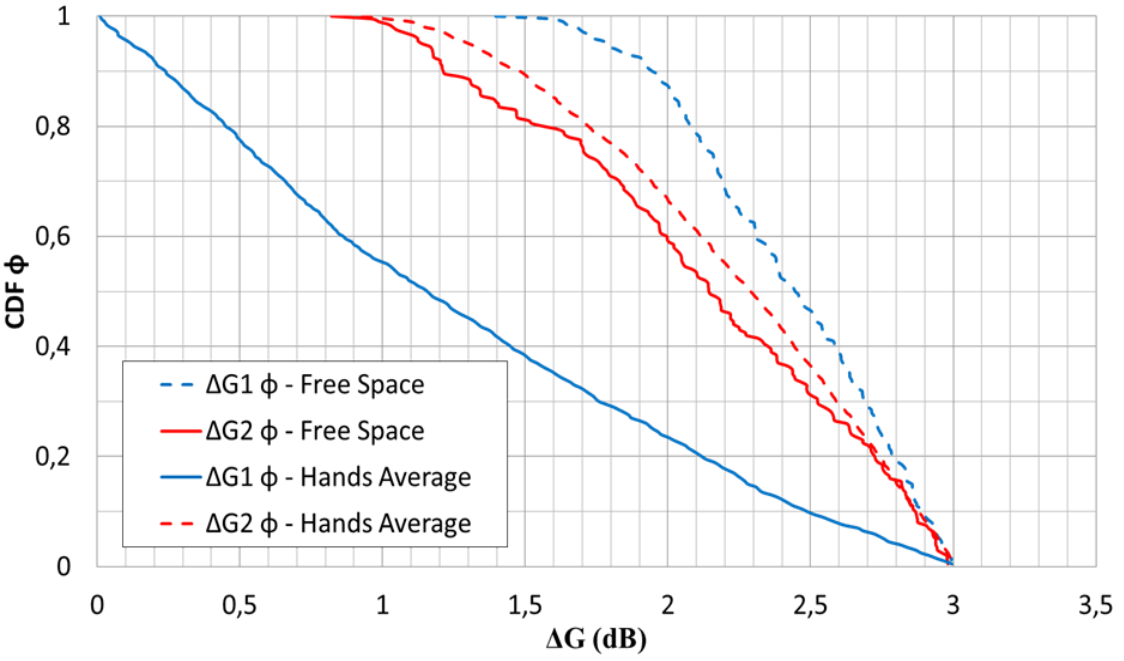

(b)

Figure 4-37: Cumulated Distributed Function of ΔG for both array in Free Space and with hand effect in the planes at (a) ϕ = 90° and (b) θ = 90°.

is at least twice less efficient than the beamforming in free space. For example, if we observe the blue lines in the horizontal plane, we can say that the probability that ΔG with hand effect becomes higher than 2 dB is only 20% while this probability rises to 85% in free space (30% vs. 100% in the vertical plane).

4.4.7. Conclusion of the study at 15 GHz

We designed and realized a mobile phone prototype at 15 GHz according to future 5G requirements to study the body loss impact on beamforming performance. We proposed a new measurement approach to investigate hand effect on a handset terminal. Influence of real user's hands has been investigated thanks to a spherical near-field scanner with fixed AUT. Results are based on a measurement campaign involving 8 people. Body dielectric properties versus frequency are not constant, and an important impact of the hand on millimeter-Wave terminals has to be expected. Indeed, results show an average decrease of 12 dB of the gain at 15 GHz for a real human hand and loss up to 25 dB in the most impacted directions while the average body loss below 6 GHz is around 6 dB. Moreover, imbalances caused by user's interferences considerably reduce the beamforming performance and avoid creating a beam in a specific direction. Antenna implementation within handset device become crucial and must take into account real use cases when it comes to high frequency bands.

4.5. Conclusion and Perspectives

The study points out the limitations of millimeter wave handset devices and highlights the importance of a smart implementation of antennas in the future 5G cellular network. We observed that the beamforming gain is far from reaching the theoretical 3 dB expected for a two antenna array when the user is covering the antennas. We noticed that user interferences cause a great gain imbalance between antennas in an array, especially at millimeter-waves where antennas are physically close to each other (with respect to the hand dimension). Moreover, the radiation pattern degradation caused by user's hand deletes the ability to choose the beamforming direction. Finally, the experiments confirmed that loss in human body increases at high frequency.

We studied a 2-elements antenna array, but we can predict that similar behavior would be obtained for bigger arrays. Millimeters bands phased arrays are known candidates for 5G handset devices, but it has become obvious that user's blockage is a great obstacle that must be overcome

before implementing this technology in smartphones. At this point, we can say that antenna configuration and implementation is a key parameter for the design of 5G handset devices. More than ever, use cases must be studied and anticipated to design efficient antenna arrays in mobile terminals. The optimal number of array and their location, as well as the number of antenna per array, should be optimized regarding the different use cases, the power consumption and the coverage efficiency. Furthermore at 28 GHz cables are very lossy or very expensive so RF front-end must be located just behind antennas. Those new constraints might lead to a complete revisit of the RF hardware architecture. This study might be generalized by testing implementations with more antennas on the device and higher order MIMO configurations. More use cases should be tested such as a two hands grip on the mobile device or the talk mode with the impact of the hand and the head. Finally, the measurement full 3D radiation pattern with hand effect might give more information.

4.6. References

[IV-1] Ericsson Mobility report, Ericsson, June 2015

[IV-2] Samsung Electronics Co., 5G vision, White Paper, February 2015

[IV-3] Huawei Technologies Co., 5G: A technology vision, White paper, February 2014

[IV-4] W. Roh et al.,"Millimeter-wave beamforming as an enabling technology for 5G cellular communications: theoretical feasibility and prototype results," in IEEE Communications Magazine, vol. 52, no. 2, pp. 106-113, February 2014.

[IV-5] J. Helander, D. Sjberg, M. Gustafsson, K. Zhao, and Z. Ying, "Characterization of millimeter wave phased array antennas in mobile terminal for 5G mobile system," 2015 IEEE International Symposium on Antennas and Propagation & USNC/URSI National Radio Science Meeting, Vancouver, BC, 2015, pp. 7-8.

[IV-6] Wei-Yu Li, Wei Chung, Tune-Hune Kao, Meng-Chi Huang and Ming-Tsung Hong, "Novel 11 GHz 2-port antenna array integrated at a corner of mobile phone casing by LIM technologies of ITRI with diverse end-fire radiation patterns" in *AP-S 2015*

[IV-7] J. Helander, K. Zhao, Z. Ying and D. Sjberg, "Performance Analysis of Millimeter-Wave Phased Array Antennas in Cellular Handsets," in IEEE Antennas and Wireless Propagation Letters, vol. 15, no. , pp. 504-507, 2016

[IV-8] W. Hong, K. Baek, Youngju Lee and Yoon Geon Kim, "Design and analysis of a low-profile 28 GHz beam steering antenna solution for Future 5G cellular applications," 2014 IEEE MTT-S International Microwave Symposium (IMS2014), Tampa, FL, 2014, pp. 1-4.

[IV-9] H. Zhou, "Phased array for millimeter-wave mobile handset," 2014 IEEE Antennas and Propagation Society International Symposium (APSURSI), Memphis, TN, 2014, pp. 933-934.

[IV-10] N. Ojaroudiparchin, M. Shen and G. F. Pedersen, "A 28 GHz FR-4 compatible phased array antenna for 5G mobile phone applications," 2015 International Symposium on Antennas and Propagation (ISAP), Hobart, TAS, 2015, pp. 1-4.

[IV-11] J. Krogerus, C. Icheln and P. Vainikainen, "Effect of Human Body on 3-D Radiation Pattern and Efficiency of Mobile Handsets," 2005 IEEE Instrumentation and Measurement Technology Conference Proceedings, Ottawa, Ont., 2005, pp. 271-276.

[IV-12] I. Syrytsin, S. Zhang and G. F. Pedersen, "Performance Investigation of a Mobile Terminal Phased Array With User Effects at 3.5 GHz for LTE Advanced," in IEEE Antennas and Wireless Propagation Letters, vol. 16, no. , pp. 226-229, 2017

[IV-13] S. S. Zhekov, A. Tatomirescu, E. Foroozanfard and G. F. Pedersen, "Experimental investigation on the effect of user's hand proximity on a compact ultrawideband MIMO antenna array," in IET Microwaves, Antennas & Propagation, vol. 10, no. 13, pp. 1402-1410, 10 22 2016.

[IV-14] V. Plicanic, B. K. Lau, A. Derneryd, and Z. Ying, "Actual Diversity Performance of a Multiband Diversity Antenna With Hand and Head Effects," in IEEE Transactions on Antennas and Propagation, vol. 57, no. 5, pp. 1547-1556, May 2009.

[IV-15] K. R. Boyle, Y. Yuan and L. P. Ligthart, "Analysis of Mobile Phone Antenna Impedance Variations With User Proximity," in IEEE Transactions on Antennas and Propagation, vol. 55, no. 2, pp. 364-372, Feb. 2007.

[IV-16] M. Pelosi, O. Franek, M. B. Knudsen, M. Christensen and G. F. Pedersen, "A Grip Study for Talk and Data Modes in Mobile Phones," in IEEE Transactions on Antennas and Propagation, vol. 57, no. 4, pp. 856-865, April 2009.

[IV-17] M. Pelosi, O. Franek, M. B. Knudsen, G. F. Pedersen and J. B. Andersen, ”Antenna Proximity Effects for Talk and Data Modes in Mobile Phones,” in IEEE Antennas and Propagation Magazine, vol. 52, no. 3, pp. 15-27, June 2010.

[IV-18] W. Hong, K. Baek, Y. Geon Kim, Y. Lee and B. Kim, ”mmWave phased array with hemispheric coverage for 5th generation cellular handsets,” The 8th European Conference on Antennas and Propagation (EuCAP 2014), The Hague, 2014, pp. 714-716.

[IV-19] K. Zhao, J. Helander, D. Sjberg, S. He, T. Bolin, and Z. Ying, ”User Body Effect on Phased Array in User Equipment for the 5G mmWave Communication System,” in IEEE Antennas and Wireless Propagation Letters, vol. 16, no., pp. 864-867, 2017.

[IV-20] I. Syrytsin; S. Zhang; G. Pedersen; K. Zhao; T. Bolin; Z. Ying, ”Statistical Investigation of the User Effects on Mobile Terminal Antennas for 5G Applications,” in IEEE Transactions on Antennas and Propagation, vol.PP, no.99, pp.1-1

[IV-21] F. Ferrero, Y. Benoit, L. Brochier, J. Lanteri, J-Y Dauvignac, C. Migliaccio, S.F. Gregson, Spherical scanning measurement challenge for future millimeters wave applications, AMTA 2015, October 2015, Long Beach, USA.

[IV-22] S. Gabriel, R.W. Lau, C. Gabriel, The dielectric properties of biological tissues: II. Measurements in the frequency range 10 Hz to 20 GHz, Phys. Med. Biol. 41 (1996), 2251-2269.

[IV-23] C. Sabatier, P. Brachat, A. Calderone, E. Seguenot, F. Devillers, ”Compact linear array at 810 MHz,” in Antennas and Propagation Society International Symposium, 1997. IEEE, 1997 Digest, vol.4, no., pp.2119-2122 vol.4, 13-18 July 1997

Conclusion

In the context of the ongoing 5G research, the thesis has focused on MIMO antennas, one of the breakthrough technology of enabling high data rates for 4G and Wi-Fi technologies. We axed the problematic around the design and the evaluation of multi-antenna systems for small devices such as a gateway, small-cell, and smartphones.

In chapter 2, we presented the development of two OTA measurements setup to assess performances of those devices. To conduct the study on multi-antenna gateways we retained the testbed developed with OpenAirInterface because of its flexibility and low cost compared to the system developed with Rhodes&Schwarz instrumentations.

In chapter 3, we presented several antenna designs based on the idea to create a new concept of Livebox for Orange. We intended to fully exploit the capabilities of the WLAN 802.11ac standard in terms of MIMO techniques. For this purpose, we studied antenna implementation inside a small access point to improve the efficiency of the global system. The originality of the work was the use of the LDS technology to print antennas on the plastic case. We compared this technology with the classic PCB solution by performing a set of free-space measurement with a VNA and a Satimo StarLab. To get deeper into the evaluation of the performance of the prototypes with performed OTA measurements thanks to the OAI measurement setup. The results have shown the benefits of LDS technology. Moreover, antenna selection has been implemented in the OAI setup and has shown interesting results. Indeed we demonstrated that a MISO 4x1 beamforming performed with antenna selection achieves quasi equivalent performance than a MISO 8x1.

We also explored directional antenna and their influence on the performance of multi-antenna gateway through the realization of an 8 antenna prototype constituted of directional antennas. Despite a high number of measurement, we were not able to draw a very clear conclusion on any improvement brought by the antenna directivity. More experiments with different position of the gateway should be conducted to sharpen the conclusions.

In chapter 4, we conducted a study on high frequency mobile phone antennas. By leveraging a 3D measurement setup, we were able to assess the beamforming capabilities of a 2-elements antenna array in the presence of user blockage at 15 GHz. The first conclusion was that loss in human body

increases at high frequencies. Moreover, the study pointed out the limitations of millimeter wave handset devices and highlighted the importance of a smart antennas implementation and configuration in the future 5G cellular network. Indeed, we observed that the beamforming gain was considerably impacted by the user's hand. Consequently, it becomes very difficult for the antenna array to radiate in a chosen direction. Even though the study was conducted only with 2 antennas at 15 GHz with can predict similar behavior in a 28 GHz devices with 4 or 8 elements.

List of publications

International Conference Papers

C. Buey, K. Bashir, J. M. Fargeas, P. Ratajczak, L. H. Trinh and F. Ferrero, "Design of a dual-band MIMO WIFI gateway," *2014 IEEE Conference on Antenna Measurements & Applications (CAMA)*, Antibes Juan-les-Pins, 2014, pp. 1-4.

C. Buey, F. Ferrero, L. Lizzi, P. Ratajczak, Y. Benoit and L. Brochier, "Investigation of hand effect on a handheld terminal at 11 GHz," *2016 10th European Conference on Antennas and Propagation (EuCAP)*, Davos, 2016, pp. 1-5.

C. Buey, T. Magounaki, F. Ferrero, P. Ratajczak, L. Lizzi and F. Kaltenberger, "MIMO antenna performance assessment based on open source software defined radio," *2017 11th European Conference on Antennas and Propagation (EUCAP)*, Paris, 2017, pp. 644-647.

C. Buey, P. Ratajczak, F. Ferrero, L. Lizzi, T. Magounaki and F. Kaltenberger, "Validation of an open source software defined radio test bed," *2017 IEEE International Symposium on Antennas and Propagation & USNC/URSI National Radio Science Meeting*, San Diego, CA, 2017, pp. 1875-1876.

C. Buey, F. Ferrero, L. Lizzi and P. Ratajczak, "Measurement set-up for the assessment of user impact on handheld terminal beyond 10 GHz," *2017 IEEE Conference on Antenna Measurements & Applications (CAMA)*, Tsukuba, 2017, pp. 327-329.

Co-Author Papers

T. Magounaki, F. Kaltenberger, X. Jiang, **C. Buey**, P. Ratajczak and F. Ferrero, "Experimental evaluation of relative calibration in a MISO-TDD system," *2017 European Conference on Networks and Communications (EuCNC)*, Oulu, 2017, pp. 1-5.

Appendix:

Polycarbonate Dielectric Properties Characterization.

In order to characterize the polycarbonate dielectric properties, we used the "N1500A Keysight Material Measurement Suite" with the dielectric probe kit. The N1500A software controls a Keysight network analyzer which measures through the probe, the material's response to RF and calculates results. The probe is used on a polycarbonate sample of dimensions 5x5x2.5 cm^3 presented in figure 1. The polycarbonate permittivity is measured between 2 GHz and 6 GHz. The measured permittivity is presented in figure 2. The estimated permittivity is $\varepsilon_r = 2.8$ at 2.4 GHz.

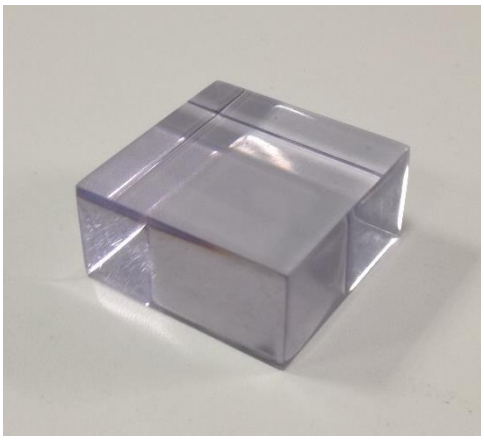

Figure Appendix-1: Picture of the polycarbonate sample.

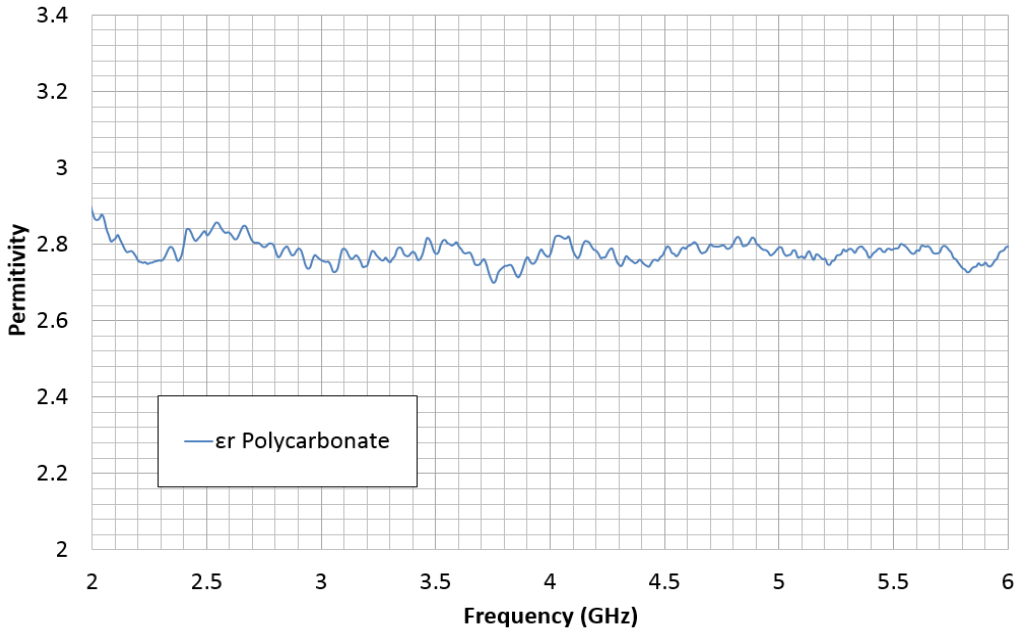

Figure Appendix-2: Measured Polycarbonate Dielectric Permittivity.

In order to validate the measured permittivity and to estimate the loss tangent of the polycarbonate, we realized a patch antenna radiating at 2.4 GHz. We simulated this patch of dimensions 35.5x43.5 mm² on a polycarbonate substrate of thickness h = 1mm, permittivity ε_r = 2.8 and loss tangent tanδ = 0.02. The feeding coaxial cable is located at 6.6 mm from the center of the patch antenna on the y axis. The simulated and realized patch antenna are presented in figure 3(a) and figure 3(b) respectively. The return loss of the patch antenna is measured and compared to the simulation. Then the patch is retro-simulated to adjust the polycarbonate permittivity and loss tangent. The return loss of the simulated, measured and retro-simulated patch antenna are presented in figure 4. We determined the polycarbonate permittivity at **ε_r = 2.69** and loss tangent **tanδ = 0.013**.

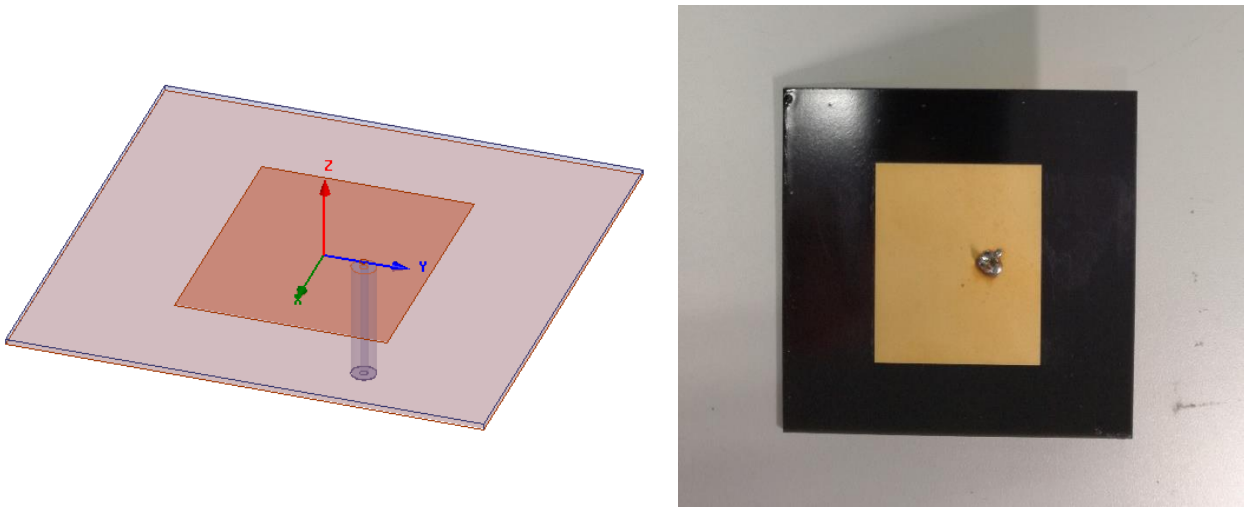

(a) (b)

Figure Appendix-3: Pictures of (a) the simulated patch antenna and (b) the realized patch antenna on the polycarbonate substrate.

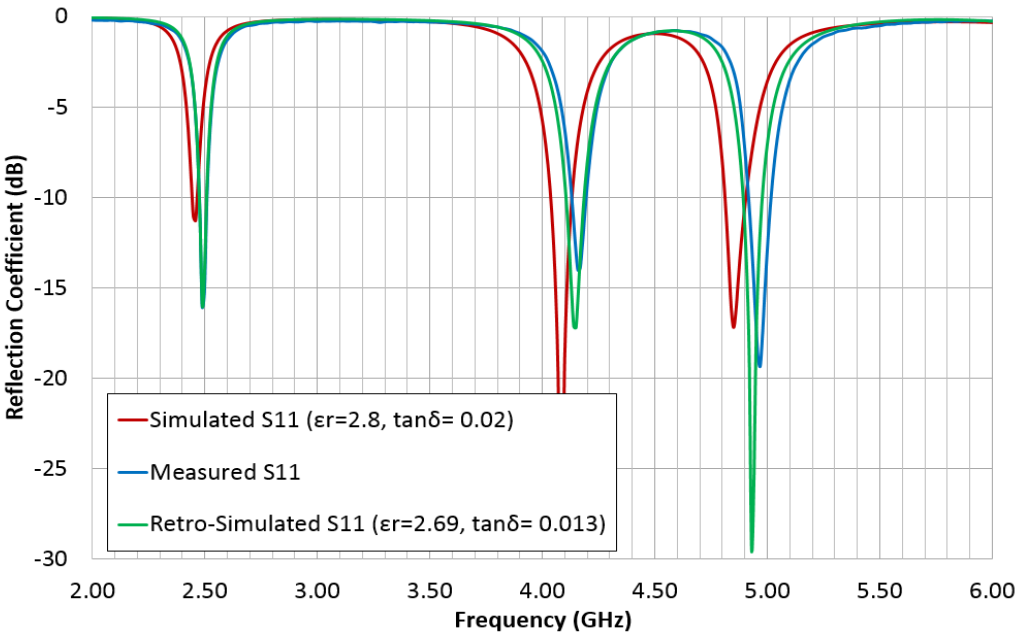

Figure Appendix-4: Simulated, Measured and Retro-Simulated Return Loss of the patch antenna.